

**^{17}O and ^{63}Cu NMR Study of Spin Dynamics in
Low-dimensional Spin 1/2 Antiferromagnets**

by

Kent R. Thurber

Submitted to the Department of Physics
in partial fulfillment of the requirements for the degree of

Doctor of Philosophy

at the

MASSACHUSETTS INSTITUTE OF TECHNOLOGY

September 1999

© Massachusetts Institute of Technology 1999. All rights reserved.

Author

Department of Physics

September 2, 1999

Certified by

Takashi Imai

Assistant Professor of Physics

Thesis Supervisor

Accepted by

Thomas J. Greytak

Professor, Associate Department Head for Education

^{17}O and ^{63}Cu NMR Study of Spin Dynamics in Low-dimensional Spin 1/2 Antiferromagnets

by

Kent R. Thurber

Submitted to the Department of Physics
on August 15, 1999, in partial fulfillment of the
requirements for the degree of
Doctor of Philosophy

Abstract

^{63}Cu and ^{17}O nuclear magnetic resonance (NMR) and nuclear quadrupole resonance (NQR) experiments are reported on copper-oxide compounds related to high temperature superconductors that are nearly ideal realizations of spin 1/2 Heisenberg antiferromagnets with different geometries of the magnetic interactions: 1 dimensional spin chains, 2 dimensional planes, two coupled chains (two-leg ladder), and three coupled chains (three-leg ladder). Comparison of the spin-lattice relaxation rate, $1/T_1$, for ^{63}Cu and ^{17}O reveals the wave-vector, q , dependence of low-energy magnetic fluctuations, and $1/T_{2G}$, the Gaussian spin-spin relaxation rate provides information about the electron spin correlation length, ξ . In the 1d material, Sr_2CuO_3 , $^{17}\text{O} 1/T_1(q=0) \propto aT + bT^2$ over the whole temperature range 10 to 700 K. Frequency dependence measurements show that diffusive contributions dominate $T_1(q \approx 0)$ for the double chain 1d material, SrCu_2O_7 . For the undoped 2d copper oxide material, $\text{Sr}_2\text{CuO}_2\text{Cl}_2$, we demonstrate that $^{17}\text{O} 1/T_1$ measures the spin wave damping in the undoped antiferromagnet for short wavelengths. We find that the spin wave damping is small, clarifying one of the unique properties of these 2d copper-oxide antiferromagnetic materials: there is a wide temperature range where short range spin excitations exist with long lifetimes, without long range 3-dimensional order. The two-leg ladder materials, SrCu_2O_3 and $\text{A}_{14}\text{Cu}_{24}\text{O}_{41}$ ($\text{A} = \text{La}, \text{Sr}, \text{Ca}$), have a large energy gap for spin excitations. There is a crossover in magnetic fluctuations from temperatures below the spin gap to above the spin gap. For the doped two-leg ladders, the effective doping of the ladders changes with temperature, and this temperature is correlated to the magnetic spin gap energy. The three-leg ladder material, $\text{Sr}_2\text{Cu}_3\text{O}_5$, demonstrates a crossover in the temperature dependence of the spin correlation length, ξ . At high temperatures, we find the $\xi \sim 1/T$ behavior characteristic of a 1d structure (isolated three-leg ladders). At lower temperatures, the spin correlation length diverges exponentially, which suggests that weak coupling between ladders is creating an effective 2d system.

Thesis Supervisor: Takashi Imai
Title: Assistant Professor of Physics

Acknowledgments

I would especially like to thank everyone that I have had the opportunity to work with here at MIT. This includes Philip Singer, Kyle Shen, Allen Hunt, and Prof. Takashi Imai. Their assistance was often invaluable. Specifically, Kyle Shen did great work on some of the doped 2 leg ladder compounds for his undergraduate thesis. In addition, Kyle has allowed me to modify a few of the figures he used for his undergraduate thesis to use here. For most of my time as a graduate student, Allen Hunt has also been here. It has been a great benefit to be able to work with and discuss with Allen.

Scientifically, I would like to thank Prof. Cory for letting us use his 14 T magnet for field dependence experiments. Of course, in order to do these experiments, the material growth is essential. Young Lee provided crystal samples to help get our first (2d) project started. Dr. F.C. Chou provides invaluable help as a local expert in crystal growth at MIT. He provided crystals of the 1d compounds. From Kyoto University, the group of T. Saitoh, M. Azuma, M. Takano provided the $\text{Sr}_2\text{Cu}_3\text{O}_5$ and SrCu_2O_3 samples. Prof. M. Matsuda gave us single crystals of several of the doped 2-leg ladder compounds. Also, various theorists have been helpful including Profs. Anders Sandvik, Peter Kopietz, and Subir Sachdev.

Most important has been the personal support of friends and family. I thank my parents for being constantly supportive. I also thank Karrie Karahalios and Tinchuck Agnes Ng for the time we could spend together, discussing anything and everything.

Contents

1	Introduction	14
2	Nuclear Magnetic Resonance and Nuclear Quadrupole Resonance	20
2.1	NMR/NQR Frequency (Knight shift)	21
2.2	Nuclear Quadrupole Interaction	24
2.3	$1/T_1$, Spin Lattice Relaxation Rate	26
2.4	Hyperfine form factor	31
2.5	$1/T_2$, Spin-Spin Relaxation Rate	34
2.6	NMR Electronics	40
2.7	Summary	44
3	Summary and Crystal Structure	45
3.1	Crystal Structure	46
4	1d $S=1/2$ Heisenberg Antiferromagnet	56
4.1	Crystal Structure of Sr_2CuO_3 and $SrCuO_2$	57
4.2	Knight shift	62
4.3	Oxygen T_1 in Sr_2CuO_3	74
4.4	Oxygen T_1 in $SrCuO_2$	79
4.5	Copper T_1 and T_{2G}	82
4.6	Spin diffusion	85
4.7	1d summary	90

5	2 dimensional S=1/2 Heisenberg Antiferromagnet	93
5.1	Theoretical Studies	94
5.1.1	Quantum nonlinear σ model	95
5.1.2	Classical-based models	97
5.2	Crystal structure of $\text{Sr}_2\text{CuO}_2\text{Cl}_2$	98
5.2.1	$\text{Sr}_2\text{CuO}_2\text{Cl}_2$ sample preparation	99
5.2.2	NMR/NQR lineshapes	101
5.3	Knight shift	102
5.4	Copper $1/T_1$ and $1/T_{2G}$	112
5.5	Oxygen $1/T_1$	120
5.6	Doped CuO_2 planes	129
5.7	2d summary	133
6	2-leg Spin Ladders	134
6.1	Structure & Experimental Details	137
6.2	Knight shift	138
6.3	T_1 & T_{2G}	146
6.4	Charge Effects	152
6.5	Summary	163
7	Three-leg ladder, $\text{Sr}_2\text{Cu}_3\text{O}_5$	164
7.1	Structure & Experimental Details	166
7.2	$1/T_1$ and $1/T_{2G}$	171
7.3	Anisotropic 2d model	178
8	Conclusions	183
A	$1/T_1$ and $1/T_{2L}$ for NQR, $\eta \neq 0$, $I=3/2$	187
A.1	$1/T_{2L}$ for $\eta \neq 0$	191
B	$1/T_{2G}$ NQR for unaligned samples	194

List of Figures

1-1	Basic phase diagram of $\text{La}_{2-x}\text{Sr}_x\text{CuO}_4$	16
1-2	Qualitative mechanism for hole pairing in antiferromagnetic lattice.	17
1-3	Magnetic structures studied in this thesis: (a) 1-d spin chain, (b) 2-d plane, (c) 2-leg ladder, (d) 3-leg ladder.	19
2-1	NMR energy levels and spectra $I=3/2$	22
2-2	NQR energy levels and resonance spectra for spin $I=3/2$	23
2-3	Diagram of $1/T_1$ measurement	27
2-4	RF pulse sequences used for measuring $1/T_1$ and $1/T_{2G}$	28
2-5	Example of T_1 measurement.	28
2-6	Typical hyperfine form factors, $F(q)$	34
2-7	Example of $1/T_2$	35
2-8	Indirect nuclear spin-spin coupling	37
2-9	Example of indirect nuclear spin-spin coupling.	38
2-10	Schematic of electronics for NMR spectrometer, Imai Labs.	42
3-1	Summary of ^{63}Cu $1/T_1$	46
3-2	Summary of ^{63}Cu $1/T_{2G}$	47
3-3	Monte Carlo data for ξ	47
3-4	Structure of the copper-oxide layer of the 3-leg ladder, $\text{Sr}_2\text{Cu}_3\text{O}_5$	48
3-5	Electron energy levels for Cu 3d orbitals. [31]	49
3-6	Superexchange mechanism.	50
4-1	Crystal structure of SrCuO_2 and Sr_2CuO_3	59

4-2	Detailed structure of the Cu-O chains	60
4-3	^{17}O NMR spectra for Sr_2CuO_3	61
4-4	^{17}O NMR spectra for SrCuO_2	61
4-5	^{17}O Knight shift Sr_2CuO_3	63
4-6	^{63}Cu Knight shift Sr_2CuO_3	64
4-7	^{17}O Knight shift SrCuO_2	64
4-8	^{63}Cu Knight shift SrCuO_2	65
4-9	$K-\chi$ for ^{17}O in Sr_2CuO_3	66
4-10	$K-\chi$ for ^{63}Cu in Sr_2CuO_3	67
4-11	$K-\chi$ for ^{17}O in SrCuO_2	68
4-12	$K-\chi$ for ^{63}Cu in SrCuO_2	69
4-13	^{63}Cu NMR central linewidth c axis for Sr_2CuO_3	70
4-14	^{17}O NMR central linewidth c axis for Sr_2CuO_3	70
4-15	Copper quadrupole interaction, $\nu_{Q,a}$, for Sr_2CuO_3	71
4-16	High temp. Knight shift of ^{17}O chain site of Sr_2CuO_3	73
4-17	Low temp. Knight shift of ^{17}O chain site and $1/T_1$ of apical site of Sr_2CuO_3	75
4-18	^{17}O $1/(T_1 T)$ for Sr_2CuO_3	76
4-19	Quantum Monte Carlo results for the $S=1/2$ 1d Heisenberg antiferro- magnet	77
4-20	Quantum Monte Carlo results for $1/T_1$ for different values of R	78
4-21	^{17}O $1/T_1$ for SrCuO_2	83
4-22	$1/(T_1 T)$ ($q=0$) for SrCuO_2	84
4-23	^{17}O $1/T_1$ for apical oxygen, SrCuO_2 and Sr_2CuO_3	84
4-24	^{63}Cu $1/T_1$ for Sr_2CuO_3	86
4-25	^{63}Cu $1/T_{2G}$ for Sr_2CuO_3	86
4-26	^{63}Cu $1/T_1$ for SrCuO_2	87
4-27	^{63}Cu $1/T_{2G}$ for SrCuO_2	87
4-28	Field dependence of $1/T_1$ for SrCuO_2	91
4-29	Field dependence of $1/T_1$ for Sr_2CuO_3	92

5-1	Phase diagram for the quantum nonlinear σ model	96
5-2	Crystal structure for $\text{Sr}_2\text{CuO}_2\text{Cl}_2$	100
5-3	^{35}Cl NMR	101
5-4	Cu NMR lineshape for $\text{Sr}_2\text{CuO}_2\text{Cl}_2$	103
5-5	Cu NQR lineshape for $\text{Sr}_2\text{CuO}_2\text{Cl}_2$	103
5-6	^{17}O NMR lineshape for $\text{Sr}_2\text{CuO}_2\text{Cl}_2$	104
5-7	^{17}O Knight shift for $\text{Sr}_2\text{CuO}_2\text{Cl}_2$	105
5-8	^{63}Cu Knight shift for $\text{Sr}_2\text{CuO}_2\text{Cl}_2$	106
5-9	Determination of K_{chem} and hyperfine interactions	107
5-10	K-chi: Knight shift as a function of bulk susceptibility	108
5-11	Uniform susceptibility theory for the $S=1/2$ 2d Heisenberg antiferromagnet	110
5-12	Comparison of experimental susceptibility	110
5-13	$^{63}\text{Cu}/T_1$ and $^{63}\text{Cu}/T_{2G}$ for $\text{Sr}_2\text{CuO}_2\text{Cl}_2$	113
5-14	$^{63}\text{Cu}/(T_1 T^{3/2})$ and $^{63}\text{Cu}/(T_{2G} T)$ for $\text{Sr}_2\text{CuO}_2\text{Cl}_2$	115
5-15	^{63}Cu ($J/T_1 T$) for $\text{Sr}_2\text{CuO}_2\text{Cl}_2$ and La_2CuO_4	116
5-16	^{63}Cu (J/T_{2G}) for $\text{Sr}_2\text{CuO}_2\text{Cl}_2$ and La_2CuO_4	117
5-17	$^{63}\text{Cu}(1/T_1)$ for $\text{Sr}_2\text{CuO}_2\text{Cl}_2$ with theoretical results.	118
5-18	$^{63}\text{Cu}/T_1$ $q=0$ contribution	119
5-19	Quantum Monte Carlo results from Sandvik and Scalapino [67].	119
5-20	$^{63}\text{Cu}/T_{2G}$ for $\text{Sr}_2\text{CuO}_2\text{Cl}_2$ with theoretical results.	120
5-21	$^{17}\text{O}/(T_1 T)$ for $\text{Sr}_2\text{CuO}_2\text{Cl}_2$	121
5-22	Hyperfine form factors and $1/T_1$ for O and Cu	122
5-23	Monte Carlo results for the spin structure factor (2d)	123
5-24	Quantum Monte Carlo results for spin-wave frequencies and damping	125
5-25	Wavevector dependence of $\Gamma(\mathbf{q})$	125
5-26	Dependence of $1/T_1$ on Γ	127
5-27	Spin wave damping, Γ	128
5-28	$^{63}\text{Cu}(1/T_1)$ for $\text{La}_{2-x}\text{Sr}_x\text{CuO}_4$ [7].	129
5-29	$^{17}\text{O} J/(T_1 T)$ for $\text{Sr}_2\text{CuO}_2\text{Cl}_2$ and for $\text{La}_{2-x}\text{Sr}_x\text{CuO}_4$	130

5-30	Spin correlation length for lightly doped $\text{La}_{2-x}\text{Sr}_x\text{CuO}_4$ (Keimer, <i>et al.</i>)	131
5-31	Comparison of Stoner excitations and spin waves	132
6-1	Structure of Cu-O layer for 2 leg ladder materials	135
6-2	Magnon dispersion of 2 leg ladder	135
6-3	Dynamical spin structure factor, $S(q, \omega)$	136
6-4	Crystal structure of SrCu_2O_3	138
6-5	Crystal structure of $\text{Sr}_{14}\text{Cu}_{24}\text{O}_{41}$	139
6-6	Cu NMR lineshape of $\text{Sr}_{11}\text{Ca}_3\text{Cu}_{24}\text{O}_{41}$	140
6-7	O NMR lineshape of $\text{Sr}_6\text{Ca}_8\text{Cu}_{24}\text{O}_{41}$	141
6-8	^{63}Cu NQR lineshape of SrCu_2O_3	142
6-9	$^{17}\text{O}(2)$ rung site Knight shift	143
6-10	^{63}Cu $1/T_{1,\perp\text{Cu-Plane}}$ for undoped 2-leg ladders	144
6-11	Knight shift ratio for La_6Ca_8 and Sr_{14}	146
6-12	Doping dependence of $1/T_1$ and $^{17}\nu_Q(1)b$	148
6-13	^{63}Cu $1/T_{1b}$ [\circ]	150
6-14	Normalized $1/T_1$	151
6-15	^{63}Cu $1/T_{1b}$ for $\text{La}_5\text{Sr}_1\text{Ca}_8\text{Cu}_{24}\text{O}_{41}$ and $\text{La}_6\text{Ca}_8\text{Cu}_{24}\text{O}_{41}$	152
6-16	^{63}Cu $1/T_{2G}$ for SrCu_2O_3 and $\text{Sr}_{14}\text{Cu}_{24}\text{O}_{41}$	153
6-17	$^{17}\nu_{Q,b}$ for the O(2) rung site	154
6-18	^{17}O η $\text{Sr}_{14}\text{Cu}_{24}\text{O}_{41}$	154
6-19	Ladder ^{63}Cu NQR line in $\text{Sr}_{14}\text{Cu}_{24}\text{O}_{41}$. [111])	155
6-20	Resistivity, ρ , data for $\text{Sr}_{14-x}\text{Ca}_x\text{Cu}_{24}\text{O}_{41}$ [119]	160
6-21	Ratio of $1/T_1$ for the two Cu isotopes	161
6-22	Chain ^{63}Cu $1/T_1$ from Takigawa, <i>et al.</i> [112]	162
6-23	Summary of doped 2-leg ladder	163
7-1	Proposed stripe order at 1/8 doping [8].	165
7-2	Structure of three leg ladder material, $\text{Sr}_2\text{Cu}_3\text{O}_5$	167
7-3	$^{63,65}\text{Cu}$ NQR lineshape for the edge chain copper site	168
7-4	Temperature dependence of the ^{63}Cu edge chain NQR resonance.	168

7-5	Cu NMR lineshape for $\text{Sr}_2\text{Cu}_3\text{O}_5$	169
7-6	^{63}Cu NMR central transition	169
7-7	$1/T_{1c}$ for both Cu sites	170
7-8	$1/T_{2G}$ for both Cu sites	171
7-9	^{63}Cu $1/T_1$ from NQR and NMR	172
7-10	^{63}Cu $1/T_{2G}$ from NQR and NMR	173
7-11	log-log plot of $^{63}\text{T}_{2G}$ for both ladders	175
7-12	$1/(T_{1c}T^{3/2})$ and $1/(T_{2G}T)$ for three-leg and 2d	176
7-13	$^{63}1/T_1$ for infinite layer compound, $\text{Ca}_{0.85}\text{Sr}_{0.15}\text{CuO}_2$	177
7-14	Ratio of T_1 and T_{2G}	181
A-1	NQR energy level diagram for the $I=3/2$ eigenstates with transition rates, W_{km} shown.	189
B-1	Geometry of H_1 and quadrupole	196
B-2	Phase space for H_1 angle	198

List of Tables

4.1	Magnitude of quadrupole interaction [kHz] measured at room temperature	60
4.2	Calculated quadrupole interaction point charge [kHz]	62
4.3	Oxygen hyperfine couplings (q=0) [kOe/ μ_B]	63
4.4	Copper hyperfine couplings at q=0 [kOe/ μ_B]	64
4.5	K_{chem} [%]	72
4.6	$1/T_1$ for different crystal axes [sec^{-1}]	80
5.1	Oxygen hyperfine coupling at q=0, (2C) [kOe/ μ_B]	105
5.2	Copper hyperfine couplings [kOe/ μ_B]	106
5.3	Chemical Knight shifts [%]	106
6.1	Magnitude of quadrupole interaction [kHz] measured at room temperature	158
6.2	Additional holes in ladder layer orbitals of $\text{Sr}_{14}\text{Cu}_{24}\text{O}_{41}$ at 500 K deduced from temperature dependence of ν_Q	159

Chapter 1

Introduction

High temperature superconductivity was discovered by Bednorz and Müller in 1986 [1]. Before the discovery of high temperature superconductivity, the highest superconducting transition temperature (T_c) of known materials was less than 25 K. Following the initial discovery of $\text{La}_{2-x}\text{Ba}_x\text{CuO}_4$ with $T_c \approx 30$ K, many related copper oxide superconducting materials were found with even higher superconducting transition temperatures. Within just a few years, copper oxides were discovered with transition temperatures well above the boiling point of liquid nitrogen (77 K), for example $\text{HgBa}_2\text{Ca}_2\text{Cu}_3\text{O}_x$ ($T_c = 133$ K). Because liquid nitrogen is much less expensive than cooling to lower temperatures with liquid helium, this greatly expands the applications of superconducting materials. High temperature superconducting materials are used in such applications as radiofrequency switches for cellular phone base stations and sensitive SQUID magnetic field sensors.

The high transition temperature also challenges the effort to explain the superconductivity in these materials. The Bardeen-Cooper-Schrieffer (BCS) theory [2] explained conventional superconductors based on pairing of electrons by the electron-phonon coupling. However, the BCS theory is not expected to be able to explain superconductivity which occurs at such high temperatures. As a result, interest in determining the mechanism behind high T_c superconductivity is high.

The material properties of the high T_c superconductors are also very different from the conventional BCS superconductors. Conventional BCS superconductors are

normal metals above the superconducting transition temperature. The behavior of high temperature superconductors is much more difficult to describe by conventional condensed matter theory. An important common feature of the high T_c superconductors is a 2 dimensional CuO_2 layer [3]. In the undoped compounds, the copper atoms each have a hole in the $3d_{x^2-y^2}$ orbital, leaving one unpaired electron spin. From a simple non-interacting electron band picture, these materials would be metallic because of the half-filled 3d band. However, the undoped materials are not metallic presumably because of strong Coulomb repulsion between the electrons. The undoped materials are insulators with an unpaired electron spin localized on the copper atoms. Experiments [4, 5, 6] have shown that these unpaired electron spins have strong antiferromagnetic interaction with one another. The strong magnetism of the copper-oxide superconductors is unusual in contrast to conventional superconductors, where magnetic impurities disrupt the superconductivity. The undoped CuO_2 planes have been shown to be a nearly ideal experimental realization of the 2 dimensional spin 1/2 Heisenberg antiferromagnet on a square lattice [6, 3]. The copper electron spins have an isotropic antiferromagnetic interaction with their nearest neighbors in the square lattice CuO_2 plane with exchange coupling, $J \sim 1500$ K.

$$\mathcal{H} = J \sum_{i,\delta} S_i \cdot S_{i+\delta} \quad (1.1)$$

Such a strong antiferromagnetic interaction raises the possibility that the magnetism is associated with the superconducting pairing. The phase diagram as a function of temperature and hole doping is shown in figure 1-1 for a typical high T_c superconductor, $\text{La}_{2-x}\text{Sr}_x\text{CuO}_4$. The undoped material is an antiferromagnetic insulator, but doping only $x = 5\%$ of holes is enough for superconductivity to occur. The occurrence of superconductivity for such a small amount of doping is suggestive that the magnetism is important for the superconductivity. This argument is also supported by the fact that superconductivity disappears if the doping is too high ($\sim 25\%$ for $\text{La}_{2-x}\text{Sr}_x\text{CuO}_4$). The increased hole doping could destroy spin correlations needed for superconductivity. Antiferromagnetic spin fluctuations persist even

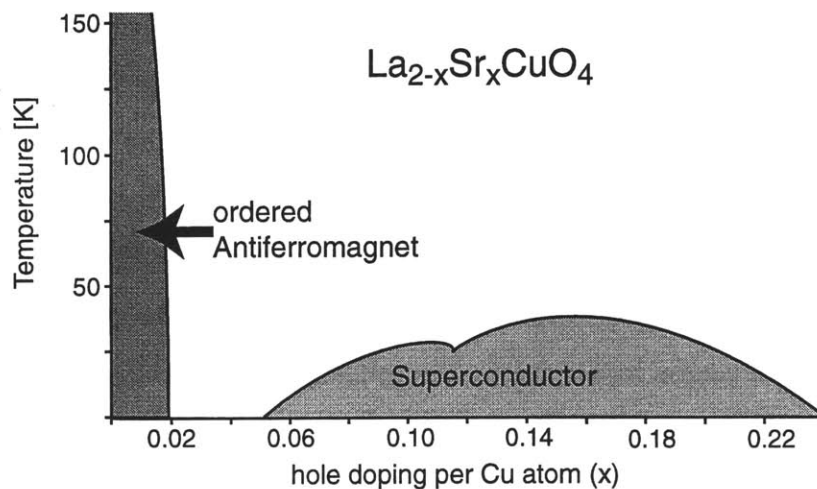


Figure 1-1: Basic phase diagram of $\text{La}_{2-x}\text{Sr}_x\text{CuO}_4$, typical high T_c superconductor.

in the region of doping where superconductivity occurs [7, 8]. It seems very likely that the spin correlations are important for high T_c superconductivity.

A non-rigorous but suggestive example of the possibility of how the antiferromagnetic spin correlations could promote a superconducting pairing interaction is shown in figure 1-2 [9]. In a lattice with antiferromagnetically ordered spins, one hole hopping through the lattice disturbs the antiferromagnetic order. The electron spins along the path of the hole have ended up pointing in the same direction as their neighbors, which is the higher energy state. However, if a second hole follows the same path through the lattice, the antiferromagnetic order is restored. This suggests the possibility that hole pairing may be promoted by the antiferromagnetic spin correlations.

Understanding the low-dimensional antiferromagnetism of various copper-oxide materials in low dimensions may help in describing the mechanism of high temperature superconductivity. This thesis describes nuclear magnetic resonance (NMR) and

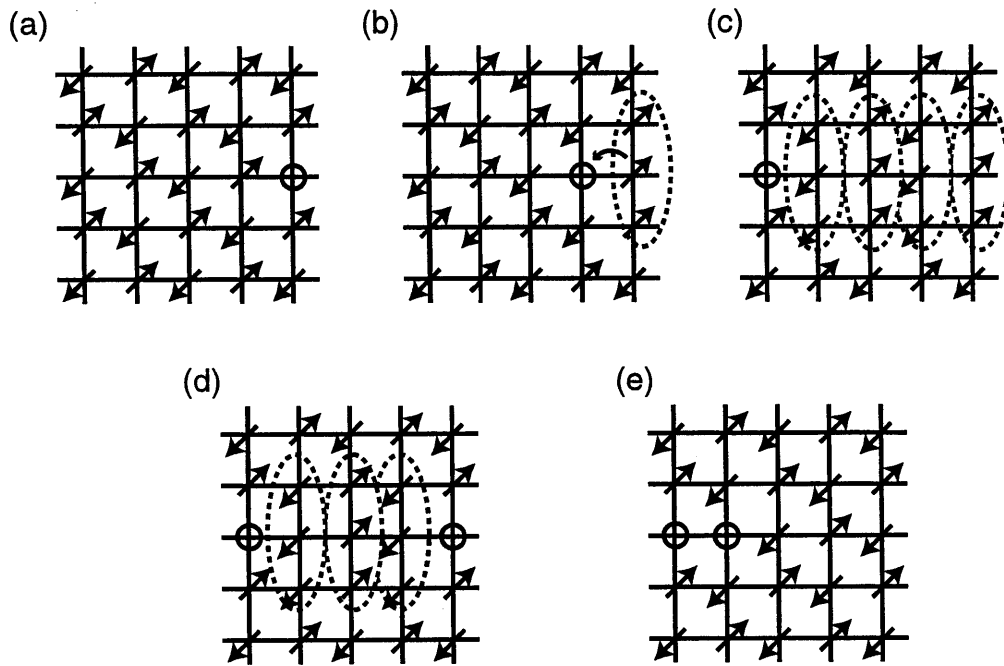




Figure 1-2: Qualitative mechanism for hole pairing in antiferromagnetic lattice. (a),(b),(c): One hole hopping across an antiferromagnetically ordered lattice of spins leaves behind unfavorable (high-energy) ferromagnetic spin bonds (marked with dashed ovals). (d),(e): If a second hole follows the same path across the lattice, the antiferromagnetic ordering is restored.[9]

nuclear quadrupole resonance (NQR) experiments on undoped copper-oxide materials similar to high temperature superconductors. The primary interest is in studying the magnetism of these materials over a wide temperature range. These materials are very good experimental realizations of low-dimensional spin 1/2 Heisenberg antiferromagnets with different geometries of the magnetic interactions. Figure 1-3 shows the different magnetic geometries studied in this thesis: 1 dimensional spin chain, 2 dimensional plane, two-leg ladders (two coupled chains), and three-leg ladders (three coupled chains).

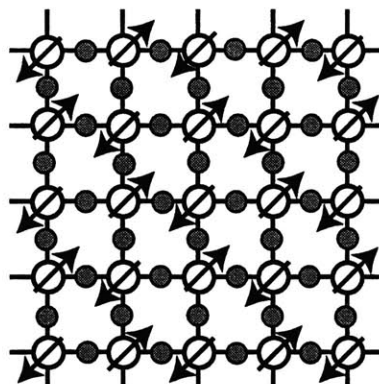
The outline of this thesis is as follows. The next chapter (Ch. 2) will describe nuclear magnetic resonance measurements. Chapter 3 gives a brief summary of the overall results and discusses common aspects of the crystal structure of these materials. Then, the following chapters will each focus on the materials with a specific geometry of the magnetic interaction. Chapter 4 describes the 1 dimensional spin chain materials, Sr_2CuO_3 and SrCuO_2 . Chapter 5 describes the 2 dimensional material, $\text{Sr}_2\text{CuO}_2\text{Cl}_2$. Some experiments on doped $(\text{La,Sr})_2\text{CuO}_4$ are discussed. Chapter 6 covers the two-leg ladder materials, SrCu_2O_3 and $\text{A}_{14}\text{Cu}_{24}\text{O}_{41}$ ($\text{A} = \text{La,Sr,Ca}$). The effects of doping are discussed for the $\text{A}_{14}\text{Cu}_{24}\text{O}_{41}$ compounds. Chapter 7 describes the three-leg ladder material, $\text{Sr}_2\text{Cu}_3\text{O}_5$. Chapter 8 summarizes the conclusions of this thesis.

 Copper atom (with spin 1/2)
 Oxygen atom

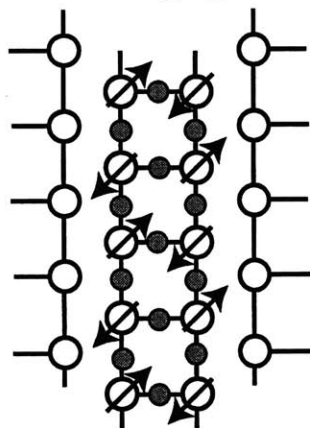
(a) 1 dimensional chain
(Sr_2CuO_3)



(b) 2 dimensional plane
square lattice
($\text{Sr}_2\text{CuO}_2\text{Cl}_2$)



(c) 2 leg ladder
(2 coupled chains)
(SrCu_2O_3)



(d) 3 leg ladder
(3 coupled chains)
($\text{Sr}_2\text{Cu}_3\text{O}_5$)

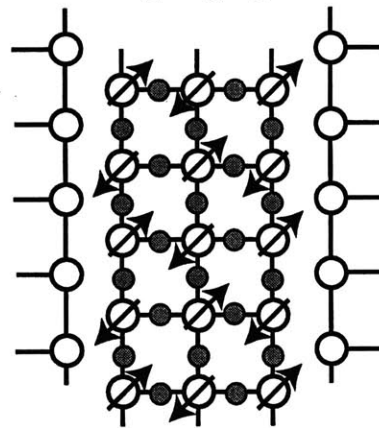


Figure 1-3: Magnetic structures studied in this thesis: (a) 1-d spin chain, (b) 2-d plane, (c) 2-leg ladder, (d) 3-leg ladder.

Chapter 2

Nuclear Magnetic Resonance and Nuclear Quadrupole Resonance

Nuclear magnetic resonance (NMR) and nuclear quadrupole resonance (NQR) are techniques used to manipulate and measure the behavior of the magnetic moment (spin) of the atomic nuclei. The magnetic moment and quadrupole moment of the nucleus are local probes, allowing measurement of the magnetic field and electric field gradient, respectively, at the position of the nucleus. Because NMR and NQR probe magnetic and electric fields at the position of the nucleus, comparison of measurements for different atomic nuclei will show the microscopic structure of charge and spin. This is a major strength of NMR and NQR because it provides answers to questions about where in the crystal structure do the doped holes or unpaired electron spins reside. Also, we can discover what roles the carriers play in connection with the macroscopic electronic properties.

For the NMR and NQR experiments described in this thesis, the atomic nuclei are used as probes into the static and dynamic properties of the electron spin and charge system. As described below, the nuclear magnetic resonance frequency provides information about the static magnetism, while the nuclear quadrupole frequency measures the charge environment. Dynamic properties are reflected in the nuclear spin-lattice relaxation rate, $1/T_1$. T_1 is the time scale for the nuclear spin system to return to thermal equilibrium. This time scale reflects the density of low energy fluctuations of

the electronic system. The Gaussian component of the nuclear spin-spin relaxation rate, $1/T_{2G}$ reflects the coupling between the nuclear spins. In these copper oxide materials, the coupling between the copper nuclear spins is enhanced by the strong magnetic correlations between the electron spins.

2.1 NMR/NQR Frequency (Knight shift)

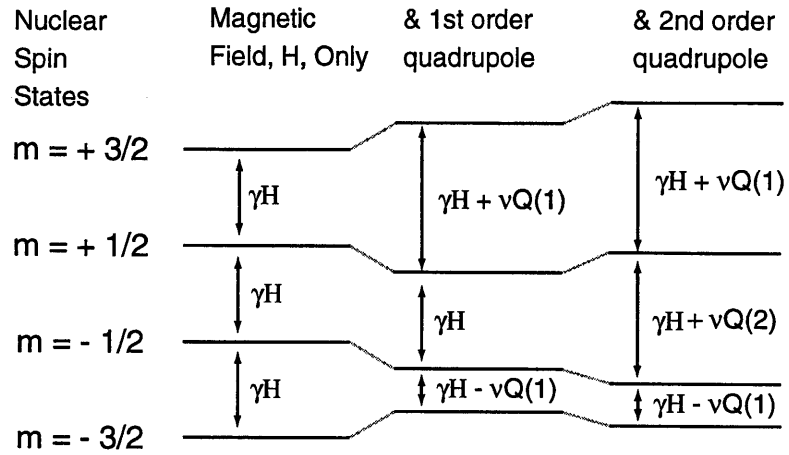
For nuclear magnetic resonance, we apply an external magnetic field, H (typically in our experiments 9 Tesla). This magnetic field interacts with the nuclear magnetic moment, μ , as

$$\mathcal{H}_{magnetic} = -\mu \cdot H_{local} \quad (2.1)$$

where H_{local} is the magnetic field at the position of the atomic nucleus. This interaction produces $2I + 1$ energy levels for nuclear spin I as shown in part (a) of figure 2-1 for spin $I = 3/2$. The $2I$ transitions between these energy levels all have energy, $E = \hbar\omega_n = \mu H_{local}/I$ with the resonance frequency ω_n . We note that while these transitions have the same energy from the magnetic interaction, the nuclear quadrupole interaction can alter the energies.

The difference between the local magnetic field, H_{local} , and the applied magnetic field, H , is a measure of the local magnetic susceptibility of the material. This difference is usually referred to as the Knight shift, K , so that $H_{local} = (1 + K)H$. The Knight shift, K , (frequency shift) accounts for the fact that the internal magnetic field at the position of the nucleus, H_{local} , will be slightly different than the applied external magnetic field, H . The Knight shift measures the magnetic susceptibility of the material at the position of the nucleus in response to the uniform applied field. The contributions to the uniform magnetic susceptibility can be broken into three parts. Most important for our purposes is the electron spin susceptibility, $\chi'(\mathbf{q} = \mathbf{0})_{spin}$. Also, contributing to the susceptibility are the electron orbital (Van Vleck) and diamagnetic susceptibility [10]. The diamagnetic susceptibility is a quantum mechanical effect that arises from the diamagnetic shielding current of the electrons [10]. The diamagnetic susceptibility does not have any temperature dependence. The orbital

(a) NMR energy levels



(b) NMR resonance spectra

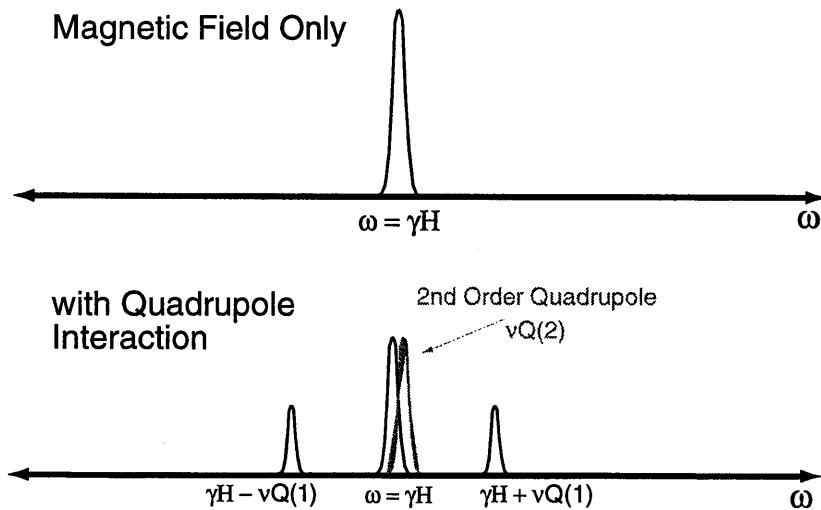


Figure 2-1: (a) Energy levels for NMR with spin $I=3/2$ nucleus. (b) NMR resonance spectra for spin $I=3/2$.

NQR energy levels and resonance spectra

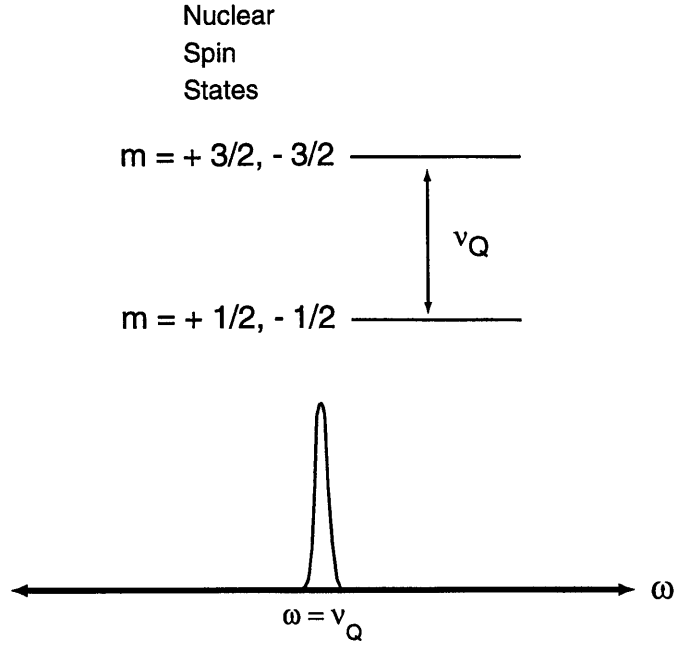


Figure 2-2: NQR energy levels and resonance spectra for spin $I=3/2$.

susceptibility arises from the mixing of the atomic energy levels in the presence of the magnetic field. In a particular crystal structure, the atomic energy levels are split by the crystal electric field splitting. In the presence of a perturbing magnetic field, these atomic orbitals are no longer eigenstates and a small amount of mixing of these atomic orbitals occurs. From perturbation theory, the orbital susceptibility is [10]

$$\chi_{orbital} = \frac{N}{V} 2\mu_B^2 \sum_n \frac{|\langle 0 | (L_z + g_0 S_z) | n \rangle|^2}{E_n - E_0} \quad (2.2)$$

The important fact is that because the energy separation between the atomic orbitals, $E_n - E_0$, caused by the crystal field is about an eV = 11,600 K, the orbital susceptibility will not have significant temperature dependence. Thus, the only part of the susceptibility with temperature dependence is the electron spin susceptibility, $\chi'(\mathbf{q} = \mathbf{0})_{spin}$. The susceptibility is related to the Knight shift as [11],

$$K = \frac{F(\mathbf{q} = \mathbf{0})}{N_A \mu_B} \chi'(\mathbf{q} = \mathbf{0})_{spin} + K_{orbital} + K_{dia} \quad (2.3)$$

$K_{orbital}$ and K_{dia} are the Knight shifts arising from the orbital and diamagnetic susceptibility, respectively. $F(\mathbf{q} = \mathbf{0})$ is the hyperfine coupling between the electron spin and the nuclear spin with wavevector $q = 0$. We can extract the hyperfine coupling by using the fact that only the electron spin susceptibility has significant temperature dependence. Therefore, any temperature dependence of the Knight shift arises from the spin susceptibility and the hyperfine coupling can be expressed as,

$$F(\mathbf{q} = \mathbf{0}) = N_A \mu_B \frac{\Delta K}{\Delta \chi'(\mathbf{q} = \mathbf{0})} \quad (2.4)$$

If we plot the Knight shift as a function of the bulk uniform susceptibility, χ' , with temperature as an implicit parameter, the slope corresponds to the hyperfine coupling, $F(\mathbf{q} = \mathbf{0})$. The hyperfine coupling between the electron spin and the nuclei spin expresses how much interaction energy there is between the spins, or alternatively, how much magnetic field is produced at the location of the nucleus by an electron spin.

2.2 Nuclear Quadrupole Interaction

In addition to magnetic interactions, the atomic nucleus will also interact with the charge environment through the charge of the nucleus. The simplest way to express the charge interactions is by the multipole expansion of the charge distribution in spherical harmonics of order l . Obviously, the nuclei has a charge monopole moment ($l = 0$), Ze , which interacts with the electric field. However, this interaction is independent of the direction of the spin of the nucleus, so the spin transitions do not show this interaction. The next moment, an electric dipole moment ($l = 1$), is prohibited by the fact that nuclear states have well-defined parity. In fact, this prohibits any charge multipoles with odd l .

The quadrupole moment ($l = 2$), Q , is allowed and is defined as [12]

$$eQ = \frac{1}{2} \int (3z^2 - r^2) \rho(\mathbf{r}) d^3x \quad (2.5)$$

where $\rho(\mathbf{r})$ is the charge distribution of the nucleus in its $I_z = I$ state. Physically, the quadrupole moment represents the deviation of the charge distribution of the nucleus from spherical symmetry. A “pancake” shaped charge distribution will have a negative quadrupole moment, while a “rocket-ship” shaped charge distribution will have a positive quadrupole moment.

Higher order moments of the charge distribution probably do exist, but the interaction effects become smaller very rapidly for higher orders. The interaction strength is expected to decrease roughly as [13]

$$\left(\frac{R_n}{R_e}\right)^l \approx (10^{-5})^l \quad (2.6)$$

where R_n is the radius of the nucleus and R_e is the radius of the electron distribution. This very rapid decrease in the interaction strength is clearly seen in the comparison of the $l = 0$ monopole and $l = 2$ quadrupole interactions. The monopole interaction between the charge of the nucleus and the electrons will be of order 10 eV, while a typical quadrupole interaction is of order 10 MHz $\sim 10^{-8}$ eV.

The quadrupole moment of the nucleus interacts with the electric field gradient at the position of the nucleus, and thus probes the local charge environment. The nuclear quadrupole Hamiltonian is [13]

$$\mathcal{H}_Q = h\nu_Q^z [3I_z^2 - I(I+1) + \frac{1}{2}\eta(I_+^2 + I_-^2)] \quad (2.7)$$

$$\nu_Q^z = \frac{e^2 q_z Q}{h4I(2I-1)} \quad (2.8)$$

where Q is the quadrupole moment of the nucleus and I is the spin of the nucleus ($I=3/2$ for $^{63,65}\text{Cu}$, $I=5/2$ for ^{17}O). eq_z is the electric field gradient at the site of the nucleus along the principle axis z of the tensor, i.e. $eq_z = \frac{\delta^2 V}{\delta z^2}$, where V is the electrostatic potential. The electric field gradient along the three principle axes of the tensor will sum to zero, because of the Laplace equation for the electrostatic potential.

$$\frac{\delta^2 V}{\delta x^2} + \frac{\delta^2 V}{\delta y^2} + \frac{\delta^2 V}{\delta z^2} = 0 \quad (2.9)$$

This implies that the three principle components of the quadrupole interaction will also sum to zero. The asymmetry parameter, η , is the deviation of the electric field gradient tensor from axial symmetry.

$$\eta = \left| \frac{\nu_Q^x - \nu_Q^y}{\nu_Q^z} \right| \quad (2.10)$$

In nuclear quadrupole resonance (NQR), we do not apply any magnetic field and use just the quadrupole interaction. The resonance frequency for an NQR experiment for $I=3/2$ is given by the separation of the two eigenstates of eq. 2.7 (figure 2-2)

$$\nu_Q = \nu_Q^z \sqrt{1 + \eta^2/3} \quad (2.11)$$

where z is the principle axis of the electric field gradient tensor.

For nuclear magnetic resonance (NMR), where a magnetic field is applied, the quadrupole interaction is still present and changes the resonance frequencies from the purely magnetic Zeeman splitting. The first order and second order perturbation effects on the energy levels of a nuclear spin $I = 3/2$ are shown in figure 2-1. We note that the exact solution can be derived fairly easily by diagonalizing the 4x4 matrix (for example, the results are given in Pennington's thesis [14]). The dramatic effect of the quadrupole interaction is to split the single Zeeman transition energy into different energies for each transition. This splitting is equal to the quadrupole interaction for the axis of the applied field. Hence, for either NMR or NQR, measurement is possible of the quadrupole interaction which is proportional to the electric field gradient. NMR offers the advantage that the quadrupole interaction along the different crystal axes can be measured by applying the magnetic field along the desired axis.

2.3 $1/T_1$, Spin Lattice Relaxation Rate

Besides the NMR and NQR frequencies, we can measure the spin lattice relaxation rate, $1/T_1$. $1/T_1$ represents the rate for the nuclear spin system to return to thermal equilibrium after it has been excited as shown in figure 2-3. Processes that cause

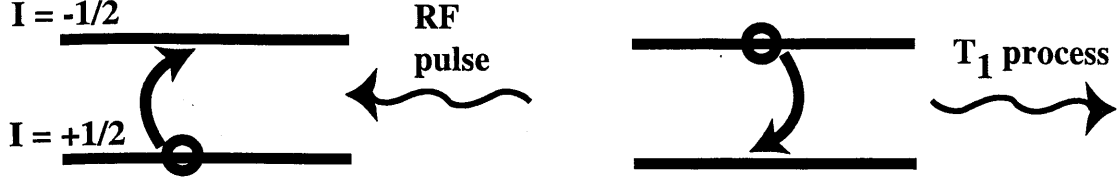


Figure 2-3: In order to measure $1/T_1$, we first excite the nuclei to a higher energy state with an RF pulse and then monitor the relaxation of the nuclei back to thermal equilibrium. Energy is transferred out of the nuclear spin system by magnetic fluctuations at the resonance frequency.

nuclear spin-lattice relaxation must involve energy transfer out of the nuclear spin system. To measure $1/T_1$, we excite the nuclear spin system with a magnetic field pulse at the resonance frequency. Then, the magnetisation of the nuclear spin system is monitored as it returns to equilibrium. The pulse sequence used to measure $1/T_1$ is shown in figure 2-4. A sample measurement of $1/T_1$ is shown in figure 2-5.

As long as the nuclear spin system may be described by a spin temperature, $1/T_1$ may be written in terms of the transition rates W_{mn} between the nuclear states with energy E_m and E_n [15]

$$\frac{1}{T_1} = \frac{(1/2) \sum_{m,n} W_{mn} (E_m - E_n)^2}{\sum_m E_m^2} \quad (2.12)$$

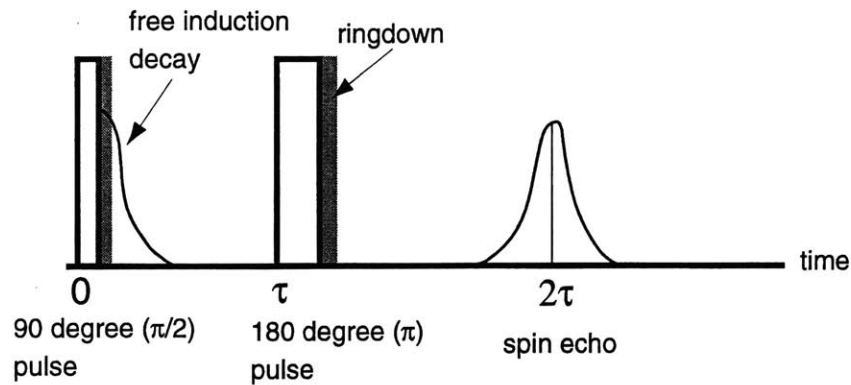
The transition rate W_{mn} is determined by the external perturbations on the nuclear spin system. In these strongly magnetic copper-oxide materials, typically the most important contribution to $1/T_1$ is from the electron-nuclear spin interaction.

With the assumption that the electron-nuclear spin interaction is the dominant contribution, $1/T_1$ is related to $S(\mathbf{q}, \omega) = \chi''(\mathbf{q}, \omega)/(1 - \exp(-\hbar\omega/k_B T))$, where $\chi''(\mathbf{q}, \omega)$ is the imaginary part of the dynamical electron spin susceptibility, as [16]

$$\left(\frac{1}{T_1}\right) = \frac{\gamma_n^2 \hbar}{2\mu_B^2} \sum_{\mathbf{q}} (F_{\perp,1}(\mathbf{q})^2 + F_{\perp,2}(\mathbf{q})^2) S(\mathbf{q}, \omega_n) \quad (2.13)$$

where ω_n is the NMR frequency, $\gamma_n = \mu/I\hbar$ is the nuclear gyromagnetic ratio. $F_{\perp}(\mathbf{q})$ is the wave vector dependent hyperfine form factor [17] perpendicular to the applied magnetic field, which will be described below. $S(\mathbf{q}, \omega)$ is the space-time Fourier

Spin echo & T_2 pulse sequence



T_1 pulse sequence

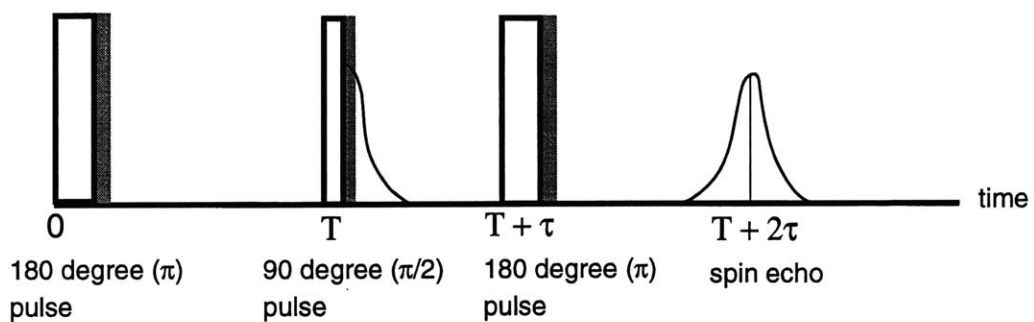


Figure 2-4: RF pulse sequences used for measuring $1/T_1$ and $1/T_2G$.

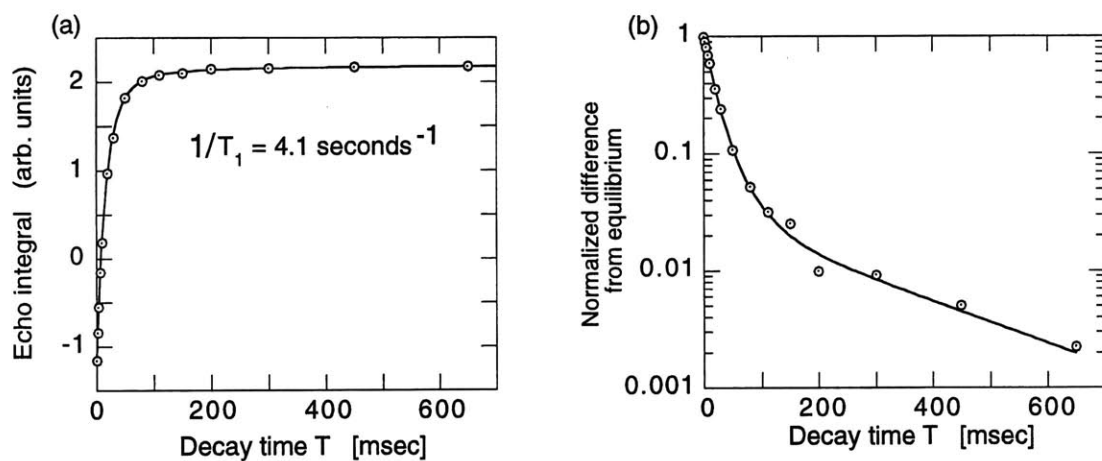


Figure 2-5: Example of T_1 measurement. (a) Exponential recovery of equilibrium nuclear magnetization, $1/T_1 = 4.1 \text{ sec}^{-1}$. (b) Normalized deviation from equilibrium on a log scale showing the multiple exponential form of the relaxation (eq. 2.17). (^{17}O in $\text{Sr}_2\text{CuO}_2\text{Cl}_2$ for $\text{H}||\text{c}$ at 290 K)

transform of the spin-spin correlation function, $S(\mathbf{r}, t) = \langle S(0, 0)S(\mathbf{r}, t) \rangle$,

$$S(\mathbf{q}, \omega) = \frac{1}{2\pi} \sum_{\mathbf{l}} \int_{-\infty}^{\infty} \langle S(0, 0)S(\mathbf{r}, t) \rangle e^{i(\mathbf{l}\mathbf{r} - \omega t)} dt \quad (2.14)$$

where the sum \mathbf{l} is over the lattice positions of the spins. Since the NMR frequency is very low ($\hbar\omega_n/k_B \approx 1$ mK), $1/T_1$ probes the \mathbf{q} -summation of the low energy part of the elementary excitation spectrum, or slow spin dynamics.

Potentially, the nuclear spins could also be perturbed by the interaction of the nuclear spin with the electron orbital magnetic moment. However, in these copper-oxide materials, fluctuations of the orbital magnetic moment will not be significant because all of the ions have closed shell configurations except for copper, which has one hole in the $3d_{x^2-y^2}$ orbital. Even for copper, the $3d_{x^2-y^2}$ orbital can only couple to the $3d_{yz}$ and $3d_{zx}$ orbitals, which is suppressed by the large crystal field splitting (≈ 2 eV) of these orbital states (see figure 3-5). Thus, in these materials, the potential orbital magnetic moment fluctuations are at very high energies and will not affect $1/T_1$. Additionally, the nuclei can interact with charge fluctuations through the quadrupole interaction. The difference between relaxation by the quadrupole interaction and the magnetic interaction can be used to distinguish these two mechanisms in several different ways. One possible check is to measure the isotope dependence of $1/T_1$. For magnetic interactions, $1/T_1$ is proportional to the magnetic moment of the nucleus squared ($1/T_1 \propto \gamma_n^2$), while for charge interactions, this is replaced by the quadrupole moment, ($1/T_1 \propto Q^2$). For Cu NMR/NQR, there are two common isotopes of Cu, ^{63}Cu (69% natural abundance) and ^{65}Cu (31%), which have different values of the magnetic and quadrupolar moment of the nucleus. Thus, we expect the ratio $(^{65}1/T_1)/(^{63}1/T_1) = (^{65}\gamma_n/^{63}\gamma_n)^2 = 1.148$ for magnetic interactions or $(^{65}Q/^{63}Q)^2 = 0.860$ for quadrupolar interactions.

An additional method to confirm if magnetic interactions are dominating $1/T_1$ is to check if the return of the nuclear magnetization to thermal equilibrium fits the expected exponential form for magnetic relaxation [18]. For example, for the

$I_z = 1/2 \leftrightarrow -1/2$ transition for nuclear spin $I = 3/2$, we expect

$$M(t)_{I=3/2, 1/2 \leftrightarrow -1/2} = M(t = \infty) + (M(t = 0) - M(t = \infty)) \cdot \left[0.9 \exp\left(\frac{-6t}{T_1}\right) + 0.1 \exp\left(\frac{-t}{T_1}\right) \right] \quad (2.15)$$

for magnetic relaxation. Also, the $1/T_1$ value obtained for the central ($1/2 \leftrightarrow -1/2$) transition from the magnetic relaxation fit should agree with the values for the satellite ($3/2 \leftrightarrow 1/2$ and $-1/2 \leftrightarrow -3/2$) transitions.

$$M(t)_{I=3/2, \pm 3/2 \leftrightarrow \pm 1/2} = M(t = \infty) + (M(t = 0) - M(t = \infty)) \cdot \left[0.4 \exp\left(\frac{-6t}{T_1}\right) + 0.5 \exp\left(\frac{-3t}{T_1}\right) + 0.1 \exp\left(\frac{-t}{T_1}\right) \right] \quad (2.16)$$

We should note here that for all of the experiments described in this thesis, the ratio of $1/T_1$ for the Cu isotopes, 63 and 65, was checked at selected temperatures covering the full temperature range of the experiments. Except where noted (doped two-leg ladders) that the ratio did not correspond to magnetic relaxation, the ratio of $^{63,65}\text{Cu}/T_1$ indicated magnetic relaxation is dominant and $^{63,65}\text{Cu}/T_1$ had a good fit to the expected exponential form. For oxygen NMR, unfortunately, there is only one isotope with a nuclear spin, ^{17}O , with spin $I = 5/2$. However, the typical quadrupole interaction of ^{17}O (~ 700 kHz) is ~ 30 times smaller than that of $^{63,65}\text{Cu}$ (10 to 30 MHz). Since quadrupolar contributions to $1/T_1 \propto \nu_Q^2$, any quadrupolar $1/T_1$ will be ~ 900 times smaller in ^{17}O than $^{63,65}\text{Cu}$. Thus, the dominance of magnetic relaxation in Cu $1/T_1$ also suggests that magnetic relaxation will dominate O $1/T_1$. In fact, we found that the fit to the following magnetic relaxation curves for $I=5/2$ was very good.

$$M(t)_{I=5/2, 1/2 \leftrightarrow -1/2} = M(t = \infty) + (M(t = 0) - M(t = \infty)) \cdot \left[0.7936 \exp\left(\frac{-15t}{T_1}\right) + 0.1778 \exp\left(\frac{-6t}{T_1}\right) + 0.0286 \exp\left(\frac{-t}{T_1}\right) \right] \quad (2.17)$$

$$M(t)_{I=5/2, \pm 3/2 \leftrightarrow \pm 1/2} = M(t = \infty) + (M(t = 0) - M(t = \infty)) \cdot \quad (2.18)$$

$$\left[\frac{25}{56} \exp\left(\frac{-15t}{T_1}\right) + \frac{25}{56} \exp\left(\frac{-10t}{T_1}\right) + \frac{1}{40} \exp\left(\frac{-6t}{T_1}\right) + \frac{3}{56} \exp\left(\frac{-3t}{T_1}\right) + \frac{1}{35} \exp\left(\frac{-t}{T_1}\right) \right]$$

$$M(t)_{I=5/2, \pm 5/2 \leftrightarrow \pm 3/2} = M(t = \infty) + (M(t = 0) - M(t = \infty)) \cdot \quad (2.19)$$

$$\left[\frac{1}{14} \exp\left(\frac{-15t}{T_1}\right) + \frac{2}{7} \exp\left(\frac{-10t}{T_1}\right) + \frac{2}{5} \exp\left(\frac{-6t}{T_1}\right) + \frac{3}{14} \exp\left(\frac{-3t}{T_1}\right) + \frac{1}{35} \exp\left(\frac{-t}{T_1}\right) \right]$$

2.4 Hyperfine form factor

The hyperfine form factor, $F(\mathbf{q})$, arises from the geometry of the hyperfine couplings between the electron spins and the nuclear spin. Typically, the nuclear spin has significant hyperfine interaction only with the electron spin of its atom and nearest neighbor atoms. The hyperfine form factor is just the Fourier transform of the local hyperfine interactions. This is defined as [17]

$$F(\mathbf{q}) = \left| \sum_i A_i e^{i\mathbf{q} \cdot \mathbf{r}_i} \right| \quad (2.20)$$

where the summation is over all electron spins, i , with hyperfine interaction, A_i , and \mathbf{r}_i is the vector from the atomic site of the electron spin to the nucleus.

In the NMR community, the hyperfine interactions, A_i , are usually given in the units of kOe/μ_B . This can be understood as the amount of magnetic field (kOe) at the site of the nucleus produced by one Bohr magneton (μ_B) of bulk electron spin susceptibility. This method of specifying the hyperfine interaction has the advantage that it is a property of the electronic structure alone and does not depend on the nucleus used to measure the field. In other areas of physics research (such as atomic physics), the hyperfine interactions are commonly quoted in terms of energy, but conversion simply involves the nuclear magnetic moment as stated in appendix C. A typical hyperfine interaction in these copper-oxide materials is $100 \text{ kOe}/\mu_B$, which

corresponds to $\sim 10^{-6}$ eV.

The hyperfine form factor is important because it determines what wavevectors, \mathbf{q} , of spin fluctuations, $1/T_1$ is sensitive to. Differences in the hyperfine form factors for different nuclear sites can be used to obtain information about the wavevector dependence of the spin susceptibility. In these antiferromagnetic copper oxide compounds, the spin susceptibility at low energies is strongly peaked at the antiferromagnetic wave vector, $\mathbf{Q} = (\pi, \pi)$ [19, 20, 21]. If the hyperfine form factor at the antiferromagnetic wave vector, \mathbf{Q} , is non-zero, then $1/T_1$ is sensitive to the antiferromagnetic spin fluctuations. But if the hyperfine form factor is 0 at $\mathbf{Q} = (\pi, \pi)$, then antiferromagnetic fluctuations do not affect $1/T_1$. Typically in these copper oxide materials, copper $^{63,65}1/T_1$ does measure antiferromagnetic electron spin fluctuations, but for oxygen in the copper oxide planes, $^{17}1/T_1$ does not.

This can be seen by looking at the typical hyperfine form factors for copper and oxygen in these materials, as shown in figure 2-6. For a copper nucleus, a hyperfine field, A , is produced by the onsite electron spins. The hyperfine interaction between the electron spins and the nucleus can be divided into four different contributions [22, 23].

$$A = A_{contact} + A_{cp} + A_{dipolar} + A_{spin-orbit} \quad (2.21)$$

The first contribution is the contact interaction, $A_{contact}$, which expresses the interaction for s-like orbitals, which have some probability for the electron to be at the site of the nucleus. This leads to a relatively large interaction proportional to the probability for the electron to be at the nucleus site. The second contribution, A_{cp} , is from core polarization. Even if the electron spins are not in an s-like orbital, the polarization of the outer electrons may cause a small polarization of the inner (core) electrons, which interact with the nucleus. Typically, this core polarization effect is negative because the core electrons are polarized opposite to the outer electron spins. These first two contributions are usually isotropic because s-like orbitals have an isotropic probability distribution. The last two effects from non-s orbitals will in general be anisotropic. The third effect is the dipolar interaction between the electron and nuclear spins,

$A_{dipolar}$. The fourth interaction, $A_{spin-orbit}$, arises from the spin-orbit interaction of the electron spin magnetic moment and the electron orbital magnetic moment. This interaction polarizes some of the orbital magnetic moment when the electron spin is polarized and this orbital magnetic moment interacts with the nuclear spin. The hyperfine interactions are discussed in more detail for the particular crystal structure of the copper oxides in the next chapter (Ch. 3).

In addition, the nearest neighbor copper spins also contribute a significant hyperfine field, B . This hyperfine field from the nearest neighbor copper spins is discussed by Mila and Rice [22] as arising from the hybridization of the copper electron orbitals to include the 4s orbital of the nearest neighbor copper ions. This means that the copper electrons spend some time on the 4s orbital of the neighboring copper ions, thus providing an isotropic contact hyperfine interaction, B , with the neighboring copper nuclei. It is this contribution from the off site electron spins which creates a wavevector dependence in the hyperfine form factor. It is simple to see from figure 2-6 that for wavevector $\mathbf{q} = 0$ where all the electron spins point the same direction, $^{63,65}F(\mathbf{q} = 0) = A + 4B$. For antiferromagnetic wavevector \mathbf{Q} where the electron spins alternate directions, $^{63,65}F(\mathbf{q} = \mathbf{Q}) = A - 4B$. The full wavevector dependence is

$$^{63,65}F(\mathbf{q}) = A + 2B(\cos(q_x) + \cos(q_y)) \quad (2.22)$$

The oxygen atoms in the copper oxide planes usually are located in the middle between two copper atoms. These two copper atoms both contribute a hyperfine field, C , at the oxygen nuclear site as shown in figure 2-6. For wavevector $\mathbf{q} = 0$, $^{17}F(\mathbf{q} = 0) = 2C$. For antiferromagnetic wavevector \mathbf{Q} where the electron spins alternate directions, $^{17}F(\mathbf{q} = \mathbf{Q}) = 0$. The full wavevector dependence is

$$^{17}F(\mathbf{q}) = 2C(\cos(q_x)) \quad (2.23)$$

where the Cu-O-Cu bond is along the x axis. Because of the symmetrical arrangement of the oxygen nucleus in between two copper atoms, the hyperfine form factor is zero at the antiferromagnetic wavevector and the $^{17}1/T_1$ is insensitive to antiferromagnetic

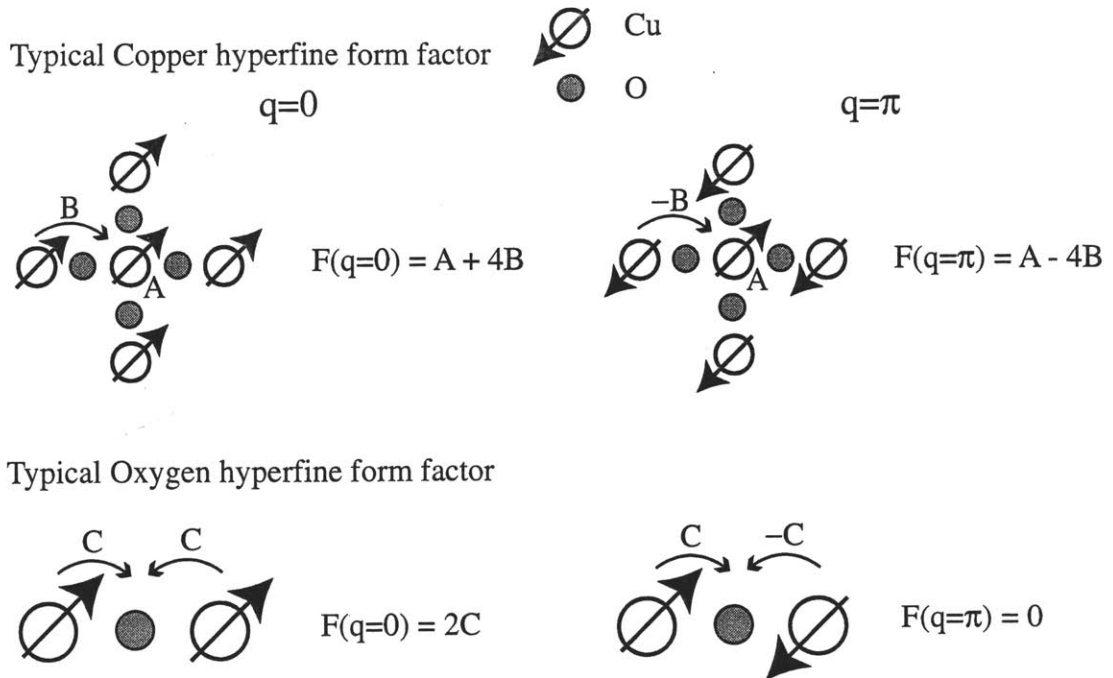


Figure 2-6: Typical hyperfine form factors, $F(q)$, for copper and oxygen atoms in the copper-oxide materials. Left hand side illustrates $F(q=0)$ and right hand side illustrates $F(q=\pi)$. Full wavevector dependence given in equations 2.22 and 2.23.

spin fluctuations. As a result, comparison of $1/T_1$ for copper and oxygen reveals wavevector dependence of the electron spin susceptibility. Copper $1/T_1$ reflects the dominant antiferromagnetic fluctuations, while Oxygen $1/T_1$ reflects spin fluctuations away from antiferromagnetic.

2.5 $1/T_2$, Spin-Spin Relaxation Rate

$1/T_2$, the spin-spin relaxation rate, measures the relaxation of the transverse component of the nuclear spin. Shown in figure 2-4 is the pulse sequence used to measure $1/T_2$. First, an rf pulse is used to create the transverse magnetization. Then at a time $t = \tau$ later, another rf pulse is applied to create a spin echo at time 2τ to measure the remaining transverse magnetization. By using this sequence with varying τ , we measure the Lorentzian (exponential) (T_{2L}) and Gaussian (T_{2G}) parts of T_2 as

$$M(2\tau) = M_0 \exp\left(\frac{-2\tau}{T_{2L}}\right) \exp\left(\frac{-(2\tau)^2}{2T_{2G}^2}\right) \quad (2.24)$$

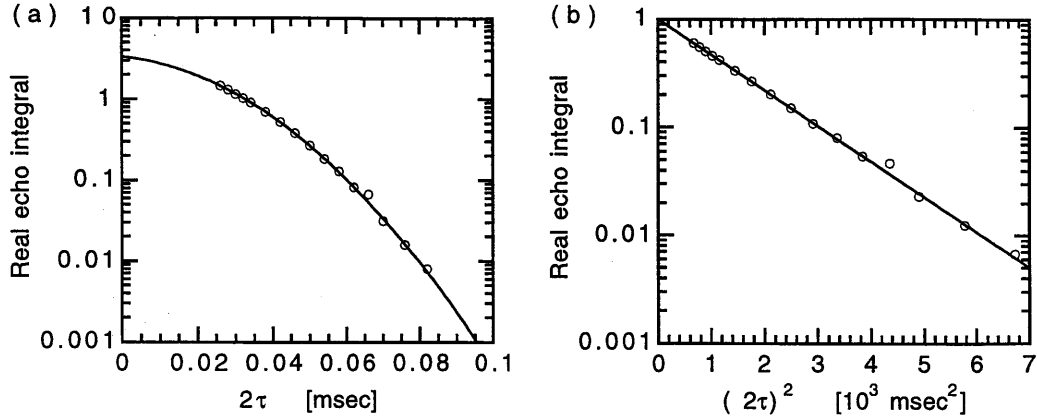


Figure 2-7: Example of relaxation of the transverse component of the nuclear spin, $1/T_2$. (a) Echo integral on a logarithmic scale as a function of 2τ . The curvature of the graph shows the non-exponential relaxation. Solid line is a fit to the Gaussian component of $1/T_2$ with the Lorentzian (exponential) component calculated from $1/T_1$. (b) Normalized Gaussian component of echo integral as a function of $(2\tau)^2$ ($M(2\tau)/M_0 \exp(-2\tau/T_{2L})$, where $T_{2L} = 13 \text{ msec}^{-1}$ as determined by $1/T_{1,NQR} = 3.0 \text{ msec}^{-1}$, $1/T_{1,ab}/1/T_{1,c} = 3.4 \pm 0.2$ and equations A.30 and A.18). Solid line shows the expected linear dependence of the echo integral on the logarithmic scale. (Example is taken from three-leg ladder material, $\text{Sr}_2\text{Cu}_3\text{O}_5$, at 325 K measured by NQR. Result from fit is $1/T_{2G} = 39 \text{ msec}^{-1}$)

An example of transverse relaxation, $1/T_2$, that is dominated by the Gaussian term is shown in figure 2-7. The curvature of the echo integral as a function of 2τ in part (a) of the figure indicates non-exponential relaxation. Part (b) of the figure confirms the Gaussian nature of the relaxation by graphing the echo integral as a function of $(2\tau)^2$. The important difference between $1/T_2$ and $1/T_1$ is that the transverse component of the nuclear spin can decay (the T_2 process) without any change in the energy of the nuclear spin system. On the other hand, spin-lattice relaxation, $1/T_1$, requires energy to be removed from the nuclear spin system.

However, the same processes that cause spin-lattice relaxation, $1/T_1$ can also cause transverse relaxation, $1/T_2$. The projection of the nuclear magnetization in the xy-plane is reduced by magnetic field fluctuations perpendicular to the nuclear

magnetization. These processes will cause Lorentzian (exponential) relaxation. In fact, for magnetic relaxation, we can calculate the expected value of the exponential component of T_2 , T_{2L} , from T_1 using Redfield theory [15]. The result is [14]

$$\left(\frac{1}{T_{2L,z}}\right)_{1/2 \leftrightarrow -1/2} = \frac{1}{2} \left(\frac{1}{T_{1,x}} + \frac{1}{T_{1,y}}\right) + 3 \left(\frac{1}{T_{1,z}}\right) \quad (2.25)$$

$$\left(\frac{1}{T_{2L,z}}\right)_{\pm 3/2 \leftrightarrow \pm 1/2} = \frac{1}{2} \left(\frac{1}{T_{1,x}} + \frac{1}{T_{1,y}}\right) + 2 \left(\frac{1}{T_{1,z}}\right) \quad (2.26)$$

where the subscripts, x,y,z, refer to the crystal axes. This calculation applies for spin $I = 3/2$ and both NMR and NQR when $\eta = 0$. For NQR when $\eta \neq 0$, the calculation is outlined in appendix A

$$\left(\frac{1}{T_{2L,z}}\right)_{NQR} = \left(\frac{1}{3 + \eta^2}\right) \left[(3 + 3\eta^2) \frac{1}{T_{1,x,y}} + 6 \frac{1}{T_{1,z}} \right] \quad (2.27)$$

Since T_{2L} provides similar information as T_1 , it is not so interesting. In fact, we usually fit the spin echo decay using the value for $1/T_{2L}$ calculated from $1/T_1$ measurements. In contrast, the Gaussian spin-spin relaxation rate, T_{2G} , provides information on the real part of the wavevector (q) dependent electron spin susceptibility, $\chi'(q)$ in these materials. The Gaussian spin-spin relaxation arises from interaction between the nuclear spins. The dipole moment of one nuclear spin produces some magnetic field at the site of a neighboring nucleus. This direct dipolar interaction is not very strong because the magnetic field of a nucleus at a distance of several Angstroms will be only a few gauss [13]. In antiferromagnets, the indirect interaction of the nuclei via the electron spins can be much larger [24, 25]. The indirect nuclear spin-spin coupling, between nuclear spins, I_z , at sites \mathbf{r}_1 and \mathbf{r}_2 , can be expressed as [26]

$$\mathcal{H}_{12} = -(\gamma_n \hbar)^2 \sum_{\mathbf{r}', \mathbf{r}} I_z(\mathbf{r}_2) F(\mathbf{r}_2, \mathbf{r}') \chi'(\mathbf{r}', \mathbf{r}) F(\mathbf{r}, \mathbf{r}_1) I_z(\mathbf{r}_1) \quad (2.28)$$

where $F(\mathbf{r}, \mathbf{r}')$ and $\chi'(\mathbf{r}', \mathbf{r})$ are the hyperfine form factor and real part of the electron spin susceptibility in real space. This Hamiltonian can be understood as shown in figure 2-8. One nucleus at position \mathbf{r}_1 is coupled to its local electron spin at \mathbf{r} by the

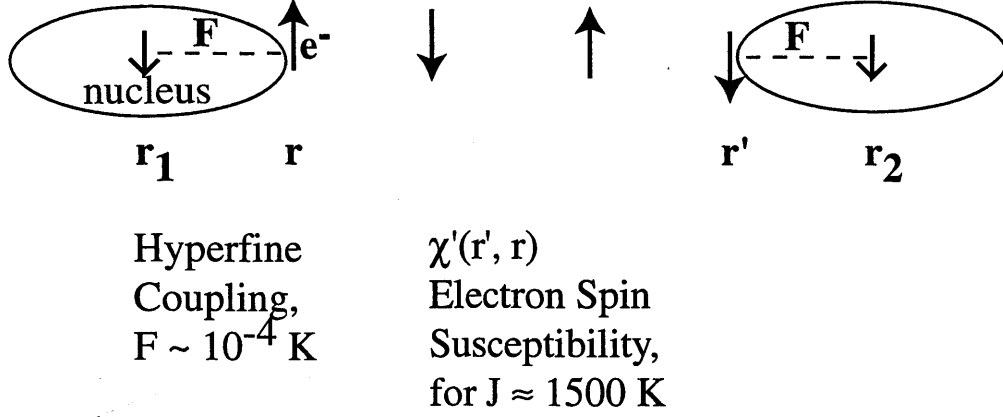


Figure 2-8: Indirect nuclear spin-spin coupling: nuclear spins are coupled through their interaction with the antiferromagnetically correlated electron spins.

hyperfine interaction, $F(\mathbf{r}, \mathbf{r}_1)$. Since the electron spins have such a strong antiferromagnetic correlation, the polarization of the local electron spin by the nucleus affects the nearby electron spin at position \mathbf{r}' according to the electron spin susceptibility, $\chi'(\mathbf{r}', \mathbf{r})$. This electron spin will interact with the nucleus of its own atom at position \mathbf{r}_2 via the hyperfine interaction, $F(\mathbf{r}_2, \mathbf{r}')$. As a result, the nuclei are indirectly coupled. The nuclear spin-spin coupling, a_{12}^z , is determined by the correlations of the electron spin system. Taking the Fourier transform of the real space expression,

$$\mathcal{H}_{12} = a_{12}^z I_z(\mathbf{r}_1) I_z(\mathbf{r}_2) \quad (2.29)$$

$$a_{12}^z = \frac{-(\gamma_n \hbar)^2}{N} \sum_{\mathbf{q}} e^{i\mathbf{q} \cdot (\mathbf{r}_2 - \mathbf{r}_1)} F(\mathbf{q})^2 \chi'(\mathbf{q}) \quad (2.30)$$

For a single nuclear spin-spin coupling, a , the time dependence of the nuclear magnetization is

$$M(t) = M(0) \cos(at) \quad (2.31)$$

The Gaussian relaxation term is an approximation for the combination of many different spin-spin couplings. Expanding the cosine terms to second order, the decay of the nuclear magnetization can be approximated as a Gaussian decay determined by

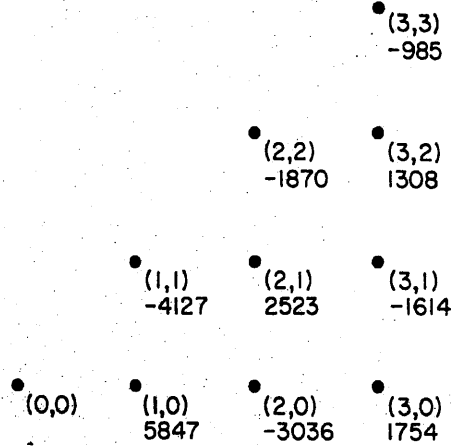


Figure 2-9: Example of indirect nuclear spin-spin coupling. The coupling strength a_{12}^z in rad/sec between the labeled nucleus and the nucleus at (0,0) for an electron spin correlation length, $\xi = 3$. The coupling is antiferromagnetic and decreases with a distance scale determined by the correlation length. (These calculations are based on a model q-dependent spin susceptibility proposed by Millis, Monien, and Pines[137] and are from Pennington and Slichter[27])

the sum of the squares of the spin-spin couplings.

$$\begin{aligned}
 M(t) &= M(0) \prod_i \cos(a_i t) & (2.32) \\
 &\approx M(0) \prod_i \left(1 - \frac{(a_i t)^2}{2}\right) \\
 &\approx M(0) \left(1 - \frac{(\sum_i a_i^2) t^2}{2}\right) \\
 &\approx M(0) e^{-\frac{(\sum_i a_i^2) t^2}{2}}
 \end{aligned}$$

Thus, the Gaussian spin-spin relaxation rate for the $I_z = 1/2 \leftrightarrow -1/2$ or $\pm 3/2 \leftrightarrow \pm 1/2$ transitions for ^{63}Cu ($I = 3/2$) NMR is [26, 27, 28]

$$\left(\frac{1}{T_{2G}}\right)_{NMR}^2 = \frac{0.69}{8\hbar^2} \sum_{\mathbf{r}_2 \neq \mathbf{r}_1} (a_{12}^z)^2 \quad (2.33)$$

where 0.69 is the natural abundance of the ^{63}Cu isotope. We note that the above equation assumes that the three transitions, $1/2 \leftrightarrow -1/2$, $3/2 \leftrightarrow 1/2$, and $-3/2 \leftrightarrow -1/2$, are split by the quadrupole interaction. This fact and the following discussion

are treated in more detail in appendix B.

The dependence of $1/T_{2G}$ on the isotope abundance and nuclear spin I arises because the Gaussian nuclear spin-spin relaxation occurs only for coupling between like spins. In order to form the spin echo, the transverse nuclear magnetization is flipped 180 degrees at time τ as shown in figure 2-4. If the nearby interacting nuclear spin is not also flipped, the extra precession from time $t = 0$ to τ due to the interaction is cancelled by the the opposite precession from time $t = \tau$ to 2τ . So, only “like spins” contribute to the Gaussian spin-spin relaxation, $1/T_{2G}$, where like spins are defined as those flipped by the rf pulse. This points towards the importance in measurements of $1/T_{2G}$ of ensuring that all of the nuclear spins considered “like” in a spectrum are flipped by the rf pulse. For measurements of $1/T_{2G}$, the strength of the rf pulse is varied to ensure that $1/T_{2G}$ is measured with a spin-flip pulse strong enough to eliminate any effect of the rf pulse on the measured value.

In addition, this creates a difference between $1/T_{2G}$ as measured by NMR or NQR. For NQR, because the sign of the spin does not matter, there are twice as many like spins as there are for NMR. Another small correction for NQR occurs when the measurement is done on unaligned powder samples. Because the crystal axes of the powder are not aligned with the rf magnetic field of the spin-flip pulse, the amount of spin transitions will differ depending on the orientation of the crystal axes. As derived in appendix B,

$$\left(\frac{1}{T_{2G}}\right)_{\text{powder NQR}} = \sqrt{2}\sqrt{\frac{6}{7}} \left(\frac{1}{T_{2G}}\right)_{\text{NMR}} \quad (2.34)$$

As seen from equations 2.30 and 2.33, the Gaussian nuclear spin-spin relaxation rate, $1/T_{2G}$, measures the real part of the electron spin susceptibility at zero frequency, $\chi'(\mathbf{q})$ [27]. Thelen and Pines [28] simplified the expression for ${}^{63}\text{Li}/T_{2G}$ from eqs. 2.30 and 2.33 to provide ease of calculation by dependence on wavevector q , rather than

in real space.

$${}^{63} \left(\frac{1}{T_{2G}} \right)^2 = \frac{0.69(\gamma_n \hbar)^4}{8\hbar^2} \left(\frac{1}{N} \sum_q F(q)^4 \chi'(\mathbf{q})^2 - \left(\frac{1}{N} \sum_q F(q)^2 \chi'(\mathbf{q}) \right)^2 \right) \quad (2.35)$$

where the factor 0.69 is the isotope abundance of ${}^{63}\text{Cu}$.

The electron spin correlation length, ξ , gives a simple picture for understanding how the Gaussian spin-spin relaxation rate, $1/T_{2G}$, measures the correlation length.

The spin correlation length, ξ , is defined as [30]

$$\frac{e^{-r/\xi}}{r^\lambda} \propto (-1)^{r_x+r_y} \frac{1}{N} \sum_n \langle S_n^z S_{n+r}^z \rangle \quad (2.36)$$

in the limit when $r \rightarrow \infty$, and $\lambda = (d - 1)/2$ where d is the dimensionality. The electron spin correlation length, ξ , gives a length scale over which the unpaired Cu electron spins are antiferromagnetically correlated. As long as the electron spins are correlated, the indirect nuclear spin-spin interaction will be significant. Therefore, a nuclear spin will be coupled to other nuclear spins in a region of length scale, ξ . This can be seen clearly in figure 2-9 from Pennington and Slichter [27] which shows calculations of the individual ${}^{63}\text{Cu}$ nuclear spin-spin couplings for a electron spin correlation length, $\xi = 3$ lattice spacings. As the electron spin correlation length increases, a nuclear spin is indirectly coupled to more nuclei which increases the Gaussian spin-spin relaxation rate, $1/T_{2G}$.

2.6 NMR Electronics

To conduct these NMR and NQR measurements, we constructed the electronics for the spectrometer. The electronics, shown in figure 2-10, are required to do two major things. First, they send out the radio frequency (RF) pulses to excite the nuclei in the sample and later when the spin echo occurs, the much smaller signal is acquired. Our NMR spectrometer is based around the Aries spectrometer by Tecmag, which communicates with the Macintosh computer. The general flow of the electronics is as

follows. The RF frequency source (PTS 310 or 500) produces continuous RF which is gated into pulses by the TTL signals from the Aries spectrometer. These RF pulses are then amplified by the power amplifier (Kalmus LP1000, 1 kW). We should note that the TTL signals from the Aries are protected using simple logic circuitry to prevent the possibility of continuous RF being fed to the power amplifier in the case of power failure or a computer crash. The Aries spectrometer has an alarming habit of leaving all TTL lines high when the computer crashes. The amplified RF pulses are fed through paired diodes into the NMR probe. The NMR probe consists of two adjustable capacitors and an inductive coil. This allows the circuit to be tuned to the chosen RF frequency and also matched to 50 ohms impedance. The sample is placed inside the inductive coil, and is thus exposed to the radio frequency oscillations of the magnetic field of the inductor. The next two parts beyond the NMR probe help shield the sensitive signal amplifiers from the large RF pulses. A quarter-wavelength cable is inserted between the NMR probe and paired diodes that are grounded. The grounded diodes prevent the large voltages of the RF pulses from entering the signal amplifiers. Since a quarter-wavelength is the distance between the zero voltage point of the wave and the peak voltage, the quarter-wavelength cable allows the voltage to be large at the NMR probe while the voltage is small at the grounded diodes.

For acquiring the signal, the same inductive coil also provides an induced voltage from the nuclear spin precession. The signal is not attenuated by the grounded diodes as long as the signal is below the threshold voltage of the diodes (~ 0.6 V). So the signal is amplified by the RF signal amplifiers (LN-2L or LN-2M by Doty, or AU-1467 by Miteq). Generally, we have two Doty amplifiers which are separated by a pair of RF mixers (Mini-circuits ZAD-1) which we use as switches. The switches are only turned on when we want to acquire the signal to avoid unnecessary saturation of the amplifiers. We used the RF mixers because we already had them, another option would be to use pin diode switches. For the third RF amplifier, we use a Mini-circuits ZFL-500LN. This amplified signal is then split (Mini-circuits ZFSC-2-1W) and mixed with the original continuous RF with two different phases, 0 and 90 degrees (phase splitters such as Mini-circuits ZSCQ2-180B). This is referred to in the NMR literature

NMR Electronics - Imai lab

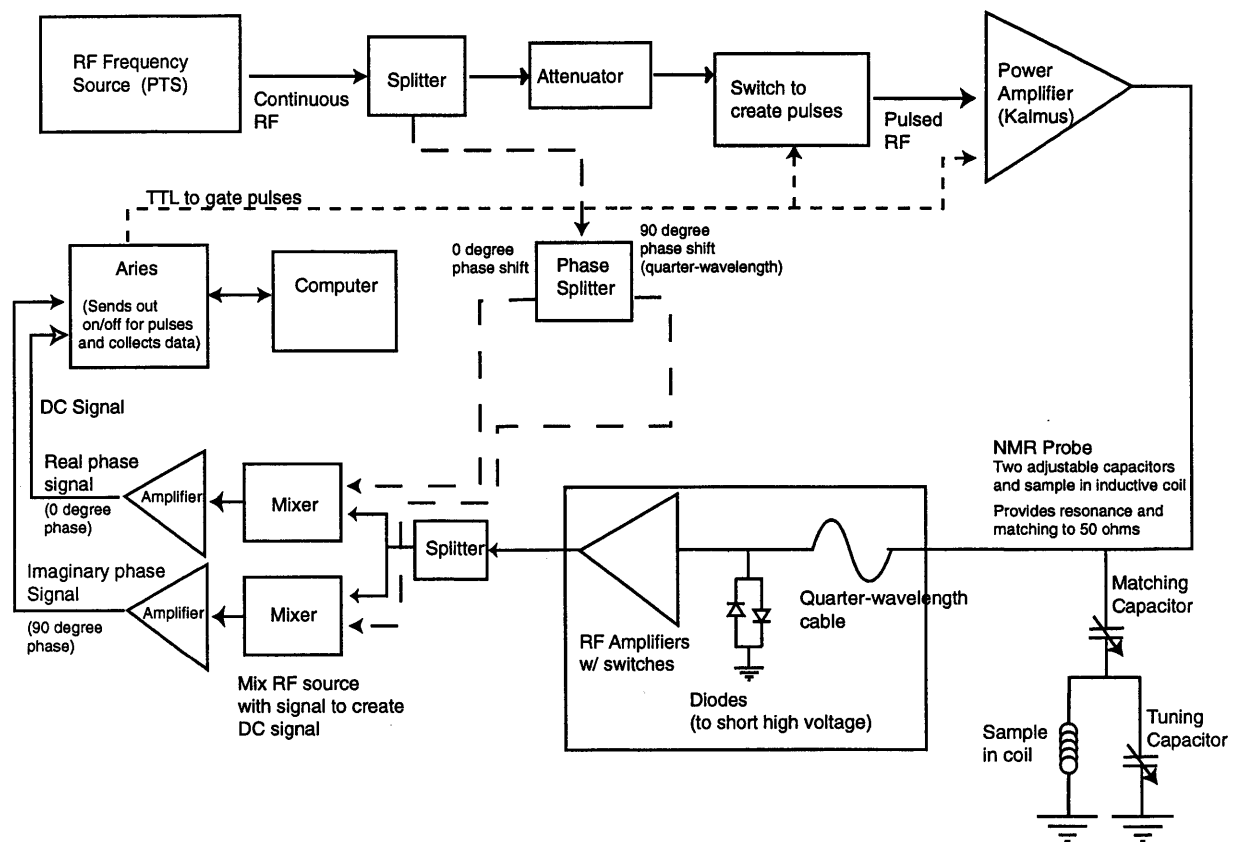


Figure 2-10: Schematic of electronics for NMR spectrometer, Imai Labs.

as quadrature detection. Mixing with the two different phases essentially allows us to get both the cosine and sine components of the signal at the chosen frequency (or equivalently the real and imaginary parts of the Fourier transform). After mixing with the original RF, the signal is close to DC. We amplify the signal once more with an op-amp (AD521) based circuit with a gain of 100 and a complementary bandwidth of ~ 100 kHz. This final signal can be viewed on an oscilloscope and is digitized by the Aries spectrometer. In addition to the software provided with the Aries spectrometer, we wrote some additional functions to provide the data analysis that we need.

A NMR technique that is crucial for separation of the small spin echo signal from the decay (ringdown) of the RF pulses is phase cycling [14]. In our resonant circuit ($Q \sim 40 - 100$), the RF pulses require some time to decay and can obscure the spin echo signal. The pulse sequences shown in figure 2-4 are repeated with different phases for the RF pulses in order to cancel the decay of the RF pulse. For example, for the spin echo sequence, we use four different phases and add or subtract the resulting signal based on the sign of the echo:

90_x	τ	180_x	τ	echo _y	Add
90_{-x}	τ	180_x	τ	echo _{-y}	Subtract
90_{-x}	τ	180_y	τ	echo _y	Add
90_x	τ	180_y	τ	echo _{-y}	Subtract

where 90 and 180 refer to the 90 degree and 180 degree pulses with the subscript indicating the phase of the RF pulse. In this sequence, any ringdown of the 90 degree or 180 degree pulses is cancelled. For the T_1 sequence, we have an additional 180 degree pulse. We repeat the above four phase sequence twice, once with 180_x for the first 180 degree pulse, and again with 180_{-x} . In addition to cancelling any ringdown of the pulses, this also cancels the stimulated echoes that can occur with three pulses [14]. The phase cycling technique dramatically helps to measure the spin echo at short τ .

2.7 Summary

In summary, NMR and NQR uses the atomic nuclei as local probes into materials. This thesis is primarily concerned with the ability of the nuclei to probe the electronic structure. The magnetic resonance frequency reveals the local uniform magnetic susceptibility, $\chi'(q = 0)$. The quadrupole resonance frequency measures the electric field gradient, which reflects the charge environment. Low energy excitations of the electron spin system, $\chi''(q, \omega_n)$, are seen in $1/T_1$, the spin lattice relaxation rate. The Gaussian spin-spin relaxation rate, $1/T_{2G}$, is dominated by the indirect nuclear-nuclear spin coupling which measures the real part of the static electron spin susceptibility, $\chi'(\mathbf{q}, \omega = 0)$. The electron spin susceptibility can be expressed in terms of the spin correlation length, ξ .

Chapter 3

Summary and Crystal Structure

This thesis describes NMR and NQR experiments in several copper-oxide materials. These materials have crystal structures that are only slightly different, but the magnetism is dramatically different. The dramatic changes in the magnetism result from the changes in the dimensionality of the magnetic interactions. The temperature dependence of the spin-lattice relaxation rate, $1/T_1$ (figure 3-1), and the Gaussian spin-spin relaxation rate, $1/T_{2G}$ (figure 3-2), for ^{63}Cu are shown to differ dramatically between these materials. In general, these results can be understood in terms of the different behavior of the electron spin correlation length, ξ , as a function of the dimensionality of the magnetic interactions. Monte Carlo results for the spin correlation length, ξ , are shown in figure 3-3. Both $1/T_1$ and $1/T_{2G}$ are, in general, related to the spin correlation length. For the three-leg ladder, $\text{Sr}_2\text{Cu}_3\text{O}_5$, and the 2d square lattice, $\text{Sr}_2\text{CuO}_2\text{Cl}_2$, the results show a qualitatively similar divergence with decreasing temperature, but the three-leg ladder $1/T_1$ diverges at a lower temperature than the 2-D material. In contrast, the two-leg ladder material, SrCu_2O_3 , has a spin excitation gap [29]. The spin excitation gap, Δ , of the 2-leg ladder is seen in the gapped behavior of $1/T_1$ ($1/T_1 \approx \exp(-\Delta/T)$) below $T \approx 425\text{K}$. The spin correlation length becomes constant at low temperatures as the Monte Carlo results show. As a consequence, $1/T_{2G}$ for the two-leg ladder also becomes roughly constant for $T < 100\text{K}$. Finally, the 1d Cu-O chain material, Sr_2CuO_3 , has a much weaker temperature dependence of $1/T_1$ and $1/T_{2G}$ than the other materials. This is primar-

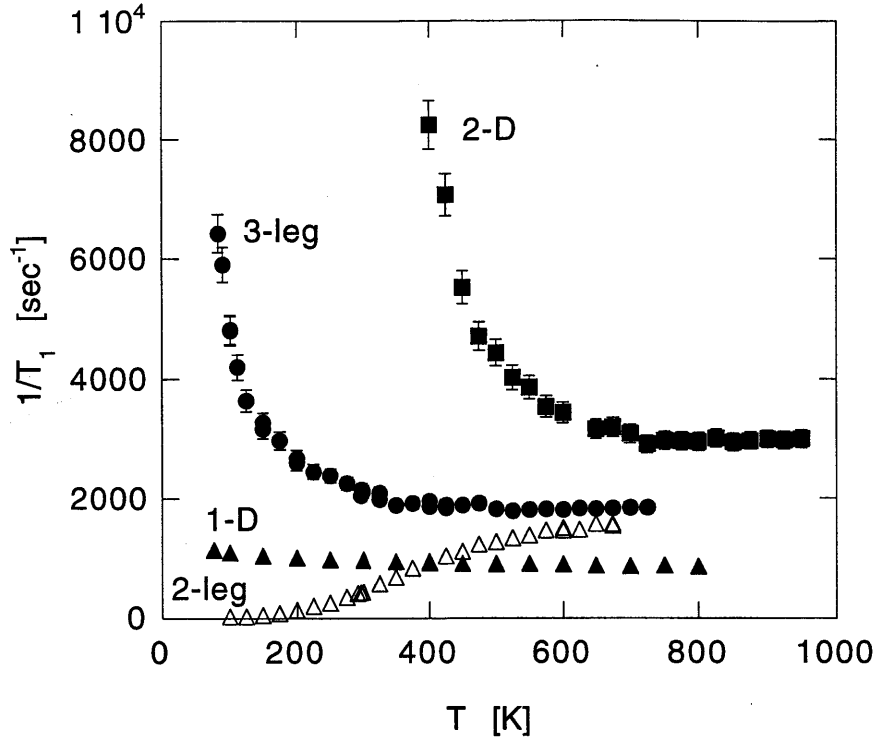


Figure 3-1: Summary of ^{63}Cu $1/T_1$. ■ $\text{Sr}_2\text{CuO}_2\text{Cl}_2$ (2d square lattice), ▲ Sr_2CuO_3 (1d), △ SrCu_2O_3 (two-leg ladder), • $\text{Sr}_2\text{Cu}_3\text{O}_5$ (three-leg ladder). Measurements for $\text{H} \perp$ to Cu-O layer, scaled from NQR measurements for the ladder materials (see app. A).

ily a result of the fact that in 1 dimension, the dependence of $1/T_1$ and $1/T_{2G}$ on the correlation length almost completely cancels out. These results will be discussed in more detail in the individual chapters on each material.

3.1 Crystal Structure

Despite the very different magnetic interaction geometries, the basic crystal structures of the undoped copper oxides described in this thesis are similar. Their three dimensional structure is made up of 2 dimensional Cu oxide layers which are separated by layers of Sr (or La,Ca) oxide layers. The copper-oxide layers have copper ions which are surrounded by a square of four oxygen ions. This is shown in figure 3-4 for the 3-leg ladder material, $\text{Sr}_2\text{Cu}_3\text{O}_5$. This material will be used as an example to explain the crystal properties which are common to these copper oxide materials.

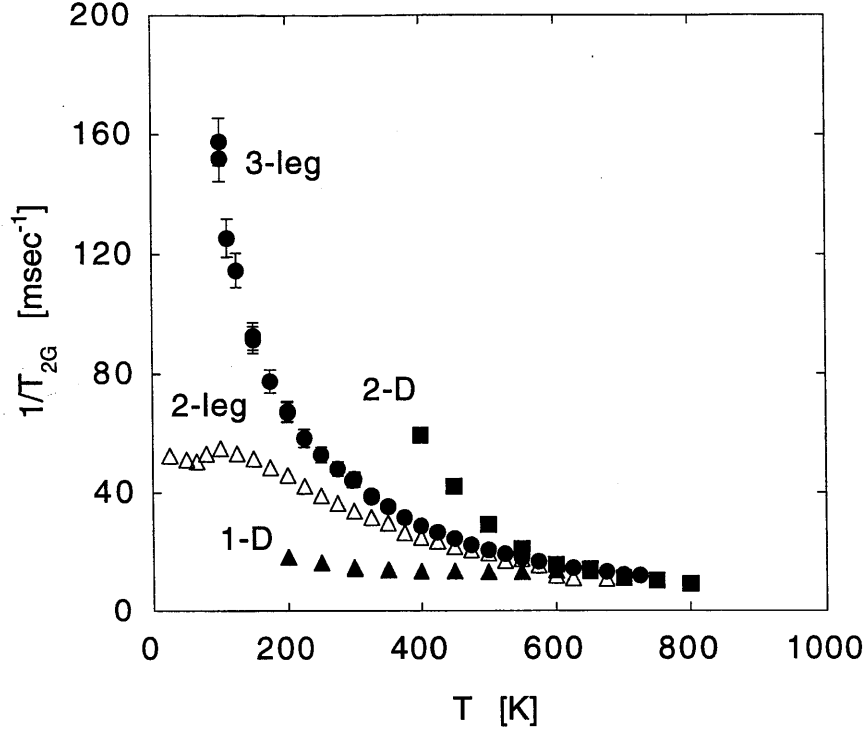


Figure 3-2: Summary of ^{63}Cu $1/T_{2G}$. ■ $\text{Sr}_2\text{CuO}_2\text{Cl}_2$ (2d square lattice), ▲ Sr_2CuO_3 (1d), △ SrCu_2O_3 (two-leg ladder), • $\text{Sr}_2\text{Cu}_3\text{O}_5$ (three-leg ladder). Measurements for NQR, scaled from NMR measurements for Sr_2CuO_3 (see app. B).

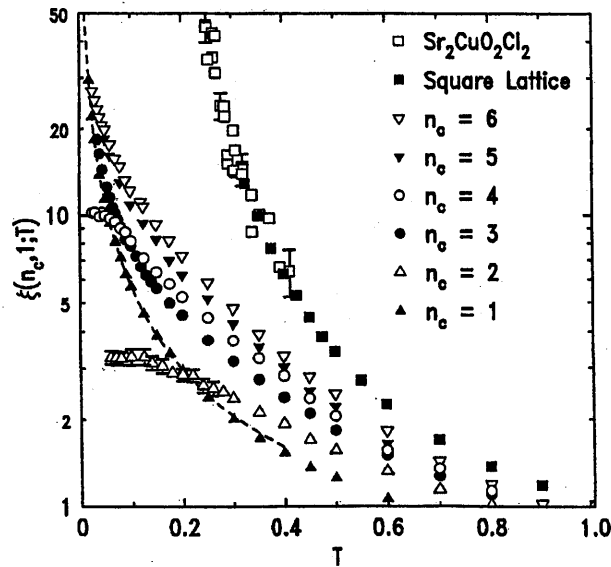


Figure 3-3: Monte Carlo data from Greven, *et al.* [30] for the spin correlation length, ξ , in the spin 1/2 Heisenberg antiferromagnet with different numbers, n_c , of isotropically coupled chains. Corresponding to the structures of the copper-oxide materials studied are ■ 2d square lattice (□ neutron experiment for $\text{Sr}_2\text{CuO}_2\text{Cl}_2$), ▲ 1d (single chain), △ two-leg ladder (two chains), • three-leg ladder (three chains).

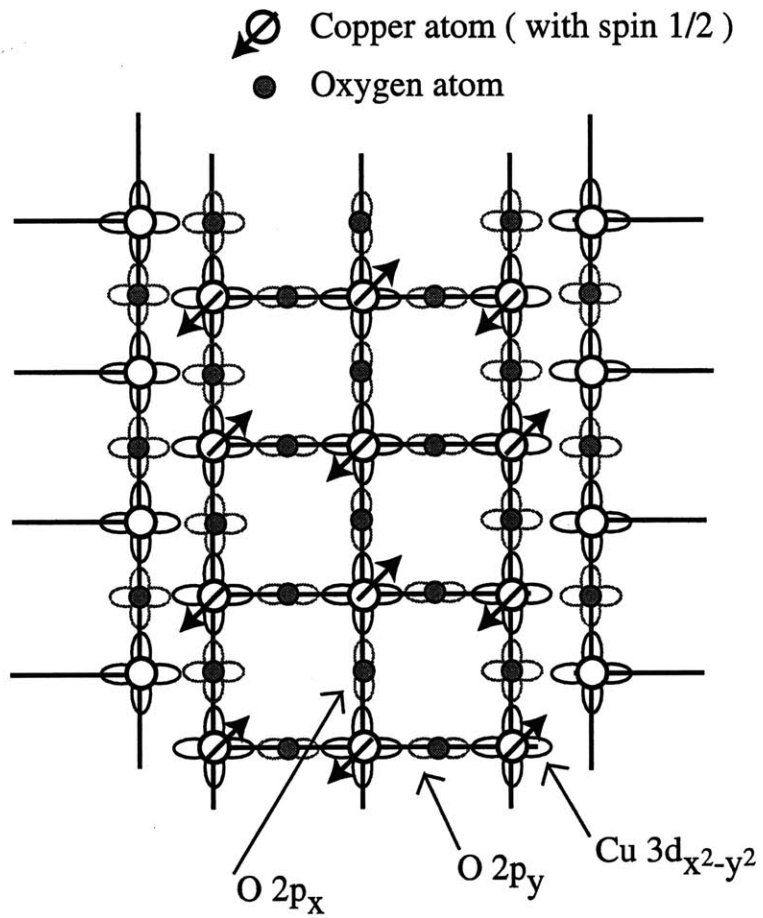


Figure 3-4: Structure of the copper-oxide layer of the 3-leg ladder, $\text{Sr}_2\text{Cu}_3\text{O}_5$, with the important electron orbitals shown.

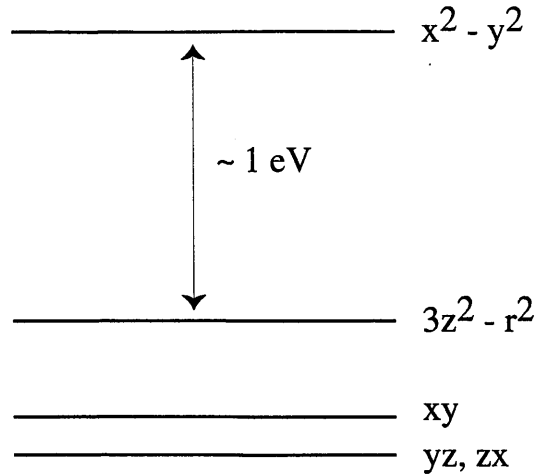


Figure 3-5: Electron energy levels for Cu 3d orbitals. [31]

The undoped materials are antiferromagnetic insulators. The atoms Sr, Cu and O, have electronic configurations Sr: $[\text{Kr}]5s^2$, Cu: $[\text{Ar}]3d^{10}4s$, and O: $[\text{He}]2s^2 2p^4$. Strontium and Oxygen have only one typical valence, which creates a closed shell configuration. Strontium will have valence 2+ ($[\text{Kr}]$) and Oxygen will have valence 2- ($[\text{He}]2s^2 2p^6 = [\text{Ne}]$). In order for the compounds, such as $\text{Sr}_2\text{Cu}_3\text{O}_5$, to have charge neutrality, the Cu atoms will be 2+ with configuration $[\text{Ar}]3d^9$. The Cu 2+ ions have one hole in the 3d electron shell, while the rest of the ions have closed electron shells.

Crucial to the chemistry of these compounds is the Cu 3d orbital in which the hole resides. This is determined by the crystal field energy splittings shown in figure 3-5. The hole in the Cu 3d electron shell resides in the highest electron energy state, the $3d_{x^2-y^2}$ orbital. This copper 3d orbital is the one which has lobes which point towards the neighboring oxygen atoms in the x,y plane, as shown in figure 3-4. The reason for this is simple. The hole, as an effective positive charge, has a lower energy when near the negatively charged oxygen 2- ions. These oxygen ions in the x,y plane are closer to the copper ion than the neighboring ions in the z direction.

The geometry of the Cu $3d_{x^2-y^2}$ orbital creates the strong antiferromagnetism in these materials by the superexchange interaction. The half-filled Cu $3d_{x^2-y^2}$ orbital contains an unpaired spin 1/2 electron. Because the lobes of the $3d_{x^2-y^2}$ orbital extend towards the nearest neighbor oxygen atoms in the plane, this orbital can hybridize

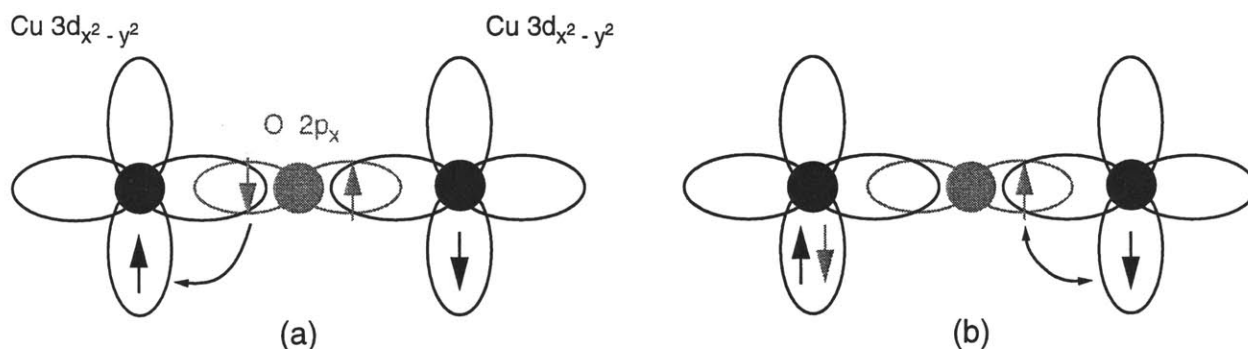


Figure 3-6: Superexchange mechanism. (a) Some electron down spin in oxygen $2p$ orbital hybridized with Cu orbital with up spin, so in (b) for remaining up spin in oxygen $2p$ orbital to hybridize with other Cu requires the Cu spins to be opposite.

with the $O 2p_\sigma$ orbitals of oxygen as shown in figure 3-6. The antiferromagnetism arises from the superexchange mechanism as described by P. Anderson [32]. The hybridization between the copper and oxygen orbitals results in an electron of the oxygen $2p_\sigma$ orbital having some probability for being in the $Cu 3d_{x^2-y^2}$ orbital. Because of the Pauli principle, the spin of this electron must be opposite to that of the Cu electron spin. The net result is that some of the unpaired electron spin of the Cu atom is transferred to the oxygen $2p$ orbital. This is also true for the other neighboring Cu atom of the oxygen. When the Cu-O-Cu bond angle is 180° , both Cu spins are transferred into the same oxygen $2p$ orbital. By the Pauli exclusion principle, the two spins in the same $2p$ orbital must be opposite. So, the 180° Cu-O-Cu bonds result in strong antiferromagnetic coupling between the unpaired Cu electron spins.

The large superexchange interaction of these copper oxides, $J \sim 1500$ K, implies that the hybridization of the copper $3d_{x^2-y^2}$ orbital with the oxygen $2p_\sigma$ orbitals is large also. Indeed, we shall estimate for the 2d compound, $Sr_2CuO_2Cl_2$, that $\sim 13\%$ of the unpaired Cu spin actually resides on the oxygen $2p_\sigma$ orbital (section

5.3). This value is larger than estimates from fluoride antiferromagnets, such as KNiF_3 (3.5% spin transfer) [33, 34], which has a much smaller value of $J = 45 \text{ K}$ [35]. The large hybridization of the orbitals in these copper oxides indicates that the electron wavefunction of the Cu electron is very extended. This large extension of the wavefunction suggests that these copper oxide materials are nearly metallic. If the Cu electrons were strongly localized, they would not have such strong antiferromagnetic interactions with one another.

In the spin ladder materials, there are also Cu-O-Cu bonds with roughly 90 degree bond angle. In contrast to the 180 degree bonds, these 90 degree bonds are expected to provide a ferromagnetic coupling that is only about one-tenth as strong as the 180 degree bonds [36, 32]. The strength of the 180 degree Cu-O-Cu antiferromagnetism relies on the Pauli exclusion principle when both Cu spins are transferred into the same oxygen 2p orbital. For a Cu-O-Cu bond with an angle close to 90 degrees, the unpaired Cu spins are transferred into different oxygen 2p orbitals. As a result, the unpaired spins interact only by the much weaker Hund's coupling, which is ferromagnetic. In addition, in these materials, the 90 degree magnetic interactions are frustrated. As shown in figure 3-4, the 90 degree interactions occur in pairs. Each copper spin has two 90 degree interactions and those two spins have a strong 180° antiferromagnetic bond. This triangle of two weak ferromagnetic interactions and one strong antiferromagnetic interaction cannot be fully satisfied and is thus frustrated. In the spin ladder materials, the 1 dimensional ladder structures have these frustrated interactions between them. However, experimentally these materials show little effect from the frustrated interactions, and are nearly ideal two-leg and three-leg spin $1/2$ antiferromagnets.

NMR and NQR are local probes of the environment of the nuclei. The local electronic structure of these materials is evident in NMR measurements in three main ways. These three ways are the quadrupole interaction, and the anisotropy of the orbital and spin Knight shifts. The quadrupole interaction measures the electric field gradient at the position of the nucleus (eq. 2.7). The contributions to the electric field gradient, eq , can be divided into two main contributions, based on a standard

ionic picture [37],

$$eq = eq_{hole} + (1 - \gamma)eq_{lattice} \quad (3.1)$$

The first contribution, eq_{hole} , arises from holes in orbitals of the ion itself [15, 23]. An isotropic distribution of charge, such as from a filled electron shell, will not produce an electric field gradient, but unfilled shells can. For the undoped compounds, the oxygen 2- ions have closed electron shells, so no contribution to the electric field gradient from eq_{hole} . On the other hand, the Cu 2+ ions have one hole in the $3d_{x^2-y^2}$ orbital. From electron-spin-resonance studies, Bleaney *et al.*[23] demonstrated that a single hole in the ^{63}Cu $3d_{x^2-y^2}$ orbital produces an axially symmetric electric field gradient of about 70 MHz. Shimizu [38] studied the quadrupole interaction data on a number of copper-oxide compounds and used the results to estimate the contribution of the Cu 3d hole. One hole in the Cu $3d_{x^2-y^2}$ orbital produces the nuclear quadrupole interaction $\approx (-38.5, -38.5, 77)$ MHz.[39, 38]

The second contribution to the electric field gradient in equation 3.1, $eq_{lattice}$, arises from the charges of the other ions of the crystal. This electric field is then modified by the distortion which it creates in the electronic orbitals of the observed ion itself. This effect is accounted for by the Sternheimer antishielding factor, γ . For CuO_2 planes in high T_c superconductors, the value of γ is estimated as $^{63}\gamma \approx -20$ and $^{17}\gamma \approx -9$ for ^{63}Cu and ^{17}O , respectively.[38, 41] We estimate the lattice contribution to the electric field gradient by using point charge lattice summations. We treat all the neighboring ions, i , as having their ionic charge, e_i , as a point charge at their position in the crystal structure. Then, we just sum the contributions to the electric field gradient at the chosen nucleus position from all the other ions.

$$eq_{lattice}^z = \sum_i e_i \frac{(3z_i^2 - r_i^2)}{r_i^5} \quad (3.2)$$

With a computer program, it is easy to do the summation out to a radius (~ 100 Å) where any further summation does not significantly alter the result. With this information, we can estimate the quadrupole interaction for both $^{63,65}\text{Cu}$ and ^{17}O from the crystal structure.

The second way NMR can provide information about the electron orbitals is by the anisotropy in the orbital component of the Knight shift, K_{orb} (eq. 2.3). The orbital Knight shift is proportional to the electron orbital susceptibility of the ion (eq. 2.2).

$$K_{orb} = 2 \left\langle \frac{1}{r^3} \right\rangle \chi_{orb} \quad (3.3)$$

where $\langle 1/r^3 \rangle$ is the expectation value of $1/r^3$ for the electron orbital. When the ion has only full electron shells, there is no significant orbital susceptibility. This implies that there is no orbital Knight shift for oxygen NMR. The copper ions, on the other hand, have one hole in the $3d_{x^2-y^2}$ orbital. The theoretical expressions for Cu K_{orb} are [39, 15]

$$K_{orb,\perp} \text{ Cu-O plane } (z) = \frac{16\mu_B^2}{E_{xy}} \left\langle \frac{1}{r^3} \right\rangle \quad (3.4)$$

$$K_{orb,\parallel} \text{ Cu-O plane } (xy) = \frac{4\mu_B^2}{E_{xz,yz}} \left\langle \frac{1}{r^3} \right\rangle \quad (3.5)$$

where $E_{xy,xz,yz}$ is the crystal field energy difference between the $3d_{x^2-y^2}$ orbital and the $3d_{xy,xz,yz}$ orbitals respectively. The important result is that the orbital Knight shift perpendicular to the Cu-O plane is 4 times larger than the orbital shift in the Cu-O plane assuming the $3d_{xy,xz,yz}$ orbitals have the same energy [31].

Anisotropy of the spin Knight shift can also reveal where in the crystal structure the unpaired electron spin resides. This derives from the form of the dipole-dipole coupling between spins [13]. In this case, we have the hyperfine coupling between the electron spin, S , and nuclear spin, I .

$$\mathcal{H}_{dip} = \frac{1}{r_{e-n}^3} \left[\vec{\mu}_I \cdot \vec{\mu}_S - 3 \frac{(\vec{\mu}_I \cdot \vec{r}_{e-n})(\vec{\mu}_S \cdot \vec{r}_{e-n})}{r_{e-n}^2} \right] \quad (3.6)$$

The dipolar coupling depends on the direction of the vector, \vec{r}_{e-n} , between the nucleus and the electron. As a consequence, the anisotropy of the coupling can tell us which orbitals contain unpaired electrons. For example, if we want the dipole hyperfine coupling along the z axis, only the z component of the spins is important. The

coupling is

$$\mathcal{H}_{dip,z} = \frac{1}{r_{e-n}^3} \mu_I \mu_S \left[1 - 3 \left\langle \left(\frac{z_{e-n}}{r_{e-n}} \right)^2 \right\rangle \right] \quad (3.7)$$

where the average $\langle (z/r)^2 \rangle$ is taken over the electron orbital. Symmetric expressions apply to the x and y axes. For a $d_{x^2-y^2}$ orbital, $\langle (x/r)^2 \rangle = \langle (y/r)^2 \rangle = 3/7$ and $\langle (z/r)^2 \rangle = 1/7$. Thus, the dipolar hyperfine field at the nucleus is

$$\frac{4}{7} \mu_B \langle r^{-3} \rangle (\langle S_x \rangle, \langle S_y \rangle, -2 \langle S_z \rangle) \quad (3.8)$$

So, unpaired spin in the Cu $3d_{x^2-y^2}$ orbital provides a negative hyperfine field along the z axis and a positive hyperfine field along x and y that is half as big. Similarly, for a p_z orbital [33, 40, 41],

$$\frac{4}{5} \mu_B \langle r^{-3} \rangle (-\langle S_x \rangle, -\langle S_y \rangle, 2 \langle S_z \rangle) \quad (3.9)$$

For the p orbital, the largest hyperfine field is along the direction of the orbital and is positive. Note that the dipolar hyperfine interaction is always traceless, the components sum to zero. For an isotropic s orbital, the dipolar hyperfine interaction cancels to zero. However, since an electron in a s orbital has a finite probability of being at the nucleus position, there is a large contact hyperfine interaction. The contact interaction magnetic field is always positive and is expressed as [15]

$$H_{int} = \frac{8\pi}{3} \mu_B R_s^2(r=0) \quad (3.10)$$

where $R_s^2(r=0)$ is the probability for the electron to be at the nucleus ($r=0$). This contact interaction can be two orders of magnitude larger than the dipole interactions from the p and d orbitals. Thus, any tiny amount of unpaired spin in an s orbital can give positive contributions to the hyperfine field. So, the contact interaction is expected to be positive and isotropic. In contrast, the core polarization effect is typically negative. This is a consequence of that the polarization of inner (core) electron spins in response to the outer electron spin polarization is typically in the

opposite direction. The resulting hyperfine field is thus negative with respect to the outer electron spin polarization.

All of the copper-oxide materials described in this thesis have the same basic local crystal structure, Cu ions surrounded by a square of oxygen ions. As discussed in the following chapters, the NMR/NQR experiments do show results consistent with the accepted picture of the electron orbital structure for these materials. That picture is that there is one hole in the Cu 3d orbital which resides in the $3d_{x^2-y^2}$ orbital and this Cu orbital strongly hybridizes with the oxygen $2p\sigma$ orbitals. The strong antiferromagnetic interaction is a consequence. The main focus of this thesis is the effect of the dimensionality of the magnetic interactions on the temperature dependence of the magnetic correlations.

Chapter 4

1d $S=1/2$ Heisenberg

Antiferromagnet

One-dimensional antiferromagnetic spin chains have been studied extensively in the past several years because of interest in the strong influence of quantum fluctuations on their properties. In addition, the 1-d systems are the simplest among various quantum Heisenberg antiferromagnets. The ground state of the 1-D spin 1/2 Heisenberg antiferromagnetic chain,

$$\mathcal{H} = J \sum \mathbf{S}_i \cdot \mathbf{S}_j \quad (4.1)$$

where J is the exchange interaction, has been well understood for a number of years [42]. The ground state does not have long range order even at $T = 0$ because the Néel (long range ordered) state is disrupted by quantum fluctuations. Instead there is short range order with power law decay of the spin correlations [43]. Recent interest in low dimensional magnetism has been promoted by the discovery of high T_c superconductivity in doped copper-oxide materials. Similar copper-oxide materials have been discovered which have nearly ideal 1 dimensional electron spin interactions. For comparison to experiments in these materials, recent calculations have been made of the finite temperature static and dynamic spin behavior in the 1 dimensional Heisenberg antiferromagnet [44, 45, 21, 46, 47, 48].

In this chapter, we report ^{17}O and ^{63}Cu nuclear magnetic resonance (NMR) mea-

measurements up to high temperatures on Sr_2CuO_3 and SrCuO_2 , nearly ideal 1-d spin 1/2 Heisenberg antiferromagnets. Using ^{17}O NMR, we reveal the wave-vector, q , dependence of the low energy spin excitations and separate the $q = 0$ and $q = \pi$ contributions. Thus, we can measure the $q = 0$ contributions to low energy spin excitations in the 1-d spin 1/2 Heisenberg antiferromagnet and test the theoretical predictions. We find that in Sr_2CuO_3 the chain oxygen $1/T_1(q = 0) \propto aT + bT^2$ over the whole temperature range 10 to 700 K. The low temperature limit of these experimental results is in reasonable agreement with the low T scaling theory of Sachdev,[44] $1/T_1(q = 0) = aT$ where $a = F_{\perp}^2(q = 0) \frac{1}{\pi^3 J^2}$, but even at the lowest temperatures measured $T = 10\text{K}$ ($T/J \approx 0.005$), $1/T_1$ does not show the expected linear temperature dependence. Frequency dependence measurements show that diffusive contributions dominate $T_1(q \approx 0)$ for SrCuO_2 . High temperature ^{63}Cu $1/T_1$ measurements in Sr_2CuO_3 and SrCuO_2 also show the increase in contributions to $1/T_1$ from $q = 0$ at high temperatures. The double chain compound, SrCuO_2 , shows 1-d behavior analogous to that of Sr_2CuO_3 in the NMR measurements above 10 K, implying that the frustrated interactions between the pairs of chains do not affect the spin dynamics above 10 K.

4.1 Crystal Structure of Sr_2CuO_3 and SrCuO_2

In this chapter, two closely related copper oxide compounds, Sr_2CuO_3 and SrCuO_2 [49], are described. These materials have a 1 dimensional Cu-O chain structure (figures 4-1 and 4-2). Sr_2CuO_3 has copper-oxygen chains along the b axis, with 180 degree Cu-O-Cu bonds which are expected to result in strong antiferromagnetic superexchange.[50] Motoyama, *et al.* measured the bulk susceptibility of Sr_2CuO_3 and found a good agreement to the theoretical prediction for the $S=1/2$ 1-d spin chain [46, 47] with the exchange interaction, $J \approx 2200\text{K}$.[51] Sr_2CuO_3 is a very good experimental model for the 1-d Heisenberg antiferromagnet because long range ordering only takes place at $T_N \approx 5\text{K}$.[52] This implies that the interchain interaction, J' , is very small in comparison to the intrachain interaction, J , $J'/J \sim 10^{-3}$.[52] As

a result, Sr_2CuO_3 should reveal ideal 1-d behavior over a wide range in temperature.

The structure of SrCuO_2 has copper-oxygen chains similar to Sr_2CuO_3 , but has a pair of these copper-oxygen chains along the c axis. The pair of copper-oxygen chains are coupled by 90 degree Cu-O-Cu bonds with frustrated exchange interaction, $J' < 0$. The magnitude of the exchange, J' , is expected to be much smaller than the intrachain exchange interaction, J , $J' = 0.1 - 0.2|J|$. [50] Thus, at high temperatures, SrCuO_2 would be expected to behave like two uncoupled chains. In fact, the bulk susceptibility [51] of SrCuO_2 shows a good fit to the theoretical 1-d susceptibility [46, 47] with $J \approx 2100\text{K}$. A spin freezing transition occurs at 5 K, only $\approx 3 \times 10^{-3} J/K_B$ [53, 54]. In addition, long range three dimensional order does not appear down to the lowest temperature studied, 0.3 K [53]. This implies that any effective inter-double chain coupling is very small or inter-double chain frustration suppresses long range order. In fact, Zaliznyak *et al.* [53] found that the spin correlation length in the direction of the frustrated double chain interaction (b axis) is only 2 lattice spacings in the “spin frozen” state, while the correlation length is much larger for the other two axes, ~ 60 for a axis and > 200 for c axis. Both SrCuO_2 and Sr_2CuO_3 are very ideal models for the 1-D spin 1/2 Heisenberg antiferromagnet, with the difference that SrCuO_2 has a frustrated interaction between pairs of chains which may affect low temperature behavior.

For our experiments, we used single crystals of the two compounds, Sr_2CuO_3 and SrCuO_2 , which were grown by F.C. Chou at MIT. Laue x-ray scattering was used in addition to NMR measurements to confirm the directions of the crystal axes in the samples. In both of these samples, there is only one copper atomic site, but there are two oxygen sites as shown in figure 4-2. One of the oxygen sites, which I will call the O(1) chain oxygen site, is in between copper atoms along the Cu-O chain. The other oxygen site, the O(2) apical oxygen site, is bonded to only one copper atom and sits off to the side of the Cu-O chain. The oxygen NMR spectra are shown in figures 4-3 (Sr_2CuO_3) and 4-4 (SrCuO_2). The two oxygen sites seen in the spectra can be unambiguously assigned to the structural sites by using the symmetry of the electric field gradient (quadrupole interaction) and Knight shift tensors. The experimentally

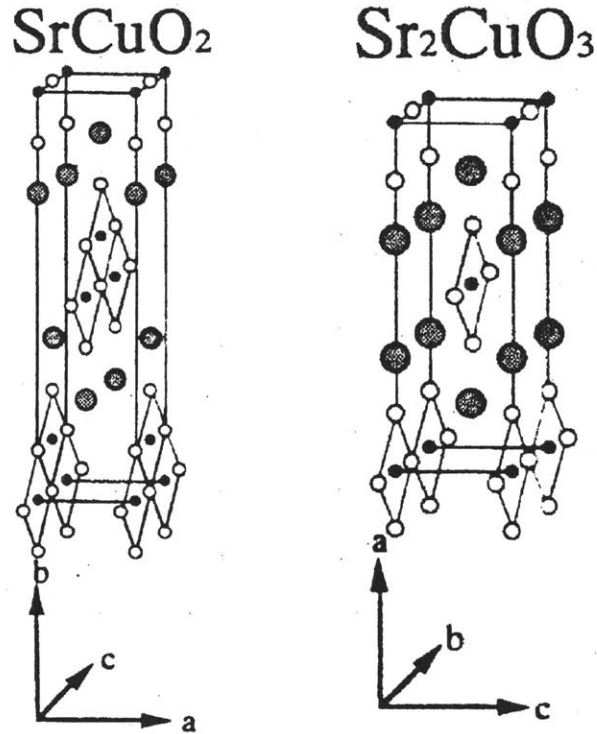


Figure 4-1: Crystal structure of SrCuO_2 and Sr_2CuO_3 . Solid circles Cu atoms, open circles O atoms, shaded circles Sr atoms. (from Motoyama, *et al.*[51])

measured quadrupole interactions and the calculated values from point charge lattice summation are shown in tables 4.1 and 4.2. The point charge lattice summations show the relative size of the quadrupole interactions, but do not include the effect of the electrons of the atom where the nucleus is located. For oxygen 2- ions, the distortion of the on-site electrons magnifies the electric field by about a factor of 10 [41]. In general, for the oxygen sites, point charge lattice summations indicate that the largest electric field gradient is along the copper-oxygen bond. Similarly, as discussed below, the oxygen Knight shift for these samples is axially symmetric around the copper-oxygen bond direction with the largest value along the copper-oxygen bond direction. These symmetries of the quadrupole interaction and Knight shift are common to all of these related copper-oxide materials discussed in this thesis. Additionally, for Sr_2CuO_3 , there are twice as many apical oxygens as chain oxygens, giving twice the intensity to the apical oxygen resonance lines. Symmetry of the Knight shift and NMR intensity provide confirmation of the site assignment.

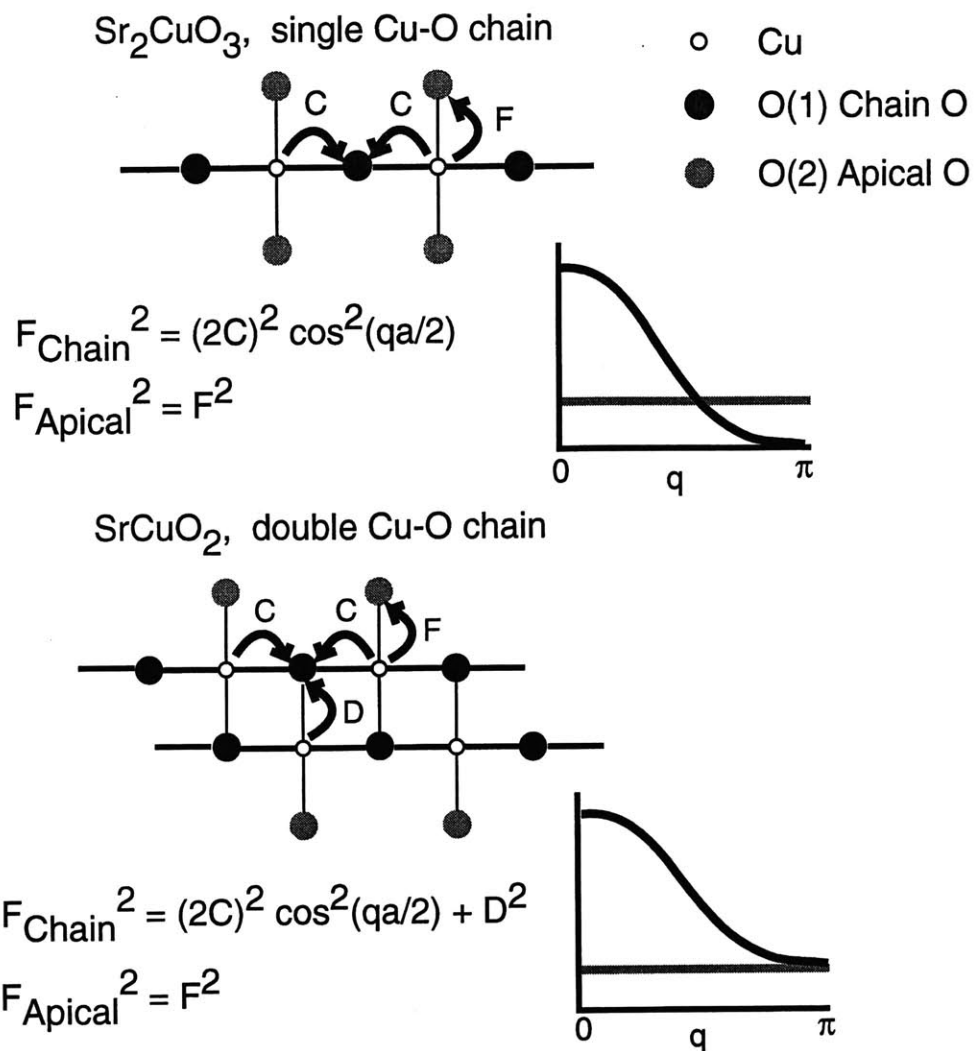


Figure 4-2: Detailed structure of the Cu-O chains of Sr_2CuO_3 (single Cu-O chain) and SrCuO_2 (double Cu-O chain). Hyperfine transfers to oxygen sites are also shown.

Table 4.1: Magnitude of quadrupole interaction [kHz] measured at room temperature

Sr_2CuO_3	a	b	c
O(1) chain	764	972	198
O(2) apical	526	383	146
Cu	2,370	3,700	1,330
SrCuO_2	a	b	c
O(1) chain	538	74	610
O(2) apical	127	461	333
Cu	6,512	1,878	8,393

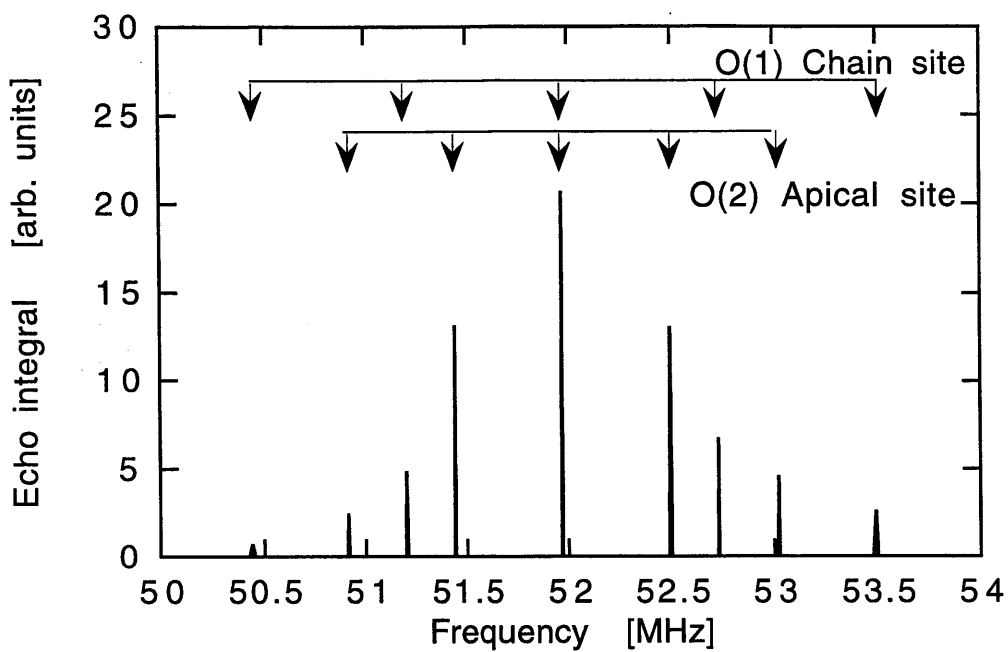


Figure 4-3: ^{17}O NMR spectra for Sr_2CuO_3 . $H = 9 \text{ T} \parallel a$ axis, room temperature.

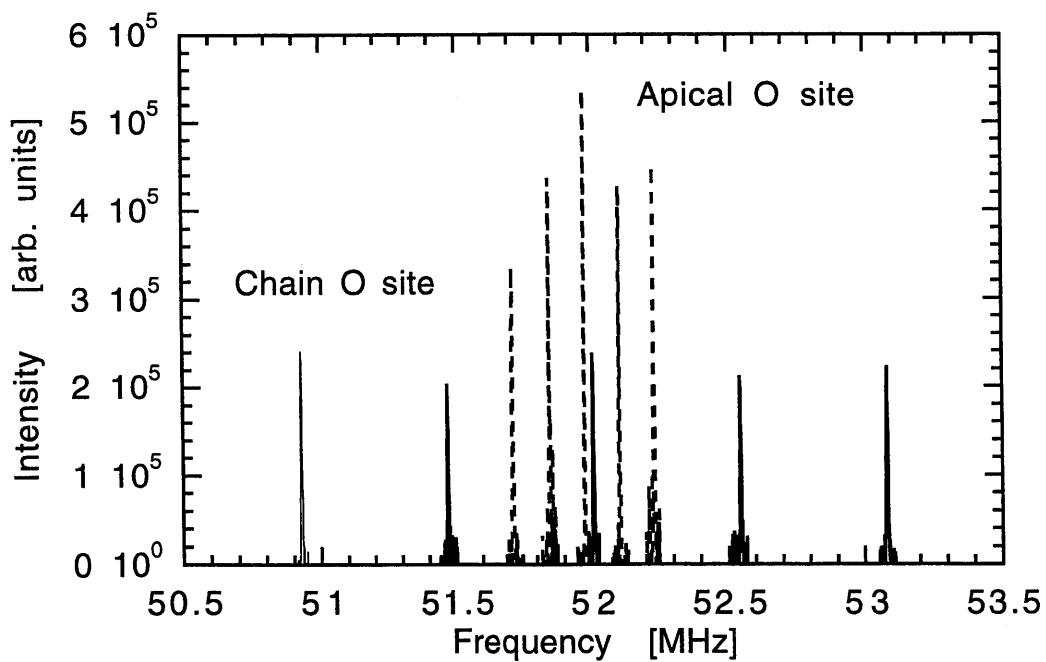


Figure 4-4: ^{17}O NMR spectra for SrCuO_2 . Solid line: Chain oxygen site, dashed line: Apical oxygen site. $H = 9 \text{ T} \parallel a$ axis, room temperature.

Table 4.2: Calculated quadrupole interaction point charge [kHz]

Sr_2CuO_3	a	b	c
O(1) chain	52.8	-67.9	15.1
O(2) apical	-41.1	23.9	17.2

SrCuO_2	a	b	c
O(1) chain	72.8	-9.2	-63.6
O(2) apical	71.9	-161	89.2

4.2 Knight shift

The Knight shift reflects the local magnetic susceptibility. The overall results are shown for Sr_2CuO_3 ^{17}O and ^{63}Cu (figures 4-5 and 4-6) and for SrCuO_2 ^{17}O and ^{63}Cu (figures 4-7 and 4-8). As discussed in chapter 2 on NMR measurements, the Knight shift from the electron spins is proportional to the uniform spin susceptibility (eq. 2.3). The proportionality measures the hyperfine form factor at $q = 0$, $F(q = 0)$. Using K- χ plot analysis to compare the Knight shift and the bulk magnetic susceptibility [51], the hyperfine form factor is determined (eq. 2.4). For these materials, since the temperature dependence of the susceptibility and Knight shift are so small, determining accurate hyperfine interactions is difficult. Covering a wide range of temperature up to as high as 800 K is essential. We present the plots of Knight shift as a function of bulk susceptibility for Sr_2CuO_3 (figures 4-9 and 4-10) and SrCuO_2 (figures 4-11 and 4-12). Even with the difficulty of very small Knight shift changes, the results for the ^{17}O hyperfine couplings in table 4.3 clearly reflect the crystal structure of the materials. All of the oxygen sites show the largest hyperfine interaction when the magnetic field is applied along the Cu-O bond direction. This reflects the covalent bonding between the Cu $3d_{x^2-y^2}$ orbital and the O $2p_\sigma$ orbital (eq. 3.9). We note that the uncertainty in the Cu hyperfine couplings is large because of the large changes in linewidth (figure 4-13) and quadrupole interaction (figure 4-15) in relation to the total change in the Knight shift over the entire temperature range ~ 10 kHz. We emphasize that the Knight shift for Cu is calculated using the full Hamiltonian for nuclear spin $I=3/2$ to account for the quadrupole shift of the central line. For oxygen,

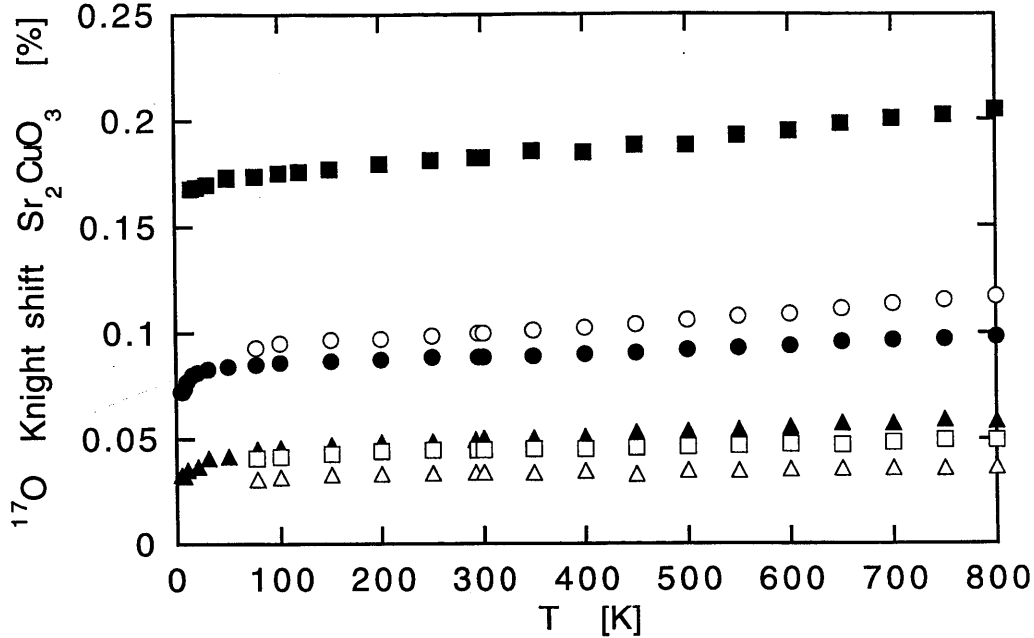


Figure 4-5: ^{17}O Knight shift Sr_2CuO_3 for chain oxygen (filled symbols) and apical oxygen (open symbols) for a (\bullet), b (\blacksquare), and c axes (\blacktriangle).

Table 4.3: Oxygen hyperfine couplings ($q=0$) [kOe/μ_B]

Sr_2CuO_3	a	b	c
O(1) chain	45 ± 30	95 ± 30	44 ± 30
O(2) apical	75 ± 30	23 ± 30	14 ± 30
SrCuO_2	a	b	c
O(1) chain	110 ± 30	142 ± 30	142 ± 30
O(2) apical	35 ± 30	76 ± 30	3 ± 30

the quadrupole shift of the central line is calculated with second order perturbation theory. The quadrupole interaction for oxygen is much smaller than that for copper and temperature independent, so temperature dependence of the quadrupole shift is not significant.

In addition to the hyperfine couplings, comparison of the bulk susceptibility and the Knight shift also provides an estimate of K_{chem} . K_{chem} includes the contributions to the Knight shift which are not from the spin portion of the susceptibility, but rather from the diamagnetic, K_{dia} , and orbital susceptibility, K_{orb} . Estimating $K_{chem} = K_{dia} + K_{orb}$ requires extrapolating the linear fit of Knight shift as a function of spin

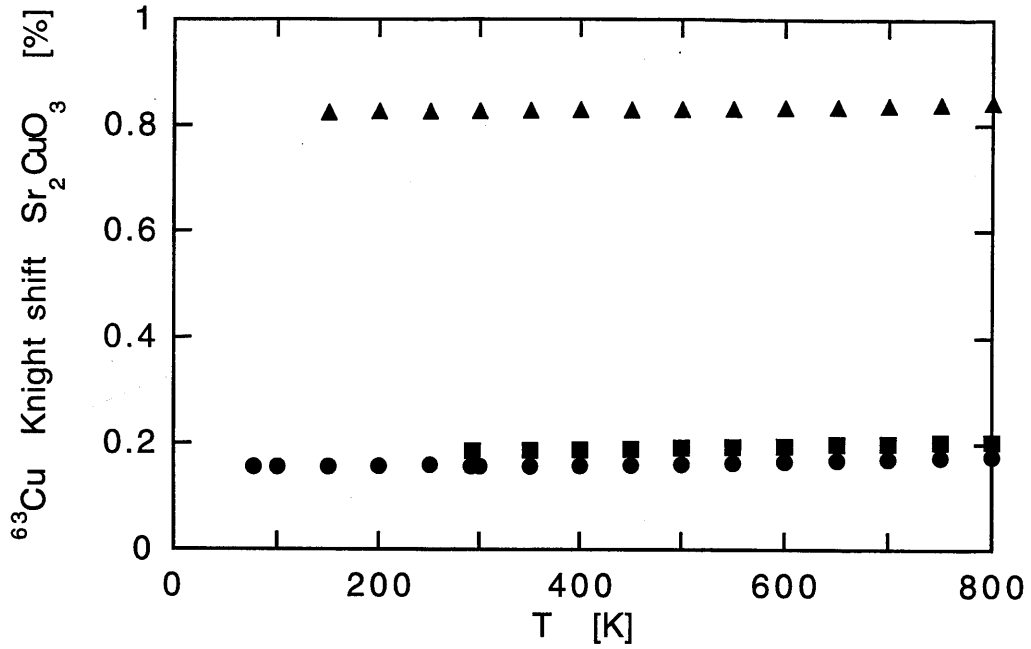


Figure 4-6: ^{63}Cu Knight shift Sr_2CuO_3 for a (\bullet), b (\blacksquare), and c axes (\blacktriangle).

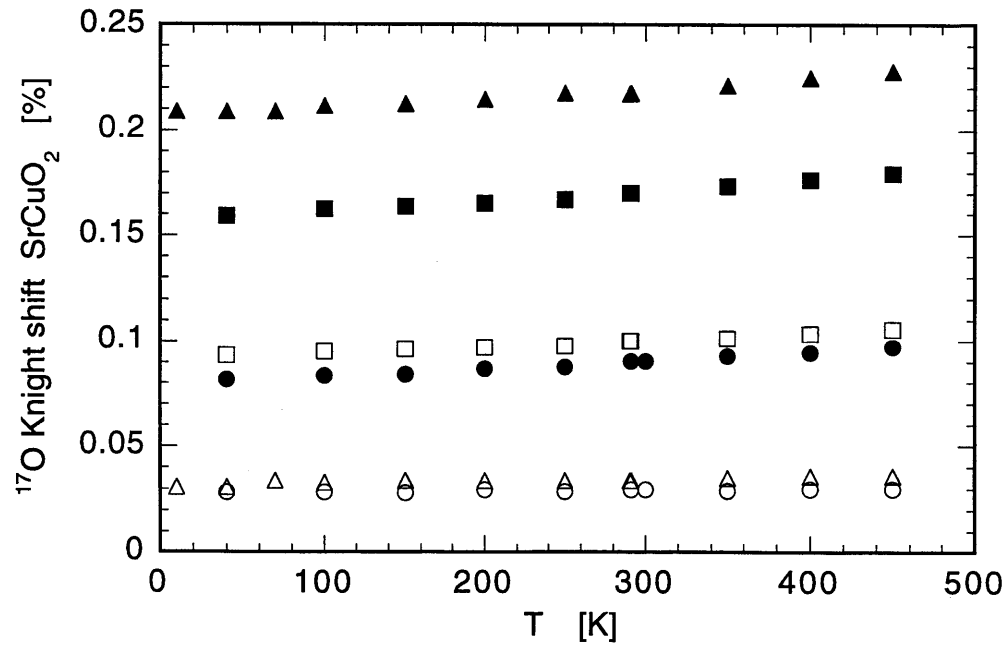


Figure 4-7: ^{17}O Knight shift SrCuO_2 for chain oxygen (filled symbols) and apical oxygen (open symbols) for a (\bullet), b (\blacksquare), and c axes (\blacktriangle).

Table 4.4: Copper hyperfine couplings at $q=0$ [kOe/μ_B]

		a	b	c
Sr_2CuO_3	Copper	80 ± 60	84 ± 60	64 ± 60
SrCuO_2	Copper	6 ± 40	52 ± 40	58 ± 40

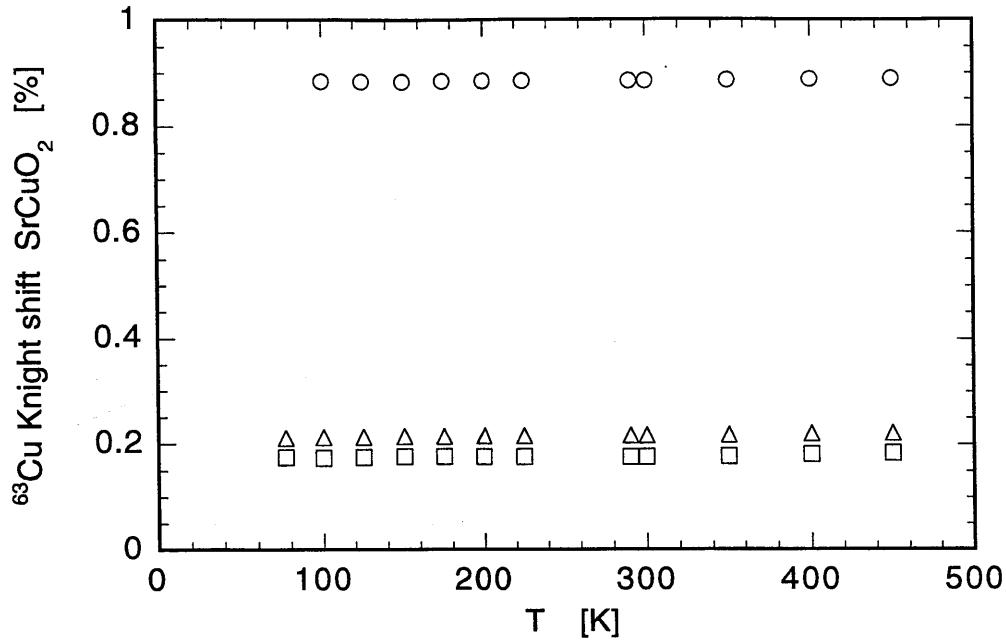


Figure 4-8: ^{63}Cu Knight shift SrCuO_2 for a (○), b (□), and c axes (△).

susceptibility to the zero of spin susceptibility. Essentially, K_{chem} represents the Knight shift when the spin susceptibility is zero. This also requires the estimation of the diamagnetic and orbital contributions to the bulk susceptibility. Motoyama, *et al.* [51] estimated the diamagnetic susceptibility as 10.7×10^{-5} emu/mole for Sr_2CuO_3 and 6.6×10^{-5} emu/mole for SrCuO_2 and the orbital susceptibility as shown in table 4.5. Using these estimates, the chemical Knight shift, K_{chem} , is also shown in table 4.5. For the oxygen 2- ions, since they have a closed shell configuration, orbital susceptibility is negligibly small. As a result, the magnitude of K_{chem} for oxygen is quite small. For the Cu 2+ ions, there is a hole in the $3d_{x^2-y^2}$ orbital, which causes significant orbital susceptibility. The symmetry of the Cu $3d_{x^2-y^2}$ orbital is reflected by a large K_{chem} in the direction perpendicular to the plane of the Cu-O bonds. The theoretical expressions are given in equations 3.4 and 3.5. The important result is that the chemical shift perpendicular to the Cu-O plane is 4 times larger than the chemical shift in the Cu-O plane assuming the $3d_{xy,xz,yz}$ orbitals have the same energy. This is a reasonable approximation for the CuO_6 octahedra in the high T_c cuprates. In these 1d materials, the ratio of the chemical shifts for copper is somewhat larger, $\sim 7 \pm 2$. The magnitude of the chemical shifts, $K_{\perp\text{Cu-O},112} = 0.895$ and $K_{\parallel\text{Cu-O},112} = 0.121, 0.130$,

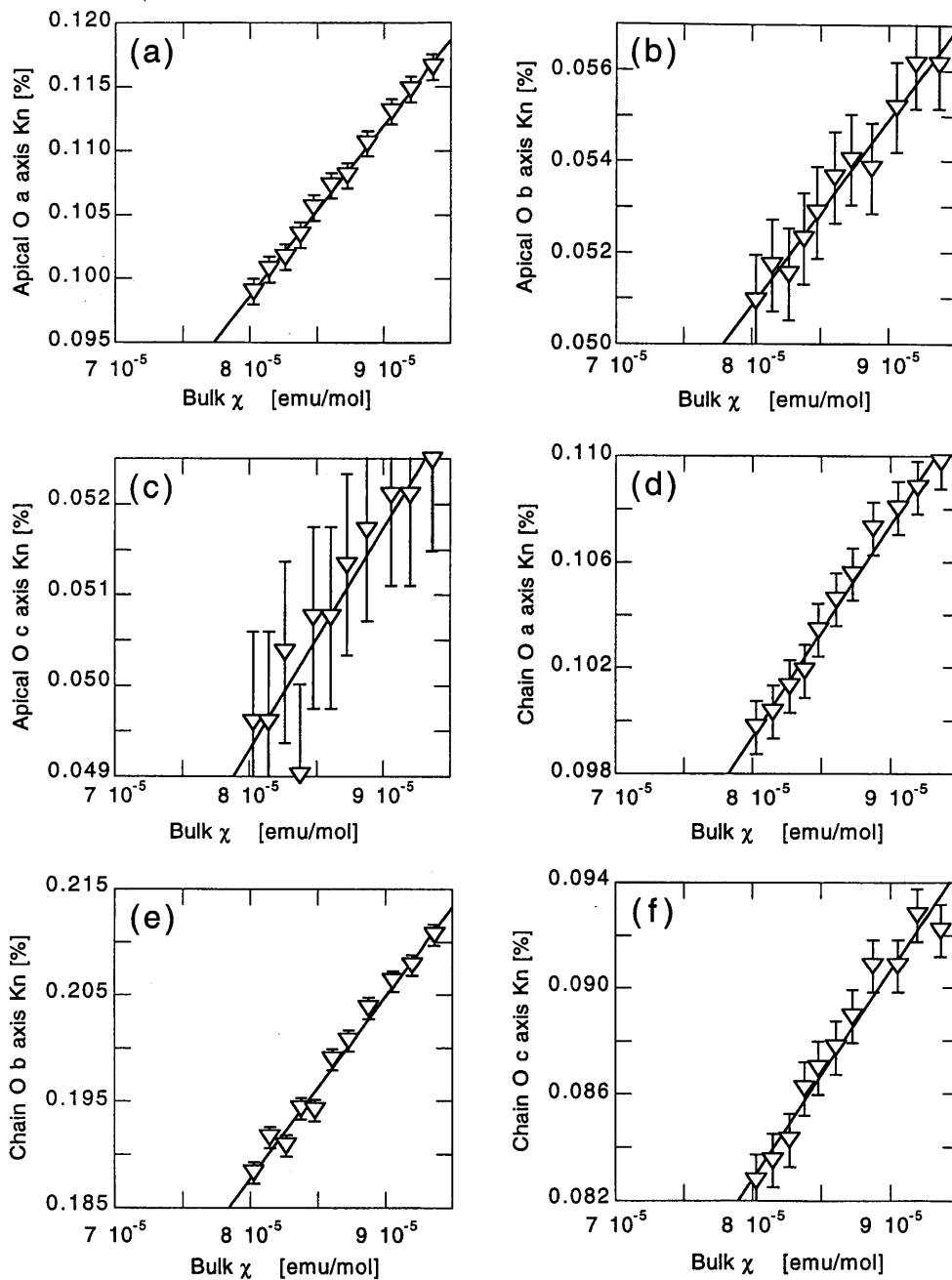


Figure 4-9: Knight shift as a function of bulk susceptibility for ^{17}O in Sr_2CuO_3 . Slope of the linear fits represents $q=0$ hyperfine coupling. (a), (b), (c) Apical oxygen Knight shift for a, b, and c axes, respectively. (d), (e), (f) Chain oxygen Knight shift for a, b, and c axes, respectively.

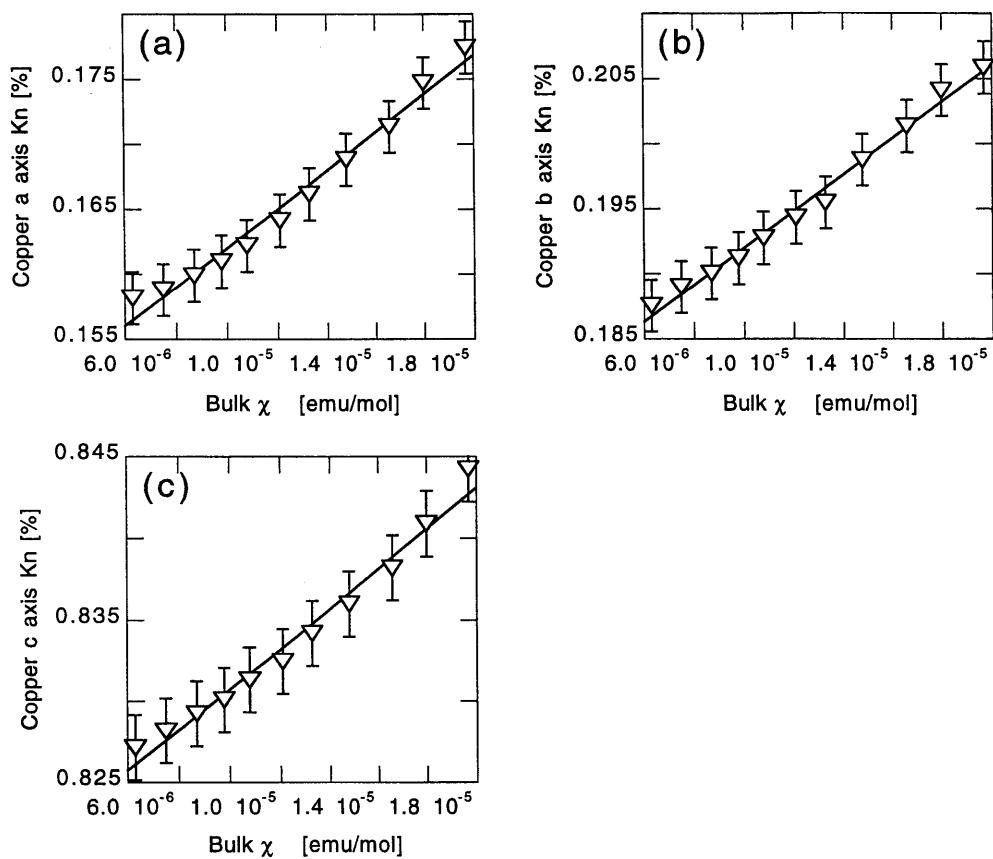


Figure 4-10: Knight shift as a function of bulk susceptibility for ^{63}Cu in Sr_2CuO_3 . Slope of the linear fits represents $q=0$ hyperfine coupling. (a), (b), (c) are for a, b, and c axes, respectively.

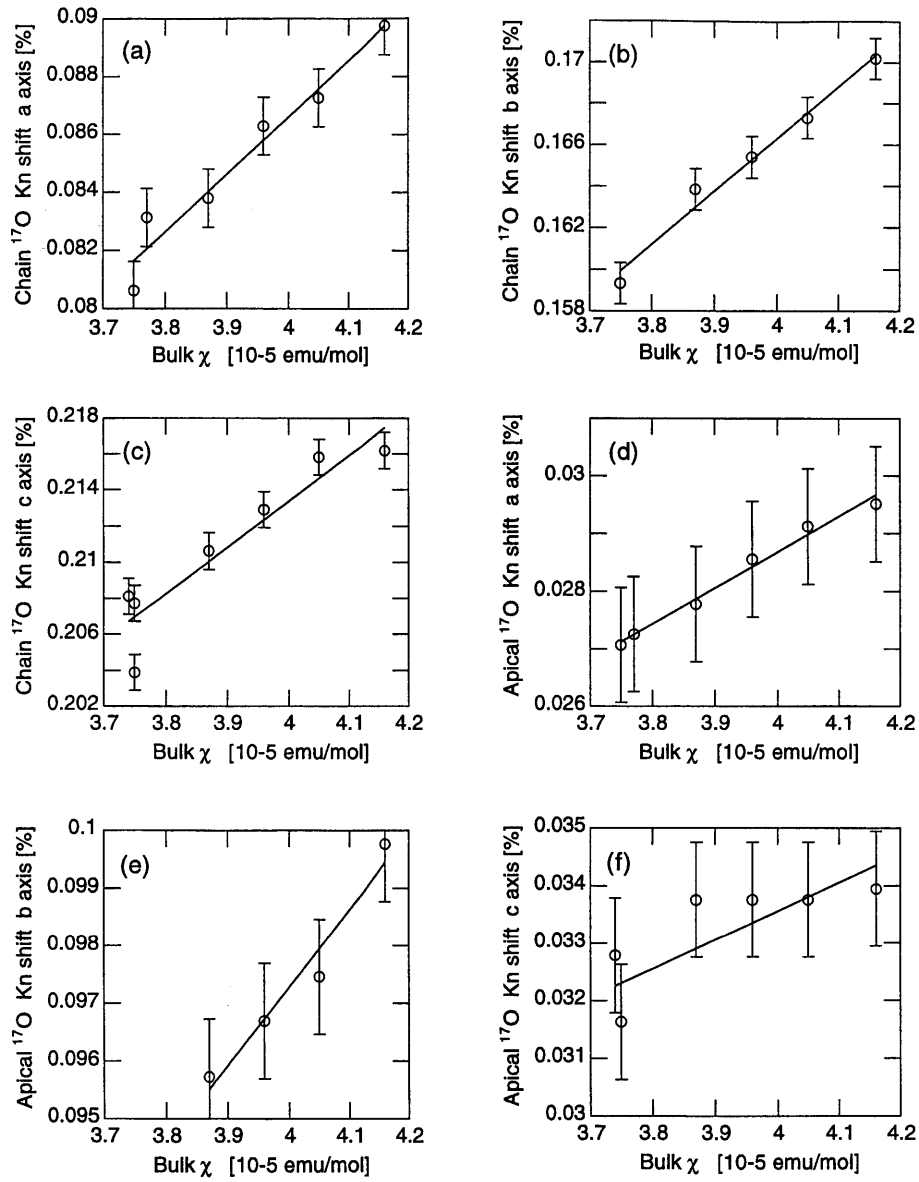


Figure 4-11: Knight shift as a function of bulk susceptibility for ^{17}O in SrCuO_2 . Slope of the linear fits represents $q=0$ hyperfine coupling. (a), (b), (c) Chain oxygen Knight shift for a, b, and c axes, respectively. (d), (e), (f) Apical oxygen Knight shift for a, b, and c axes, respectively.

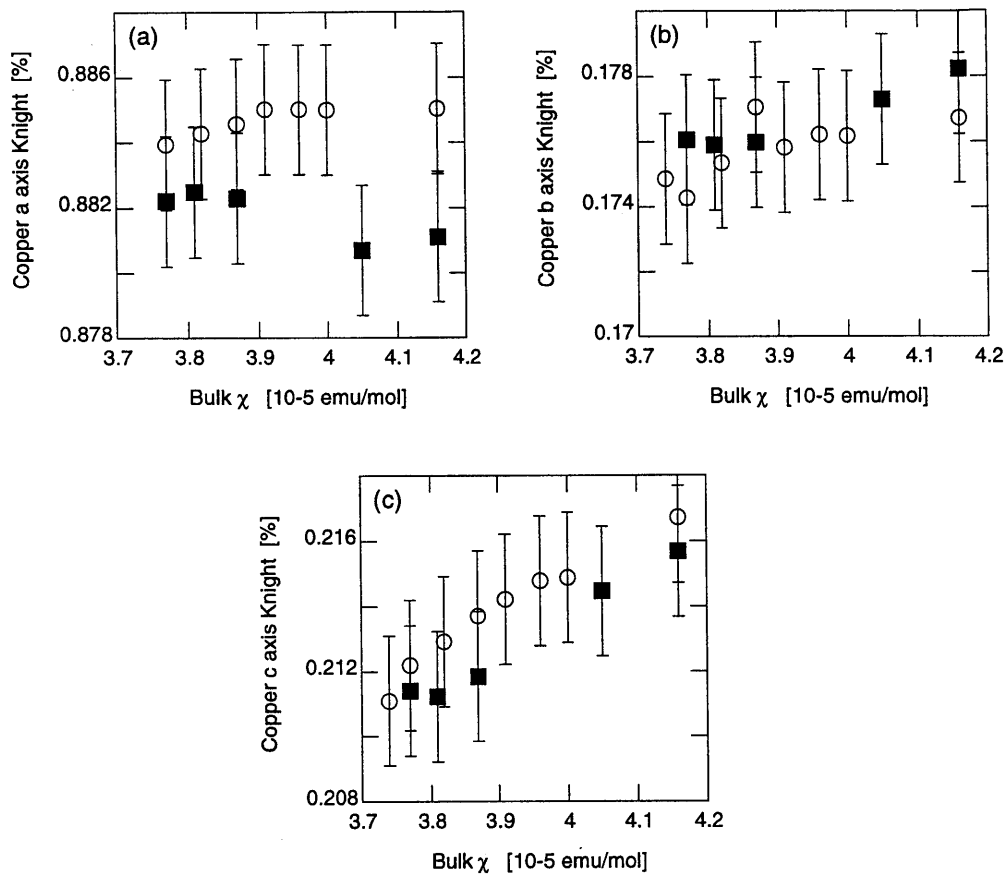


Figure 4-12: Knight shift as a function of bulk susceptibility for ^{63}Cu in SrCuO_2 . ○ and ■ are data from two separate measurement runs. (a), (b), (c) are for a, b, and c axes, respectively.

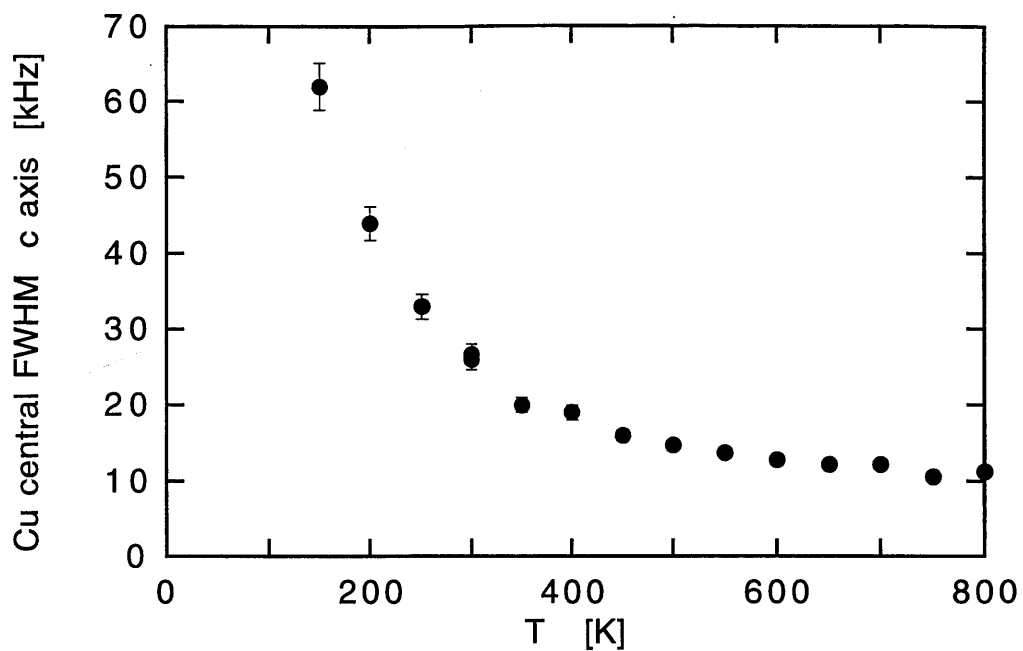


Figure 4-13: ^{63}Cu NMR central (-1/2, +1/2) linewidth c axis for Sr_2CuO_3 .

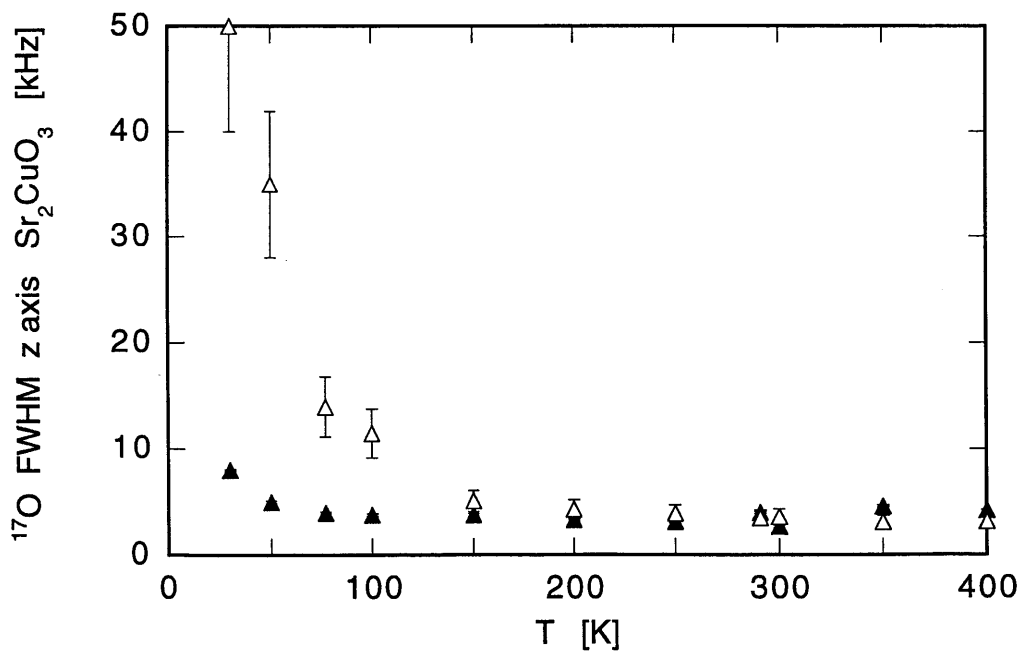


Figure 4-14: ^{17}O NMR central (-1/2, +1/2) linewidth c axis for Sr_2CuO_3 . \blacktriangle chain oxygen, \triangle apical oxygen.

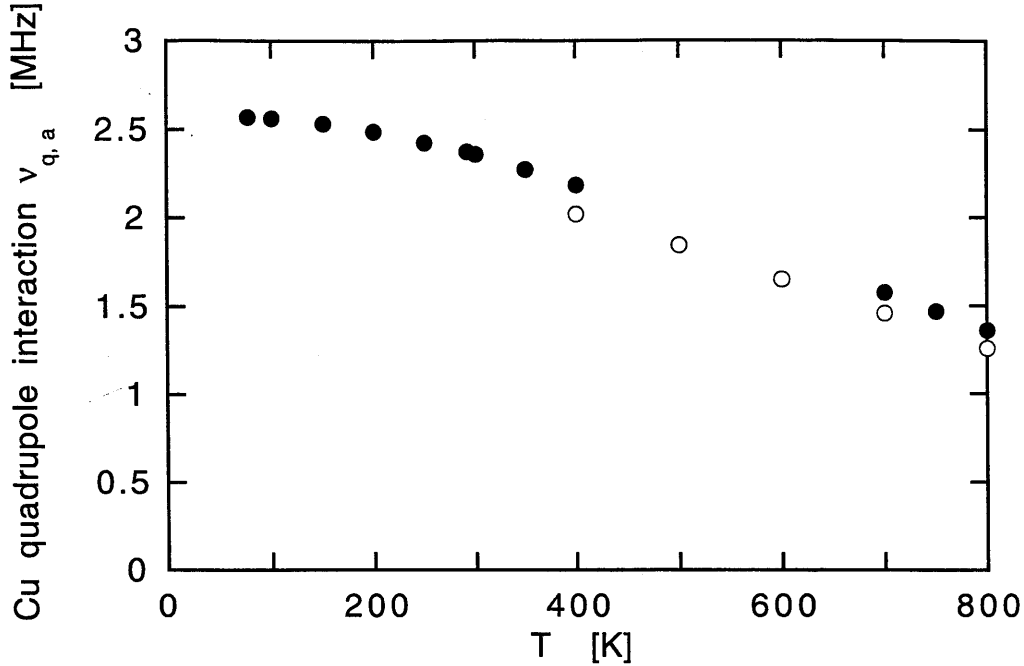


Figure 4-15: Copper quadrupole interaction, $\nu_{Q,a}$, a axis for Sr_2CuO_3 . \bullet ^{63}Cu , \circ ^{65}Cu .

are smaller than those for related high T_c copper-oxides, $K_{\perp} = 1.28 \pm 0.01\%$ and $K_{\parallel} = 0.28 \pm 0.01\%$ for $\text{YBa}_2\text{Cu}_3\text{O}_7$ [39] and $\text{Sr}_2\text{CuO}_2\text{Cl}_2$. This suggests that the crystal field energy splitting is larger in these 1d copper-oxide materials than in the 2d materials. This is logical because these 1d compounds have only a CuO_4 square structure with no oxygen nearest neighbor in the z direction. This will more strongly favor the orbitals along x and y , which increases the crystal field splitting, and makes $E_{xy} < E_{xz,yz}$. This is exactly what we see experimentally; using $\langle 1/r^3 \rangle = 6$ atomic units[14], we obtain $E_{xy} = 3.9$ eV and $E_{xz,yz} = 6.7-7.2$ eV.

Besides providing information about the structure of the electron orbitals, the Knight shift can also be compared to theoretical results for the spin susceptibility of the spin 1/2 1d Heisenberg antiferromagnet. The Knight shift for the chain oxygen in Sr_2CuO_3 along the a axis is shown in figure 4-16. The Knight shift has two main features: first a temperature dependence much weaker than related copper-oxide materials with higher dimensionality of the spin interactions as described in this thesis. Second, below 20 K, the Knight shift sharply decreases. Both of these

Table 4.5: K_{chem} [%]

Sr_2CuO_3	a	b	c
O(1) chain	0.02 ± 0.05	0.05 ± 0.05	0.00 ± 0.05
O(2) apical	-0.01 ± 0.05	0.01 ± 0.05	0.02 ± 0.05
Cu	0.036 ± 0.08	0.072 ± 0.08	0.725 ± 0.08
χ_{orb} (Motoyama) 10^{-5} emu/mole	3.4	3.3	7.2
$SrCuO_2$	a	b	c
O(1) chain	-0.06 ± 0.03	-0.03 ± 0.05	0.02 ± 0.05
O(2) apical	-0.02 ± 0.02	0.00 ± 0.04	0.03 ± 0.02
Cu	0.895 ± 0.05	0.121 ± 0.05	0.130 ± 0.05
χ_{orb} (Motoyama) 10^{-5} emu/mole	7.9	2.3	2.3

characteristics are expected of a 1 dimensional Heisenberg antiferromagnet. In figure 4-16, the Knight shift is compared to a high temperature analytic calculation for the spin susceptibility by Takahashi, *et al.* [47] based on the Bethe ansatz. Agreement is good with $J = 2200$ K and the parameters from above, hyperfine coupling $2C_a = 45$ kOe/ μ_B , and $K_{a,chem} = 0.024\%$.

The sharp decrease in the susceptibility of Sr_2CuO_3 at low temperatures, $T < 20$ K, can be seen more clearly in figure 4-17. This sharp drop in susceptibility is seen in the chain oxygen Knight shift for all three crystal axes. It was also seen in the bulk susceptibility measured by Motoyama *et al.*[51], but the presence of the large Curie contribution at low temperature makes quantitative comparison of the bulk susceptibility difficult. For the copper and apical oxygen NMR, strong line broadening at low temperatures prevents accurate measurement of the Knight shift (figures 4-13 and 4-14). A sharp drop in the susceptibility at low temperatures is expected in theories for the spin 1/2 1d Heisenberg antiferromagnet. This is shown in figure 4-17 by the solid line showing the conformal field theory calculation of Eggert, *et al.* [46]. This calculation, in agreement with Bethe ansatz methods, shows a logarithmic decrease in the susceptibility at low temperatures [46].

$$J\pi^2\chi(T) \approx 1 + \frac{1}{2\ln(T_0/T)} \quad (4.2)$$

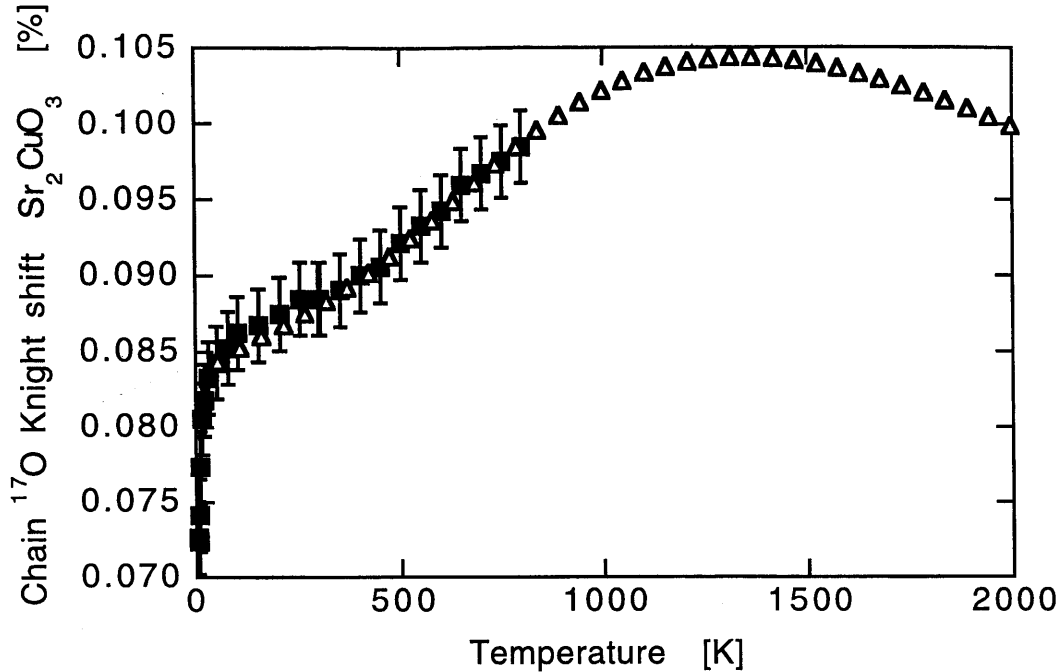


Figure 4-16: Knight shift of ^{17}O chain site of Sr_2CuO_3 (■) compared to analytic calculations of Takahashi, *et al.* [47] (Δ) for $J = 2200$ K, hyperfine coupling $2C = 45$ kOe/ μ_B , and $K_{chem} = 0.024\%$.

where $T_0 \approx 7.7J$ from comparison of the field theory and Bethe ansatz calculations. Strikingly, this form for the susceptibility has the same qualitative features as the experimental data, a slow decrease of the susceptibility with a steep decline at low temperatures. However, as can be seen from figure 4-17, this theoretical calculation deviates markedly from the experimental results below about 25 K. The experimental results show a steeper decline at higher temperatures than expected. This could imply that T_0 has been underestimated. Also, the actual material, Sr_2CuO_3 , has some small inter-chain coupling and long range order occurs at $T_N \approx 5$ K [52]. These inter-chain interactions may alter the susceptibility close to T_N . The effect of the 3d long range ordering can be clearly seen in the increase of apical oxygen $1/T_1$ at 4.2 K (figure 4-17(b)). However, the increase in $1/T_1$ is only seen at the lowest temperature point, 4.2 K, and the value of $1/T_1$ at 10 K is not significantly higher than the higher temperature values. This suggests that the decrease in the susceptibility which begins at about 25 K is truly a 1 dimensional phenomenon and is not caused purely by 3

dimensional ordering. We should note that this low temperature decrease in the susceptibility does not occur for SrCuO₂ [51], presumably because the frustrated interactions between the pairs of chains mask the logarithmic term.

4.3 Oxygen T₁ in Sr₂CuO₃

With the spin-lattice relaxation rate, $1/T_1$, we probe the low energy spin fluctuations. Figure 4-18 clearly shows the striking difference in the temperature dependence of $1/(T_1 T)$ for the two oxygen sites of Sr₂CuO₃. The apical oxygen shows $1/(T_1 T) \approx 1/T$ or nearly constant $1/T_1$. The chain oxygen on the other hand, shows the strongly increasing temperature dependence $1/(T_1 T) \propto T$. This different temperature dependence arises because the two oxygen sites measure the spin fluctuations in different regions of wavevector because of the wavevector dependence of the hyperfine form factors.

As mentioned in chapter 2, the sensitivity of the ¹⁷O nuclear spin-lattice relaxation rate, $1/T_1$, to the Cu electron spin fluctuations at a particular wavevector, q , depends on the geometry of the hyperfine interactions between the electron and nuclear spins. The two oxygen sites in these materials have very different hyperfine form factors. Using the hyperfine couplings as shown in figure 4-2, the hyperfine form factors for Sr₂CuO₃ are

$${}^{17}F_{\alpha}(q)_{chain213} = 2C_{\alpha} \cos(q/2) \quad (4.3)$$

$${}^{17}F_{\alpha}(q)_{apical} = E_{\alpha} \quad (4.4)$$

$${}^{63}F_{\alpha}(q) = A_{\alpha} + 2B \cos(q) \quad (4.5)$$

where the subscript, α , refers to the crystal axis direction. The chain oxygen hyperfine form factor has an important property, ${}^{17}F(q = \pi)_{chain213} = 0$. This is important because in these antiferromagnetic materials, the antiferromagnetic spin fluctuations ($q = \pi$) will be dominant at low temperatures. This can be seen theoretically by Monte Carlo results for the spin fluctuations at low energy ($\omega \rightarrow 0$) by Starykh, *et al.* [45] (figure 4-19). However, there are also low energy spin fluctuations around

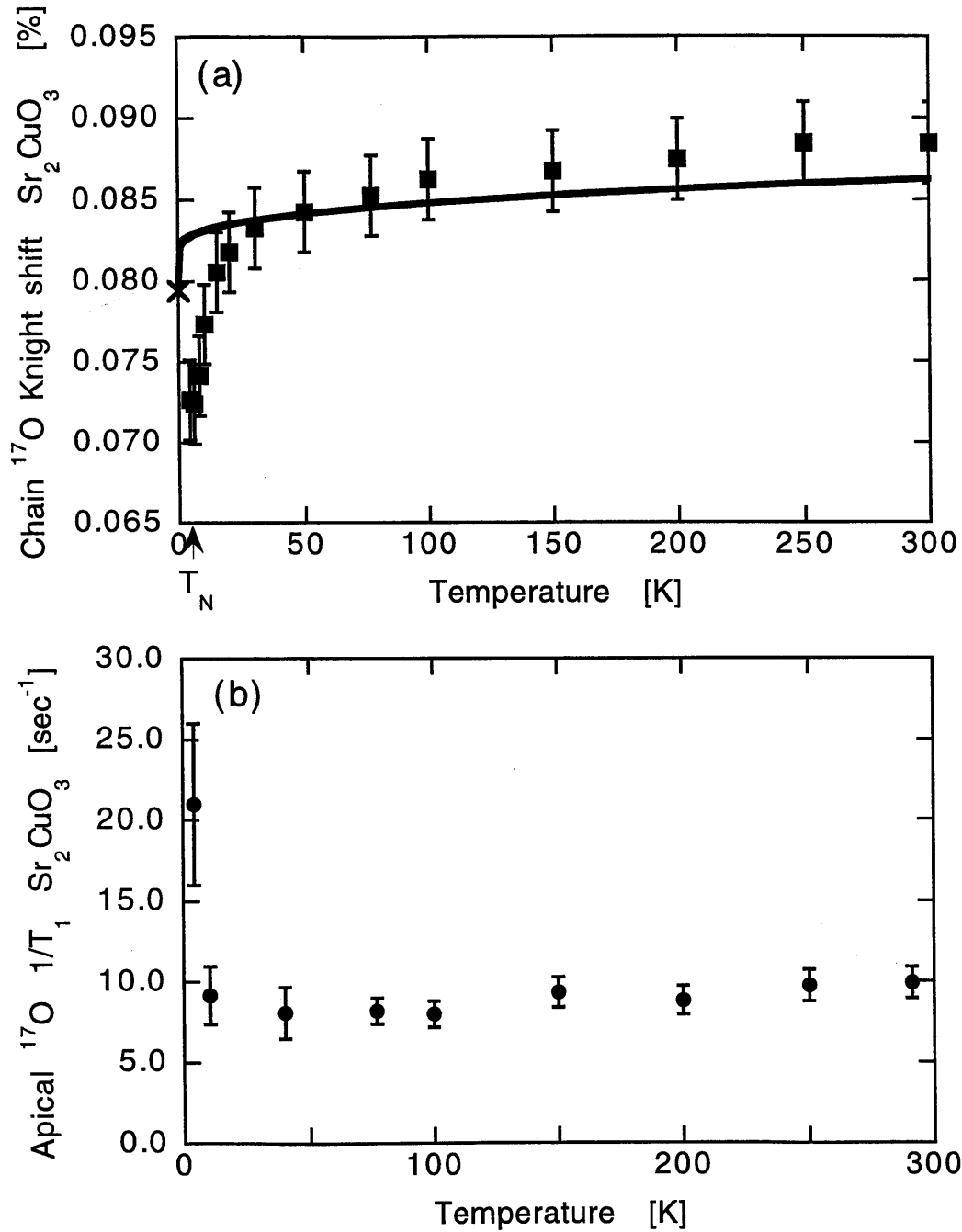


Figure 4-17: (a) Knight shift of ^{17}O chain site of Sr_2CuO_3 (■) compared to spin susceptibility from conformal field theory of Eggert, *et al.* [46] (line) for $J = 2200$ K, hyperfine coupling $2C = 45$ kOe/ μ_B , and $K_{chem} = 0.024\%$. x shows zero temperature limit of theory. (b) $1/T_1$ for the ^{17}O apical site (a axis). Note big increase only at 4.2 K (lowest T point) from 3d ordering and not at the next highest point at 10 K.

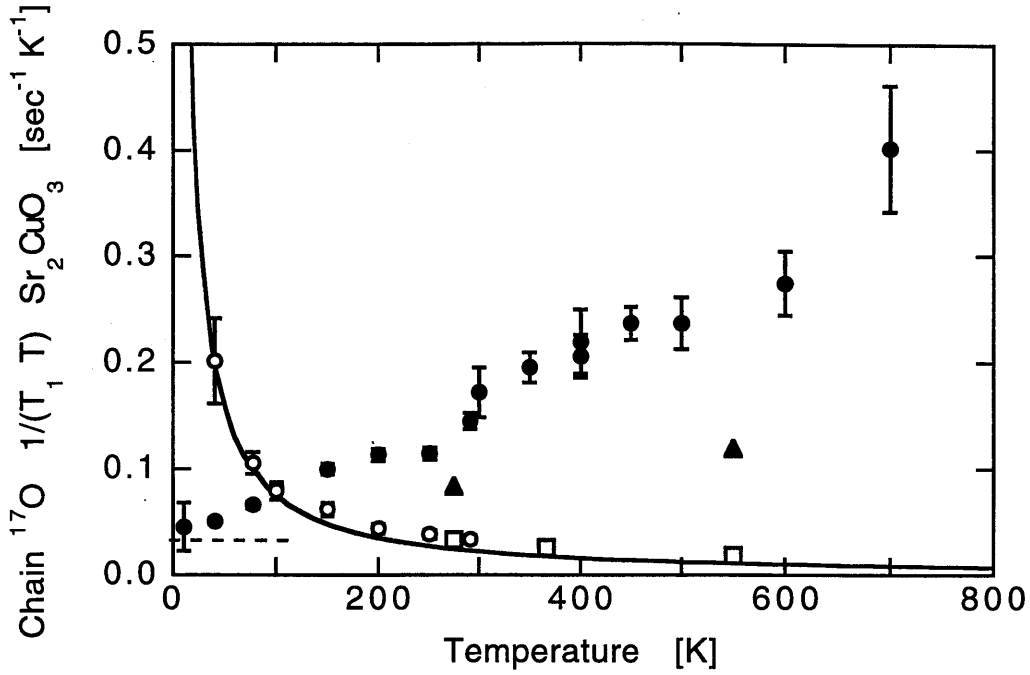


Figure 4-18: ^{17}O $1/(T_1 T)$ for Sr_2CuO_3 , a axis. Chain oxygen site (\bullet), Apical oxygen site (\circ), Monte Carlo for chain oxygen (\blacktriangle), Monte Carlo for apical oxygen (\square) [21]. Dotted line shows low T prediction of Sachdev [44] for $q \approx 0$ (Chain oxygen). Solid line $q = \pi$ theory of Starykh, *et al.* [48] (\approx Apical oxygen) for perpendicular hyperfine couplings $11.5 \text{ kOe}/\mu_B$.

$q = 0$. Since the chain oxygen hyperfine form factor is 0 at $q = \pi$, chain oxygen $1/T_1$ is not sensitive to the antiferromagnetic spin fluctuations. Therefore, we get a picture of the wavevector dependence of the spin fluctuations with apical oxygen and copper $1/T_1$ dominated by $q = \pi$ and chain oxygen $1/T_1$ reflecting $q = 0$.

Several theoretical estimates of ^{17}O $1/T_1$ can be made. Sachdev predicted based on the quantum critical scaling limit that the susceptibility for wavevectors q near 0, [44]

$$\chi(q, \omega) = \frac{c}{2\pi\hbar} \frac{q^2}{c^2 q^2 - (\omega + i\epsilon)^2} \quad (4.6)$$

where $c = \pi J/(2\hbar)$ is the spin wave velocity and ϵ is a positive infinitesimal. Using equation 2.13, we can derive the expression for $1/T_1$ for $q \approx 0$,

$$\frac{1}{T_1}(q \approx 0) = \frac{k_B T}{\hbar} [F_{11}^2(q) + F_{12}^2(q)] \frac{1}{4\pi(\hbar c)^2} \quad (4.7)$$

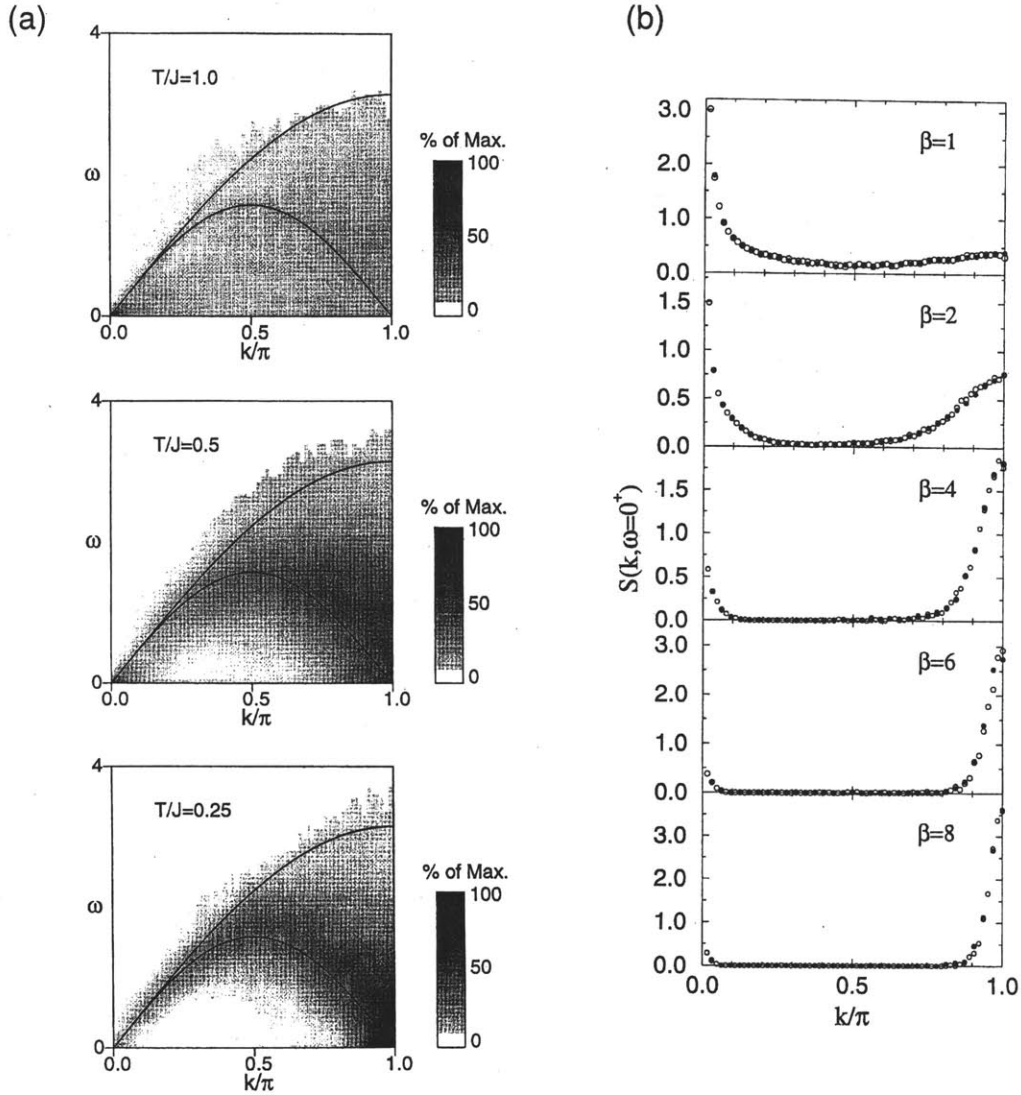


Figure 4-19: Quantum Monte Carlo results for the $S=1/2$ 1d Heisenberg antiferromagnet from Starykh, *et al.*[45]. (a) The spin excitation spectrum (dynamic spin structure factor $S(q, \omega)$) as a function of temperature. (b) The spin structure factor, $S(q, \omega = 0)$, as a function of $\beta = J/T$. $1/T_1$ is proportional to $S(q, \omega = 0)$, weighted by the hyperfine form factor.

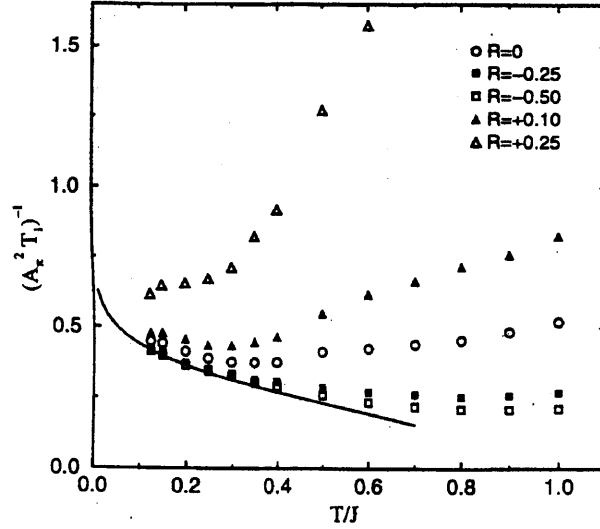


Figure 4-20: Quantum Monte Carlo results for $1/T_1$ for different values of R . R is the ratio of the transferred hyperfine coupling, B , and the onsite hyperfine coupling, A , ($R = B/A$). (from Sandvik [21])

This expression for $1/T_1$ is proportional to temperature, so $1/(T_1 T)$ is predicted to be a constant. For the hyperfine parameters of Sr_2CuO_3 , this implies ^{17}O Chain $1/(T_1 T)_a = 0.029 \pm 0.017 \text{ sec}^{-1}\text{K}^{-1}$. This is reasonable agreement with our data at low temperature, for at 10 K ^{17}O Chain $1/(T_1 T) = 0.046 \pm 0.02$. But the experimental $1/(T_1 T)$ increases linearly with temperature, rather than being constant as predicted. Thus at finite temperatures, $1/(T_1 T)$ increases strongly and is much larger than Sachdev's low temperature prediction. Sachdev notes that his expression does not show any damping of the peaks of the susceptibility even at finite temperature [44]. Corrections to the scaling limit would be expected to produce some damping, suppressed by powers of T/J [44]. This lack of damping also implies that there is not any spin diffusion. The increase of $1/(T_1 T)$ suggests that damping and spin diffusion are important at finite temperatures, even at temperatures as low as $T/J \approx 0.005$.

Monte Carlo calculations of the spin structure factor, $S(q, \omega = 0)$, have been done by Starykh, *et al.* as shown in the figure 4-19. Results for $1/T_1$ are obtained by taking the summation of these results over wavevector q with the appropriate hyperfine form factor. The results shown on figure 4-18 are in good agreement for the apical oxygen

site, but underestimate $1/(T_1T)$ for the chain oxygen site. Calculating $S(q, \omega = 0)$ is difficult for $q \approx 0$ in these calculations because a finite number of atomic sites is used (here, 64) which determines a minimum wavevector value, $q = \pi/64$. The diverging wavevector dependence as $q \rightarrow 0$ may not be well represented by the finite wavevector Monte Carlo data.

For the apical oxygen $1/T_1$, the hyperfine form factor is uniform over wavevector and $1/T_1$ will be dominated by $q = \pi$. Theoretically, Sachdev predicted based on the scaling analysis that $1/T_1(q = \pi)$ should be independent of temperature and that ${}^{63}1/T_{2G} \propto 1/\sqrt{T}$ [44]. This prediction was refined by Starykh, Singh, and Sandvik, [55, 48] to include a marginally irrelevant operator. This modification adds a logarithmic divergence at low temperatures to both $1/T_1(q = \pi)$ and ${}^{63}1/T_{2G}$. The full expressions for $1/T_1$ and ${}^{63}1/T_{2G}$ are [48]

$$\frac{1}{T_1} = \frac{2^{5/2-2\Delta} F^2(\pi) 2D}{\pi^2 \hbar J} \sin(2\pi\Delta) I_1(\Delta) \ln^{1/2}(T_0/T) \quad (4.8)$$

$$\frac{{}^{63}\sqrt{T}}{T_{2G}} = \frac{\sqrt{p} F^2(\pi) 2^{-5/2+2\Delta} D}{\pi^{3/2} (J/\hbar)^{1/2}} \sin(2\pi\Delta) \Gamma^2(1-2\Delta) I_2(\Delta) \ln^{1/2}(T_0/T) \quad (4.9)$$

with $\Delta = (1/4)[1 - \frac{1}{2\ln(T_0/T)}]$, $I_1(\Delta) = \int_0^\infty dx \frac{x}{(\sinh x)^{4\Delta}}$, and $I_2^2(\Delta) = 4 \int_0^\infty dx \left| \frac{\Gamma(\Delta-ix)}{\Gamma(1-\Delta-ix)} \right|^4$. Comparison with Quantum Monte Carlo results indicated $T_0 \approx 4.5J$ and $D = 0.075$. This theoretical result is shown to follow the apical oxygen $1/T_1$ reasonably well in figure 4-18 with $F(\pi) = 11.5 \text{ kOe}/\mu_B$. We should note however that the apical oxygen $1/T_1$ deviates from this theory with the onset of long range order at $\approx 5 \text{ K}$. Near the spin ordering temperature, $1/T_1$ of the apical oxygen site increases dramatically to $1/T_1 = 21 \text{ sec}^{-1}$ at 4.2 K, compared to only 9.2 sec^{-1} at 10 K.

4.4 Oxygen T_1 in SrCuO_2

The oxygen T_1 of SrCuO_2 offers another striking view of the contrast between the antiferromagnetic susceptibility ($q = \pi$) and the susceptibility away from antiferromagnetic ($q \approx 0$). Because SrCuO_2 has a structure with pairs of chains, the chain

Table 4.6: $1/T_1$ for different crystal axes [sec^{-1}]

Sr_2CuO_3	a	b	c
O(1) chain (150 K)	15.1 ± 0.8	7.5 ± 0.8	17.9 ± 1.9
O(2) apical (150 K)	9.4 ± 0.9	59 ± 2	56 ± 2
SrCuO_2	a	b	c
O(1) chain (150 K)	92 ± 3	58 ± 2	96 ± 3
O(2) apical (150 K)	63 ± 2	9.0 ± 0.5	67 ± 2

oxygen sites are also “apical” oxygen sites for the other Cu-O chain of the pair. So, the chain oxygen site for SrCuO_2 has a different form factor from Sr_2CuO_3 .

$${}^{17}F_\alpha(q)_{\text{chain}112} = 2C_\alpha \cos(q/2) + D_\alpha \quad (4.10)$$

The other hyperfine form factors are the same for SrCuO_2 as Sr_2CuO_3 . The additional term in the hyperfine form factor arises because the chain oxygen can have a hyperfine coupling, D , with the neighboring chain. Assuming that the Cu electron spins on the two chains are uncorrelated, we can ignore the interference of the hyperfine fields. With this assumption, there are no cross terms between C and D . The chain oxygen is in an “apical” oxygen position with respect to the neighboring chain. Indeed, we do find that this symmetry is experimentally true with $D \approx E$.

In addition to measuring the $q = 0$ susceptibility of its own chain, the chain oxygen also sees fluctuations of all wavevectors in the neighboring Cu-O chain. This is clearly illustrated in the ${}^{17}1/T_1$ data shown in figure 4-21. For each crystal axis, the chain oxygen and apical oxygen sites have nearly equal $1/T_1$ at low temperatures. At higher temperatures, the chain oxygen site $1/T_1$ increases while the apical oxygen $1/T_1$ is roughly constant. These results can be simply understood as follows. At low temperatures, $q = \pi$ antiferromagnetic excitations are much larger than any $q = 0$ spin excitations, as indicated by Sr_2CuO_3 above. The fact that $1/T_1$ is the same for the apical and chain oxygen sites indicates that the hyperfine interactions follow the symmetry suggested by the crystal structure. That is, the hyperfine couplings to the “apical” oxygen sites does not depend on whether that oxygen atom is also in its own

Cu-O chain ($D \approx E$). So, because the chain oxygen site is also an “apical” oxygen for the neighboring chain, the chain oxygen site has the same hyperfine coupling at $q = \pi$ as the apical oxygen site. This explains why the two oxygen sites have the same $1/T_1$ at low temperatures.

At high temperatures, $1/T_1$ of the two oxygen sites have a very different temperature dependence. The chain site $1/T_1$ increases, showing the temperature dependence of the $q = 0$ spin fluctuations. To a good approximation, the temperature dependence of the apical $1/T_1$ reflects the $q = \pi$ spin excitations, while the difference between the chain and apical $1/T_1$ reflects the $q = 0$ spin excitations. Plotted in figure 4-21(d) is this difference, (chain oxygen $1/T_1$) minus (apical oxygen $1/T_1$). This difference is also shown divided by temperature, $1/(T_1 T)$, in figure 4-22 for comparison with the figure for Sr_2CuO_3 (4-18). The $q = 0$ component of $1/T_1$ of SrCuO_2 does not increase with temperature as much as Sr_2CuO_3 , and the low temperature value at 100 K is about 3 times larger even though the hyperfine couplings are about the same. While a linear increase in $1/T_1$ was predicted in the scaling limit by Sachdev, the magnitude of $1/(T_1 T)$ for SrCuO_2 is 3 to 7 times larger than the scaling limit prediction. We will show later that instead diffusive contributions dominate $1/T_1(q=0)$ in SrCuO_2 at finite temperatures.

Of course, the approximation that apical oxygen $1/T_1$ is completely dominated by the $q = \pi$ excitations will not hold at high temperatures. The chain oxygen $1/T_1$ clearly shows that $q = 0$ spin excitations increase strongly with increasing temperature. At some temperature, $q = 0$ excitations will be significant in comparison to $q = \pi$ excitations. At what temperature this occurs depends on the relative strength of the hyperfine interactions at $q = 0$ and π . In figure 4-20, Monte Carlo calculations by Sandvik [21] show the clear influence of $q = 0$ spin excitations and the dependence on the hyperfine form factor. If the hyperfine form factor includes only $q \approx \pi$ ($R = -0.5$), $1/T_1$ show a logarithmic decrease. On the other hand, if the hyperfine form factor is significant at $q = 0$, at high temperatures, $1/T_1$ strongly increases with temperature. In figure 4-23, apical oxygen $1/T_1$ for Sr_2CuO_3 and SrCuO_2 are shown along with a fit to the $q = \pi$ theory at low temperatures. Clearly

at high temperatures, $1/T_1$ increases slightly, rather than decreasing as the $q = \pi$ theory. This can be explained by the importance of $q = 0$ spin excitations. The apical oxygen site has no wavevector dependence in the hyperfine form factor, so the hyperfine coupling to excitations at $q = 0$ and $q = \pi$ are the same. In Sandvik's notation, this corresponds to $R = 0$. The 1d spin chain Monte Carlo results do show a similar temperature dependence to the data, suggesting that the increase is due to the influence of $q = 0$ fluctuations. Apical oxygen $1/T_1$ demonstrates that for a uniform hyperfine interaction, $q = 0$ excitations are important even at temperatures as low as $T \sim 0.15J$.

4.5 Copper T_1 and T_{2G}

Copper $1/T_1$ is similar to $1/T_1$ of the apical oxygen because the hyperfine form factor will be sensitive to spin fluctuations at both $q = 0$ and $q = \pi$, but with the additional complication that ${}^{63}F(q = 0) \neq {}^{63}F(q = \pi)$ because of the transferred hyperfine coupling, B . In figure 4-24, we show the ${}^{63}\text{Cu}$ $1/T_1$ results for Sr_2CuO_3 . $1/T_1$ for copper is nearly constant with temperature, but shows an upturn at low temperatures (below 100 K) and also increases at higher temperatures for the a and b axes. These results can be compared to the theory for $q = \pi$ and Monte Carlo results. The low temperature data ($T < 300$ K) on ${}^{63}\text{Cu}$ $1/T_1$ and $1/T_{2G}$ have been compared previously by Takigawa, *et al.* [48] and he showed good agreement. Takigawa, *et al.* estimated the hyperfine interaction at $q = \pi$ from impurity effects on the copper lineshape as (62, 73, -220) kOe/ μ_B for the crystal axes a, b, and c respectively, in Sr_2CuO_3 for $J=2200$ K [56]. For the high temperature copper $1/T_1$ measurements, for the c axis with slow $1/T_1$, the $q = \pi$ temperature dependence is followed even up to 800 K. On the other hand, for the other two directions, $1/T_1$ increases at high temperatures. The same behavior is seen in the SrCuO_2 $1/T_1$ results (figure 4-26). As suggested by the Monte Carlo results [21], this indicates that the $q = 0$ spin excitations become significant at high temperatures. On the other hand, why the $q = 0$ contribution is significant only for the b and c axes is not clear. As shown

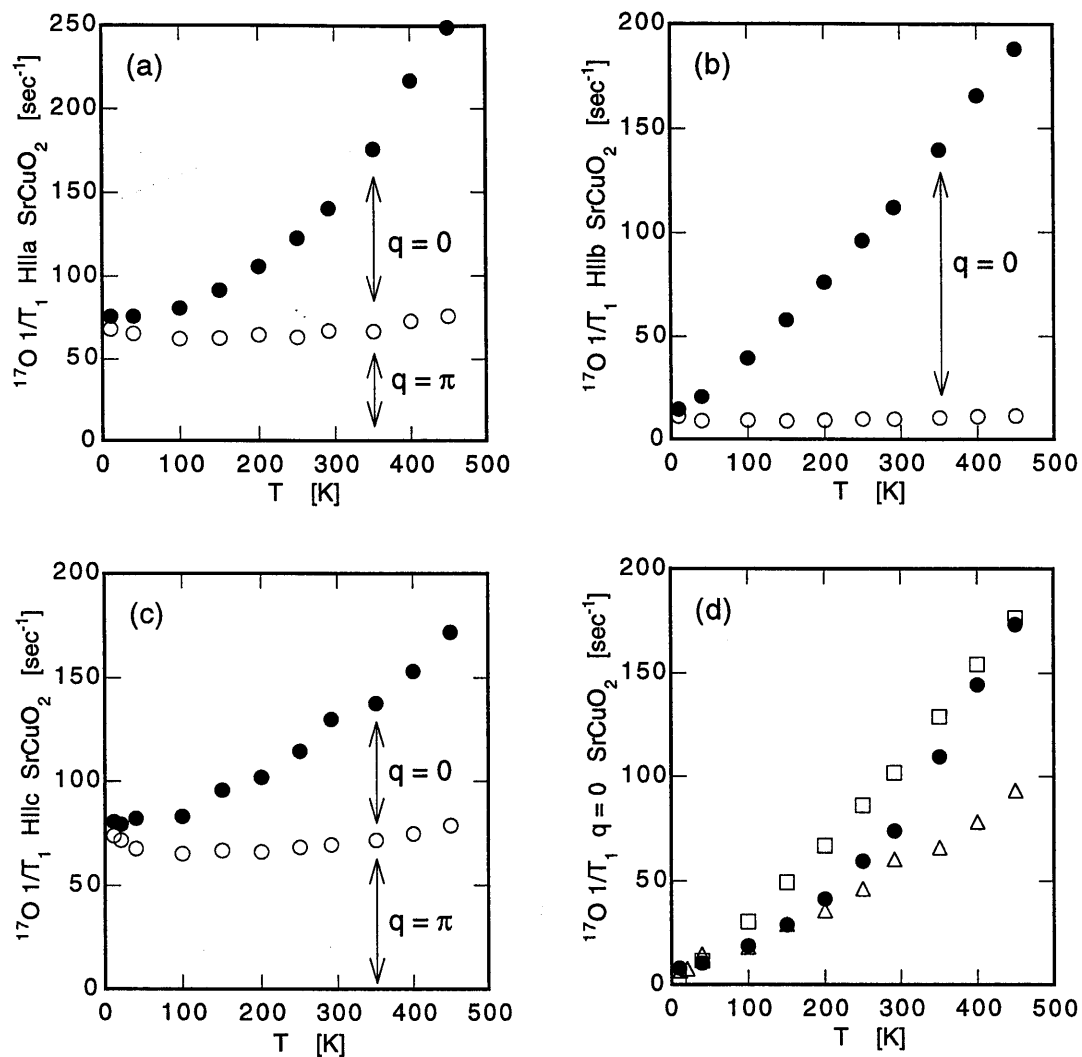


Figure 4-21: ^{17}O $1/T_1$ for SrCuO_2 . (a), (b), (c) $1/T_1$ for the respective crystal axes. Filled symbols - chain oxygen, Open symbols - apical oxygen. (d) Difference between $1/T_1$ of chain oxygen and $1/T_1$ of apical oxygen ($1/T_1(q=0)$). • a axis, \square b axis, Δ c axis.

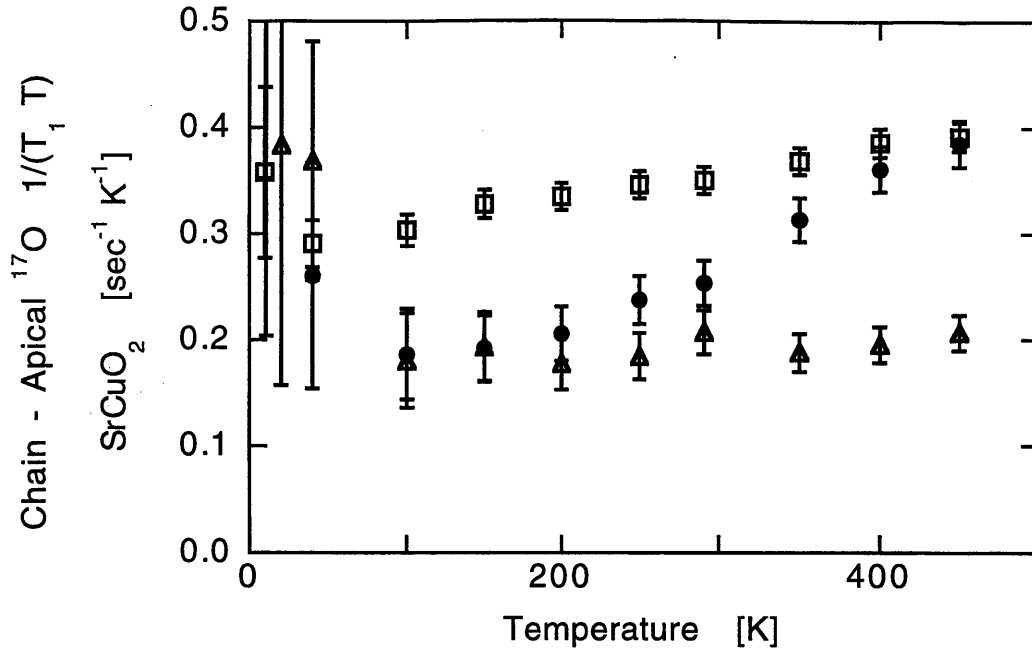


Figure 4-22: Chain - Apical ^{17}O $1/(T_1 T)$ for SrCuO_2 . This closely corresponds to the $q=0$ contributions to $1/(T_1 T)$. \bullet a axis, \square b axis, Δ c axis. Data below 100 K have such large error because of the small $q=0$ component relative to $q = \pi$.

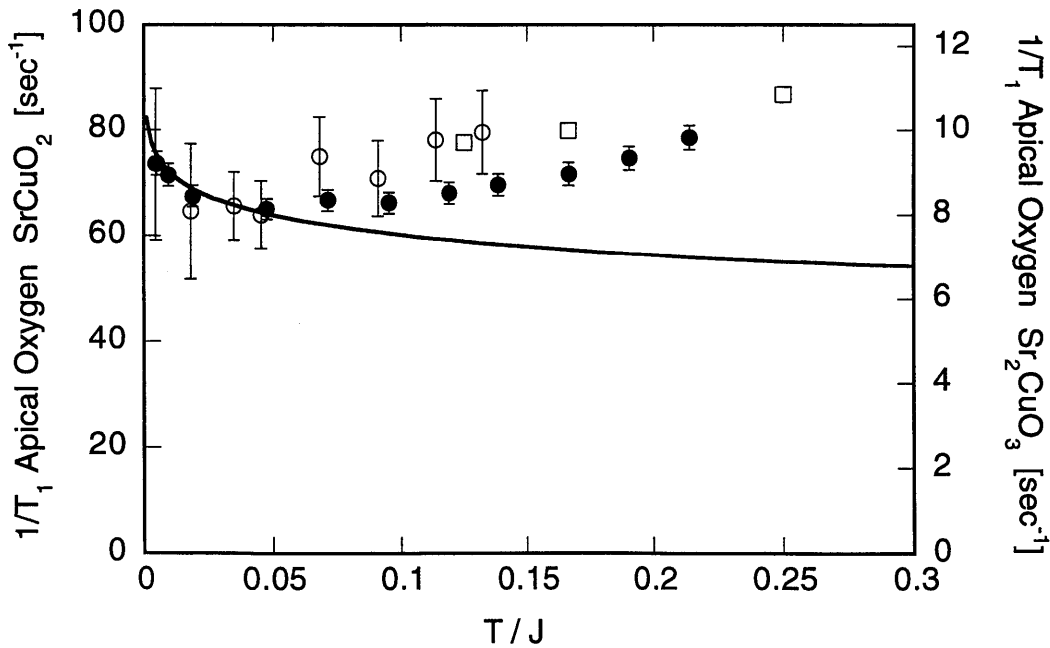


Figure 4-23: ^{17}O $1/T_1$ for SrCuO_2 apical oxygen c axis (\bullet , left axis) and for Sr_2CuO_3 (\circ , right axis) compared to theoretical results. Solid line $1/T_1(q = \pi)$ by Starykh, *et al.*[48] with $D = 0.062$ and $T_0 = 4.5J$, \square Monte Carlo by Sandvik and Naef [21]. Both theoretical results using hyperfine (45, 14) kOe/μ_B for SrCuO_2 scale and (12, 12) kOe/μ_B for Sr_2CuO_3 scale.

in table 4.4, the $q = 0$ hyperfine for ^{63}Cu in SrCuO_2 is largest for the b and c axes. Since $1/T_1$ measures spin fluctuations for the two perpendicular axes, this suggests that the a axis $1/T_1$ should have the largest contribution from $q = 0$. We do not understand why this is not the case. One possibility is a dependence of the $q = 0$ spin diffusion on the magnetic field direction.

$^{63}1/T_{2G}$ reflects the $q = \pi$ spin susceptibility at zero frequency, $\chi'(q = \pi, \omega = 0)$. Results for Sr_2CuO_3 and SrCuO_2 , respectively, are shown in figures 4-25 and 4-27. From the theory for the $q = \pi$ susceptibility by Starykh, *et al.* [48], $1/T_{2G}$ is expected to be $\propto 1/\sqrt{T}$ with the same logarithmic corrections found for $1/T_1$ (eq. 4.9). The results for SrCuO_2 and Sr_2CuO_3 are well represented by the $q = \pi$ theory and by Monte Carlo results using the same hyperfine interaction as used for the $1/T_1$ comparison. The $q = \pi$ scaling ansatz of Starykh, *et al.* [55] quantitatively reproduces $^{63}1/T_{2G}$ because these comparisons do not have any adjustable parameters.

Unfortunately, poor fits of the spin echo decay as a function of τ for Sr_2CuO_3 limited the high temperature range of measurement of $1/T_{2G}$. We speculate that this may be caused by the sample quality. Annealing the sample at high temperatures to introduce ^{17}O could possibly add excess oxygen or other defects. At low temperatures, the limit to measuring accurate values of $1/T_{2G}$ is the rapidly increasing linewidth with decreasing temperatures. The strength of the spin excitation pulse needs to cover the entire linewidth, otherwise $1/T_{2G}$ will be systematically underestimated. Low temperature ($T < 300$ K) measurements of $1/T_{2G}$ were conducted previously for Sr_2CuO_3 by Takigawa, *et al.* [48]

4.6 Spin diffusion

Since oxygen NMR has revealed the spin fluctuations away from $q = \pi$, it is natural to ask what the nature of these spin fluctuations are. We find strong evidence that the spin fluctuations away from $q = \pi$ are dominated by $q = 0$ diffusive fluctuations, especially for SrCuO_2 . Spin diffusion is based on the argument that at high temperatures, the modes of the system may be treated as independent, Gaussian

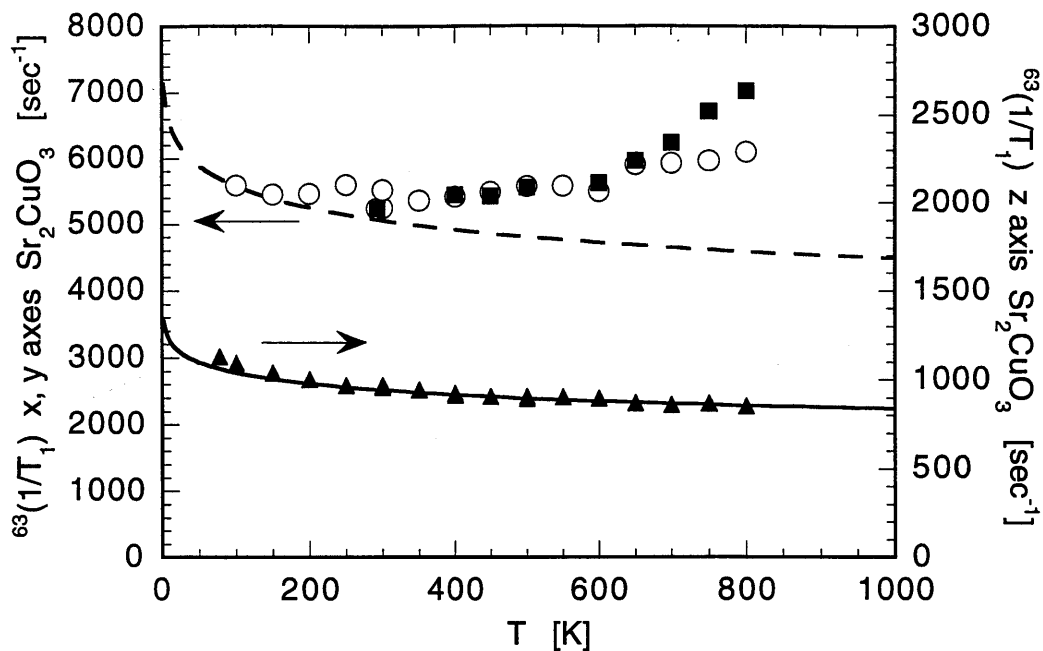


Figure 4-24: ^{63}Cu $1/T_1$ for Sr_2CuO_3 . a (\circ), b (\blacksquare), and c axes (\blacktriangle). $q = \pi$ theory of Starykh, *et al.* shown for c axis (solid line) and for a,b axes (dotted line) for hyperfine interactions $F(\pi) = 70, 70, 220 \text{ kOe}/\mu_B$.

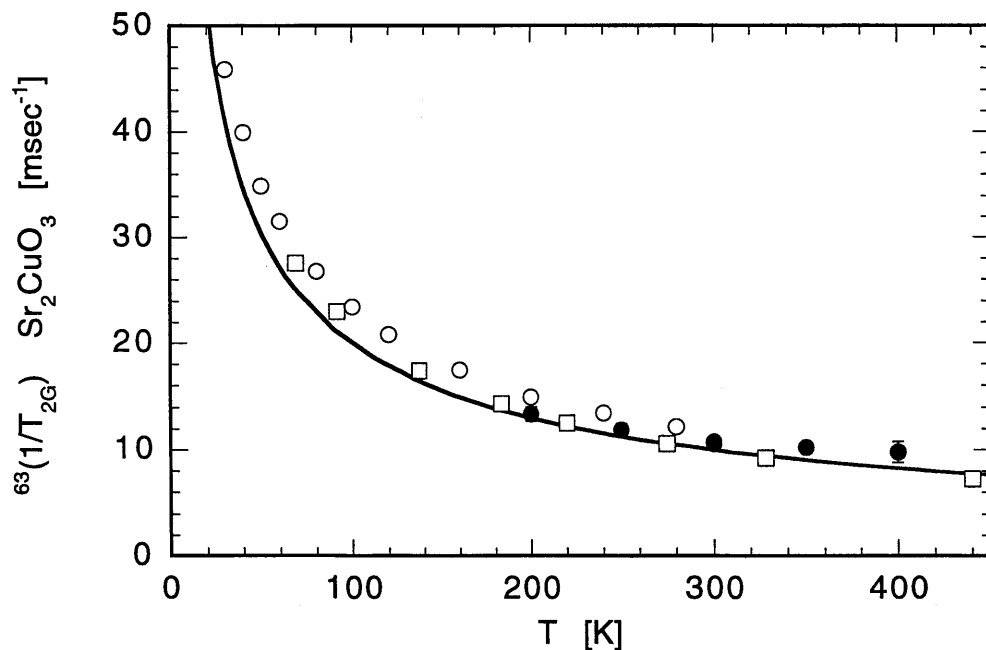


Figure 4-25: ^{63}Cu $1/T_{2G}$ for Sr_2CuO_3 (\bullet). Also shown data from Takigawa, *et al.* (\circ) [48]. Monte Carlo (\square) [21], and $q = \pi$ theory of Starykh, *et al.* (solid line) shown for hyperfine interaction, $F_c(\pi) = 220 \text{ kOe}/\mu_B$.

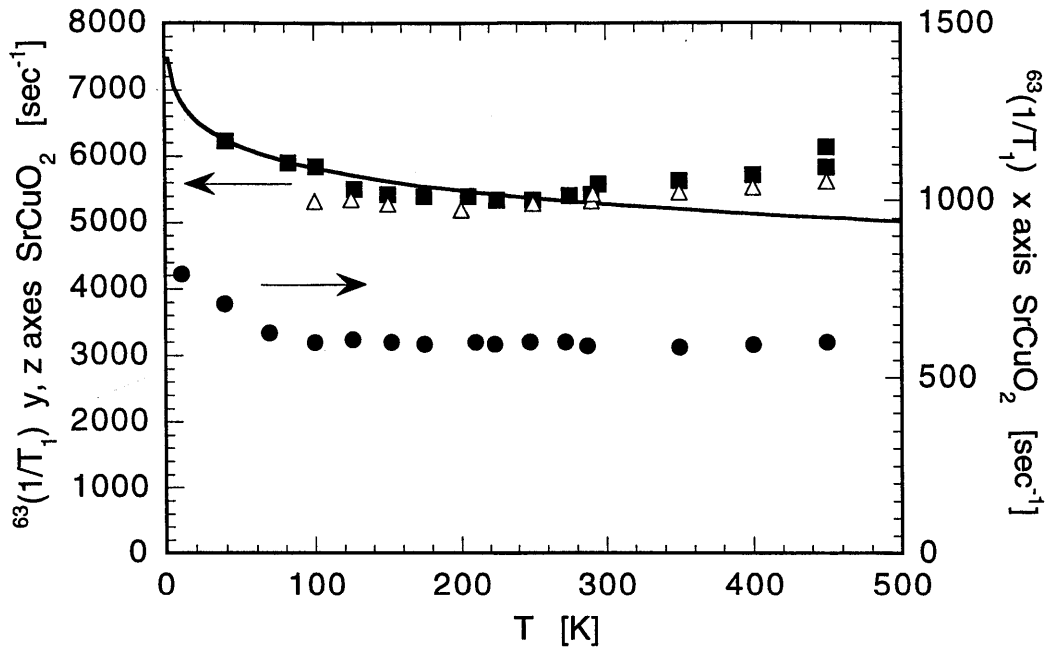


Figure 4-26: ^{63}Cu $1/T_1$ for SrCuO_2 . a (●), b (□), and c axes (▲). $q = \pi$ theory of Starykh, *et al.* [48] shown for b axis (solid line) for hyperfine interaction $F(\pi) = 70, 70, 220 \text{ kOe}/\mu_B$.

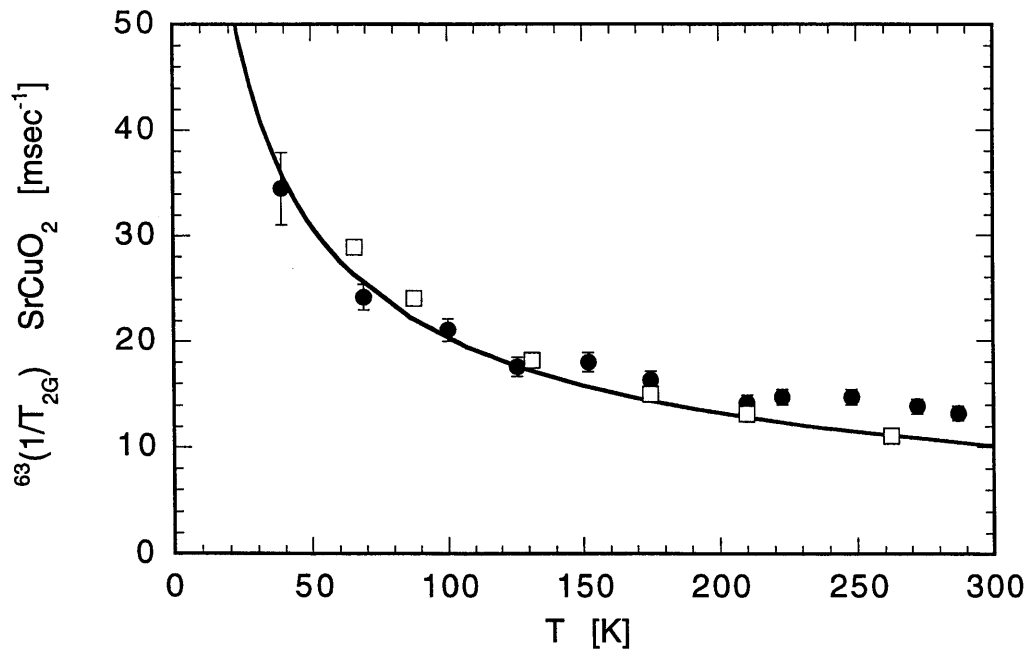


Figure 4-27: ^{63}Cu $1/T_{2G}$ for SrCuO_2 (●). Also, Monte Carlo (□) [21], and $q = \pi$ theory of Starykh, *et al.* (solid line) [48] shown for hyperfine interaction, $F_c(\pi) = 220 \text{ kOe}/\mu_B$.

fluctuations [57, 58]. One result of this is that at infinite temperature, a spin that obeys a conservation law will have a correlation function with a long time behavior, [57]

$$S(t) \sim t^{-d/2} \quad (4.11)$$

for dimension, d . In our case, the total component of spin along a particular axis such as z , $\sum S_z$, commutes with the 1-d spin 1/2 Heisenberg Hamiltonian, so it is a conserved quantity. By taking the Fourier transform of the long time behavior, the low frequency behavior for diffusive dynamics is

$$S_z(\omega) \sim \omega^{-1/2} \text{ for } \omega \rightarrow 0 \quad (4.12)$$

This diffusive behavior will only be important at low frequencies ($\omega \ll J/\hbar$). In addition, in any real material, there may be small interactions which limit the one dimensional diffusive behavior by violating the above assumptions of conservation of the total component of spin or the one-dimensional nature of the interactions. These interactions would include any interchain coupling or anisotropic spin interactions. As a consequence, below a “cutoff” frequency determined by these interactions, $S_z(\omega)$ should become practically frequency independent [59].

The question of whether spin diffusion is expected in the 1-d spin 1/2 Heisenberg antiferromagnet has been discussed theoretically in several papers [44, 60, 57]. In general, these papers have suggested that the low frequency dynamics will not follow the diffusive form. Sachdev [44] indicated that in the low temperature limit, there was no diffusive dynamics, in fact no frequency dependence at all. This, however, does not exclude that spin diffusion could occur at finite temperatures. Narozhny [60] suggested that any spin diffusion in actual materials would be caused by extra interactions not present in the Heisenberg hamiltonian, such as electron-phonon interaction.

To test for spin diffusion, we need to measure the frequency dependence of $1/T_1$, or equivalently the magnetic field dependence since $\omega = \gamma H$. For the 1-d antiferro-

magnet, the spin diffusion component to $1/T_1$ should be [59, 48]

$$\left(\frac{1}{T_1}\right)_{diff} = [F(q=0)_\perp^2 + F(q=0)_\parallel^2] \frac{k_B T \chi(0)}{2\hbar\sqrt{2g\mu_B\hbar D_S H}} \quad (4.13)$$

where D_S is the diffusion constant. In figures 4-28 and 4-29, we show the dependence of $1/T_1$ on magnetic field for the oxygen and copper in SrCuO_2 and Sr_2CuO_3 at room temperature. Clearly the chain oxygen sites which are dominated by $q \approx 0$ show the most significant field dependence. We can separate the diffusive and non-diffusive components of $1/T_1$ by fitting the field dependence of $1/T_1$ with

$$\left(\frac{1}{T_1}\right) = A + B \left(\frac{1}{\sqrt{H}}\right) \quad (4.14)$$

where A represents the non-diffusive component of $1/T_1$ and B the diffusive component. The results for SrCuO_2 chain - apical oxygen $1/T_1$ indicate that the diffusive component dominates $1/T_1(q \approx 0)$ at least for measurements with $H \parallel b$. The spin diffusion constant, D , is estimated as $D_{112} = 7 \times 10^{15} - 8 \times 10^{16} \text{ sec}^{-1}$. The field dependence results for Sr_2CuO_3 have larger uncertainty. For Sr_2CuO_3 chain oxygen, the non-diffusive and diffusive components are roughly equal at room temperature and $D_{213} \approx 3 \times 10^{16} \text{ sec}^{-1}$. These values for D fall within the range estimated by Takigawa based on Cu NMR in Sr_2CuO_3 at 280 K, $D = 1 \times 10^{16} - 4 \times 10^{17}$ [48]. These values for the spin diffusion constant are \sim two orders of magnitude larger than the high temperature limit for D_S in the classical 1-d Heisenberg antiferromagnet, $D_S = (J/\hbar)\sqrt{2\pi S(S+1)/3} = 3.6 \times 10^{14} \text{ sec}^{-1}$ [59]. We should note that this formula was found to be of the correct order of magnitude (within $\sim 50\%$) for a spin 5/2 1-d chain at $T/J = 300/6.5 = 46$ [59]. It is perhaps not surprising that the spin diffusion constant is much higher than the high temperature limit. The diffusion constant would be expected to increase strongly with decreasing temperature. $D_S \propto 1 + C^2(J/k_B T)$ at high temperatures [59, 44]. Experimentally, an increasing diffusion constant with decreasing temperature has been measured in a spin 1 1d antiferromagnet [61].

From the $1/T_1$ data on Sr_2CuO_3 , it is evident that there is little or no diffusive behavior at low temperatures, as predicted by Sachdev. However, $1/T_1$ deviates from the prediction beginning even at the lowest temperatures measured. In addition, presuming that the T^2 temperature dependence of ^{17}O $1/T_1$ for the chain oxygen site of Sr_2CuO_3 is dominated by diffusive contributions, this indicates that the spin diffusion constant is roughly $D_S \sim 1/T^2$. In contrast, the ^{17}O $1/T_1$ for SrCuO_2 would indicate a spin diffusion constant with little temperature dependence. This difference between the two materials may be caused by the frustrated interchain interactions in SrCuO_2 which may affect the spin diffusion.

4.7 1d summary

Using ^{17}O NMR, we can probe the $q \approx 0$ low energy spin fluctuations in these nearly ideal 1-d spin 1/2 Heisenberg antiferromagnetic materials. In Sr_2CuO_3 , $1/T_1(q \approx 0) \propto aT + bT^2$ from 10 K up to 700 K. This striking temperature dependence is different from theoretical predictions, probably because of the significance of the diffusive component to T_1 . This leads to the speculation that $D \propto 1/T^2$. ^{17}O $1/T_1$ of SrCuO_2 shows the $\omega^{-1/2}$ frequency dependence characteristic of spin diffusion. The spin diffusion constant is estimated to be roughly two orders of magnitude larger at room temperature ($T/J \approx 0.13J$) than the high temperature value for the classical 1d spin chain.

We have extended measurements of ^{63}Cu $1/T_1$ up to 800 K. For the magnetic field applied perpendicular to the Cu-O squares (long T_1), the results follow the theoretical prediction for $q = \pi$. For the other two directions, which have much shorter T_1 values, $1/T_1$ increases above room temperature, indicating the importance of $q = 0$ contributions at high temperatures.

Comparison of the results between SrCuO_2 and Sr_2CuO_3 show that SrCuO_2 , even though it has two copper-oxide chains physically close together, has similar low energy spin fluctuations to the single chain of Sr_2CuO_3 . The uniform susceptibility differs only at very low temperatures ($T < 15$ K), where Sr_2CuO_3 Knight shift and χ [51]

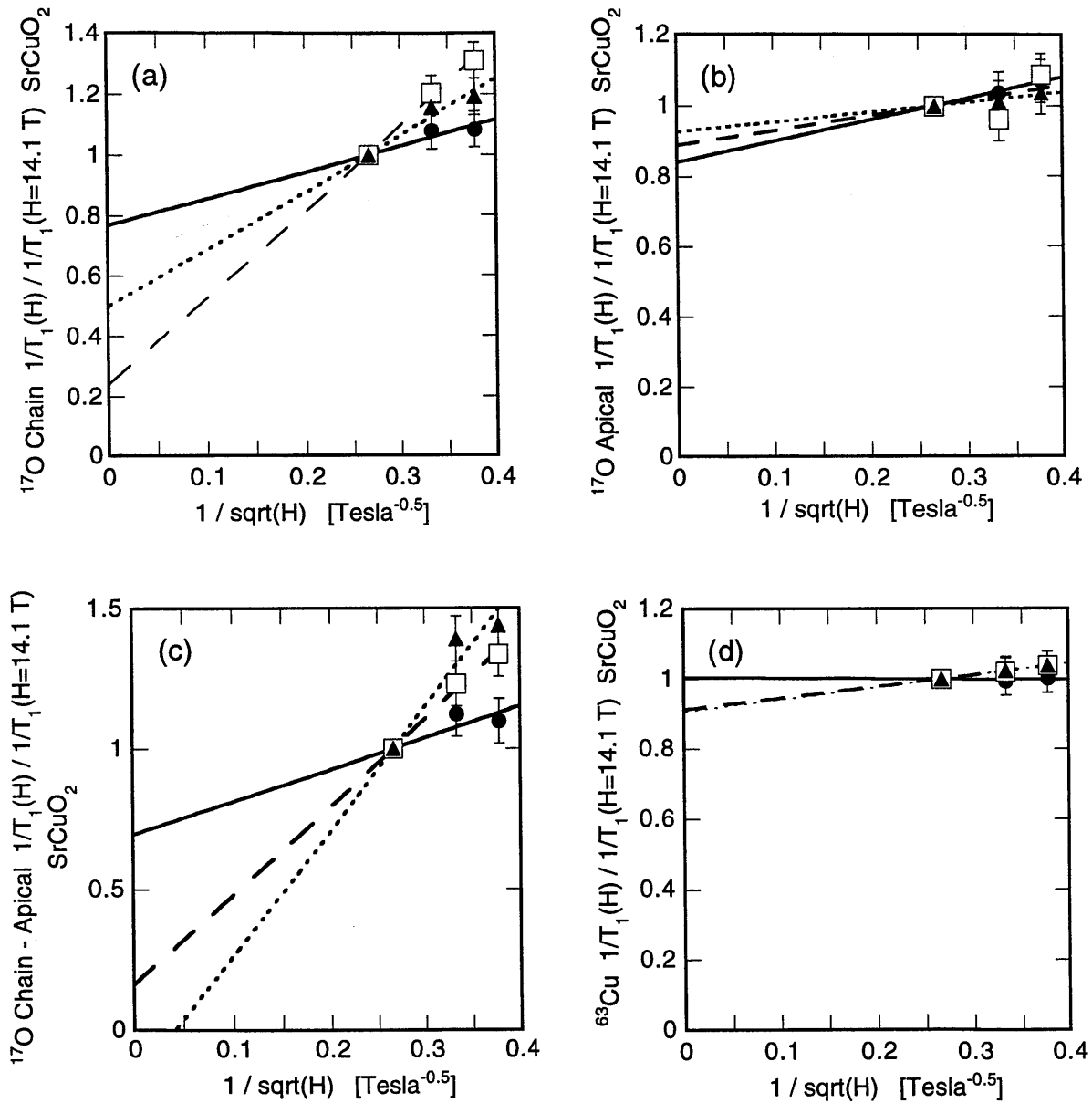


Figure 4-28: Field dependence of $1/T_1$ for SrCuO_2 normalized at 14 T for (a) ^{63}Cu , (b) ^{17}O Apical, (c) ^{17}O Chain, and (d) difference of ^{17}O Chain and Apical. \bullet a axis, \square b axis, \blacktriangle c axis. Fits to $a + b(1/\sqrt{H})$ are solid lines for a axis, dashed for b axis, and dotted for c axis.

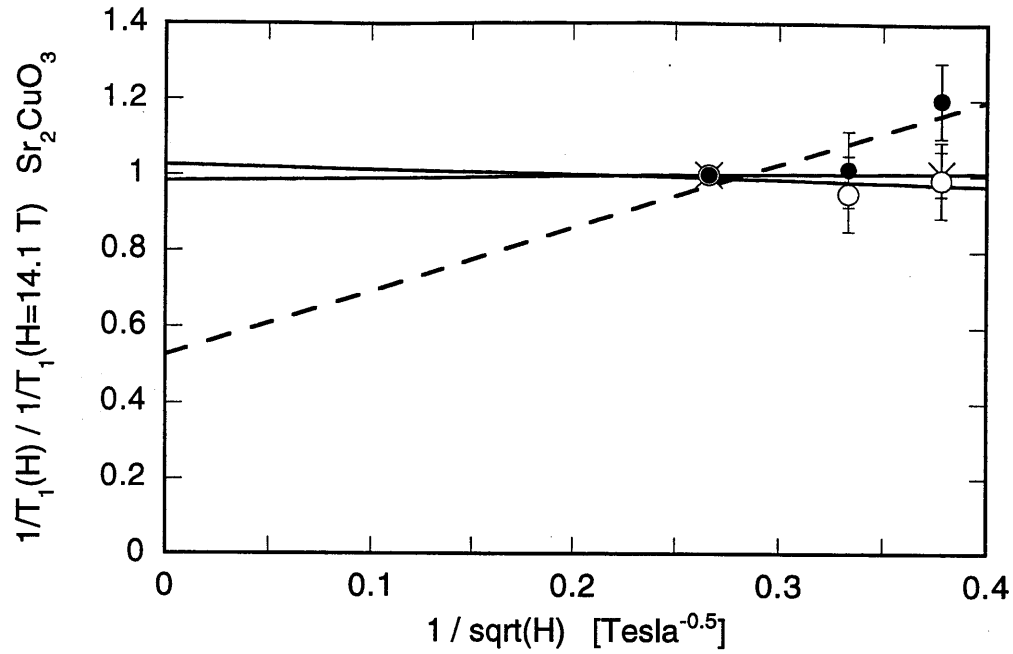


Figure 4-29: Field dependence of $1/T_1$ for Sr_2CuO_3 normalized at 14 T. \bullet chain oxygen site, \circ apical oxygen site, \times copper. Fits to $a + b(1/\sqrt{H})$ are solid lines for apical oxygen and copper and dashed line for chain oxygen.

show a sharp decrease. Despite the frustrated 90 degree Cu-O bonds between the two chains in SrCuO_2 , the two Cu-O chains in SrCuO_2 act as independent 1d chains at high temperatures.

Chapter 5

2 dimensional $S=1/2$ Heisenberg Antiferromagnet

The discovery of high T_c superconductivity in hole-doped CuO_2 planes has focused strong interest on the spin $S = 1/2$ two-dimensional (2d) Heisenberg antiferromagnet, $H = J \sum \mathbf{S}_i \cdot \mathbf{S}_j$ where $J (\approx 1500 \text{ K})$ is the exchange interaction [62, 3]. The fact that the CuO_2 planes of high T_c superconductors are nearly ideal 2d Heisenberg antiferromagnets has suggested that the magnetism may be connected to the mechanism for high T_c superconductivity. Supporting this idea is the high energy of the exchange interaction, $J \approx 1500 \text{ K}$, which could provide the energy necessary to support superconductivity at such high temperatures ($\sim 100 \text{ K}$). As a result, there has been significant theoretical and experimental effort to understand the two-dimensional magnetism. Perhaps with an understanding of how the undoped antiferromagnetic insulators behave, this can lead to the discovery of how superconductivity occurs in these materials when doped holes are introduced.

In this chapter, some recent theoretical work on the $S=1/2$ 2d Heisenberg antiferromagnet is reviewed. $^{63,65}\text{Cu}$ and ^{17}O NMR and NQR experiments on the undoped 2d copper oxide material, $\text{Sr}_2\text{CuO}_2\text{Cl}_2$, are described [63]. We demonstrate that ^{17}O NMR measures the spin wave damping in the undoped antiferromagnet for short wavelengths. The spin wave damping is small even at temperatures as high as $T = 0.4J$, well above T_N . This clarifies one of the unique properties of these 2d copper-oxide

antiferromagnetic materials: there is a wide temperature range where short range spin excitations exist with long lifetimes, without long range 3-dimensional order. Finally, the magnetic properties of the undoped material are compared to previous results for doped samples.

5.1 Theoretical Studies

Because of the discovery of high T_c superconductivity in CuO_2 planes, new theoretical work has been done on the 2 dimensional spin $S=1/2$ Heisenberg antiferromagnetic model,

$$\mathcal{H} = \sum_{i,j} S_i \cdot S_j \quad (5.1)$$

where nearest neighbor spins, $S_{i,j}$, interact isotropically on a 2 dimensional square lattice.

The dimensionality of the magnetic interactions has a strong influence on the spin ordering of the material. The Hohenberg-Mermin-Wagner theorem [64] showed that in 2 dimensions, long range order will not occur at any finite temperature in a Heisenberg system. In actual materials, even a very small coupling in the third dimension will drive 3d long range order when the 2 dimensional correlations become long enough. Three dimensional ordering will occur at a temperature, T_N , roughly when the two dimensional spin correlation length, ξ , satisfies [65]

$$k_B T_N \sim J_c \xi^2 (N_0/S)^2 \quad (5.2)$$

where J_c is the exchange coupling between the 2d CuO_2 planes and (N_0/S) is the reduction of the $T = 0$ staggered moment by the 2d quantum fluctuations.

The 2 dimensional spin $1/2$ Heisenberg model on a square lattice has been studied by numerous techniques including: spin wave theory [66], quantum nonlinear σ model [65], quantum Monte Carlo [67], high temperature expansion [68]. Here, the quantum nonlinear σ model will be discussed. The results for this model and the other methods will be compared with the experimental data when appropriate.

5.1.1 Quantum nonlinear σ model

Chakravarty, Halperin, and Nelson (CHN) proposed a continuum field theory described by creating a quantum mechanical generalization of the classical nonlinear σ model [65]. This quantum nonlinear σ model is expected to have the same low energy, long wavelength behavior as the quantum Heisenberg model. The model is characterized by two independent parameters, such as the spin stiffness, ρ_S , and the uniform susceptibility perpendicular to the direction of the local staggered magnetization, χ_{\perp} . Since this is a continuum model, the exchange interaction J is replaced by the spin stiffness, $\rho_S \propto J$, of the continuous spin structure. The spin wave velocity, c , is related to the spin stiffness, $2\pi\rho_S \propto (\hbar c/a)$.

Even though this system is disordered at all finite temperatures in 2 dimensions, they identify three regions in the phase diagram (figure 5-1) which are characterized by the behavior of the correlation length as a function of temperature. The phase diagram is given as a function of the dimensionless coupling constant, $\bar{g} = g_0/g_c$, and the temperature scale, $\bar{t} = k_B T / (2\pi\rho_S^0)$. The dimensionless coupling constant, \bar{g} , depends only the dimensionality and spin S of the system. The critical coupling constant, g_c , defines the zero-temperature transition between the ordered and disordered states. As a result, for $\bar{g} > 1$ the $T = 0$ state is quantum disordered, while for $\bar{g} < 1$ the $T = 0$ state is ordered. The temperature scale is defined by the unrenormalized spin stiffness, $2\pi\rho_S^0$, which is $2\pi JS^2$ [65] for the limit of large spin S .

The three regions of the phase diagram are the quantum disordered region, the renormalized classical region, and the quantum critical region which separates them. These different regions arise from the approach to different $T = 0$ ground states and have very different behaviors of the spin correlation length, ξ .

The quantum disordered region is dominated by the approach to the quantum disordered ground state with a finite energy gap. The quantum disordered ground state will have a finite correlation length. In the quantum disordered region ($\bar{g} > 1 + \bar{t}$), the temperature dependence of the correlation length is expected to be weak. This is characteristic of a gap in the excitation spectrum, and CHN suggest the possibility

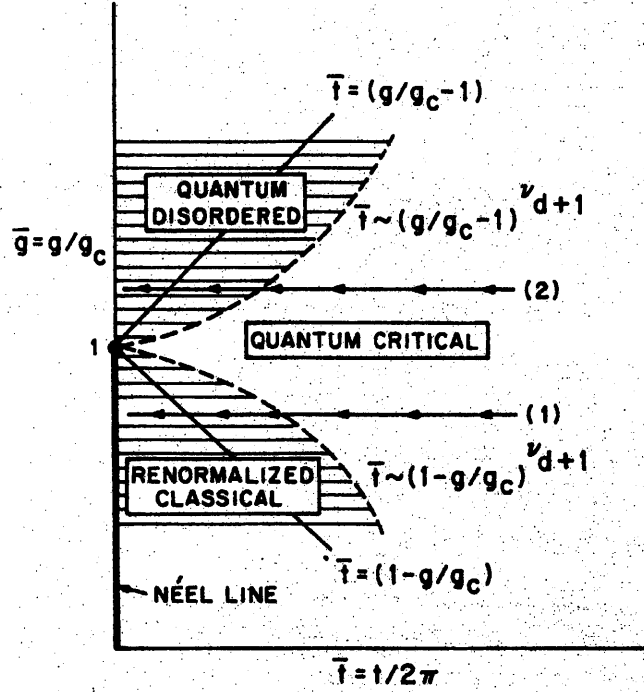


Figure 5-1: Phase diagram for the quantum nonlinear σ model by Chakravarty, Halperin, and Nelson [65].

of a gap $\Delta \sim \bar{g} - 1$ for $\bar{g} > 1$ [65].

The renormalized classical region is where the approach to the ordered ground state is dominant. In the renormalized classical regime ($\bar{g} < 1 + \bar{t}$), the correlation length diverges exponentially with lowering temperature [65, 69, 70]

$$\xi = \frac{e \hbar c}{8 \pi \rho_S} \exp\left(\frac{2\pi \rho_S}{T}\right) \left[1 - \frac{T}{4\pi \rho_S} + O(T^2)\right] \quad (5.3)$$

This region of the phase diagram is called renormalized classical because this exponential dependence of the correlation length is also the expectation for a classical model. The quantum effects are contained in the altered (renormalized) values of the spin stiffness, $\rho_S = 0.18J$, and spin wave velocity, $c = \sqrt{2}Z_c Ja/\hbar$ where $Z_c = 1.18$ [68].

Between the quantum disordered and renormalized classical regions is the quantum critical region where the system behavior is dominated by the quantum critical point at $\bar{g} = 1$. In the central quantum critical region ($1 + t > g_0 > 1 - t$), asymptotically

as $T \rightarrow 0$, [71, 65]

$$\xi = C_Q \frac{\hbar c}{k_B T} \quad (5.4)$$

where C_Q is a constant of order unity. The experimental consequences of this quantum critical region have been theoretically studied extensively by Chubukov, Sachdev, and Ye [71].

Chakravarty, Halperin, and Nelson argue that the CuO_2 planes have a coupling weaker than the critical coupling, $\bar{g} < 1$ [65]. Their argument is based on the idea that if the CuO_2 planes had a quantum disordered ground state, a large interlayer coupling, J' , would be necessary to account for the $0.5\mu_B$ staggered magnetization seen at low temperatures [72]. Thus, the non-linear σ model predicts a temperature dependence of the spin correlation length for the undoped CuO_2 plane corresponding to line (1) on figure 5-1, quantum critical at high temperatures, and renormalized classical at lower temperatures.

5.1.2 Classical-based models

Another approach to the Heisenberg antiferromagnet model is to start with the classical spin model and then to attempt to put in the effects of quantum fluctuations. As mentioned above, the classical spin model for the 2d square lattice Heisenberg antiferromagnet has an exponential temperature dependence of the correlation length [65] just as in the renormalized classical regime of Chakravarty, Halperin, and Nelson.

$$\xi = 0.0125 \frac{T}{2\pi\rho_{cl}} e^{2\pi\rho_{cl}/T} \left[1 - b_1 \frac{T}{2\pi\rho_{cl}} + O(T^2) \right] \quad (5.5)$$

The spin stiffness, $\rho_{cl} = J$, for classical unit vector spins. For large spin S , the classical limit is approached smoothly when the temperature is measured in units of $JS(S+1)$ [6, 3]. This suggests that for finite spin S , ρ_{cl} should be taken as $JS(S+1)$ [6]. The result is that for $S=1/2$, the classical temperature scale, $2\pi\rho_{cl} = 4.7J$, while the renormalized classical result is $2\pi\rho_S = 1.13J$. This large difference in ρ_S distinguishes the classical and renormalized classical behaviors, especially since ρ_S

determines the exponential temperature dependence.

Cuccoli *et al.* [73] proposed a model by which they attempt to correct the classical model for quantum fluctuations. Their approach is called the purely quantum self-consistent harmonic approximation, and they renormalize the temperature scale of the quantum expression for the correlation length in order to account for quantum fluctuations. Since the temperature scale is set by the spin stiffness, ρ_{cl} , renormalization of the temperature scale amounts to a renormalization of the spin stiffness. This approach is naturally most appropriate when the quantum corrections are less important. In fact, this approach gives results for the correlation length that are very similar ($\lesssim 20\%$ different) to the renormalized classical model for the high temperature region ($\xi \approx 2$ to 15). This indicates that the crossover from the low temperature renormalized classical regime of Chakravarty, Halperin, and Nelson to a high temperature regime is smooth. In addition, this implies that the renormalized classical results for the correlation length are reasonable even when the correlation length is as small as $\xi \sim 2$.

5.2 Crystal structure of $\text{Sr}_2\text{CuO}_2\text{Cl}_2$

For the study of the undoped CuO_2 plane, the material $\text{Sr}_2\text{CuO}_2\text{Cl}_2$ has several advantages over other undoped high T_c materials. First, this material has been seen in previous experiments to be a very ideal realization of a two-dimensional $S=1/2$ Heisenberg antiferromagnet. The three dimensional spin ordering temperature, $T_N^{3d} = 257$ K [74], is low relative to the strong exchange interaction, $J = 1450$ K [75]. Neutron scattering results on $\text{Sr}_2\text{CuO}_2\text{Cl}_2$ showed that the magnetic anisotropy is very weak ($J_{xy}/J \sim 10^{-4}$ [5]) so that the isotropic 2D Heisenberg behavior is robust even down to ≈ 280 K [5, 74]. The spin correlation length, ξ , was found to agree quantitatively with the prediction of the renormalized classical regime of the non-linear sigma model over the temperature range $T = 275$ up to 600 K, ($\xi \approx 6$ to 200) for $J = 1450$ K [5].

For our NMR and NQR measurements, $\text{Sr}_2\text{CuO}_2\text{Cl}_2$ has the additional advantage

of having only one copper atomic site and one oxygen atomic site, which precludes any possibility of superposition of the resonance lines. The structure of $\text{Sr}_2\text{CuO}_2\text{Cl}_2$ as shown in figure 5-2 is like that of the prototypical superconductor, La_2CuO_4 , but with Cl instead of O in the apical positions above and below the Cu atoms. In addition, unlike La_2CuO_4 , $\text{Sr}_2\text{CuO}_2\text{Cl}_2$ does not have a structural phase transition to the low-temperature orthorhombic phase, so the crystal structure is tetragonal down to the lowest temperatures measured ($T < 10$ K) [72]. The lack of the tetragonal distortion prevents the Dzyaloshinski-Moriya spin interaction which disturbs the Heisenberg state in La_2CuO_4 [3]. However, $\text{Sr}_2\text{CuO}_2\text{Cl}_2$ is very difficult to dope. Superconducting samples of $\text{Ca}_{2-x}\text{Na}_x\text{CuO}_2\text{Cl}_2$ ($T_c \lesssim 28$ K) have been made only using high pressure synthesis [76]. This is a benefit for the experiments on the undoped compound because of the reduced risk of unwanted doping. Excess oxygen doping is known to alter the NMR properties of La_2CuO_4 with as little as 0.035 excess oxygen [7]. On the other hand, because of the difficulty of doping $\text{Sr}_2\text{CuO}_2\text{Cl}_2$, the doped experiments we use for comparison were conducted on $(\text{La,Sr})_2\text{CuO}_4$ [7].

5.2.1 $\text{Sr}_2\text{CuO}_2\text{Cl}_2$ sample preparation

The powder sample of $\text{Sr}_2\text{CuO}_2\text{Cl}_2$ was prepared by solid state synthesis from SrCO_3 (99.999%), CuO (99.995%), and SrCl_2 (grade 1 Johnson-Matthey), based on a suggested recipe of F.C. Chou. First, the SrCO_3 and CuO were ground together with mortar and pestle and pre-reacted at 800 C for 24 hours. Then, the SrCl_2 was ground in after being dried at 110 C to remove any water. This mixture was baked at 700 C for about 48 hours. The sample was completed with two repetitions of grinding and baking at 900 C. The samples for ^{17}O NMR were annealed at 900 C in $^{17}\text{O}_2$ gas for one to three days.

The single crystal samples of $\text{Sr}_2\text{CuO}_2\text{Cl}_2$ were prepared at MIT by Young Lee by the melt-growth method in a Pt crucible. He made them by slow cooling from the liquid and mechanically removing the crystals that formed on the surface of the melt. Some experiments used powder samples that were uniaxially aligned along the c axis in epoxy (Stycast 1266). Applying a high magnetic field (9 T) while the epoxy

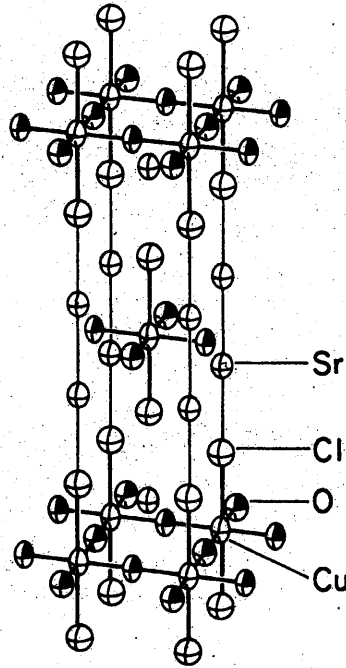


Figure 5-2: Crystal structure for $\text{Sr}_2\text{CuO}_2\text{Cl}_2$ (2d square lattice). (from Miller, *et al.*[77])

dries aligns the crystallites of the powder along the c axis because of the larger bulk susceptibility for field applied along the c axis. Since Stycast is not stable above ~ 500 K, some measurements were also performed for powder loosely aligned by shaking it in high magnetic field.

The sample quality was checked with x-ray scattering to determine the crystal structure and by ^{35}Cl NMR and susceptibility to determine the Néel temperature, T_N , for 3 dimensional magnetic ordering. We determined the bulk Néel temperature as $T_N^{3d} = 257$ K, in agreement with Suh, *et al.*[74]. The ^{35}Cl NMR linewidth and relaxation rate, $1/T_1$, show clear signs of the 3d ordering transition (figure 5-3). The ^{35}Cl linewidth is broadened in the magnetically ordered state by the static hyperfine field of the electron spins. The spin-lattice relaxation rate, $^{35}1/T_1$, shows a sharp increase at the Néel temperature caused by the slow spin fluctuations in the nearly ordered state. Note that in the figure the applied magnetic field of 9 Tesla shifts the Néel temperature up to 266 ± 4 K, as also seen by Suh, *et al.* [74]. The interaction of the applied magnetic field with the electron spins provides a small anisotropic

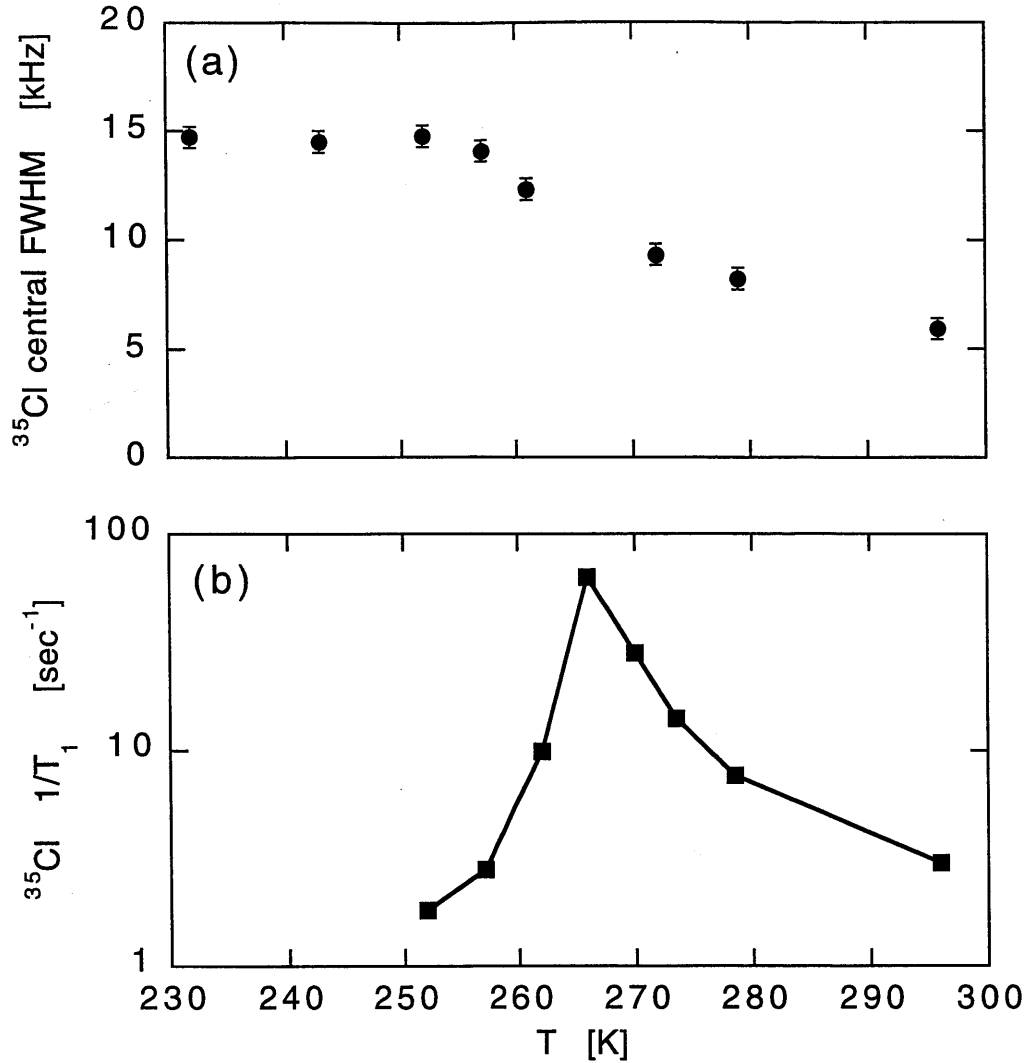


Figure 5-3: (a) ^{35}Cl NMR central transition (-1/2, +1/2) linewidth, (b) ^{35}Cl NMR $1/T_1$ ($H = 9\text{ T}$) for $\text{Sr}_2\text{CuO}_2\text{Cl}_2$. Line is a guide for the eye.

interaction, $\lesssim 6\text{ K} \approx 4 \times 10^{-3}J$, which can cause 3 dimensional ordering at a slightly higher temperature.

5.2.2 NMR/NQR lineshapes

The $^{63,65}\text{Cu}$ NMR and NQR lineshapes are shown in figures 5-4 and 5-5. The NQR frequency of ^{63}Cu is 26.55 MHz at 500 K. From high field NMR, we found that the electric field gradient is axially symmetric about the c axis ($\eta = 0$) as expected from the symmetry of the crystal structure around the Cu site. The ^{17}O NMR lineshape

is shown in figure 5-6. In this case, the crystal structure is not axially symmetric around the oxygen site. The quadrupole interactions are (± 841 , ∓ 577 , ∓ 264) kHz for the Cu-O bond direction, the direction with H \perp Cu-O bond in the ab plane, and the c axis, respectively ($\eta = 0.37$).

These values for the quadrupole frequencies of ^{63}Cu and ^{17}O compare well with the expectations for undoped CuO_2 planes with one hole in the Cu $3d_{x^2-y^2}$ orbital. Point charge calculations for the electric field gradient at the oxygen site yield quadrupole interactions of $(1 - \gamma)(-59.2, 38.6, 20.6)$ kHz for the Cu-O bond direction, the direction with H \perp Cu-O bond in the ab plane, and the c axis, respectively. These calculations provide the correct symmetry of the quadrupole interactions and imply a value for the Sternheimer antishielding factor $(1 - \gamma)$ of ≈ 14 . A value of 10 was previously estimated for the doped compound $\text{YBa}_2\text{Cu}_3\text{O}_7$ by Takigawa, *et al.* [41]. The quadrupole interaction allows us to distinguish the two crystal axes in the ab plane. The quadrupole interaction is much larger along the Cu-O bond direction than for the direction perpendicular to the Cu-O bond in the ab plane. This is simply because of the electric field gradient produced at the oxygen atom by the nearest neighbor copper 2+ ions.

5.3 Knight shift

The Knight shift was measured for both ^{63}Cu (figure 5-8) and ^{17}O NMR (figure 5-7). As discussed in the chapter 2, Knight shift measures the local uniform spin susceptibility, $\chi'(\mathbf{q}=0)$. Since $\text{Sr}_2\text{CuO}_2\text{Cl}_2$ has the basic CuO_2 square lattice structure, the hyperfine form factors for $\text{Sr}_2\text{CuO}_2\text{Cl}_2$ are those discussed in the NMR chapter.

$$^{63}F(\mathbf{q}) = A_\alpha + 2B[\cos(q_x) + \cos(q_y)] \quad (5.6)$$

$$^{17}F(\mathbf{q}) = 2C_\alpha \cos(q_{\text{Cu-Obond}}/2) \quad (5.7)$$

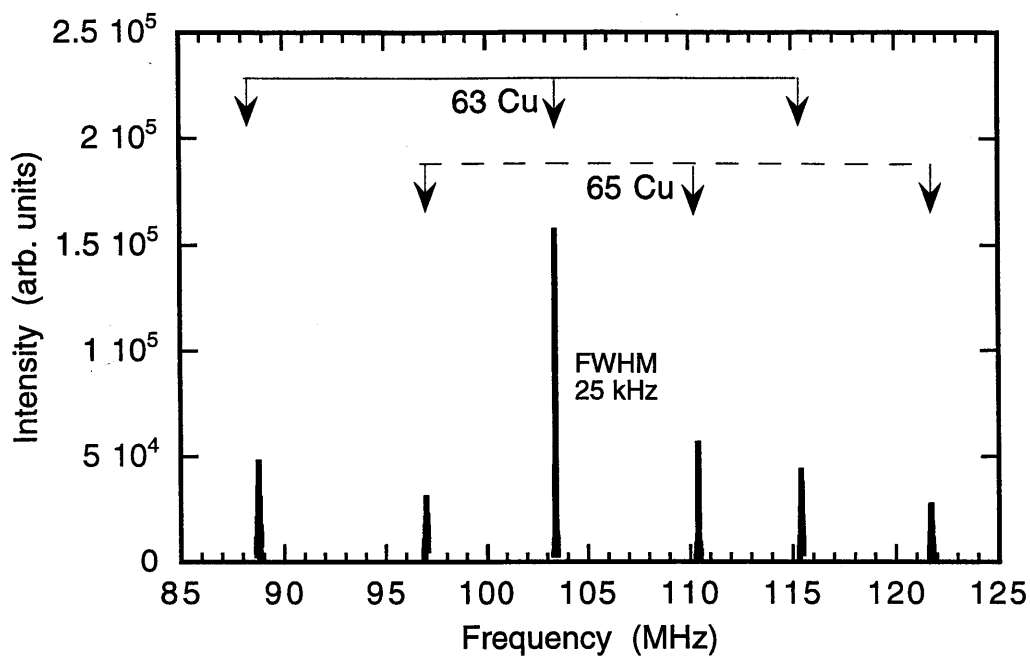


Figure 5-4: Cu NMR lineshape for $\text{Sr}_2\text{CuO}_2\text{Cl}_2$ at 800 K. $H = 9 \text{ T} \parallel ab$, 26mg single crystal.

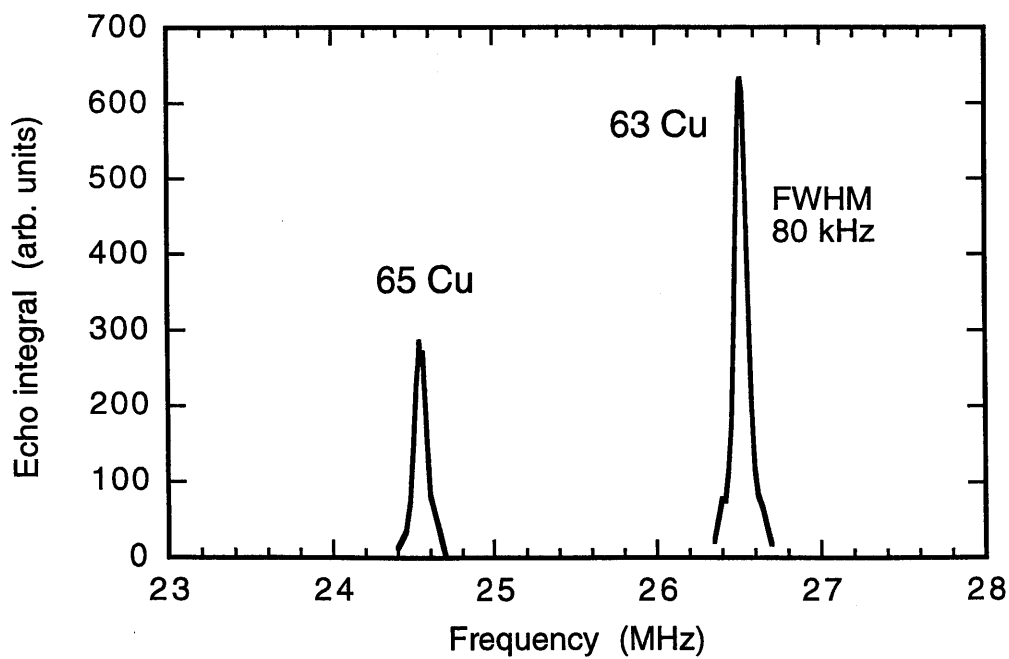


Figure 5-5: Cu NQR lineshape for $\text{Sr}_2\text{CuO}_2\text{Cl}_2$ at 500 K.

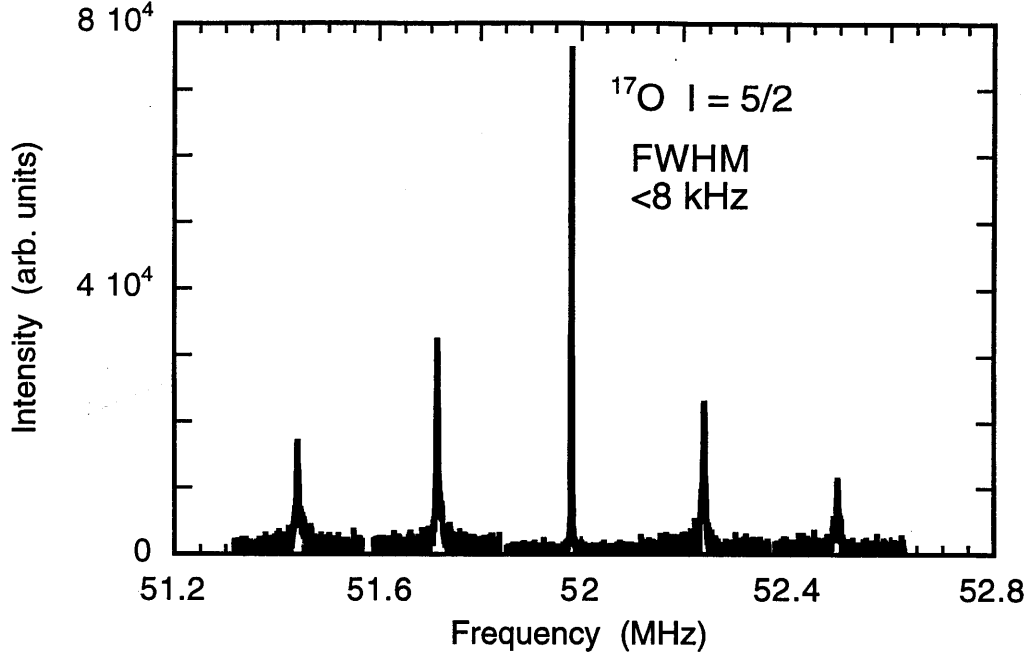


Figure 5-6: ^{17}O NMR lineshape for $\text{Sr}_2\text{CuO}_2\text{Cl}_2$ at 290 K. $H = 9 \text{ T} \parallel c$, aligned powder sample.

where the subscript α refers to the axis of the applied magnetic field.

$${}^{63}K_{\alpha} = \frac{A_{\alpha} + 4B}{N_A\mu_B} \chi'(\mathbf{q} = \mathbf{0}) + {}^{63}K_{\alpha,chem} \quad (5.8)$$

$${}^{17}K_{\alpha} = \frac{2C_{\alpha}}{N_A\mu_B} \chi'(\mathbf{q} = \mathbf{0}) + {}^{17}K_{\alpha,chem} \quad (5.9)$$

${}^{63,17}K_{\alpha,chem}$ is the temperature independent chemical shift. In order to determine the chemical shifts, we need to know the magnitude of the spin susceptibility. To establish the magnitude of the spin susceptibility, we use a value for ${}^{17}K_{bond} = 0.04\%$ found for $\text{YBa}_2\text{Cu}_3\text{O}_{6.63}$ [78]. In order to determine the other chemical shifts, we compare the Knight shifts for the other axes with the Knight shift for the Cu-O bond axis and extrapolate to ${}^{17}K_{bond} = 0.04\%$ as shown in figure 5-9. The results are summarized in table 5.3 and compared with other results for another 2d copper-oxide material, $\text{YBa}_2\text{Cu}_3\text{O}_{6+x}$ [79]. The oxygen chemical shift values are all small as expected from the closed shell electron configuration of the oxygen 2- ions. Notably, the chemical shift of the Cu-O bond direction and the perpendicular direction in the ab plane are

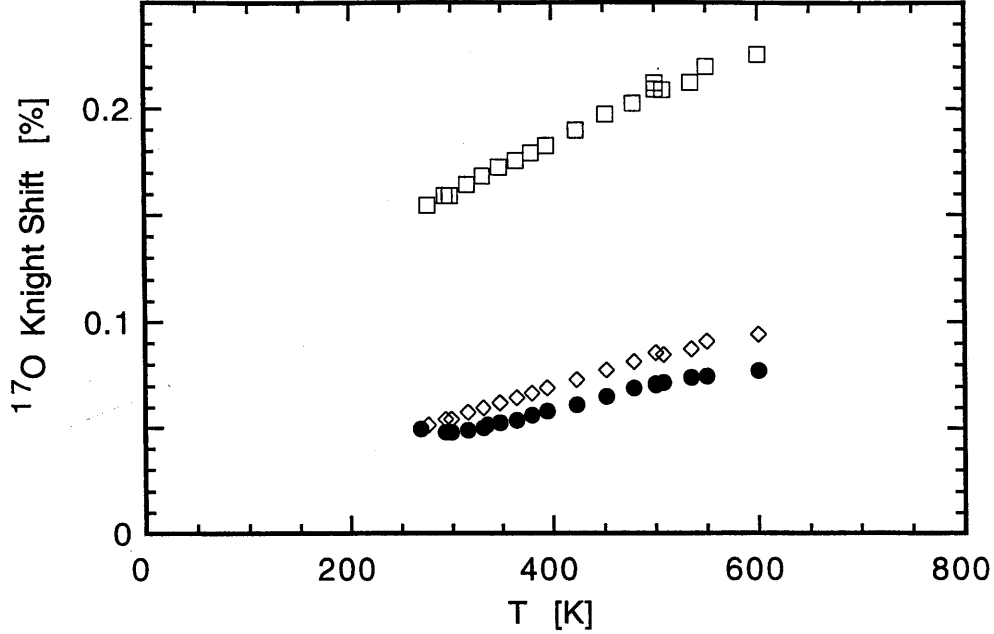


Figure 5-7: ^{17}O Knight shift for $\text{Sr}_2\text{CuO}_2\text{Cl}_2$. • c axis, □ || to Cu-O bond, ◇ \perp to both c axis and Cu-O bond.

Table 5.1: Oxygen hyperfine coupling at $q=0$, (2C) [kOe/μ_B]

Oxygen	Cu-O bond	\perp Cu-O bond	c
$\text{Sr}_2\text{CuO}_2\text{Cl}_2$	166 ± 14	106 ± 22	80 ± 8
$\text{YBa}_2\text{Cu}_3\text{O}_{6+x}$ [79]	158	98	90

close. The large difference in the Knight shift for these directions (see figure 5-7) is primarily from the difference in the local spin susceptibility.

The hyperfine parameters can be estimated by applying standard K - χ plot analysis (figure 5-10) [11] to $\text{Sr}_2\text{CuO}_2\text{Cl}_2$. The Knight shift and bulk susceptibility are plotted with the temperature as an implicit parameter. The hyperfine interaction determines the slope of the linear relation between the spin susceptibility and the Knight shift. The hyperfine parameters are summarized in tables 5.1 and 5.2 along with comparisons to other high T_c copper oxides [79, 39].

The Knight shift and bulk susceptibility results can be compared to various theoretical results. In figure 5-11, theoretical spin susceptibility results are shown for the 2d spin 1/2 Heisenberg model calculated by spin wave expansion [66], high temperature expansion [68], Monte Carlo [81], and renormalized classical [65]. The theoret-

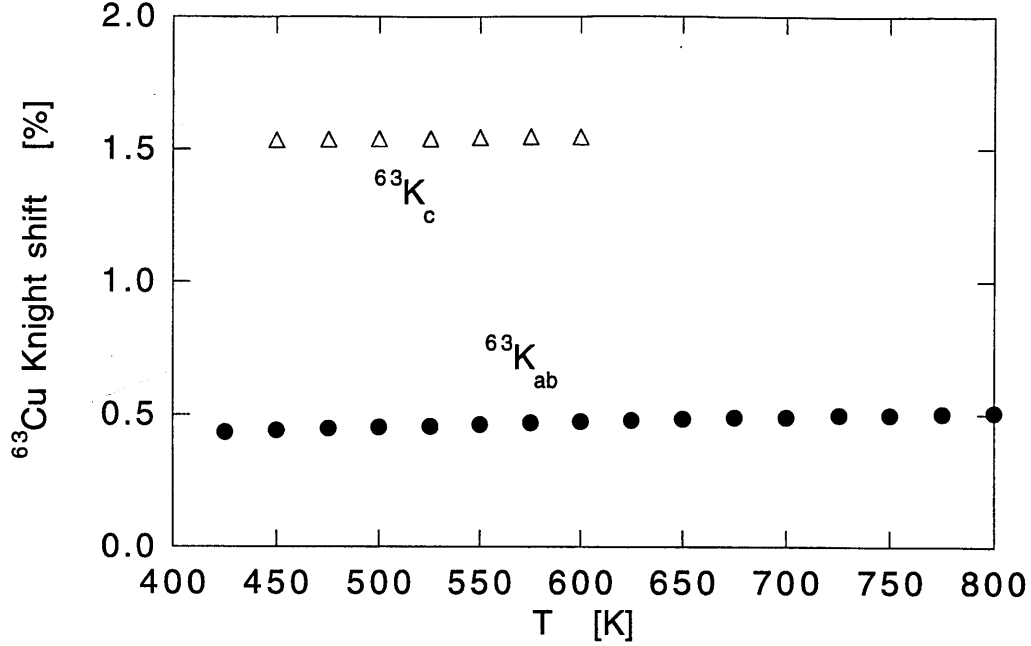


Figure 5-8: ^{63}Cu Knight shift for $\text{Sr}_2\text{CuO}_2\text{Cl}_2$. \bullet ab axes, Δ c axis.

Table 5.2: Copper hyperfine couplings [kOe/μ_B]

	ab	c	
$\text{Sr}_2\text{CuO}_2\text{Cl}_2$ ($q=0$) = $A_\alpha + 4B$	180 ± 32	65 ± 16	
$\text{Sr}_2\text{CuO}_2\text{Cl}_2$ ($q=\pi$) = $A_\alpha - 4B$	-112 ± 10	-250 ± 20	
La_2CuO_4 ($q=\pi$) [7]	-120 ± 10	-300 ± 20	
$\text{YBa}_2\text{Cu}_3\text{O}_{7-\delta}$ ($q=\pi$) [80]	-129	-335	
	A_{ab}	A_c	B
$\text{Sr}_2\text{CuO}_2\text{Cl}_2$	34	-92	38
$\text{YBa}_2\text{Cu}_3\text{O}_{7-\delta}$ [80]	38	-167	42

Table 5.3: Chemical Knight shifts [%]

Oxygen	Cu-O bond	\perp Cu-O bond	c
$\text{Sr}_2\text{CuO}_2\text{Cl}_2$	0.04	-0.02 ± 0.04	-0.01 ± 0.07
$\text{Sr}_2\text{CuO}_2\text{Cl}_2$ matched	0.015	-0.035 ± 0.04	-0.02 ± 0.07
$\text{YBa}_2\text{Cu}_3\text{O}_{6+x}$ [79]	0.08	0.03	-0.008
Cu	ab	c	
$\text{Sr}_2\text{CuO}_2\text{Cl}_2$	0.27 ± 0.02	1.47 ± 0.07	
$\text{YBa}_2\text{Cu}_3\text{O}_7$ [39]	0.28	1.28	

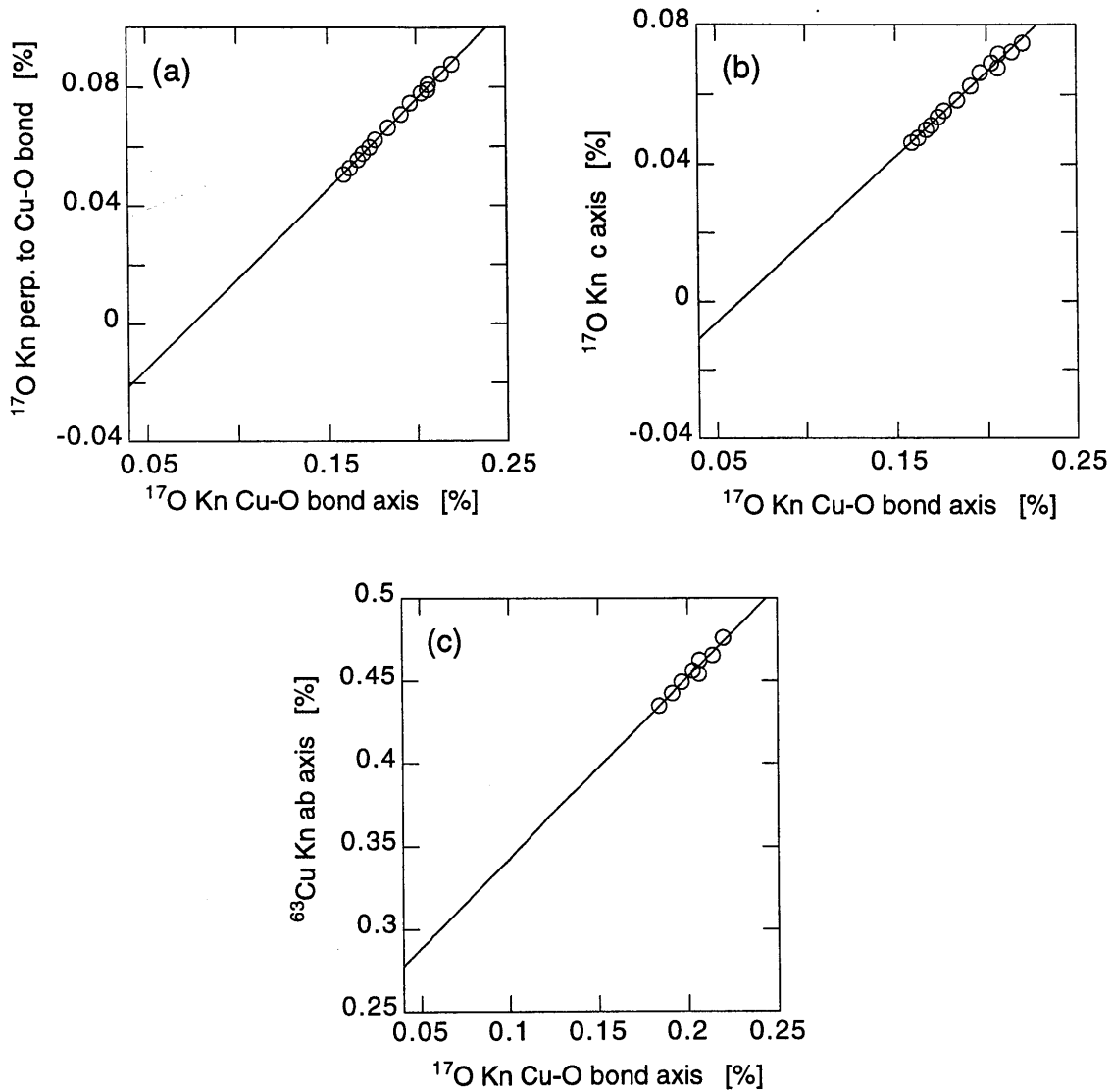


Figure 5-9: Comparison of ^{17}Kn for the Cu-O bond axis with (a) $^{17}\text{Kn}_{\perp\text{Cu-O}}$, (b) $^{17}\text{Kn}_c$, and (c) $^{63}\text{Kn}_{ab}$ with temperature as an implicit parameter. Solid lines are linear fits. The slope of the line is the ratio of the hyperfine interactions, and the y value when $^{17}K_{bond} = 0.04$ is the chemical shift, $^{63,17}K_{\alpha,chem}$.

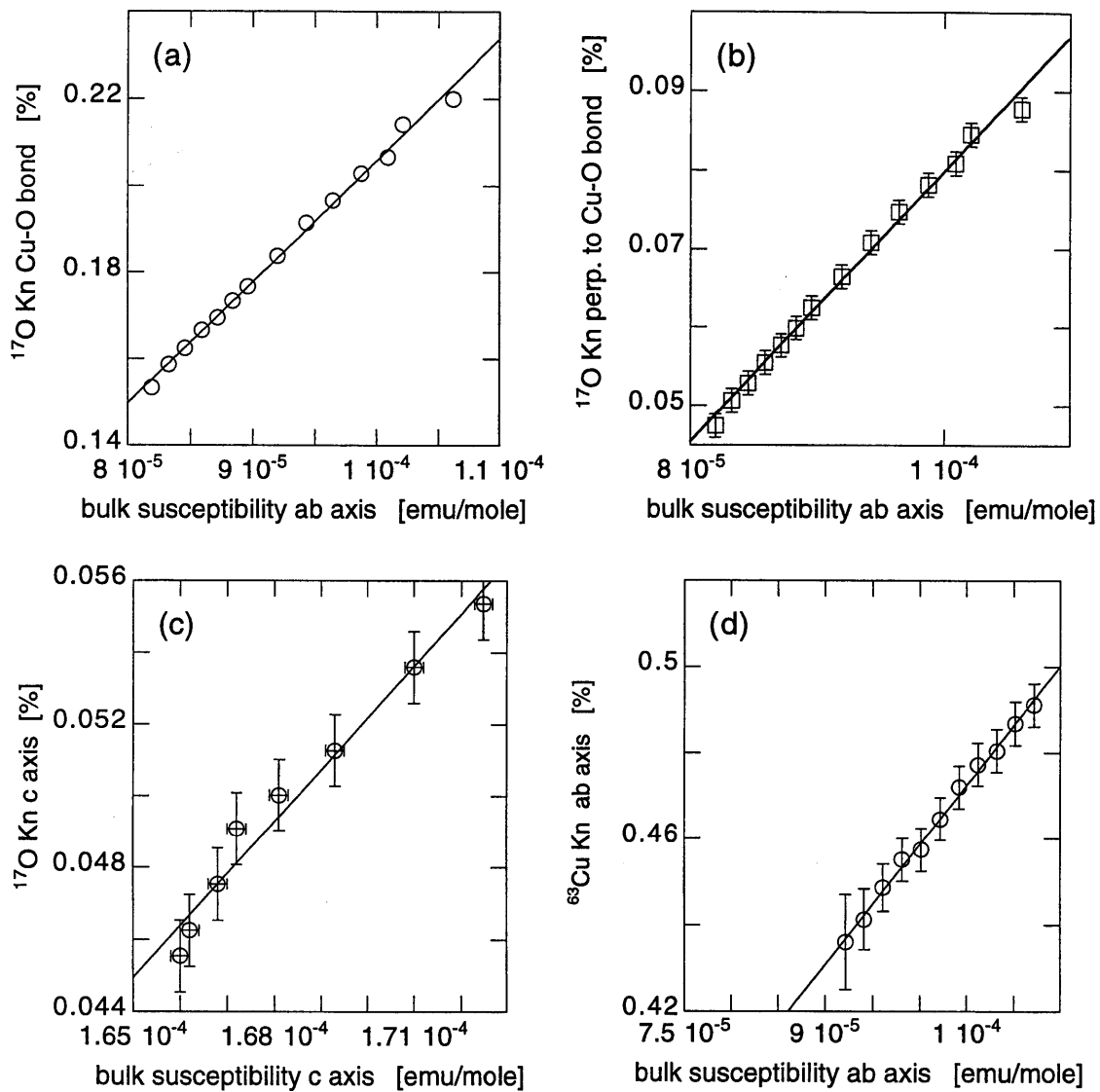


Figure 5-10: Knight shift as a function of bulk susceptibility for (a) $^{17}\text{K}_{bond}$, (b) $^{17}\text{K}_{\perp}$, (c) $^{17}\text{K}_c$, and (d) $^{63}\text{K}_{ab}$. Solid lines are linear fits. The slope of the line is the hyperfine interaction.

ical results are in agreement that at high temperatures the susceptibility follows a Curie-Weiss-like temperature dependence. As the temperature decreases and antiferromagnetic spin correlations increase, the spin susceptibility is suppressed. The peak in the spin susceptibility occurs at around J . For $\text{Sr}_2\text{CuO}_2\text{Cl}_2$, we have data over a wide temperature range from the Néel temperature, 257 K to 800 K ($T/J = 0.18$ to 0.55 for $J = 1450$ [75]). Over this temperature region, the spin susceptibility is linear with temperature with the expectation that the slope decreases at higher temperatures. Figure 5-12 shows the spin susceptibility as measured by bulk susceptibility, and oxygen and copper Knight shift using the orbital Knight shifts and hyperfine couplings determined above. For comparison, the theoretical Monte Carlo result of Makivic and Ding [81] is shown. The slope of the theoretical results is the same, but they are about $1 \times 10^{-5} \text{ cm}^3/\text{mole}$ larger in magnitude. This is not surprising because this amount of change in the magnitude would correspond to a small overestimate of K_{chem} . In figure 5-12 and table 5.3, we show that a small adjustment of K_{chem} that is well within error can match the theoretical spin susceptibility. If we choose $^{17}K_{chem}^{bond} = 0.015 \%$ instead of 0.04% , the theoretical and experimental spin susceptibilities match. Thus, the uniform susceptibility of $\text{Sr}_2\text{CuO}_2\text{Cl}_2$ fits the expectation for the spin $1/2$ 2d Heisenberg antiferromagnet for a wide temperature range, 276 K to 800 K ($T/J = 0.19$ to 0.55).

Because Knight shift is a measure of the local susceptibility (the susceptibility at the nucleus position), the Knight shift can provide additional information about the local electronic structure. Figure 5-7 shows the oxygen Knight shift of $\text{Sr}_2\text{CuO}_2\text{Cl}_2$ as a function of the direction of the applied magnetic field. The most striking fact is that the Knight shift for the applied field along the Cu-O bond is much larger than for the other two crystal axes. The Knight shift of the other two crystal axes is very similar. It should be noted that the Cu-O bond direction can be distinguished from the orthogonal direction in the ab plane by the quadrupole interactions.

The reason why the Knight shift is larger with the magnetic field along the Cu-O bond is based on the theory of Abragam and Pryce [33, 40] and has been discussed by Takigawa, *et al.* [41] for the specific case of these copper oxides. A larger Knight

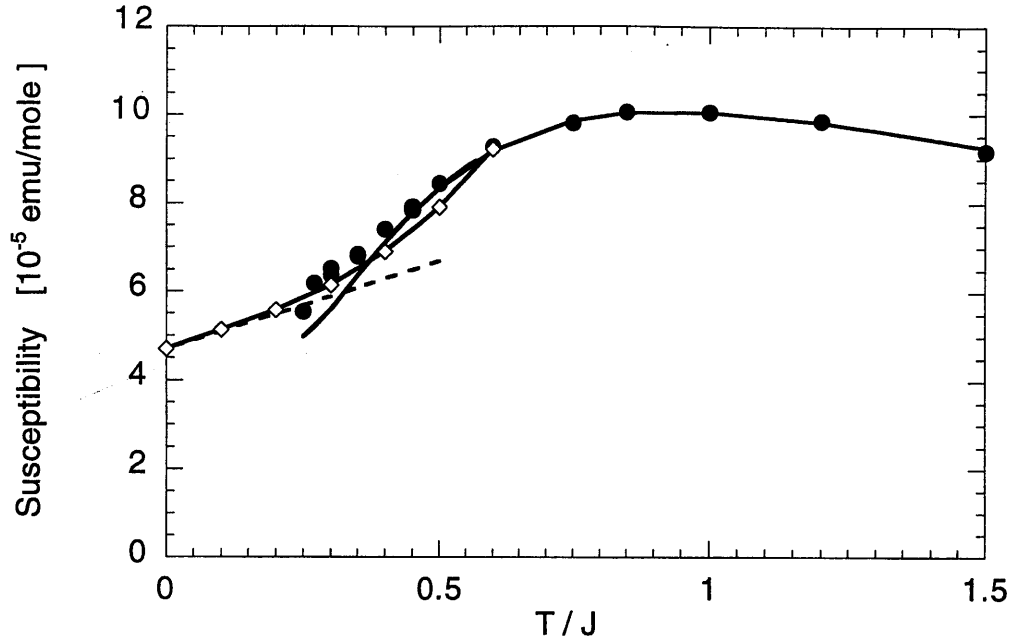


Figure 5-11: Uniform susceptibility theory for the $S=1/2$ 2d Heisenberg antiferromagnet ($J=1450$ K). \bullet Monte Carlo [81], solid line high temperature expansion [68], \diamond spin wave expansion [66], dashed line Renormalized Classical regime of non-linear σ model [65].

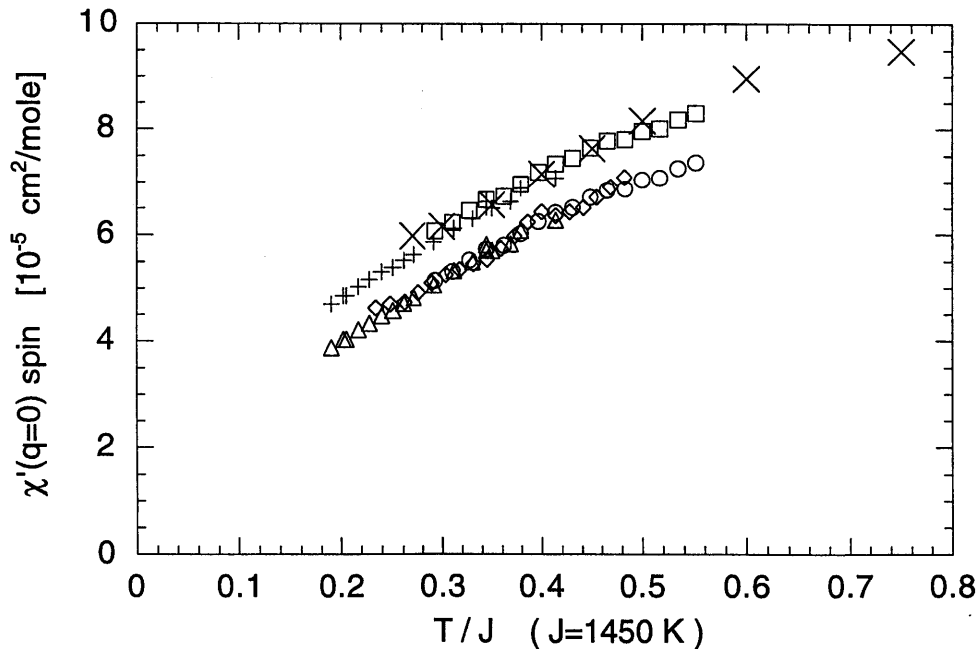


Figure 5-12: Comparison of $^{63}\text{K}_{ab}$ (\circ $K_{chem}=0.27\%$, \square $K_{chem}=0.24\%$), $^{17}\text{K}_{bond}$ (\triangle $K_{chem}=0.04\%$, $+$ $K_{chem}=0.015\%$), and bulk susceptibility (\diamond) with Monte Carlo results [81] (\times).

shift in the Cu-O bond direction gives support to the idea that the copper and oxygen atoms bond by the hybridization of the Cu $3d_{x^2-y^2}$ orbital with the oxygen $2p_\sigma$ orbital. The hybridization results in some spin transfer into the oxygen $2p_\sigma$ orbital, which points along the Cu-O bond. A spin in a p_z orbital gives an axial Knight shift, $2A_p(-\langle S_x \rangle, -\langle S_y \rangle, 2\langle S_z \rangle)$ where $A_p = \frac{2}{5}\mu_B \langle r^{-3} \rangle$ [40, 41]. $\langle r^{-3} \rangle$ is the average of r^{-3} over the p orbital. $A_p = 91 kOe/\mu_B$ using $\langle r^{-3} \rangle = 3.63$ atomic units which is 70% of the free oxygen 2p value [82, 41]. This gives us an estimate of the hyperfine interaction expected from an electron spin in the oxygen 2p orbital.

Since the hyperfine interactions have been measured, we can estimate the amount of spin transferred to the oxygen 2p orbital. However, there is one obvious difference between the measured hyperfine interactions and the predicted values for a p orbital. For the p orbital, the hyperfine interactions are traceless, that is the sum over all three crystal axes equals zero. The measured hyperfine interactions are all positive. So far, we have not mentioned any effect of the s oxygen orbitals on the hyperfine interactions. In fact, the s orbitals can have a large contribution to the hyperfine interactions because they have a finite probability for the electron to be at the position of the nucleus (eq. 3.10). For oxygen, $H_{int} \sim 4000 kOe/\mu_B$ using an estimate for the probability of the electron being at the nucleus, $R_{2s}^2(0)$ of 7.5 [40]. Any unpaired electron spin in the 2s orbital has an almost 50 times larger effect than in the 2p orbital, $91 kOe/\mu_B$. The s orbitals have isotropic spacial structure, so their hyperfine interactions will also be isotropic. This suggests a way to separate the effect of s and p orbitals on the hyperfine interactions: the s interactions are isotropic, while the p interactions have no isotropic component. So, we separate the hyperfine interactions,

$$C_{iso} = \frac{1}{3} [C_{bond} + C_\perp + C_c] \quad (5.10)$$

$$C_{axi} = \frac{1}{3} \left[C_{bond} - \frac{1}{2} (C_\perp + C_c) \right] \quad (5.11)$$

For $Sr_2CuO_2Cl_2$, we get $C_{iso} = 59 kOe/\mu_B$ and $C_{axi} = 12 kOe/\mu_B$. The isotropic hyperfine interaction implies $f_s \sim 1.5\%$ of the total unpaired electron spin in the oxygen 2s orbital, or a tiny $\sim 0.03\%$ in the 1s orbital. On the other hand, the axial

hyperfine interaction requires a significant amount of the unpaired spin to reside in the oxygen $2p_\sigma$ orbital, $f_\sigma \sim 13\%$. These values are larger than estimates from other fluoride antiferromagnets, such as KNiF_3 ($f_s \sim 0.5\%$, $f_\sigma \sim 3.5\%$) [33, 34], reflecting a larger hybridization with the oxygen $2p$ orbital.

These oxygen Knight shift results confirm that the copper $3d_{x^2-y^2}$ orbital is strongly hybridized with the oxygen $2p_\sigma$ orbital. As a result, a large amount of the unpaired electron spin of $\text{Sr}_2\text{CuO}_2\text{Cl}_2$ actually resides on the oxygen orbital. This accounts for the very large exchange interaction $J = 1450$ K between the Cu electron spins because the spins from nearest neighbor Cu atoms are hybridizing with the *same* oxygen $2p_\sigma$ orbital. To be specific, Owen and Thornley [40] derived an expression for J based on P. Anderson's superexchange model [32].

$$J = f_\sigma^2 \left[\frac{4(E_d - E_p)^2}{U} \right] \quad (5.12)$$

where E_d and E_p are the energies of the Cu $3d$ and O $2p$ orbitals and U is the Coulomb repulsion energy, the energy required to put two holes on the same Cu ion. As a rough quantitative estimate, if we take $(E_d - E_p) = 3$ eV and $U = 3$ eV [83] and insert $f_\sigma = 0.13$, then $J = 0.2$ eV = 2350 K. This is a reasonable estimate in comparison to the measured $J = 1450$ K for this simple model of J . Qualitatively, in order to both hybridize with the same orbital, the two spins must have opposite spins because of the Pauli exclusion principle. As a result, the Cu nearest neighbor spins are strongly antiferromagnetically coupled.

5.4 Copper $1/T_1$ and $1/T_{2G}$

The relaxation rates for copper, ${}^{63}\text{1}/T_1$ and ${}^{63}\text{1}/T_{2G}$, both reflect the spin correlation length. Qualitatively, both increase strongly with lowering temperature (figure 5-13), which corresponds to the increase in the correlation length. Very thorough ${}^{63}\text{Cu}$ NMR experiments have been previously done on La_2CuO_4 by Imai, *et al.* [7, 26], so we can compare the results for $\text{Sr}_2\text{CuO}_2\text{Cl}_2$ and La_2CuO_4 . In addition, we can compare the

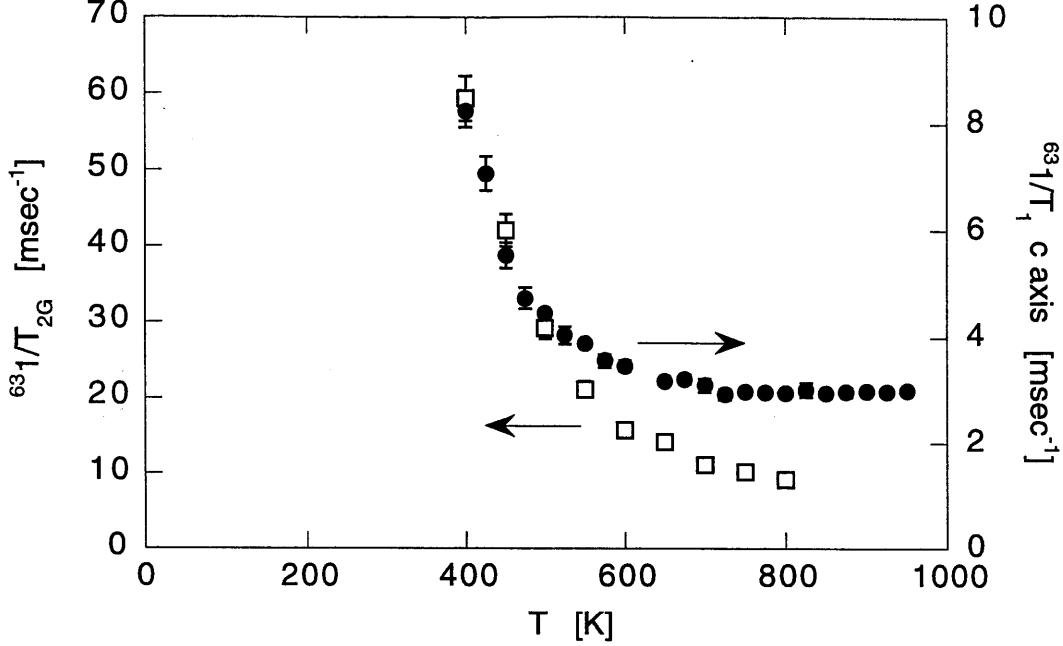


Figure 5-13: $^{63}\text{Ni}/T_1$ (\bullet , right axis) and $^{63}\text{Ni}/T_{2G}$ (\square , left axis) for $\text{Sr}_2\text{CuO}_2\text{Cl}_2$.

results with the expectations from the renormalized classical regime of the quantum non-linear σ model discussed above and other theoretical results.

For the renormalized classical regime of the non-linear σ model, the exponential temperature dependence of the spin correlation length directly results in a primarily exponential temperature dependence of $1/T_1$ [84] and $1/T_{2G}$ [26, 69].

$$\frac{1}{T_1} = \frac{1}{T_{1\infty}} \frac{\xi}{a} \frac{0.8}{Z_c} \left(\frac{T}{2\pi\rho_S} \right)^{3/2} \left(\frac{1}{1 + T/2\pi\rho_S} \right)^2 \quad (5.13)$$

$$\frac{1}{T_{1\infty}} = \frac{F(q = \pi)^2 \sqrt{\pi\hbar}}{\hbar^2 4J} \quad (5.14)$$

where $2\pi\rho_S = 1.13J$, $Z_c = 1.18$ [68]. For $1/T_{2G}$ [28]

$$\left(\frac{1}{T_{2G}} \right)^2 = \frac{0.69}{2\hbar^2} \left[\frac{1}{N} \sum_q F(q)^4 \chi'(q)^2 - \left(\frac{1}{N} \sum_q F(q)^2 \chi'(q) \right)^2 \right] \quad (5.15)$$

For the renormalized classical regime, $\chi'(q)$ is expressed as [69]

$$\chi'(q) = \chi'(q = \pi) f((q - \pi)\xi) \quad (5.16)$$

$$\chi'(q = \pi) = \frac{B_S \xi^2 N_0^2}{k_B T [(2\pi\rho_S/T) + 1]^2} \quad (5.17)$$

$$f(x) \approx \frac{1 + \frac{1}{2} B_f \ln(1 + x^2)}{1 + x^2} \quad (5.18)$$

where $B_S \approx 90$ [85], $B_f = (4\pi/B_S)$, and $N_0 \approx 0.3$. The important thing to note is that both $1/T_1$ and $1/T_{2G}$ are proportional to the correlation length, ξ . To the lowest order in $T/2\pi\rho_S$, the temperature dependencies are

$$\frac{1}{T_1} \propto T^{3/2} \exp(2\pi\rho_S/T) \quad (5.19)$$

$$\frac{1}{T_{2G}} \propto T \exp(2\pi\rho_S/T) \quad (5.20)$$

To test whether this exponential dependence with inverse temperature is true, $1/(T_1 T^{3/2})$ and $1/(T_{2G} T)$ are plotted as a function of inverse temperature in figure 5-14. On the logarithmic scale, we expect linear behavior with the slope equal to $2\pi\rho_S$. The renormalized classical behavior is only expected to be valid for $T/2\pi\rho_S < 0.5$ [65]. Indeed, the experimental results do show this renormalized classical behavior with $J = 2\pi\rho_S/1.13 = 1450$ K and we obtained hyperfine couplings $F_{ab}(q = \pi) = A_{ab} - 4B = -112 \pm 10$ kOe/ μ_B and $F_c(q = \pi) = A_c - 4B = -250 \pm 20$ kOe/ μ_B .

These results are very similar to those found for La_2CuO_4 [7, 26]. Figures 5-15 and 5-16 show the comparison between $\text{Sr}_2\text{CuO}_2\text{Cl}_2$ and La_2CuO_4 for $1/T_1$ and $1/T_{2G}$. In order to directly compare the materials, we must consider the difference in the magnitude of J . J of La_2CuO_4 has been found to be slightly larger, $J_{214} = 1530$ [20], than $\text{Sr}_2\text{CuO}_2\text{Cl}_2$ ($J_{2122} = 1450$ [75]). The temperature scale is set by J . In addition, both $1/T_1$ and $1/T_{2G}$ are $\propto 1/J$ as can be seen for the renormalized classical expressions above. So, we graph J/T_1 and J/T_{2G} because these values will be independent of J . There is also the possibility that the hyperfine couplings of the two materials may be different. For $1/T_1$, the temperature dependence and magnitude are very similar for the two materials. This implies that the hyperfine coupling along the ab axes are similar for the two materials. Indeed, the fits to the renormalized classical form yield $F_{ab}(q = \pi) = -120 \pm 10$ kOe/ μ_B for La_2CuO_4 , in comparison to

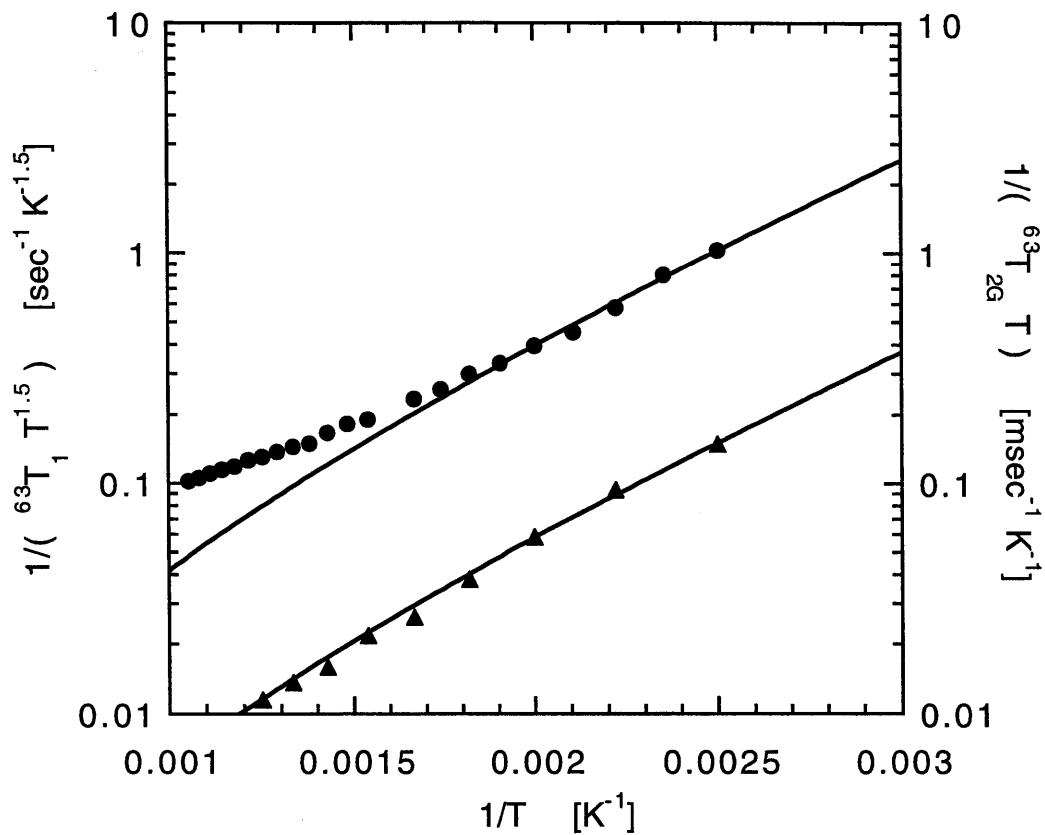


Figure 5-14: $^{63}\text{1}/(\text{T}_1 T^{3/2})$ (●, left axis) and $^{63}\text{1}/(\text{T}_{2G} T)$ (▲, right axis) for $\text{Sr}_2\text{CuO}_2\text{Cl}_2$. Solid lines show fits to Renormalized Classical form with $J = 1450$ K. Fit results in hyperfine values $F_{ab}(q = \pi) = -112 \pm 10 \text{ kOe}/\mu_B$ and $F_c(q = \pi) = -250 \pm 20 \text{ kOe}/\mu_B$.

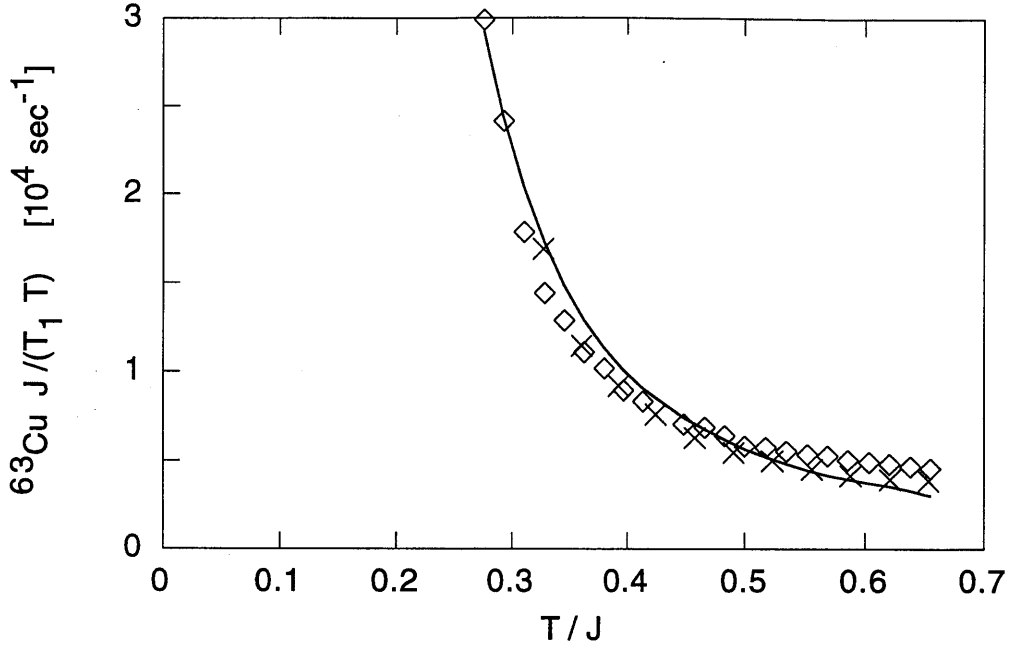


Figure 5-15: ^{63}Cu $J/(T_1 T)$ for $\text{Sr}_2\text{CuO}_2\text{Cl}_2$ (\diamond) and La_2CuO_4 (\times). Solid line shows spin wave theory for $1/T_1$ described in the text (eq.5.22).

$-112 \pm 10 \text{ kOe}/\mu_B$ for $\text{Sr}_2\text{CuO}_2\text{Cl}_2$. (I should note that this value for La_2CuO_4 differs from the value, $-139 \pm 10 \text{ kOe}/\mu_B$ given in Imai, *et al.* [7] because of the use here of the new calculation of the correlation length [70] and $J = 1530$ rather than $J = 1590$.) For $1/T_{2G}$, the two materials do not have the same magnitude, suggesting that the hyperfine couplings along the c axis are different by $\sim 20\%$ ($F_{c,214}(q = \pi) = -300 \pm 20 \text{ kOe}/\mu_B$, $F_{c,2122}(q = \pi) = -250 \pm 20$). These results are summarized in table 5.2 along with a comparison to another 2d material, $\text{YBa}_2\text{Cu}_3\text{O}_x$ [80]. The agreement between the results for $\text{Sr}_2\text{CuO}_2\text{Cl}_2$ and La_2CuO_4 assures us that the behavior of $1/T_1$ and $1/T_{2G}$ is characteristic of the Cu-O planes, and is not specific to any particular material.

One curious fact about this analysis of $1/T_1$ and $1/T_{2G}$ based on the renormalized classical regime is that the renormalized classical fit to $1/T_{2G}$ is reasonable over the entire temperature range (400 to 800 K). On the other hand, $1/T_1$ clearly deviates at high temperatures. In fact, $1/T_1$ at high temperatures is constant (figure 5-13). A very likely reason for the high temperature behavior of $1/T_1$ is the importance of spin excitations for $q \neq \pi$ as discussed by Sokol, Gagliano, and Bacci [86]. The renormal-

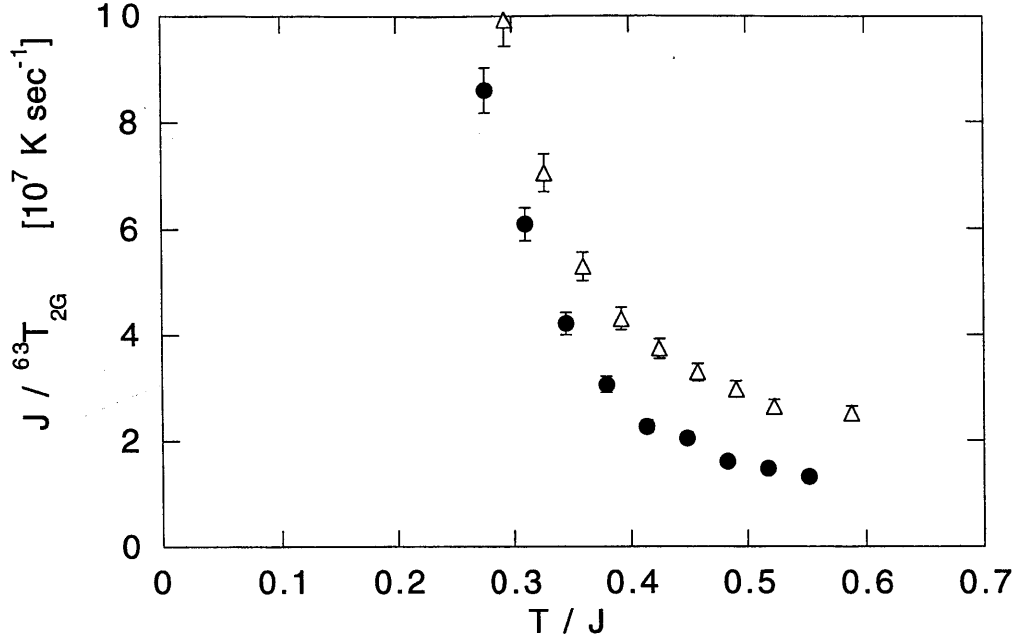


Figure 5-16: ^{63}Cu (J/T_{2G}) for $\text{Sr}_2\text{CuO}_2\text{Cl}_2$ (\bullet) and La_2CuO_4 (Δ).

ized classical regime of the non-linear σ model just considers $q \approx \pi$. As discussed in the previous chapter on 1d Heisenberg antiferromagnets, at high temperatures, spin excitations at other wavevectors besides π become important. Qualitatively, theoretical results show (figure 5-17) that there will be some region of weak temperature dependence for $1/T_1$. At low temperatures, $1/T_1$ rapidly decreases with temperature. High temperature expansion [68] predicts an increasing $1/T_1$ with temperature. In between we may expect a region of weak temperature dependence. Indeed, Sokol, Gagliano, and Bacci [86] calculated the contribution to $1/T_1$ from $q \approx 0$ excitations and showed that the total temperature dependence of $1/T_1$ is expected to be weak (figure 5-18). Such a weak temperature dependence seems to depend on the wavevector dependence of the hyperfine form factor. Monte Carlo results by Sandvik [67] indicate that a form factor that is constant over wavevector produces an increasing $1/T_1$ at high temperatures (left graph of figure 5-19), while including the significant transferred hyperfine interaction of the Cu site suppresses the temperature dependence of $1/T_1$ (right graph of figure 5-19). However, this explanation depends on the details of the hyperfine interaction which does not seem to account for why $1/T_1$ is constant over such a wide range of temperature for various copper-oxide materials.

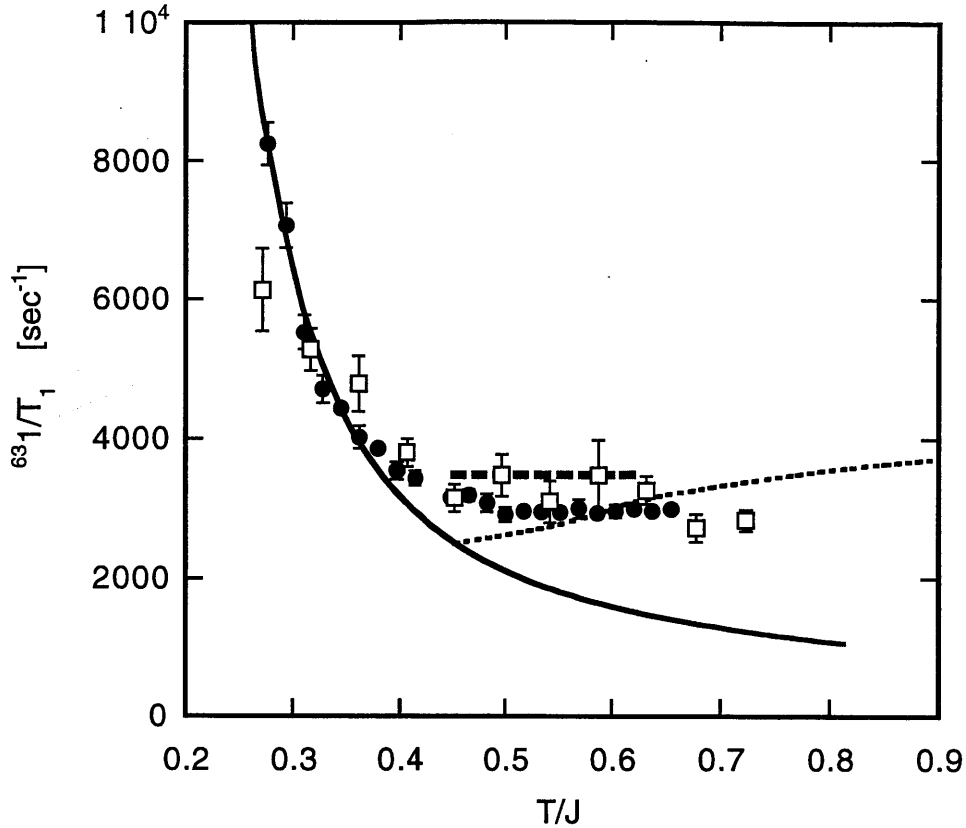


Figure 5-17: $^{63}(1/T_1)$ for $\text{Sr}_2\text{CuO}_2\text{Cl}_2$ (●). Theoretical results: Solid line - Renormalized Classical [65], Dashed line - Quantum Critical [71], Dotted line - high temperature expansion [68], □ Quantum Monte Carlo [67]. ($J = 1450$, $F_{ab}(q = \pi) = -112$ kOe/ μ_B).

Constant $^{63}\text{Cu } 1/T_1$ at high temperatures also occurs for the 3-leg ladder $\text{Sr}_2\text{Cu}_3\text{O}_5$, and also hole-doped materials such as doped 2-leg ladders and 2d $\text{La}_{2-x}\text{Sr}_x\text{CuO}_4$.

Another explanation offered for constant $^{63}1/T_1$ is the existence of the quantum critical region in the non-linear σ model [71]. As seen in figure 5-17, this region would be expected to have a constant $1/T_1$. However, the quantum critical region is also predicted to have $1/T$ dependence in $1/T_{2G}$ [71, 67]. For $1/T_{2G}$, we find that the renormalized classical prediction fits well over the entire temperature range (figure 5-20). In contrast, the temperature dependence of the quantum critical prediction is too weak. Hence, it is not clear that any temperature region exists in the spin 1/2 2d Heisenberg antiferromagnet that corresponds to the quantum critical region of the non-linear σ model.

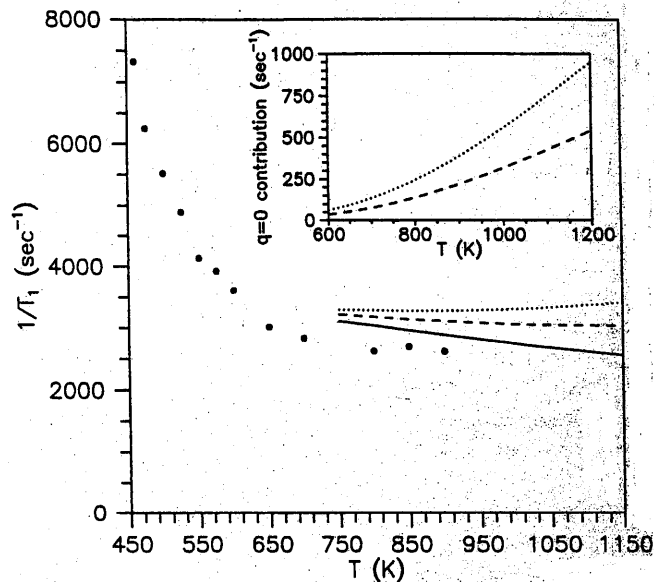


Figure 5-18: Calculated $^{63}\text{Li}/T_1$ as a function of temperature with no spin diffusion contribution (solid line) and with a spin diffusion contribution with cutoff of 10 lattice spacings (dashed line) and 20 lattice spacings (dotted line). Dots are the experimental result of reference [7]. (from Sokol, Gagliano, Bacci [86])

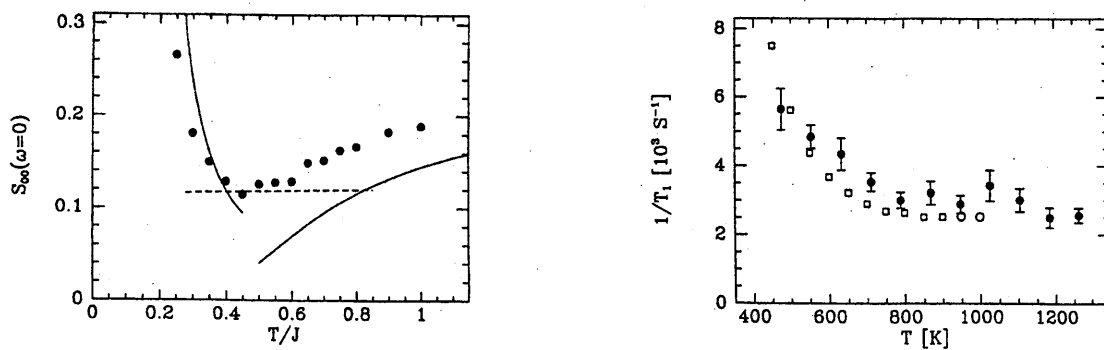


Figure 5-19: Quantum Monte Carlo results from Sandvik and Scalapino [67]. Left graph shows results for a hyperfine form factor with constant wavevector dependence (dots). Right graph shows the results for hyperfine ratio $A/B = 0.84$ (solid dots). Open symbols are experimental data [7].

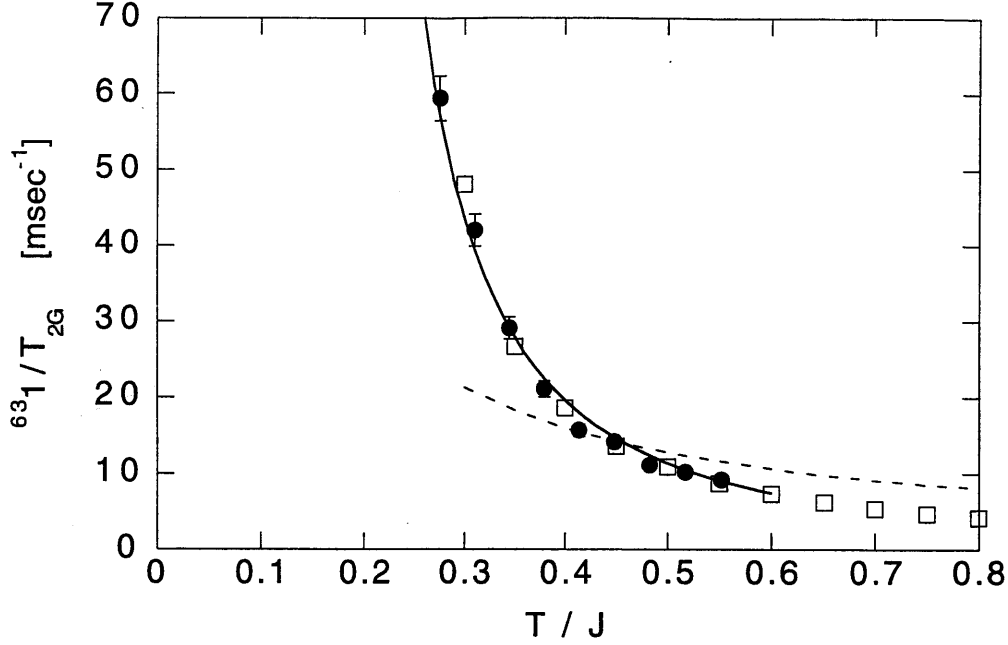


Figure 5-20: ${}^{63}\text{Cu}/T_{2G}$ for $\text{Sr}_2\text{CuO}_2\text{Cl}_2$ (●). Theoretical results: Solid line - Renormalized Classical [65], Dashed line - Quantum Critical [71], □ Quantum Monte Carlo [67]. ($J = 1450$, $F_c(q = \pi) = -250 \text{ kOe}/\mu_B$).

To summarize the results on ${}^{63}\text{Cu}$ NQR/NMR, ${}^{63}\text{Cu}/T_1$ and ${}^{63}\text{Cu}/T_{2G}$ of $\text{Sr}_2\text{CuO}_2\text{Cl}_2$ have good agreement with the expectations of the renormalized classical regime of the non-linear σ model at low temperatures. The behavior for $\text{Sr}_2\text{CuO}_2\text{Cl}_2$ is the same as for the prototypical undoped copper-oxide material, La_2CuO_4 . This provides confidence that the low energy spin excitations around $q = \pi$ in these copper-oxide materials are well-described.

5.5 Oxygen $1/T_1$

${}^{17}\text{O}$ $1/(T_1 T)$ is shown in figure 5-21. Most notably, the temperature dependence of the oxygen spin-lattice relaxation is completely different from that of copper. As discussed in the previous section, because of the critical slowing down of the long wavelength, antiferromagnetic spin fluctuations at $\mathbf{q} \approx \mathbf{Q}$, ${}^{63}\text{Cu}/T_1$ for the undoped 2d Heisenberg antiferromagnet diverges exponentially toward $T = 0$ ($= T_N^{2d}$) following ${}^{63}\text{Cu}/T_1 \approx T^{1.5} \exp(1.13J/T)$ [7, 84]. On the other hand, the oxygen atom

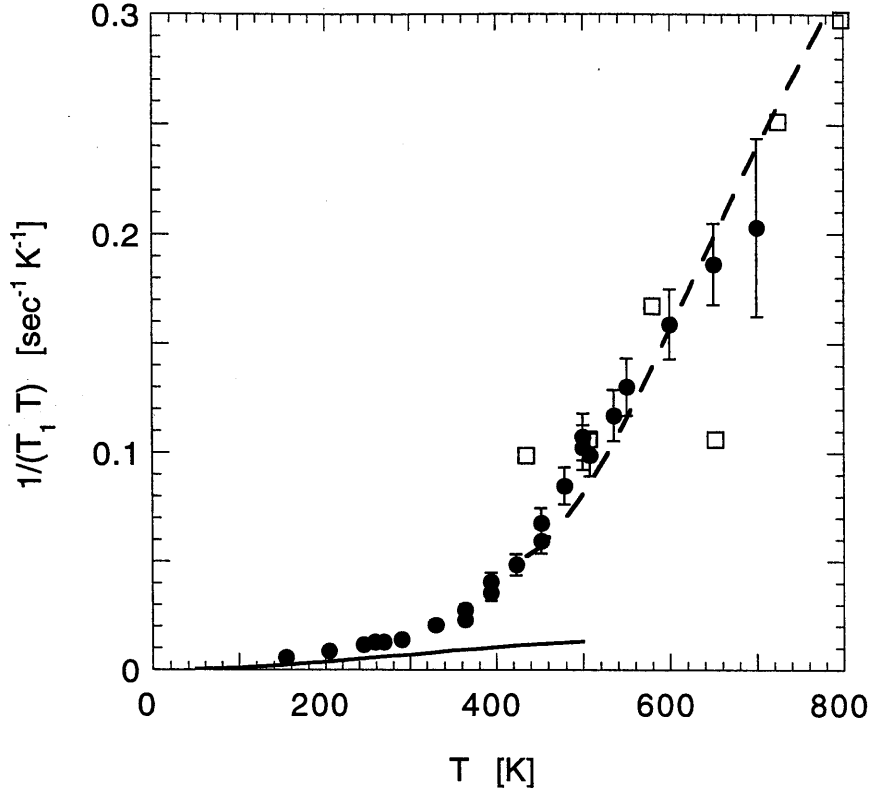


Figure 5-21: $^{17}1/(T_1 T)$ for $\text{Sr}_2\text{CuO}_2\text{Cl}_2$, $H||c$ (\bullet). Theoretical results: Solid line - low T expansion [87], Dashed line - high T expansion [68], \square Quantum Monte Carlo [67].

sits in between two copper atoms which results in a hyperfine form factor, $^{17}F(q) = 2C \cos(q_x/2)$. Since $^{17}F(\mathbf{q} = \mathbf{Q}) = 0$, $^{17}1/T_1$ is insensitive to the long wavelength critical dynamics around $\mathbf{q} = \mathbf{Q}$ [17], and senses the short wavelength mode ($1/\xi \lesssim \mathbf{q} < \mathbf{Q}$) of $S = 1/2$ Cu spin fluctuations. This can be seen theoretically by comparing the expectations from Quantum Monte Carlo [67] for the contributions to $^{63,17}1/T_1$ as a function of wavevector (figures 5-22 and 5-23).

According to the renormalization group analysis, the elementary excitations at short wavelengths in 2d Heisenberg antiferromagnets are spin waves with asymptotic freedom[65, 88]. This property allowed Chakravarty, Kopietz *et al.* to use a spin wave expansion to calculate $^{17}1/T_1$ at $T_N < T \ll J$ as [89, 87]

$$^{17} \left(\frac{1}{T_1} \right) = \frac{2\pi C^2 a}{3\hbar^2 c} \left(\frac{Ta}{\hbar c} \right)^3 \left[1 + C_o^{(2)} \left(\frac{T}{2\pi\rho_s} \right) + O(T^2) \right] \quad (5.21)$$

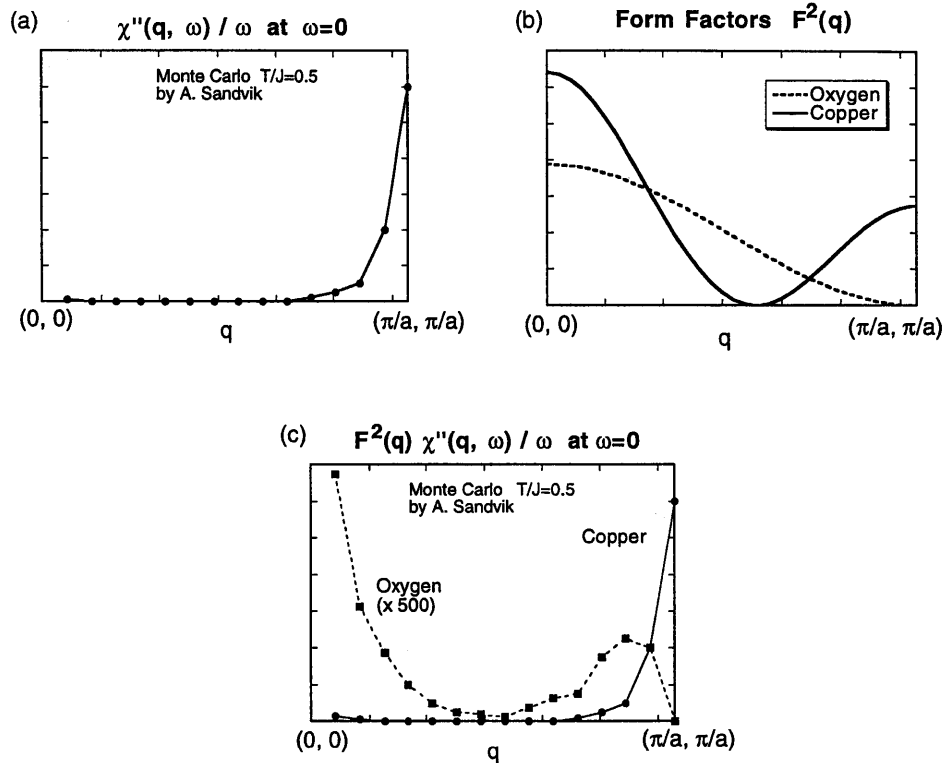


Figure 5-22: Quantum Monte Carlo results [67] showing (a) $\omega \rightarrow 0$ spin susceptibility $\chi(\omega)/\omega$, (b) Hyperfine form factors for Cu (solid line) and O (dashed line), (c) = (a)x(b) Contribution to $1/T_1$ for ^{63}Cu (solid line) and ^{17}O (dashed line). Contribution given by product of hyperfine form factor and spin susceptibility. All graphs shown for the line across the Brillouin zone $(q_x, q_y) = (q, q)$.

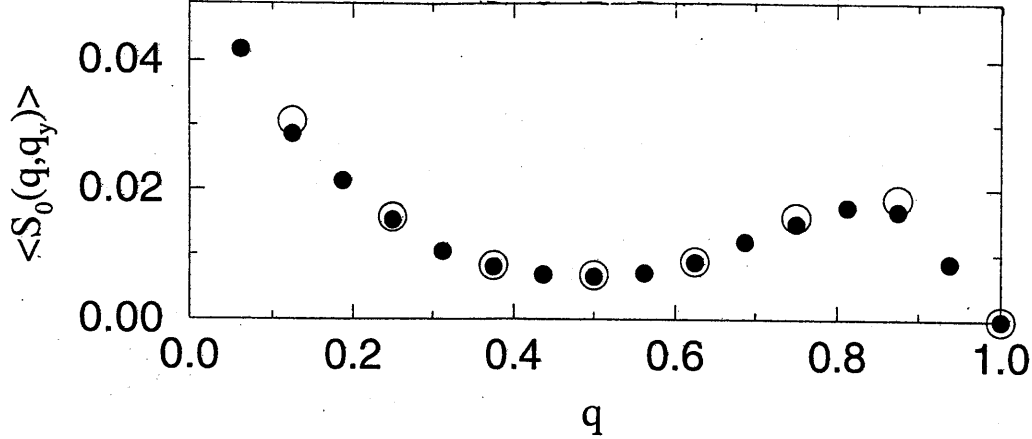


Figure 5-23: Monte Carlo results for the spin structure factor combined with the oxygen form factor, $S(0) \cos^2(q_x/2) \propto {}^{17}1/T_1$ [67]. Note that q_y has been summed over in order to show the contributions from the whole 2 dimensional Brillouin zone in this plot.

where $c = \sqrt{2}Z_cJa/\hbar$ is the spin wave velocity with $Z_c \approx 1.18$, and $C_o^{(2)} \approx -1.88$ [87]. This theoretical prediction is shown in figure 5-21 (solid line) together with a high temperature expansion (dashed line) by Singh and Gelfand [68] and Monte Carlo results (open squares) by Sandvik and Scalapino [67]. These parameter-free theoretical predictions agree well with our data.

Our results of ${}^{17}1/T_1$ indicate that free spin waves are indeed a good description of the quasi-particle excitations at short wavelengths even at $T \gtrsim T_N^{3d}$. Even without long range order, the short wavelength excitations can be described as free spin waves because of the significant short range order in the 2d Heisenberg antiferromagnet. Using the results for ${}^{17}1/T_1$, we can deduce the effective thermal damping Γ of the spin waves at finite temperatures from ${}^{17}1/T_1$ as follows. For damped spin waves, we can express $\chi''(\mathbf{q}, \omega)$ as,

$$\chi''(\mathbf{q}, \omega) = \chi'(\mathbf{q}) \left(\frac{\omega\Gamma(\mathbf{q})}{(\omega - \omega(\mathbf{q}))^2 + \Gamma(\mathbf{q})^2} + \frac{\omega\Gamma(\mathbf{q})}{(\omega + \omega(\mathbf{q}))^2 + \Gamma(\mathbf{q})^2} \right) \quad (5.22)$$

where $\omega(\mathbf{q}) = 2JZ_c\sqrt{1 - (\cos(q_x) + \cos(q_y))^2/4}$ is the spin wave dispersion ($\gg \omega_n$), and $\Gamma(\mathbf{q})$ represents the spin wave damping[20, 90, 69, 91]. The spin wave dispersion and damping for the 2d spin 1/2 Heisenberg antiferromagnet is shown in figure 5-24

as calculated by Makivić and Jarrell based on quantum Monte Carlo. For the \mathbf{q} -dependence of $\chi'(\mathbf{q})$, an isotropic spin wave calculation provides an analytical form [85],

$$\chi'(\mathbf{q}) = C \frac{1 + 4\xi^2}{1 + 2\xi^2(2 + \cos(q_x) + \cos(q_y))} \quad (5.23)$$

The normalization C is determined by using the results for the uniform susceptibility, $\chi'(\mathbf{q} = \mathbf{0})$, in figure 5-12. We should note that near $q = \pi$, both this form for $\chi'(\mathbf{q})$ and the renormalized classical form have the same Lorentzian q dependence.

Then the only unknown parameter in eq. 5.22 is $\Gamma(\mathbf{q})$. However, Monte Carlo results by Makivic and Jarrell (figure 5-24) and analytic results by Kopietz indicate that $\Gamma(\mathbf{q})$ shows little dependence on the wave vector \mathbf{q} in most of the Brillouin zone except near $\mathbf{q} = \mathbf{0}$ and \mathbf{Q} [90, 87]. Therefore, we let $\Gamma(\mathbf{q}) = \Gamma$ be independent of \mathbf{q} except for the regions near $\mathbf{q} = \mathbf{0}$ and \mathbf{Q} , and consider Γ as the wave vector averaged damping at short wavelengths. The \mathbf{q} -dependence of $\Gamma(\mathbf{q})$ used for the calculation is shown schematically in figure 5-25. Near $\mathbf{q} = \mathbf{Q}$ where the dynamical scaling form of the damping $\gamma(\mathbf{q})$ [69] satisfies $\gamma(\mathbf{q}) < \Gamma$, we let $\Gamma(\mathbf{q}) = \gamma(\mathbf{q})$.

$$\gamma(x) = \frac{1 + \mu(x)^2}{[1 + \theta \ln(1 + (x)^2)]^{3/2}} \quad (5.24)$$

where the scaling variable $x = (\mathbf{q} - \mathbf{Q})\xi$ and the parameters $\mu = 0.85$ and $\theta = 0.23$ [90]. This guarantees that *the same form of $\chi''(\mathbf{q}, \omega)$* used to fit $^{17}\text{1}/T_1$ reproduces the low temperature behavior ($T \ll J$) of $^{63}\text{1}/T_1$ as shown in figure 5-15, consistent with the earlier finding for La_2CuO_4 [7].

The other unusual region is for $\mathbf{q} \approx \mathbf{0}$. In the limit of $\mathbf{q} = \mathbf{0}$, eq.5.22 is not valid, instead we expect a diffusive contribution, $^{17}\text{1}/T_{1,diff} \propto (1/D(T)) \ln(1/\omega_n)$ [89]. However, Chakravarty *et al.* predicted that this contribution is small because the diffusion constant $D(T)$ diverges exponentially at low temperatures[65]. Experimentally, the value of $^{17}\text{1}/T_1$ for both $\text{Sr}_2\text{CuO}_2\text{Cl}_2$ and $\text{La}_{2-x}\text{Sr}_x\text{CuO}_4$ ($x = 0.035$) at room temperature was the same at 14.1 Tesla ($\omega_n = 81.4$ MHz), and 9 Tesla ($\omega_n = 52.0$ MHz), indicating no diffusive enhancement at 9 Tesla. Therefore, for the region near $\mathbf{q} = \mathbf{0}$, we neglect the contribution from $q < 1/\xi$. Monte Carlo calculations by Sandvik and

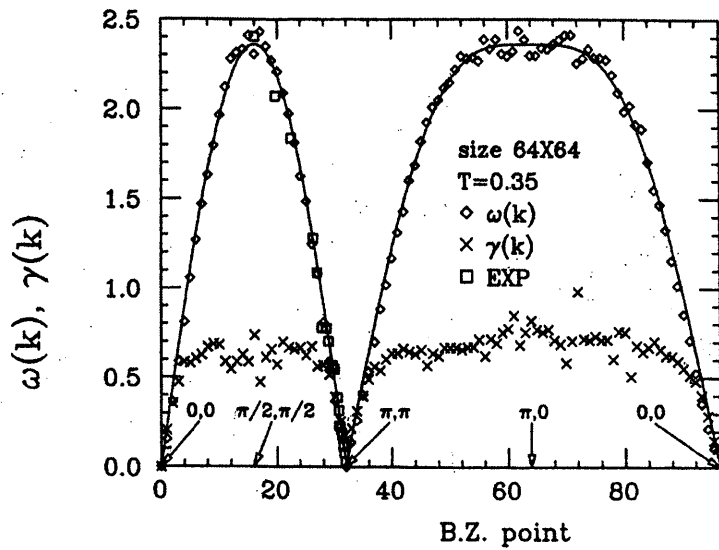


Figure 5-24: Quantum Monte Carlo results for spin-wave frequencies ($\omega(k)$, \diamond) and damping ($\gamma(k)$, \times) by Makivic and Jarrell [90].

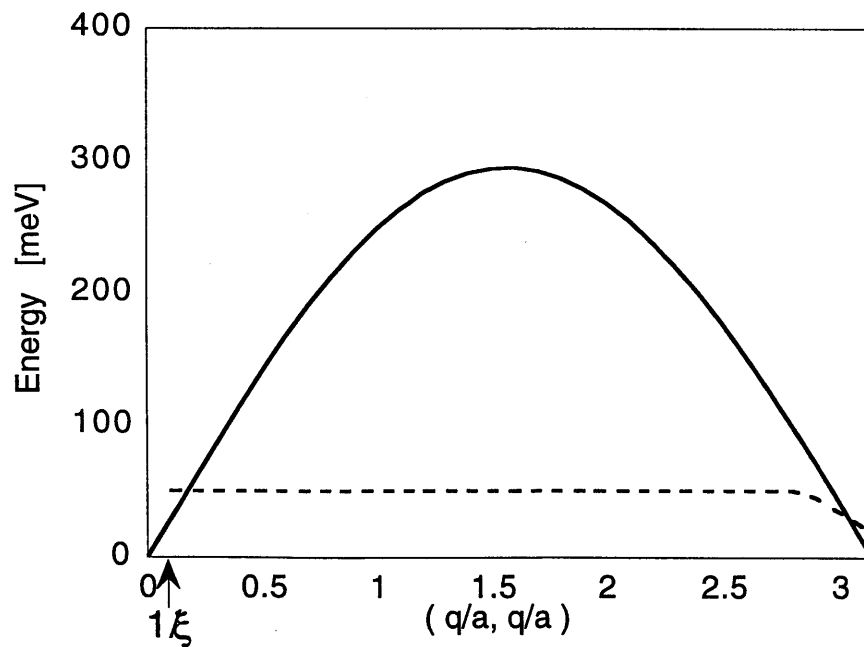


Figure 5-25: Wavevector dependence of $\Gamma(\mathbf{q})$ used in calculations (dashed line). Spin wave energies shown by solid line.

Scalapino[67] indicate that this contribution is $\lesssim 25\%$ at $T = 0.5J$ and decreases with lowering temperature ($\lesssim 10\%$ at $T = 0.4J$). Including this contribution would lower our calculated value of the damping Γ by the amount of the contribution (but within the error bars).

The fact that $q = 0$ diffusive contributions do not dominate oxygen $1/T_1$ in 2d is one clear difference between the low energy spin excitations of the 2 dimensional and 1 dimensional Heisenberg antiferromagnets. For the 1d magnetism discussed in the previous chapter, we found that $q = 0$ diffusive behavior was significant for oxygen $1/T_1$. Here, in 2 dimensions, we find that $q = 0$ is at most a minor contribution, and the short wavelength region in between $q = 0$ and $q = \pi$ is significant because of the greater phase space available in the 2 dimensional area of the wavevector space. This contrast between 2d and 1d can be seen graphically in the comparison of the Monte Carlo results of Sandvik, *et al.* (figure 5-23 2d and figure 4-19 1d) [67, 21].

Essentially, we are measuring the damping Γ by the fact that the size of the tail of $\chi''(\mathbf{q}, \omega)$ at $\omega = \omega_n \approx 0$ is determined by the energy width Γ . This is illustrated in figure 5-26. In the short wavelength region, the peak of $\chi''(\mathbf{q}, \omega)$ is at high energies. $1/T_1$ measures the contribution at very low energies ($\sim 10^{-4}$ K), so a large width Γ provides more contribution at low energy. The energy width, Γ , increases the low energy contributions by broadening the peak of $\chi''(\mathbf{q}, \omega)$. The contribution to $171/(T_1T)$ is $\propto \Gamma$ for the short wavelength region. We note that the deviation of $\chi''(\mathbf{q}, \omega)$ from the Lorentzian form of eq.5.22 can change our estimate of the magnitude of Γ , but this does not affect the conclusions. For example, using a squared Lorentzian form for $\chi''(\mathbf{q}, \omega)$ barely changes the half-width Γ of $\chi''(\mathbf{q}, \omega)$ derived from ^{17}O for $T \geq 500$ K, though the derived Γ increases up to a factor ~ 3 at the lowest temperatures.

We plot the temperature dependence of Γ deduced from eq. 5.22 in Fig. 5-27. We emphasize two key findings. First, the damping Γ is smaller than the highest excitation energy $\omega(\mathbf{q}) \approx 0.3$ eV[20] of the short wavelength magnons in the entire temperature range we studied. This observation establishes that magnons are well defined (long lifetime) elementary excitations for short wavelengths even in the paramagnetic state up to $T \approx 0.4J$ in S=1/2 2d quantum Heisenberg antiferromagnets.

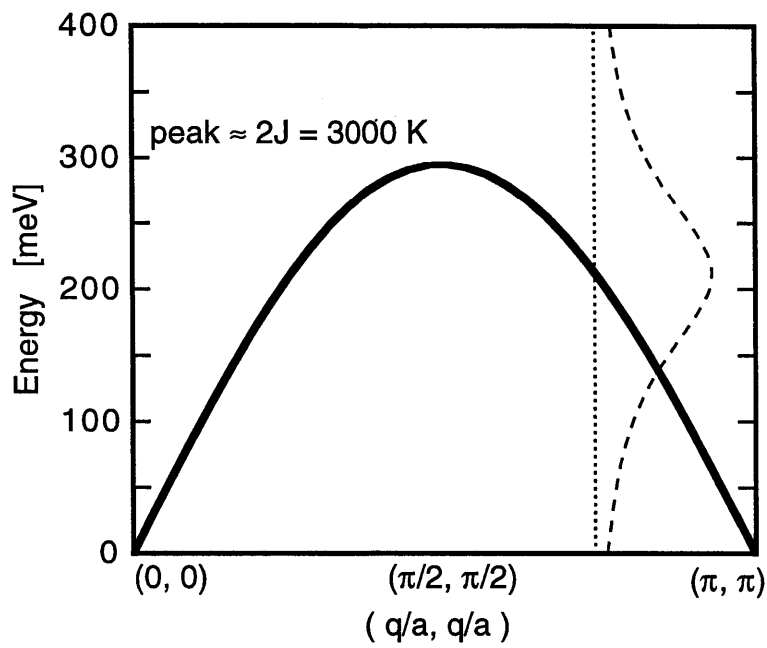


Figure 5-26: Solid line marks the peak of spin wave energy spectrum for wavevector $\mathbf{q} = (q, q)$. Dashed line shows the ω dependence of the dynamic susceptibility $\chi''(\mathbf{q}, \omega)$ with width $\Gamma = 80$ meV for $\mathbf{q} = (3\pi/4, 3\pi/4)$ (The zero of dynamic susceptibility is indicated by the dotted line)

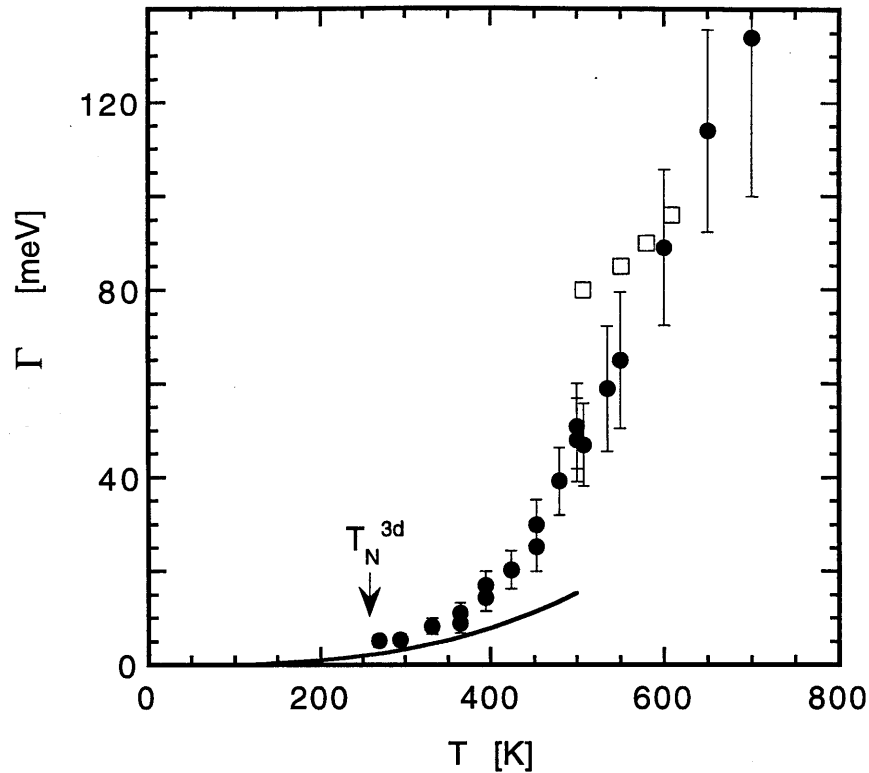


Figure 5-27: Spin wave damping, Γ , for $\text{Sr}_2\text{CuO}_2\text{Cl}_2$ estimated from $^{171}\text{T}_1$ (●). Solid line - low temperature expansion [87], □ Monte Carlo [90].

Second, the value of Γ is in good agreement with theoretical predictions based on low temperature analytic calculations, $\hbar\Gamma \sim 3J(T/J)^3$, and high temperature Monte Carlo simulations [87, 90].

We should mention that in addition to the damping, Γ , changing as a function of temperature, the peak of the magnon dispersion, $\omega(\mathbf{q})$, may also change with temperature. Our calculations kept the peak of the magnon dispersion fixed as a function of temperature. A second note about these results is that since $1/T_1$ measures the low energy excitations, we are measuring the damping Γ as seen from the low energy side of the magnon dispersion. Thus, our results do not exclude the possibility of a “spinon” continuum on the higher energy side of $\omega(\mathbf{q})$ (as is seen for example, in 1 dimension, figure 4-19).

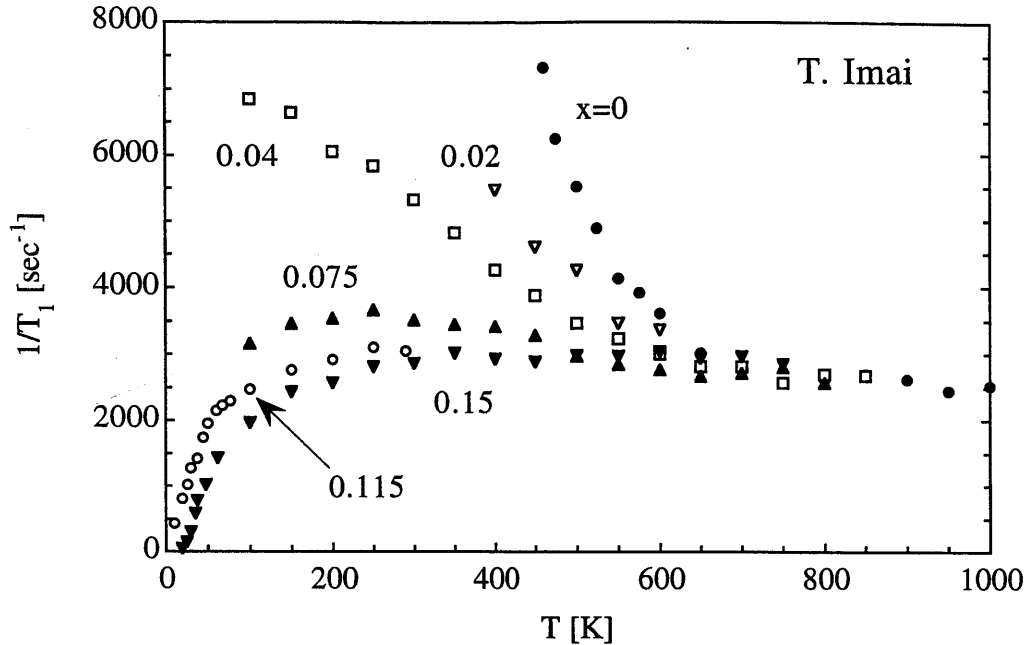


Figure 5-28: $^{63}(1/T_1)$ for $\text{La}_{2-x}\text{Sr}_x\text{CuO}_4$ [7]. $x=0$ ●, $x=0.02$ ▽, $x=0.04$ □, $x=0.075$ ▲, $x=0.115$ ○, $x=0.15$ ▼.

5.6 Doped CuO_2 planes

Next, we would like to address another fundamental question; how do the elementary excitations evolve when we dope holes into the CuO_2 planes and transform the system to metallic behavior? Figures 5-28[7] and 5-29 show the doping dependence of copper and oxygen $1/T_1$. $\text{Cu } ^{63}1/T_1$ is dominated by the long-wavelength spin fluctuations around $\mathbf{q} = \mathbf{Q}$. $\text{Cu } ^{63}1/T_1$ increases at low temperatures from the critical slowing down of the spin fluctuations with short range ordering. This behavior persists even for doping levels where superconductivity occurs ($x = 0.075$, $T_c = 23$ K). Also notable is the fact that the high temperature constant $^{63}1/T_1$ is independent of doping within $\sim 12\%$.

$^{17}1/T_1$ is better suited to probing the excitations of the doped materials, because ^{17}O NMR may be sensitive to the electron-hole pair excitations at the Fermi surface, while $^{63}1/T_1$ is dominated by the divergently large, long-wavelength collective spin dynamics at $\mathbf{q} \approx \mathbf{Q}$. The measurements of $^{17}1/(T_1T)$ in hole-doped $\text{La}_{2-x}\text{Sr}_x\text{CuO}_4$ ($x = 0.025$ and 0.035) [93] were conducted by A.W. Hunt and T. Imai, and are

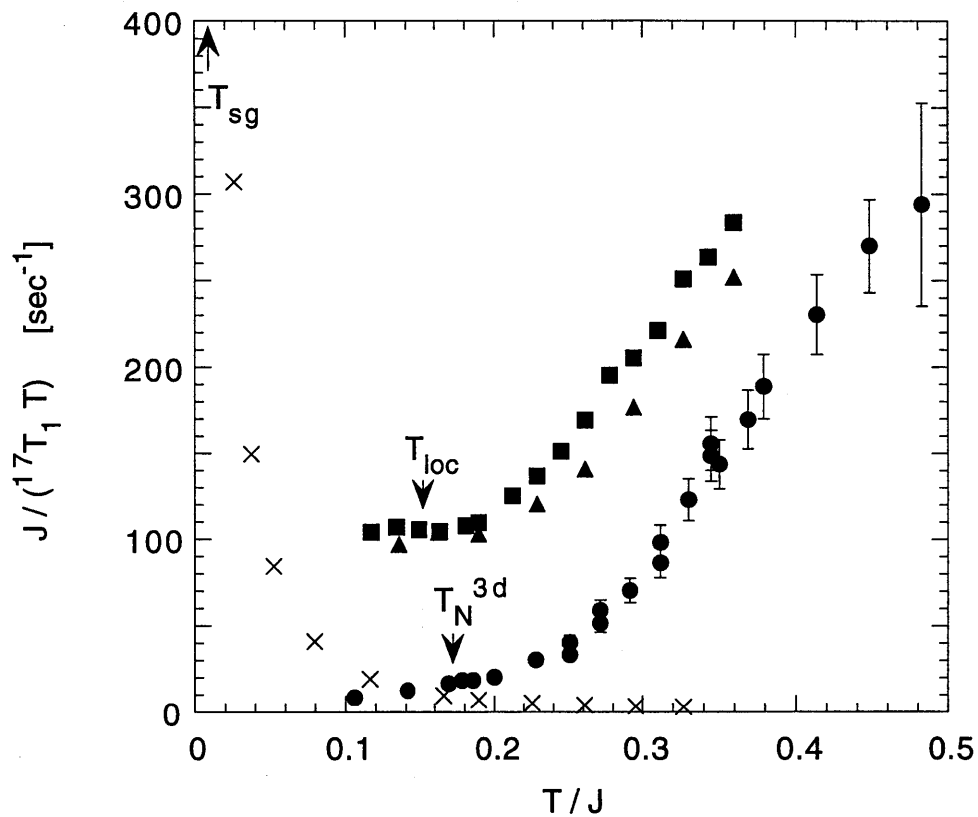


Figure 5-29: $^{17} J/(T_1 T)$ for undoped $\text{Sr}_2\text{CuO}_2\text{Cl}_2$ (●) and for $\text{La}_{2-x}\text{Sr}_x\text{CuO}_4$ planar oxygen sites ($x=0.025$ ▲, $x=0.035$ ■) and apical oxygen sites ($x=0.035$ ×).

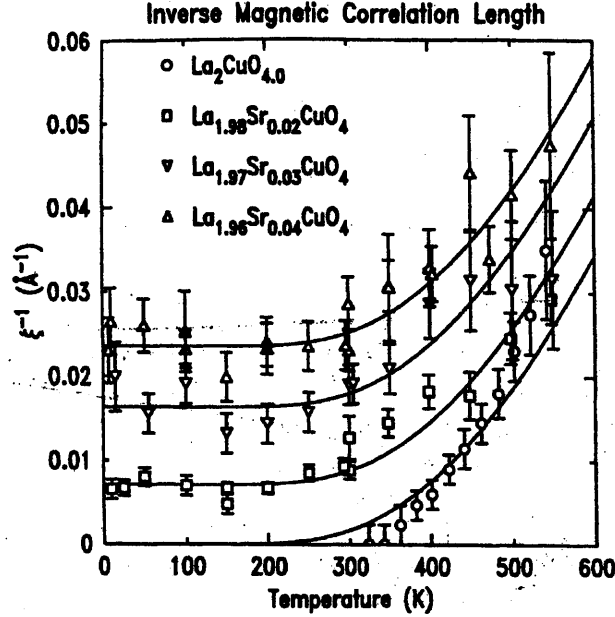


Figure 5-30: Inverse of spin correlation length, ξ^{-1} , for lightly doped $\text{La}_{2-x}\text{Sr}_x\text{CuO}_4$ measured by neutron scattering (Keimer, *et al.*) [92].

compared with the results of undoped $\text{Sr}_2\text{CuO}_2\text{Cl}_2$ in figure 5-29. At these doping levels, previous studies established that the resistivity is linear in temperature down to $T_{loc} (< 300 \text{ K})$ [94, 92], where holes begin to localize, followed by the spin-glass transition at $T_{sg} (\approx 10 \text{ K})$ [95, 96]. We identified T_{loc} as $\approx 250 \text{ K}$ from the onset of the dramatic increase of $^{17}\text{I}/T_{1,Apex}$ at the apical oxygen sites. At T_{sg} , $^{17}\text{I}/T_{1,Apex}$ diverged (see Fig. 5-29 for the results observed for $x=0.035$). In what follows, we will focus our attention on the temperature dependence of $^{17}\text{I}/(T_1T)$ at the planar site above T_{loc} , where carriers are mobile and resistivity is roughly proportional to temperature.

The temperature dependence of $^{17}\text{I}/(T_1T)$ is surprisingly similar for the undoped and lightly hole-doped samples, but with a weakly temperature dependent increase of $^{17}\text{I}/(T_1T)$ for the doped samples. We estimate this increase as $^{17}\text{I}/(T_1T)_{e-h} = 0.05 \sim 0.065 \text{ sec}^{-1}\text{K}^{-1}$ and $0.06 \sim 0.085 \text{ sec}^{-1}\text{K}^{-1}$ for $x=0.025$ and 0.035 , respectively. It is also interesting to recall that Reven *et al.* observed $^{17}\text{I}/(T_1T) \approx 0.4 \text{ sec}^{-1}\text{K}^{-1}$ at $T \lesssim 300\text{K}$ in optimally doped $\text{La}_{1.85}\text{Sr}_{0.15}\text{CuO}_4$ [97]. The increase in

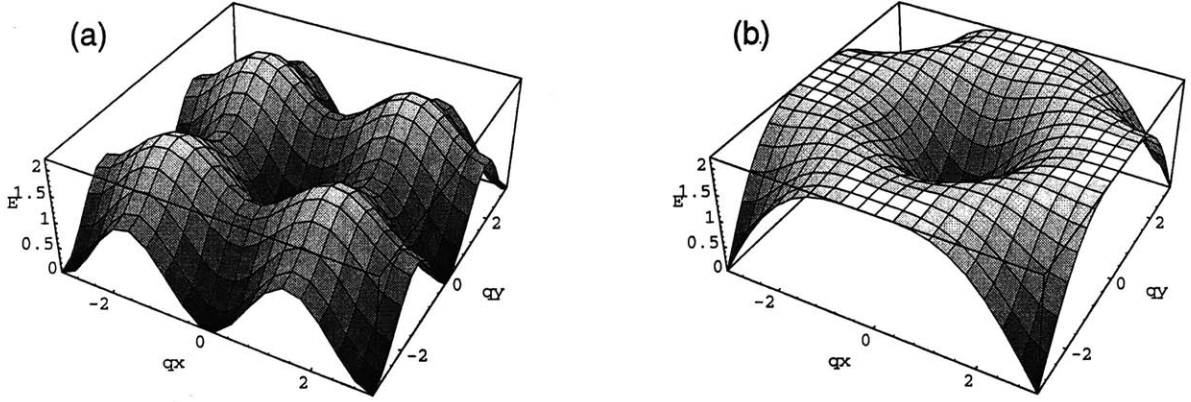


Figure 5-31: (a) Energy of electron-hole pair (Stoner) excitations and (b) Energy of spin wave excitations as a function of wavevector \mathbf{q} . Energy scale is in units of the exchange interaction, J . (calculation for part a by Allen Hunt.)

$^{17}1/(T_1T)$ appears to be proportional to the amount of hole-doping x . Angle resolved photo emission experiments for undoped $\text{Sr}_2\text{CuO}_2\text{Cl}_2$ by Wells *et al.* show that the highest occupied band is peaked at $\mathbf{q} = (\pm\pi/2a, \pm\pi/2a) = \mathbf{Q}/2$ with a bandwidth $(2.2 \pm 0.5)J$ [98]. Therefore, the simplest interpretation is that the electron-hole pair (Stoner) excitations with wave vectors, $(0, 0)$, $(\pm\pi/a, 0)$, $(0, \pm\pi/a)$, $(\pm\pi/a, \pm\pi/a)$, connecting the hole pockets at $\mathbf{Q}/2$ give rise to an additional contribution to $^{17}1/(T_1T)$ without changing the spin wave contribution. However, our calculations (see figure 5-31) based on the rigid band picture showed that the Stoner continuum is very close to the spin wave dispersion over most of the Brillouin zone except near $\mathbf{q} = (\pm\pi/a, 0)$ and $(0, \pm\pi/a)$ because the width of the spin wave dispersion $\approx 2.36J$ is within experimental error equal to the bandwidth, $(2.2 \pm 0.5)J$. The conventional wisdom for the spin waves in metals is that the electron-hole pair excitations damp the spin waves if the dispersion of the spin wave merges into the Stoner continuum[99]. This suggests that the magnons and the electron-hole pair excitations will interact strongly, perhaps resulting in complete renormalization of the damping, $\Gamma(\mathbf{q})$. We note that the temperature T and doping x dependence of $^{17}1/(T_1T)$ is quite similar to that of $1/\xi(T, x)$ observed by Keimer *et al.*[92] (figure 5-30). Knowing that $^{17}1/(T_1T) \propto \Gamma$, comparison of figures 5-29 and 5-30 suggests the speculation that the renormalized quasi-particle damping, $\Gamma(T, x)$, is related to $\xi(T, x)$ as $\Gamma(T, x) \propto c/\xi(T, x)$.

5.7 2d summary

To summarize, we deduced the effective damping Γ of the short wavelength magnons of the $S = 1/2$ 2d Heisenberg antiferromagnet in a broad range of temperature ($0.2 \leq T/J \leq 0.5$), contrary to the prevailing perception in the community that Γ was not measurable with current technology [3]. Our results establish the temperature dependence of the spin wave damping. These experiments demonstrate an interesting property of the 2d Heisenberg antiferromagnet: there is significant short range order without long range order. The short wavelength spin waves are very weakly damped over a wide temperature range even though there is not long range order.

The low energy excitations in the hole-doped, weakly-metallic CuO_2 planes show a similar temperature dependence to the undoped sample, but with a weakly temperature dependent increase from the addition of electron-hole pair excitations. We suggest that the spin waves may interact strongly with electron-hole pair excitations.

Chapter 6

2-leg Spin Ladders

Spin ladders consist of several 1 dimensional chains with antiferromagnetic exchange interaction, $J_{\parallel} \approx 1500$ K, coupled by an interchain antiferromagnetic exchange interaction, J_{\perp} , as shown in figure 6-1, forming a structure that is in between the single 1 dimensional chain and a 2 dimensional plane. However, because of the quantum nature of the spins, the magnetic properties of spin ladders do not vary continuously between 1-d and 2-d. Instead, as predicted by Haldane [100], the properties of spin 1/2 spin ladders depend on whether the number of coupled chains (legs of the ladder) is even or odd. For an even number of coupled chains, the ground state is a many-body singlet state [101, 102, 36]. This many-body singlet state has been theoretically described as a resonance valence bond (RVB) state [101]. The spin singlet formation of the resonance valence bond state was originally proposed for T_c superconductors by P. Anderson [103, 104]. Studying the effect of doping on the spin singlet state in the two-leg ladder may indicate whether this mechanism is also involved in the doped 2d materials. The origin of the singlet state in the two-leg ladder is clear in the strong coupling limit where $J_{\perp} \gg J_{\parallel}$. In this case, the two spins $S=1/2$ coupled on each rung of the ladder will form a singlet ground state. Above this ground state, the excitation spectrum is gapped. Perhaps surprisingly, the singlet ground state with an energy gap still persists even with $J_{\parallel} \geq J_{\perp}$ [36, 105, 30]. For the two-leg spin ladder, the minimum of the energy gap, the spin gap Δ is $\sim 0.5J_{\perp}$, and is at the antiferromagnetic wavevector, $q = (\pi, \pi)$ (see figures 6-2 and 6-3) [101, 105]. In contrast, for

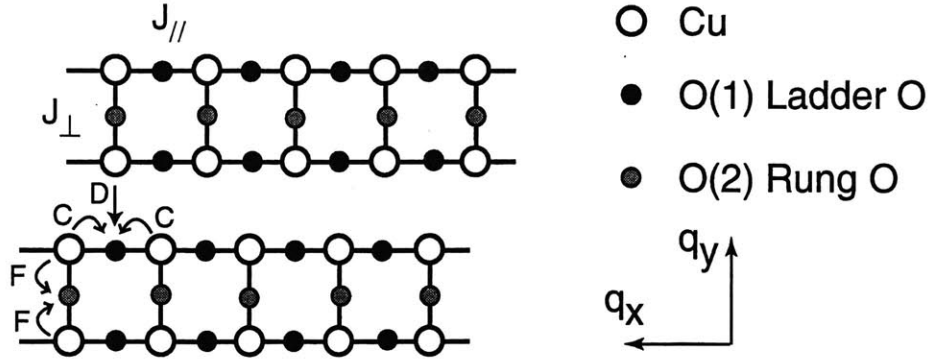


Figure 6-1: Structure of Cu-O layer for 2 leg ladder materials. The two oxygen sites are labeled: O(1) ladder site, and O(2) rung site. Hyperfine couplings between the Cu electron spin and the oxygen nuclear spin are marked.

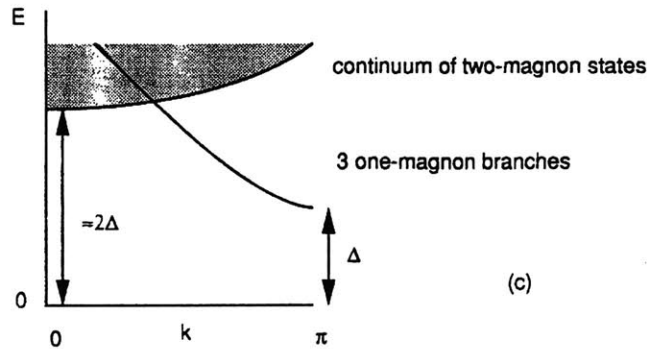


Figure 6-2: Qualitative picture of magnon dispersion of the 2 leg ladder for $J_{\parallel} = J_{\perp}$. Note spin gap Δ at $q = \pi$. (from Troyer, Tsunetsugu, and Wurtz [105])

an odd number of coupled chains, there is no spin excitation energy gap. Thus, spin ladders with even or odd numbers of legs have different magnetic properties. Besides the study of these quantum magnetic properties, interest in the two-leg spin ladder has increased with the discovery of superconductivity at 12 K under high pressure in hole-doped $A_{14}Cu_{24}O_{41}$ [106].

In this chapter, NMR/NQR experiments on undoped and doped two-leg $S=1/2$ spin ladder materials, $SrCu_2O_3$ and $A_{14}Cu_{24}O_{41}$ ($A = La, Sr, Ca$), are described. Previous Cu NMR and NQR measurements have been reported for $SrCu_2O_3$ [108] and $A_{14}Cu_{24}O_{41}$ [109, 110, 111, 112, 113]. However, because the spin gap Δ is generally ≥ 300 K for these materials, the earlier experiments mostly probed the properties in the low temperature limit below the spin gap temperature. Estimates of the spin

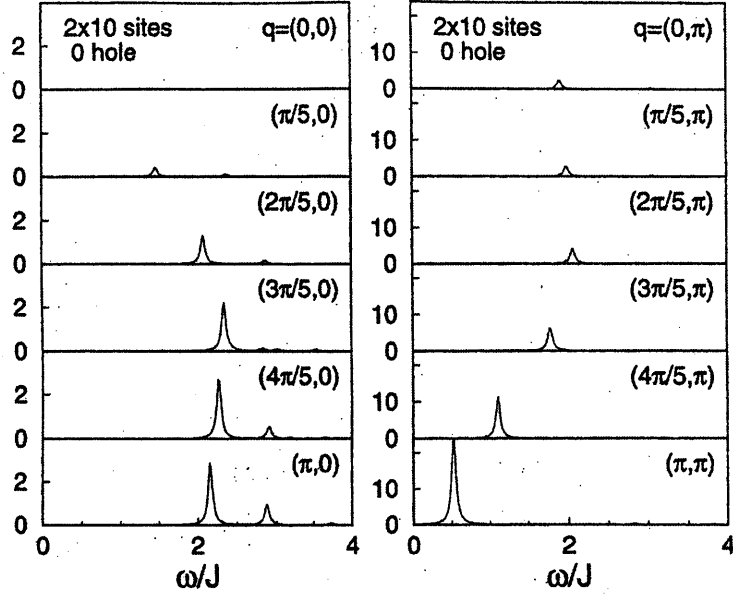


Figure 6-3: Dynamical spin structure factor, $S(q, \omega)$, for the undoped 2 leg ladder. Note that the lowest energy excitations are at $q = (\pi, \pi)$ with energy $\sim 0.5J$. (Calculated for a 10 rung ladder using Lanczos diagonalization in Troyer, Tsunetsugu, and Rice [101].)

gap Δ were obtained from fitting the NMR results to exponential activated behavior, $\exp(-\Delta/k_B T)$. However, the resulting estimates of the spin gap, Δ , differed by 50% between susceptibility and $1/T_1$ measurements [108]. Experiments to clearly show the crossover from the low temperature spin-gapped regime to the high temperature regime were needed.

Reported here are the first ^{17}O NMR results as well as ^{63}Cu NMR/NQR not only in the gapped low temperature regime, but also in the high temperature paramagnetic regime. We can demonstrate the crossover in spin dynamics from temperatures below the spin gap to temperatures above the spin gap. Comparison of Cu and O NMR results provides wave vector dependent information about spin excitations. Oxygen NMR can also allow us to estimate J_{\perp}/J_{\parallel} . In the doped two-leg ladder materials, $\text{A}_{14}\text{Cu}_{24}\text{O}_{41}$, the crossover of the spin excitations from the spin gapped regime to the paramagnetic regime is accompanied by changes in the charge properties.

6.1 Structure & Experimental Details

For the experiments on undoped 2-leg ladder, we used a polycrystalline sample of SrCu_2O_3 that was prepared using high pressure synthesis at Kyoto University. The structure of SrCu_2O_3 is shown in figure 6-4. This material has stacked Cu_2O_3 two-leg ladder layers separated by Sr ions. Even though SrCu_2O_3 is an ideal 2-leg ladder, hole-doping this material is very difficult.

To look at the properties of two-leg ladders as a function of hole doping, the $\text{A}_{14}\text{Cu}_{24}\text{O}_{41}$ material was used which has a much more complicated structure. Fortunately, the physical properties of undoped Cu_2O_3 layers in $\text{La}_6\text{Ca}_8\text{Cu}_{24}\text{O}_{41}$ are virtually identical with those of SrCu_2O_3 as we demonstrate below. The $\text{A}_{14}\text{Cu}_{24}\text{O}_{41}$ material was studied with several different combinations, $\text{A}_{14} = \text{La}_6\text{Ca}_8, \text{Sr}_{14}, \text{Sr}_{11}\text{Ca}_3,$ and Sr_6Ca_8 . $\text{La}_6\text{Ca}_8\text{Cu}_{24}\text{O}_{41}$ is an undoped material, with a nominal copper valence of 2+. Because the $\text{A}_{14}\text{Cu}_{24}\text{O}_{41}$ material has both a Cu_2O_3 two-leg ladder layer and a CuO_2 chain layer (figure 6-5), the doped holes could reside in either layer. The amount of doping (P_L) in the two-leg ladder layer of this material has been studied by optical conductivity [114] with estimates for $\text{Sr}_{14}\text{Cu}_{24}\text{O}_{41}$ ($P_L \sim 0.06$ per ladder Cu site), $\text{Sr}_{11}\text{Ca}_3\text{Cu}_{24}\text{O}_{41}$ ($P_L \sim 0.12$), and $\text{Sr}_6\text{Ca}_8\text{Cu}_{24}\text{O}_{41}$ ($P_L \sim 0.17$) at 300 K. Since the expected valence of Sr (2+) and Ca (2+) are the same, substituting Ca for Sr does not change the total number of holes in the material. However, the smaller ionic radius of Ca causes the lattice parameters to decrease with Ca doping [115] which transfers some of the holes to the ladder layer.

Single crystal samples of $\text{La}_6\text{Ca}_8\text{Cu}_{24}\text{O}_{41}$ and $\text{Sr}_{14}\text{Cu}_{24}\text{O}_{41}$ were grown at MIT by Dr. F.C. Chou using the floating zone technique. For $\text{Sr}_{11}\text{Ca}_3\text{Cu}_{24}\text{O}_{41}$ and $\text{Sr}_6\text{Ca}_8\text{Cu}_{24}\text{O}_{41}$, polycrystalline powder samples were uniaxially aligned in epoxy along the b axis by K.M. Shen. As shown in figure 6-5, $\text{A}_{14}\text{Cu}_{24}\text{O}_{41}$ has two copper-oxide layers, a Cu_2O_3 two-leg ladder layer and a CuO_2 chain layer. Because NMR/NQR is a local probe, we can separately detect the NMR signal from the ladder and chain Cu sites and the O(1) ladder and O(2) rung sites, as shown in figure 6-1, and from the additional oxygen site in the CuO_2 chain layer [112]. To illustrate the different

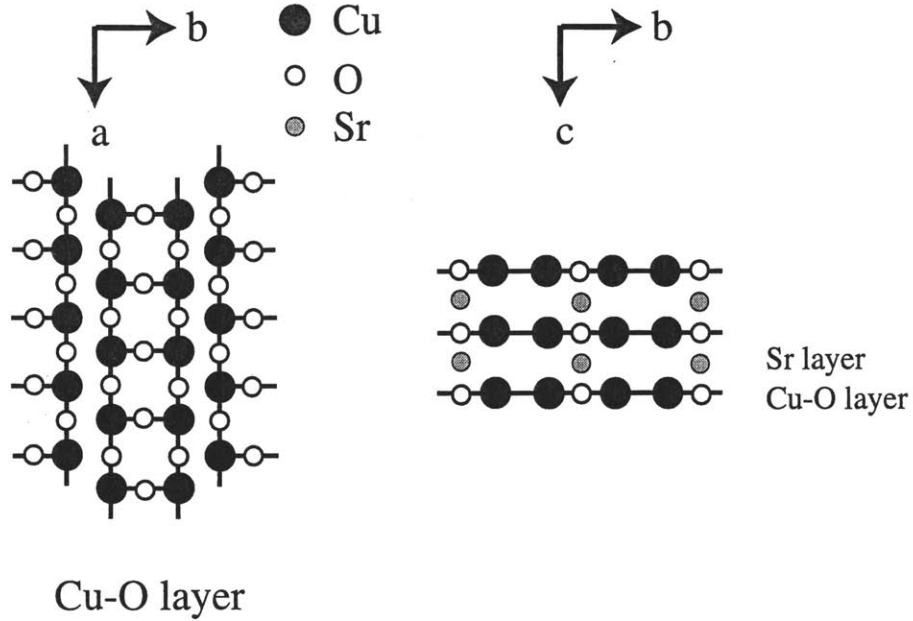


Figure 6-4: Crystal structure of SrCu_2O_3 . Cu-O layers with the 2-leg ladder structure are separated by Sr layers.

NMR/NQR signals from different crystal sites, figures 6-6 and 6-7 show examples of Cu and O NMR lineshapes for $\text{A}_{14}\text{Cu}_{24}\text{O}_{41}$ and figure 6-8 shows the ^{63}Cu NQR lineshape for SrCu_2O_3 . The samples of $\text{A}_{14}\text{Cu}_{24}\text{O}_{41}$ were enriched with ^{17}O isotope by annealing in $^{17}\text{O}_2$ gas at 900°C . Most of the NMR experiments were done in 7 or 9 T magnetic field. Many of the experiments on $\text{A}_{14}\text{Cu}_{24}\text{O}_{41}$ were conducted by Kyle Shen for his undergraduate thesis and also by Prof. Takashi Imai [107].

6.2 Knight shift

In figure 6-9, the ^{17}O Knight shift for the $\text{A}_{14}\text{Cu}_{24}\text{O}_{41}$ materials is presented. The Knight shift is a local probe of the uniform susceptibility, χ_L , of the Cu_2O_3 ladder layer, while bulk susceptibility measurements are dominated by the CuO_2 chain layer because of the order of magnitude smaller J of the chains. A prediction for the uniform susceptibility of the undoped two-leg ladder was made by Troyer, *et al.* [101]

$$\chi_L(T) \propto \frac{1}{\sqrt{T}} \exp\left(\frac{-\Delta_\chi}{k_B T}\right) \quad (6.1)$$

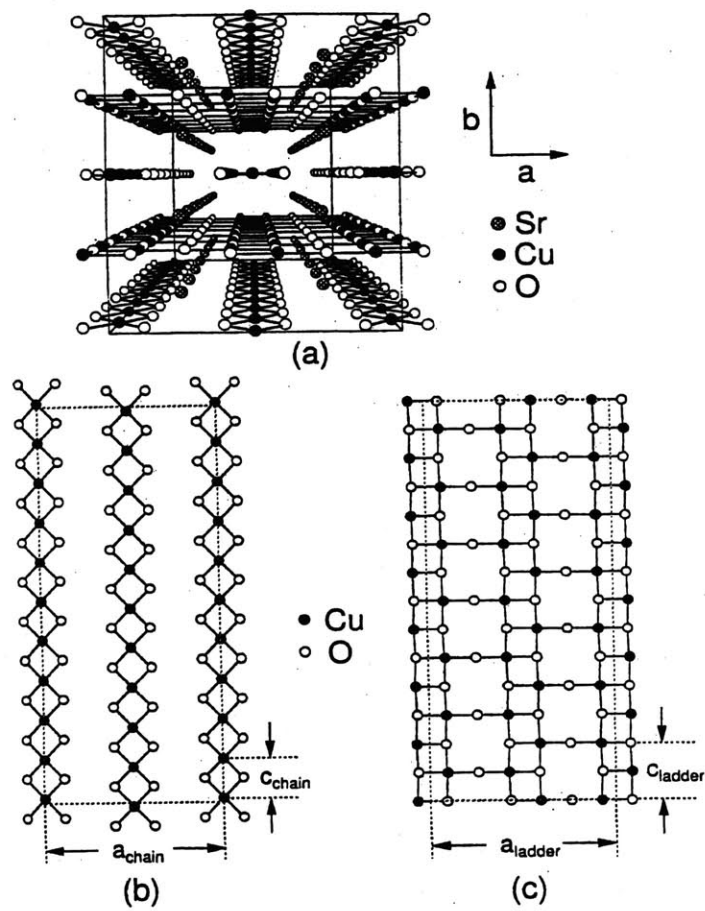


Figure 6-5: Crystal structure of $\text{Sr}_{14}\text{Cu}_{24}\text{O}_{41}$. (a) Complete crystal structure showing ladder Cu_2O_3 and chain CuO_2 layers separated by Sr layers. (b) CuO_2 chain layer. (c) Cu_2O_3 2-leg ladder layer.

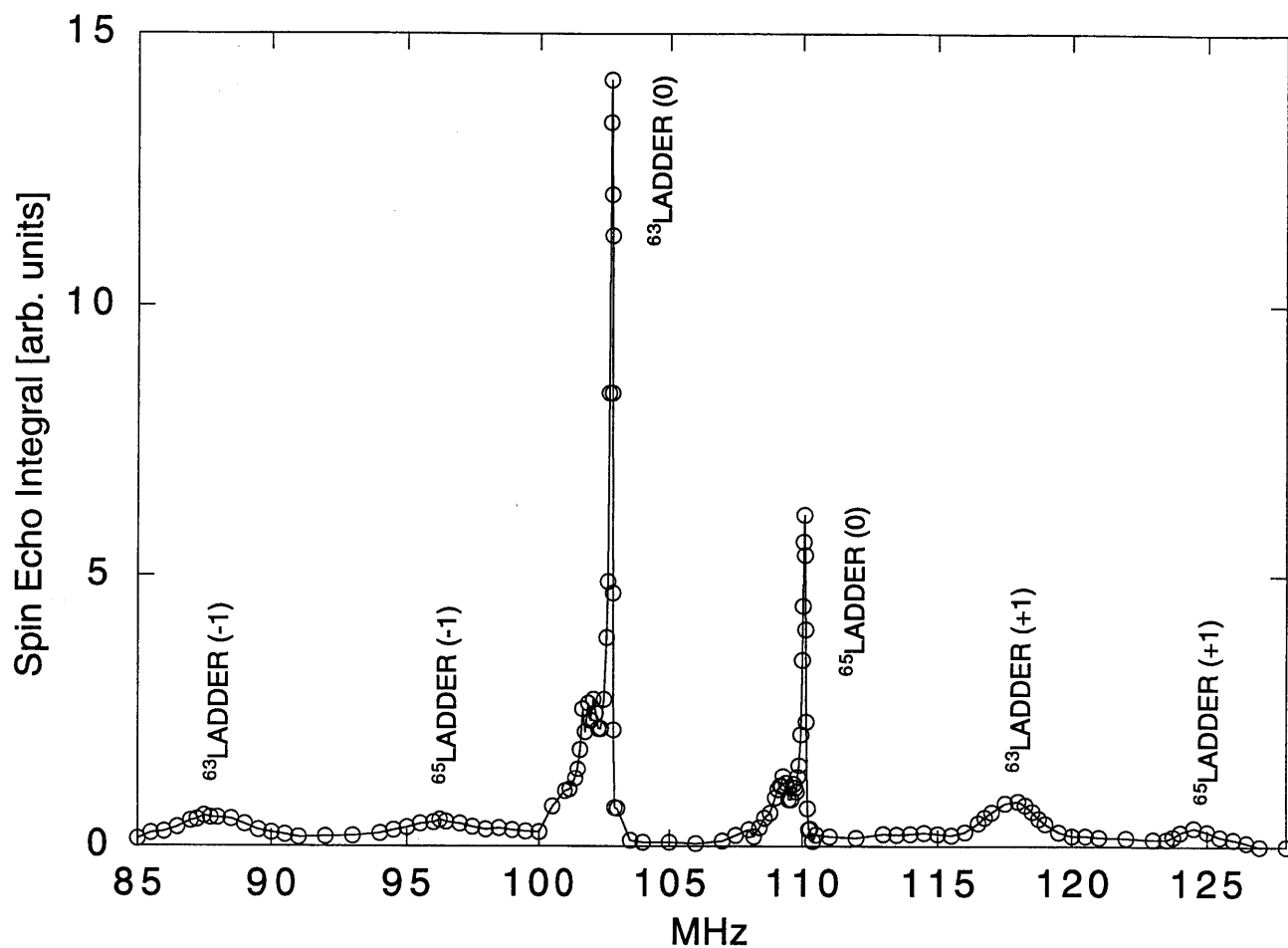


Figure 6-6: Cu NMR lineshape of $\text{Sr}_{11}\text{Ca}_3\text{Cu}_{24}\text{O}_{41}$ at 300 K. $H = 9$ Tesla \parallel b axis, aligned powder

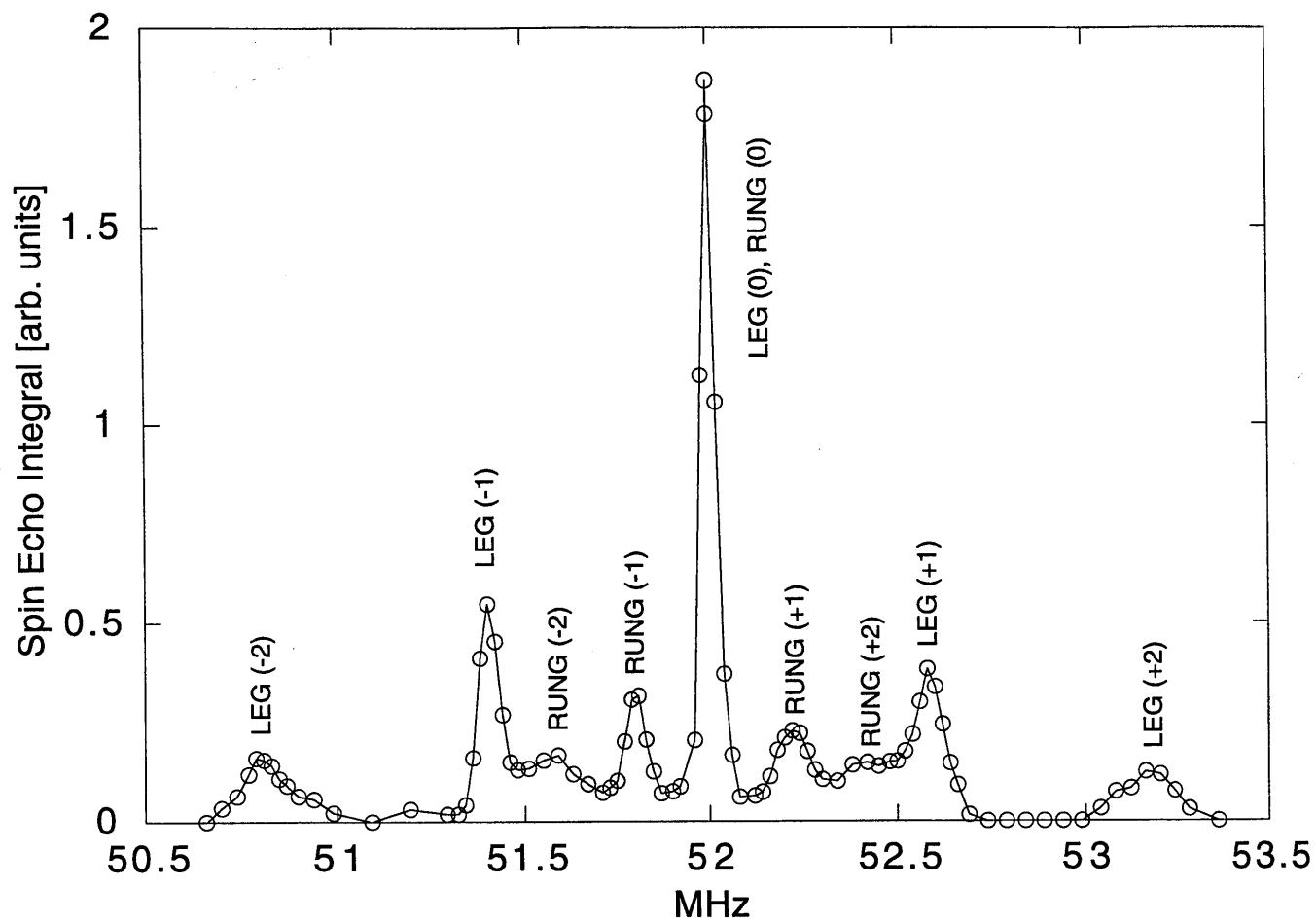


Figure 6-7: O NMR lineshape of $\text{Sr}_6\text{Ca}_8\text{Cu}_{24}\text{O}_{41}$ showing O(1) ladder and O(2) rung sites at 300 K. $H = 9$ Tesla \parallel b axis, aligned powder

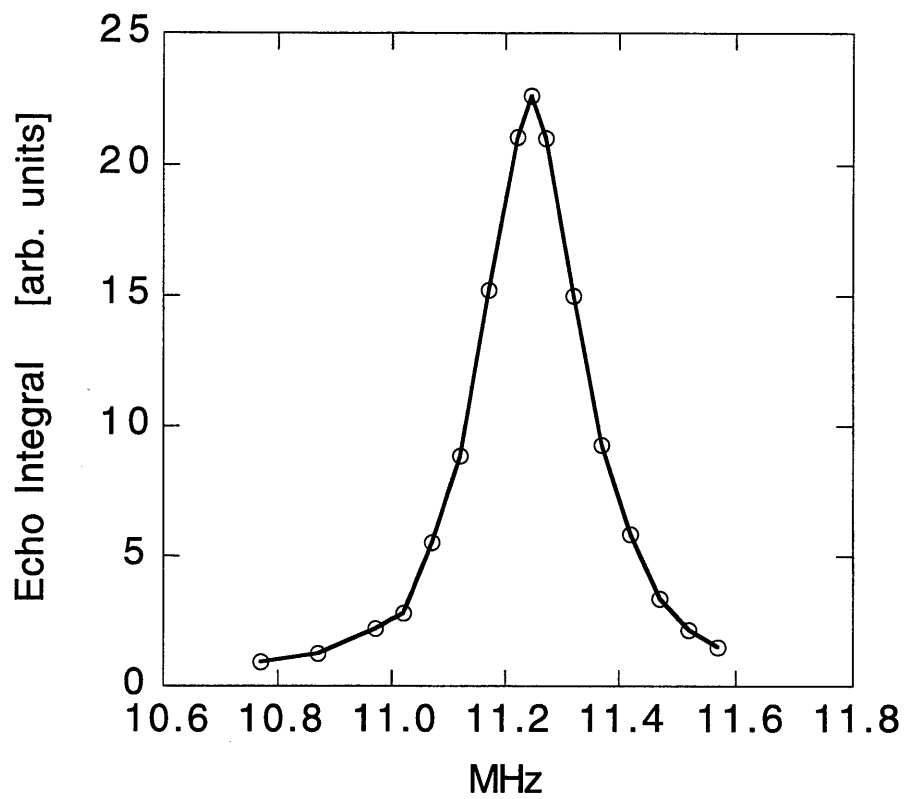


Figure 6-8: ^{63}Cu NQR lineshape of SrCu_2O_3 observed at room temperature.

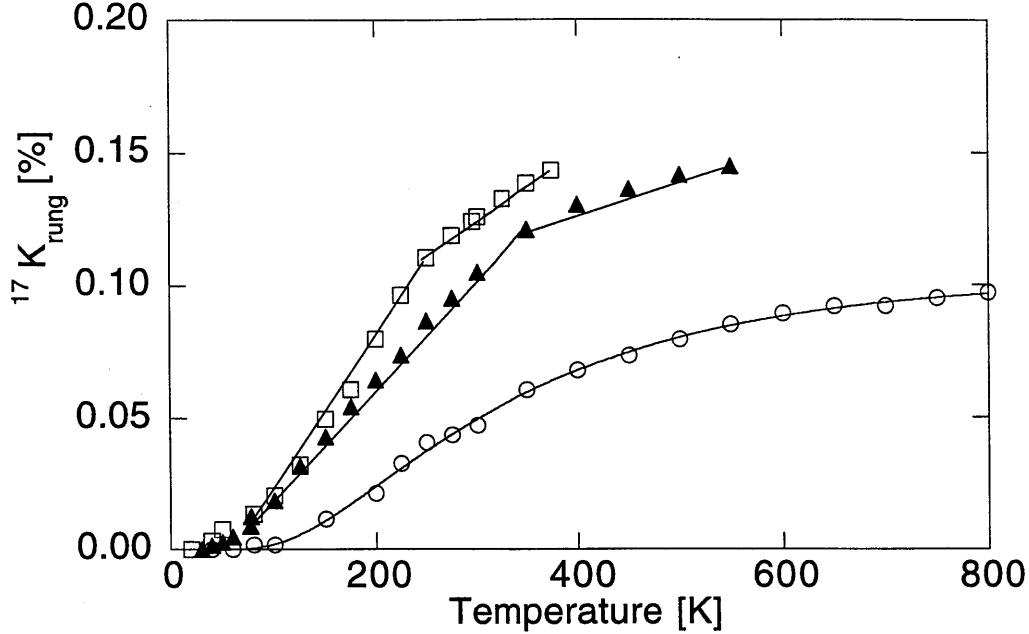


Figure 6-9: $^{17}\text{O}(2)$ rung site Knight shift for undoped $\text{La}_6\text{Ca}_8\text{Cu}_{24}\text{O}_{41}$ [\circ], and $\text{Sr}_{14}\text{Cu}_{24}\text{O}_{41}$ [\triangle] and $\text{Sr}_{11}\text{Ca}_3\text{Cu}_{24}\text{O}_{41}$ [\square].

This expression fits the Knight shift data well and results in $\Delta_\chi = 510 \pm 40$ K. This value of Δ_χ is somewhat larger than $\Delta_\chi = 420$ K deduced by Azuma et al. [29] for SrCu_2O_3 from a bulk susceptibility measurement.

For the doped materials, the Knight shift increases strongly with temperature for lower temperatures, and has a change in the slope of the temperature dependence at higher temperatures. This change in the temperature dependence casts doubt on the validity of a fit based on Troyer's expression for the undoped ladder. Still, we can identify the onset of the saturating tendency of $^{17}\text{K}(1,2)^{\text{spin}}$ as the spin gap Δ_χ . The result is $\Delta_\chi = 325 \pm 25$ K for $\text{Sr}_{14}\text{Cu}_{24}\text{O}_{41}$ and $\Delta_\chi = 225 \pm 25$ K for $\text{Sr}_{11}\text{Ca}_3\text{Cu}_{24}\text{O}_{41}$. We will present additional evidence for a magnetic crossover at Δ_χ from $1/T_1$.

For $\text{Sr}_6\text{Ca}_8\text{Cu}_{24}\text{O}_{41}$, accurate Knight shift data is not available because of broader ^{17}O linewidths at lower temperatures. In addition, ^{63}Cu NMR in $\text{Sr}_6\text{Ca}_8\text{Cu}_{24}\text{O}_{41}$ has a decrease in measured intensity around 50 K, which makes measurement difficult. This is perhaps a result of the fact that $\text{Sr}_6\text{Ca}_8\text{Cu}_{24}\text{O}_{41}$ is on the border between insulating and metallic behavior [115]. This may cause slow charge fluctuations from hole movement at low temperatures.

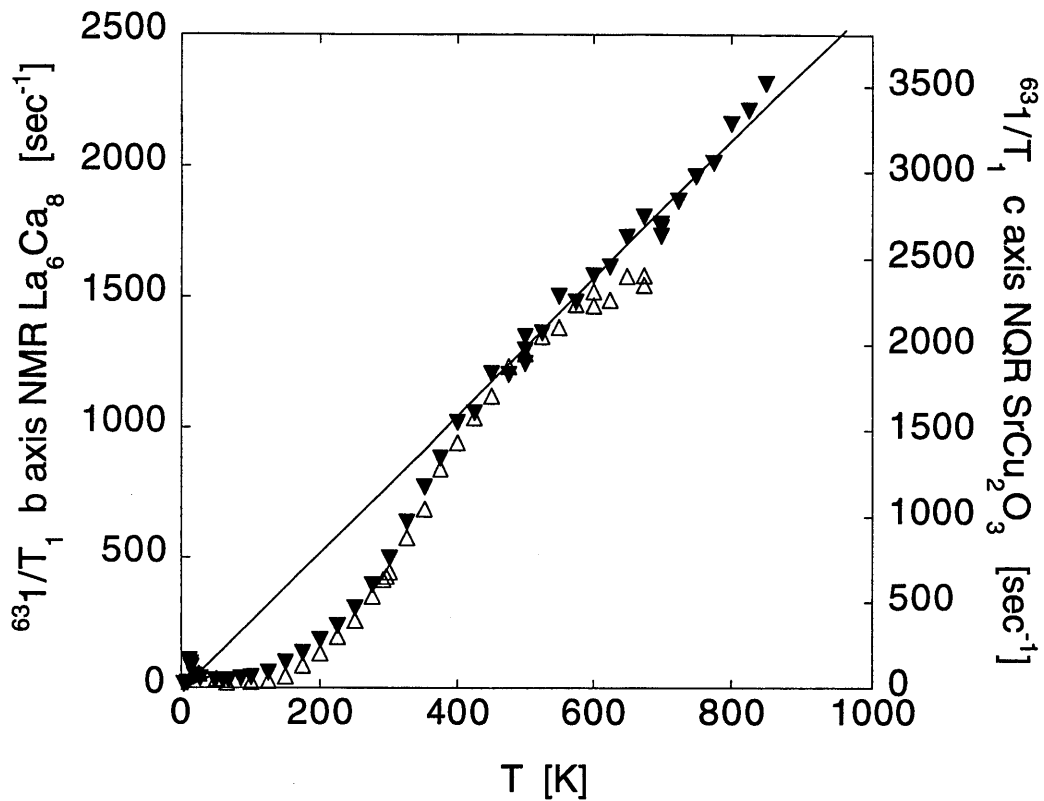


Figure 6-10: ^{63}Cu $1/T_{1,\perp\text{Cu-Plane}}$ for undoped 2-leg ladders $\text{La}_6\text{Ca}_8\text{Cu}_{24}\text{O}_{41}$ [\blacktriangledown] and SrCu_2O_3 [\triangle]. Note that the scale for SrCu_2O_3 is multiplied by 1.5 to account for the fact that $1/T_1(\text{NQR}) = 1.5 1/T_{1,\perp}(\text{NMR})$ because $\eta = 0.68$.

In addition to information about the susceptibility, comparing Oxygen Knight shift for the two oxygen sites, we can estimate the ratio of J_{\perp}/J_{\parallel} . Because the superexchange interaction between the Cu electron spins is mediated through the bonding oxygen atom, the amount of spin transfer to the oxygen orbital is related to the strength of the superexchange. From equation 5.12 [40] $J = 4f_{\sigma}^2(E_d - E_p)^2/U$, where f_{σ} is the fraction of unpaired spin density of the Oxygen ligand orbital along the exchange path. As noted in equation 2.3, $^{17}K^{spin}$ is proportional to the oxygen hyperfine coupling. The oxygen hyperfine coupling, in units of kOe/μ_B , represents the magnetic field at the nucleus that results when there is one electron spin, μ_B , of bulk spin susceptibility (see app. C). The size of the oxygen hyperfine coupling is determined by the distance, r , of the unpaired electrons that account for the bulk spin susceptibility from the oxygen nucleus, because the dipole interaction $\propto 1/r^3$ (eq. 3.7). Unpaired electrons that are located in the oxygen orbitals will provide the dominant contribution to the oxygen hyperfine coupling. Thus, the oxygen hyperfine coupling is proportional to the amount of unpaired spin density residing in the oxygen orbital, f_{σ} . So, the unpaired spin density in the oxygen orbital, f_{σ} , is proportional to the oxygen spin Knight shift, $^{17}K^{spin}$. Because the spin contribution to the Knight shift has the only significant temperature dependence, we can find the ratio of the spin contributions to the Knight shift as the ratio of the temperature dependence of the Knight shift for corresponding crystal axes, $^{17}K(2)^{spin}/^{17}K(1)^{spin} = d^{17}K(2)_a/d^{17}K(1)_c$. The Knight shift along the Cu-O-Cu bond direction is chosen because it is the largest and should be the direction most strongly affected by transferred spin. The experimental result, $d^{17}K(2)_a/d^{17}K(1)_c \sim 0.7$, for both $\text{La}_6\text{Ca}_8\text{Cu}_{24}\text{O}_{41}$ and $\text{Sr}_{14}\text{Cu}_{24}\text{O}_{41}$ (figure 6-11), implies that $J_{\perp}/J_{\parallel} \sim [f_{\sigma}(2)/f_{\sigma}(1)]^2 \sim (0.7)^2 \sim 0.5$ in both undoped and hole-doped ladders. Comparison with the results for the square-lattice system, $\text{Sr}_2\text{CuO}_2\text{Cl}_2$, provides an estimate of the magnitude, $J_{\perp} = 950 \pm 300$ K. To my knowledge, this was the first microscopic measurement of $J_{\parallel,\perp}$ in the undoped Cu_2O_3 two-leg ladder. The result is consistent with neutron scattering results $J_{\perp}/J_{\parallel} \sim 0.5$ and $J_{\perp} \sim 57 - 72$ meV $\sim 660 - 840$ K [116, 117] and also consistent with calculations based on local density approximation [118].

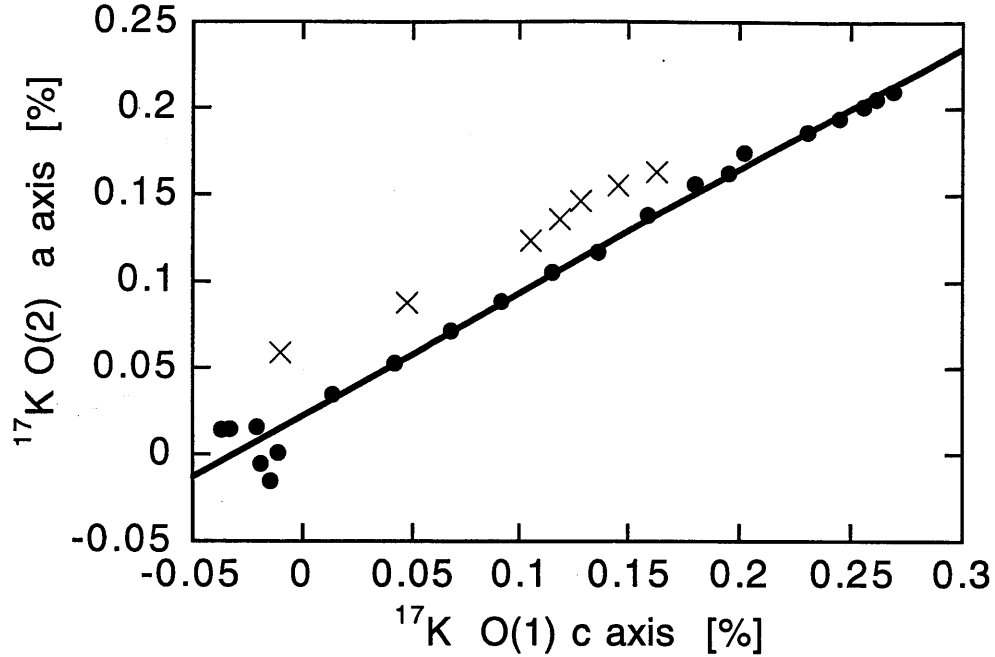


Figure 6-11: Knight shifts for the Cu-O bond directions of the O(1) ladder site (c axis) and O(2) rung site (a axis) plotted with temperature as an implicit parameter for $\text{La}_6\text{Ca}_8\text{Cu}_{24}\text{O}_{41}$ (\times) and $\text{Sr}_{14}\text{Cu}_{24}\text{O}_{41}$ (\bullet). Solid line is a linear fit to the $\text{Sr}_{14}\text{Cu}_{24}\text{O}_{41}$ data with resulting slope of 0.7

6.3 T_1 & T_{2G}

In figure 6-10 the temperature dependence of the spin-lattice relaxation rates, $^{63}\text{1}/T_1$, are shown for the undoped two-leg ladder materials, SrCu_2O_3 and $\text{La}_6\text{Ca}_8\text{Cu}_{24}\text{O}_{41}$. Both materials show quantitatively similar gapped behavior of $^{63}\text{1}/T_1$ at low temperatures. The magnitude of $1/T_1$ is the same. The figure (6-10) is shown with the scale for SrCu_2O_3 multiplied by 1.5 to account for the difference between $1/T_{1,c}(\text{NMR})$ and $1/T_1(\text{NQR})$. For SrCu_2O_3 , $1/T_1(\text{NQR}) = 1.5 \pm 0.1 1/T_{1,c}(\text{NMR})$ for the measured $\eta = 0.68$ and anisotropy of T_1 , $(1/T_{1,ab}) / (1/T_{1,c}) = 3.8 \pm 0.2$. The relationship between $1/T_1$ from NMR and NQR for SrCu_2O_3 was confirmed experimentally with $1/T_1(\text{NQR}) = 1.59 \pm 0.06 1/T_{1,c}(\text{NMR})$. The small peak in $1/T_1$ for $\text{La}_6\text{Ca}_8\text{Cu}_{24}\text{O}_{41}$ at low temperatures is caused by magnetic ordering in the chain layer at 12.2 K [119].

$1/T_1$ measures spin excitations which are suppressed at low temperatures because of the energy gap, Δ , above the ground state. At low temperatures, $1/T_1$ for copper shows the expected exponentially activated temperature dependence \sim

$\exp(-\Delta/k_B T)$. There is a clear crossover in the Cu T_1 to a high temperature regime with ${}^{63}\text{1}/T_1 \propto T$ above 425 K. For both materials, we therefore estimate a spin gap from this crossover $\Delta_{T_1} = 425 \pm 25$, in good agreement with $\Delta_\chi = 420$ K deduced by Azuma et al. [29] for SrCu_2O_3 from a bulk susceptibility measurement. For $\text{La}_6\text{Ca}_8\text{Cu}_{24}\text{O}_{41}$, this is in reasonable agreement with the $\Delta_\chi = 510 \pm 40$ K from the Knight shift.

In figure 6-12(a), the results of ${}^{63}\text{1}/T_1$ are shown for the ladder site of the undoped and doped $\text{A}_{14}\text{Cu}_{24}\text{O}_{41}$ materials. Clearly, the spin gap Δ decreases with increasing doping. In addition, a dramatic crossover occurs from the low temperature gapped regime to the high temperature paramagnetic regime. From the crossover temperature of T_1 , the spin gap is estimated as $\Delta_{T_1} = 325 \pm 25$, 225 ± 25 , and 160 ± 25 K for $\text{Sr}_{14}\text{Cu}_{24}\text{O}_{41}$, $\text{Sr}_{11}\text{Ca}_3\text{Cu}_{24}\text{O}_{41}$, and $\text{Sr}_6\text{Ca}_8\text{Cu}_{24}\text{O}_{41}$, respectively, in comparison to 425 ± 25 K for the undoped $\text{La}_6\text{Ca}_8\text{Cu}_{24}\text{O}_{41}$ and SrCu_2O_3 .

These results for the magnitude of the spin gap are in good agreement with recent neutron scattering measurements for the undoped two-leg ladders, $\Delta = 33$ meV (380 K) for SrCu_2O_3 [120] and 35 meV (406 K) for $\text{La}_6\text{Ca}_8\text{Cu}_{24}\text{O}_{41}$ [117]. However, there is one obvious discrepancy between neutron and NMR results. Neutron measurements on doped samples [120, 116, 121] have indicated that the spin gap energy stays constant with doping even up to $\text{Sr}_{2.5}\text{Ca}_{11.5}\text{Cu}_{24}\text{O}_{41}$ [121], rather than decreasing as clearly demonstrated by NMR. This discrepancy can be understood as arising from the difference in what is actually measured by neutron scattering and NMR, as discussed by Azuma *et al.*. The NMR/NQR relaxation rate $1/T_1$ measures low energy spin fluctuations ($\omega_n \approx 10^{-3}$ K), while the neutron scattering measurements detect the peak of the density of states for spin excitations at the spin gap energy, $\Delta \sim 425$ K. Therefore, NMR $1/T_1$ is sensitive to any transfer of spin excitations from above the spin gap to lower energies, but in neutron scattering, lower energy excitations are masked by large elastic scattering backgrounds. So, the neutron scattering and NMR results are consistent if hole doping transfers density of states from the peak at the spin gap to lower energies. In fact, this is exactly what Azuma *et al.* [120] found in their neutron studies of Zn doped SrCu_2O_3 , that the density of states at the peak

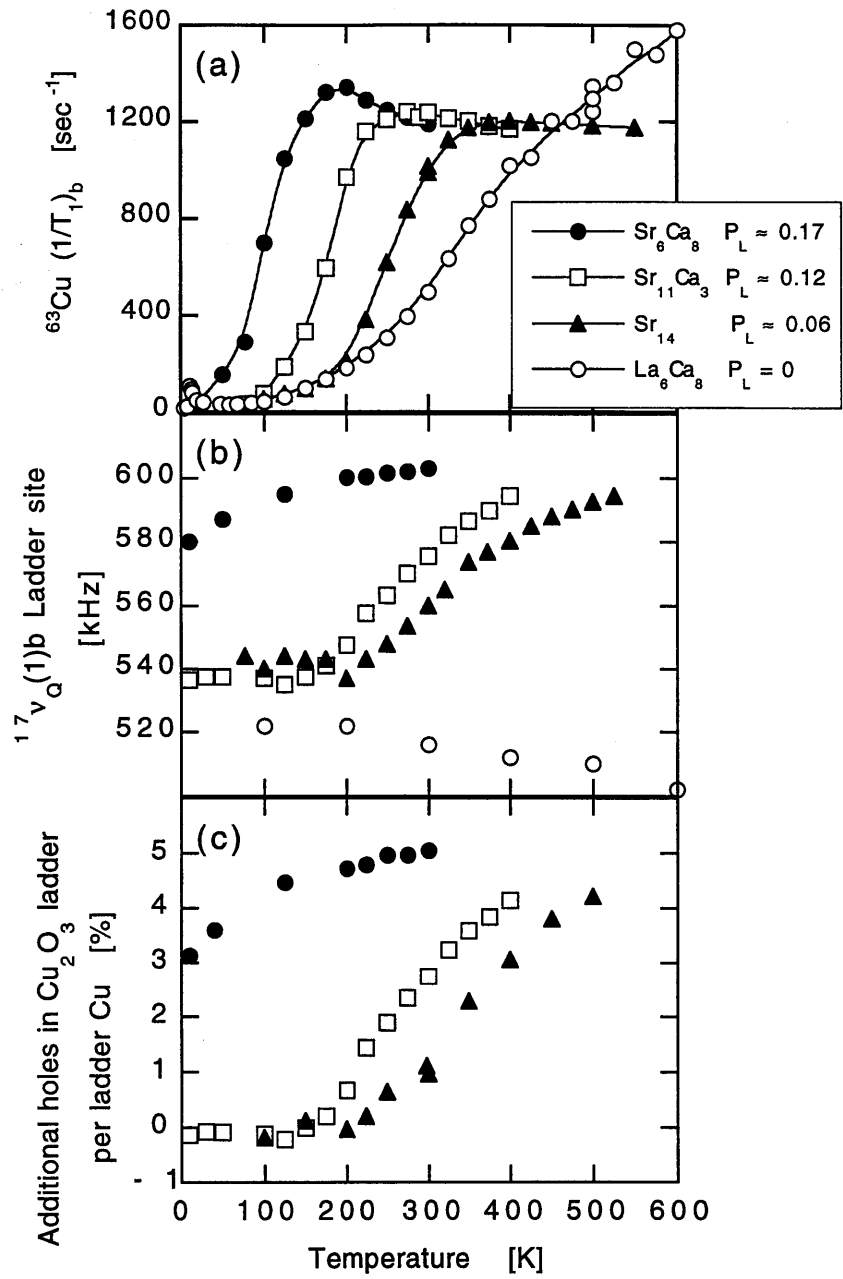


Figure 6-12: (a) ^{63}Cu $1/T_{1b}$, (b) $^{17}\nu_Q(1)b$, nuclear quadrupole interaction for the ladder oxygen site along the b axis, (c) calculated additional holes required to account for changes in quadrupole interactions for $\text{La}_6\text{Ca}_8\text{Cu}_{24}\text{O}_{41}$ (\circ , $P_L = 0$), $\text{Sr}_{14}\text{Cu}_{24}\text{O}_{41}$ (\blacktriangle , $P_L \sim 0.06$), $\text{Sr}_{11}\text{Ca}_3\text{Cu}_{24}\text{O}_{41}$ (\square , $P_L \sim 0.12$), $\text{Sr}_6\text{Ca}_8\text{Cu}_{24}\text{O}_{41}$ (\bullet , $P_L \sim 0.17$).

at the spin gap energy decreases with Zn doping, and presumably these excitations are occurring at lower energies instead as suggested by NMR. An additional difference between the neutron and NMR measurements is that the neutron measurements are typically done at very low temperatures where the doped holes may be immobile or microscopically segregated.

By comparing ^{17}O $1/T_1$ with ^{63}Cu $1/T_1$, we can obtain information about the wavevector dependence of the spin excitations. This relies on the fact that the form factors for the Cu and O site are significantly different. The important difference is whether the nuclei are sensitive to the antiferromagnetic fluctuations with wavevector $q \sim (\pi, \pi)$. As shown in figure 6-1, since the oxygen atoms sit in between two copper atoms, they are not sensitive to antiferromagnetic fluctuations in that direction. To be more quantitative, the form factors will be

$${}^{63}F_{\alpha}(q) = A_{\alpha} \quad (6.2)$$

$$O(1) {}^{17}F_{\alpha}(q) = 2C_{\alpha} \cos\left(\frac{q_x}{2}\right) + D_{\alpha} \quad (6.3)$$

$$O(2) {}^{17}F_{\alpha}(q) = 2F_{\alpha} \cos\left(\frac{q_y}{2}\right) \quad (6.4)$$

where A_{α} is the onsite hyperfine interaction for Cu, and small supertransferred hyperfine fields, B , have been neglected for simplicity. For the O(1) leg site, it has a nearest neighbor copper atom in the neighboring 2-leg ladder which contributes the D terms to the hyperfine form factor. In the above expression for the O(1) form factor, we have assumed that the spin fluctuations of neighboring 2-leg ladders are not correlated, so there is no interference of the C and D terms. The important considerations are that $^{17}1/T_1(2)$ is insensitive to fluctuations with wavevector $q_y \approx \pi$ and $^{17}1/T_1(1)$ is mostly insensitive to fluctuations with wavevector $q_x \approx \pi$ because $D_{\alpha}^2 \ll 4C_{\alpha}^2$.

The comparison of ^{17}O and ^{63}Cu $1/T_1$ is shown for each sample in figures 6-13. As can be clearly seen in figure 6-14 where ${}^{63,17}1/T_1$ are normalized to match the magnitude at low temperature, the temperature dependence below the spin gap is

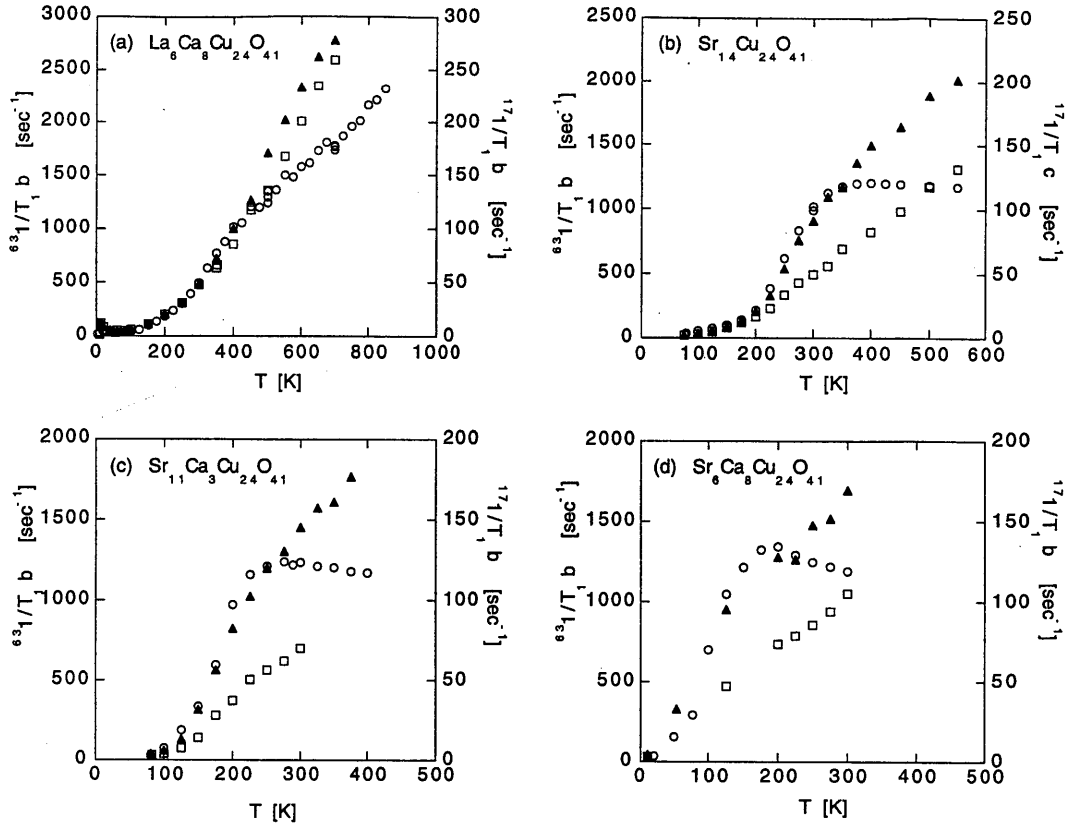


Figure 6-13: ,
 $^{17}\text{O } 1/T_{1b}$, $^{63}\text{Cu } 1/T_{1b}$ [o], $^{17}\text{O } 1/T_{1c}$ for O(1) ladder [\blacktriangle] and O(2) rung [\square] sites for
 (a) $\text{La}_6\text{Ca}_8\text{Cu}_{24}\text{O}_{41}$ ($P_L = 0$), (b) $\text{Sr}_{14}\text{Cu}_{24}\text{O}_{41}$ ($P_L \sim 0.06$), (c) $\text{Sr}_{11}\text{Ca}_3\text{Cu}_{24}\text{O}_{41}$
 ($P_L \sim 0.12$), (d) $\text{Sr}_6\text{Ca}_8\text{Cu}_{24}\text{O}_{41}$ ($P_L \sim 0.17$).

the same, but above the spin gap $^{63}\text{Cu } 1/T_1$ becomes constant in the doped samples, while $^{17}\text{O } 1/T_1$ continues to strongly increase. This leads to several conclusions. First, at temperatures below the spin gap, the spin excitations are dominated by those with nearly zero momentum transfer $q \sim (0, 0)$ as predicted [101]. In contrast, at high temperatures, the difference between the temperature dependence of $^{63}\text{Cu } 1/T_1$ and both oxygen $^{17}\text{O } 1/T_1$ indicates that $^{63}\text{Cu } 1/T_1$ is dominated by processes with wavevector $q \sim (\pi, \pi)$, mostly likely the direct magnon process, in agreement with Monte Carlo results by Sandvik, Dagotto, and Scalapino [122].

A calculation by D.A. Ivanov and P.A. Lee [123] showed that in the weak coupling limit, the contribution to $1/T_1$ from $q \sim (\pi, \pi)$ processes is very similar to the behavior of the doped samples, nearly constant at temperatures above the spin gap. This is in

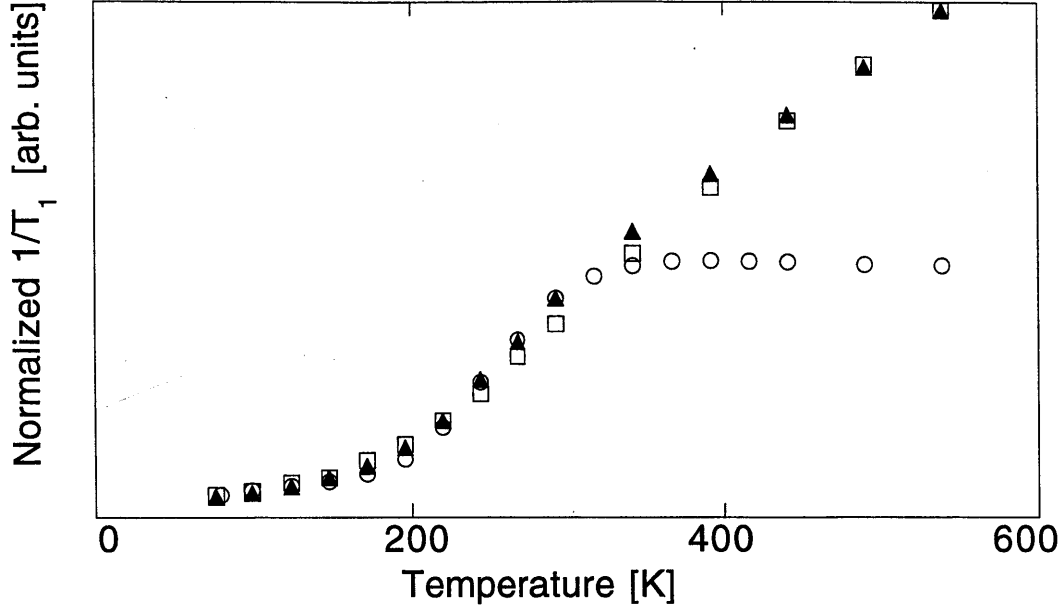


Figure 6-14: ^{63}Cu $1/T_{1b}$ [o], ^{17}O $1/T_{1b}$ for O(1) ladder [\blacktriangle] and O(2) rung [\square] sites for (b) $\text{Sr}_{14}\text{Cu}_{24}\text{O}_{41}$ ($P_L \sim 0.06$), normalized to match magnitude below spin gap.

strong contrast to the $1/T_1 \sim T$ seen in the undoped samples.

This contrast between the doped and undoped samples is not understood. The undoped samples have ^{63}Cu $1/T_1 \propto T$ above the spin gap, while the doped samples have constant ^{63}Cu $1/T_1$ at high temperatures. Perhaps, it is associated with the presence of additional holes in the chain layers that could be mobile at high temperatures. Preliminary experiments on lightly doped materials, $\text{La}_5\text{Sr}_1\text{Ca}_8\text{Cu}_{24}\text{O}_{41}$, and $\text{La}_4\text{Ca}_{10}\text{Cu}_{24}\text{O}_{41}$, suggested that the lightly doped La series of samples have ^{63}Cu $1/T_1$ similar to the undoped $\text{La}_6\text{Ca}_8\text{Cu}_{24}\text{O}_{41}$ (figure 6-15). However, these lightly doped samples may have all the doped holes residing in the chain layer and thus have effectively undoped ladder layers. This is suggested by the fact that Osafune, *et al.*[114] found a very small number of holes in the ladder layer ($\sim 2\%$) for a sample with slightly higher doping, $\text{Sr}_{11}\text{Y}_3\text{Cu}_{24}\text{O}_{41}$.

The Gaussian spin-spin relaxation rate provides a measure of the electron spin correlation length. As predicted by Monte Carlo and analytic calculations [30, 122], the electron spin correlation length will saturate to a constant at low temperatures ($T < \Delta$), causing $1/T_{2G}$ to also saturate. This behavior is seen in both the un-

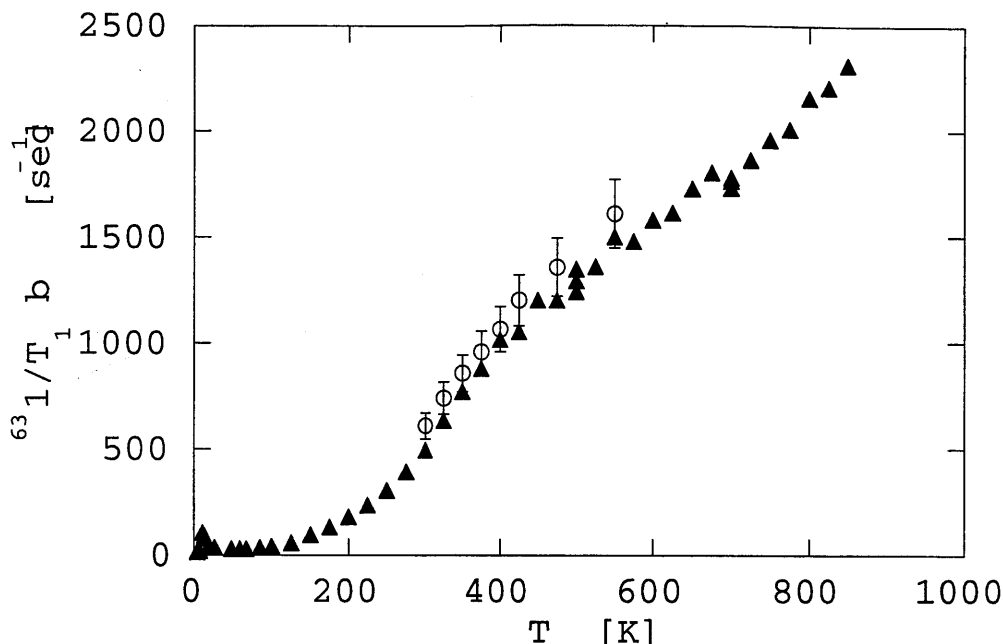


Figure 6-15: ^{63}Cu $1/T_{1b}$ for $\text{La}_5\text{Sr}_1\text{Ca}_8\text{Cu}_{24}\text{O}_{41}$ [o], and $\text{La}_6\text{Ca}_8\text{Cu}_{24}\text{O}_{41}$ [•].

doped SrCu_2O_3 and the slightly doped $\text{Sr}_{14}\text{Cu}_{24}\text{O}_{41}$ (figure 6-16). The NMR results for $1/T_{2G}$ are very similar for the two materials. This would imply that the correlation length has a similar temperature dependence with the assumption that the Cu hyperfine couplings are the same. The hyperfine couplings cannot be directly measured for $\text{A}_{14}\text{Cu}_{24}\text{O}_{41}$ because of the dominant contribution of the chain layer to the bulk susceptibility. Unfortunately, direct measurement of $1/T_{2G}$ for $\text{La}_6\text{Ca}_8\text{Cu}_{24}\text{O}_{41}$ is not possible due to the large linewidth caused by the distribution in quadrupole interaction.

6.4 Charge Effects

In addition to the decrease in the spin gap, charge effects are seen in the doped two-leg ladders with NMR. The most dramatic effect is the large change in the oxygen quadrupole interaction as seen in figure 6-12(b). This figure presents the b-axis component of the oxygen nuclear quadrupole interaction, $^{17}\nu_Q[b]$, for the O(1) leg

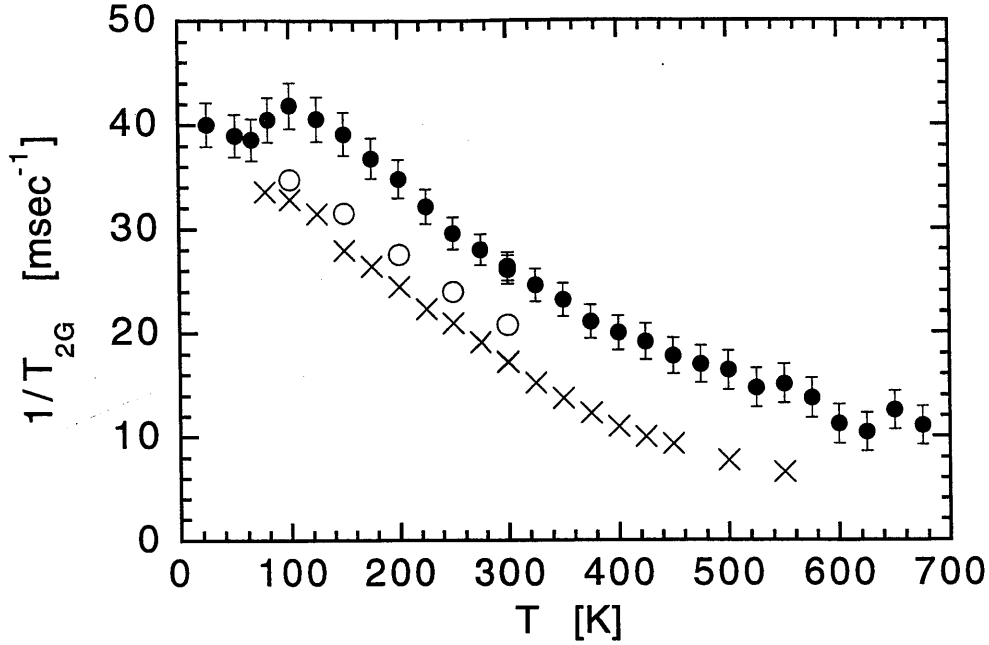


Figure 6-16: ^{63}Cu $1/T_{2G}$ for SrCu_2O_3 [NMR, \circ , NQR results converted ($/1.31$), \bullet] and $\text{Sr}_{14}\text{Cu}_{24}\text{O}_{41}$ [NMR, \times]. We must note that the conversion of T_{2G} from NQR to NMR does not agree with the NMR results in this case.

site. The nuclear quadrupole interaction measures the electric field gradient at the nuclear site. A dramatic change in $^{17}\nu_Q$ occurs only for the doped samples, while the undoped $\text{La}_6\text{Ca}_8\text{Cu}_{24}\text{O}_{41}$ exhibits a minor decrease of $^{17}\nu_Q$ due to thermal expansion. We define the temperature where this dramatic change begins as T^* and estimate $T^* = 210$ K, 140 K, ≈ 0 K for $\text{Sr}_{14}\text{Cu}_{24}\text{O}_{41}$, $\text{Sr}_{11}\text{Ca}_3\text{Cu}_{24}\text{O}_{41}$, and $\text{Sr}_6\text{Ca}_8\text{Cu}_{24}\text{O}_{41}$ respectively. We also observed a similar temperature dependence at the O(2) rung site for these samples (figure 6-17) and for $^{63}\nu_Q$ at the copper site in $\text{Sr}_{14}\text{Cu}_{24}\text{O}_{41}$ (figure 6-19). [111, 112] Extremely broad ^{63}Cu NMR lineshapes in $\text{La}_6\text{Ca}_8\text{Cu}_{24}\text{O}_{41}$ and $\text{Sr}_{14-x}\text{Ca}_x\text{Cu}_{24}\text{O}_{41}$ have prevented us from measuring $^{63}\nu_Q$ accurately, so the comparison between ^{63}Cu and ^{17}O has not been made.

In order to understand the dramatic temperature dependence of $^{17}\nu_Q$, we consider the electric field gradient, eq , based on a standard ionic picture, [37]

$$eq = eq_{hole} + (1 - \gamma)eq_{lattice} \quad (6.5)$$

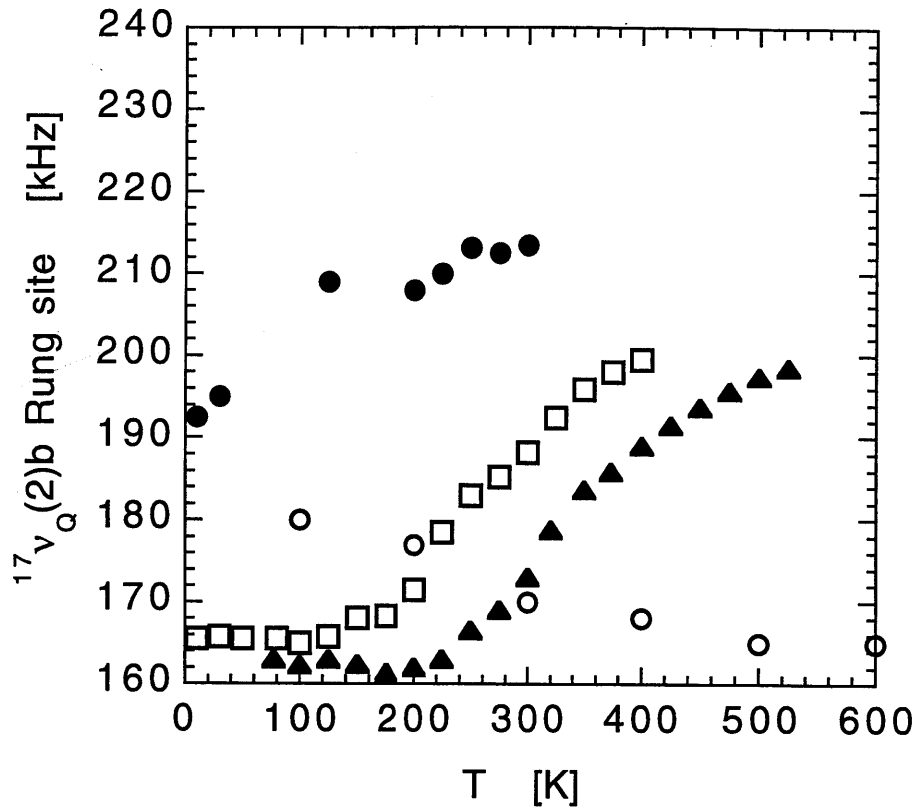


Figure 6-17: $^{17}\nu_Q[b]$ for the O(2) rung site for $\text{La}_6\text{Ca}_8\text{Cu}_{24}\text{O}_{41}$ (\circ , $P_L = 0$), $\text{Sr}_{14}\text{Cu}_{24}\text{O}_{41}$ (\blacktriangle , $P_L \sim 0.06$), $\text{Sr}_{11}\text{Ca}_3\text{Cu}_{24}\text{O}_{41}$ (\square , $P_L \sim 0.12$), $\text{Sr}_6\text{Ca}_8\text{Cu}_{24}\text{O}_{41}$ (\bullet , $P_L \sim 0.17$).

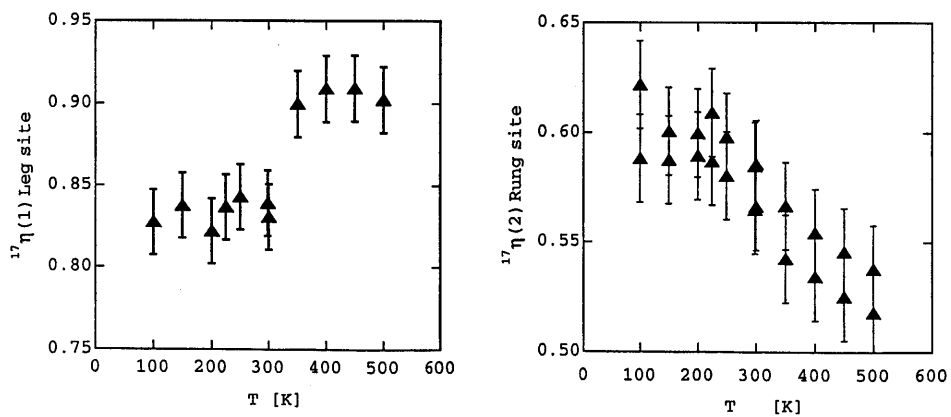


Figure 6-18: ^{17}O Nuclear quadrupole interaction asymmetry parameter η for $\text{Sr}_{14}\text{Cu}_{24}\text{O}_{41}$ (a) O(1) ladder site and (b) O(2) rung site.

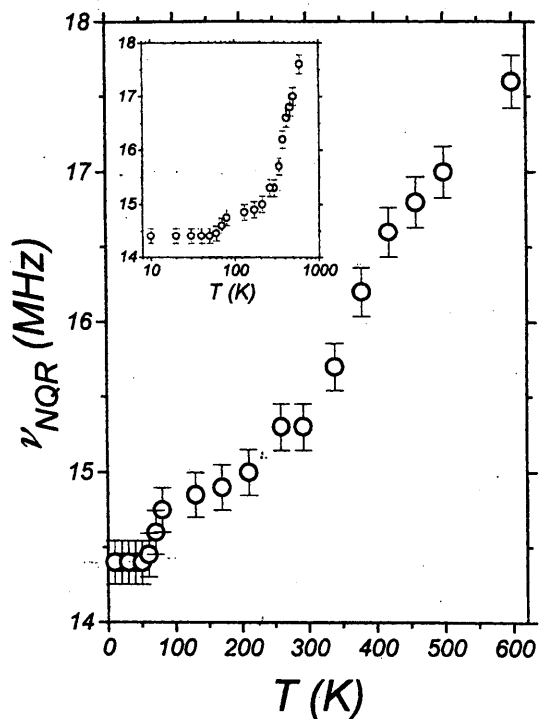


Figure 6-19: Temperature dependence of the ladder ^{63}Cu NQR line in $\text{Sr}_{14}\text{Cu}_{24}\text{O}_{41}$. (from Carretta, *et al.* [111]) We confirmed this temperature dependence by measuring the b axis quadrupole $^{63}\nu_{Q,b}$. $^{63}\nu_{Q,b} = 14.9, 15.75, 16.4 \pm 0.1$ MHz for 350 K, 450 K and 550 K, respectively ($\eta = 0.66$). The inset shows the same data with a logarithmic temperature scale to illustrate the constant frequency at low temperatures.

The first contribution, eq_{hole} , arises from holes in orbitals of the ion itself. An isotropic distribution of charge, such as from a filled electron shell, will not produce an electric field gradient, but unfilled shells can. If there is one hole in an oxygen 2p orbital, the electric field gradient at the nucleus is axial with the largest component along the lobe of the p orbital, $\nu_Q = (\frac{3}{20})(\frac{4}{5})e^2Q \langle r^{-3} \rangle$ [13]. For our calculations, we take $\langle r^{-3} \rangle = 3.63$ atomic units, which is 70% of the value for a free atom.[82, 41] This results in a nuclear quadrupole interaction of (2.66, -1.33, -1.33) MHz for ^{17}O 2p_x, for example. The second contribution to the electric field gradient, $eq_{lattice}$, arises from the charges of the other ions of the crystal. This electric field is then modified by the distortion which it creates in the electronic orbitals of the observed ion itself. This effect is accounted for by the Sternheimer antishielding factor, γ .

Thus, in principle, the observed change in electric field gradient could arise from changes in one or more of the three parts of equation (2), $eq_{lattice}$, γ , and eq_{hole} . A change in the lattice contribution, $eq_{lattice}$, would be caused by a change in the crystal structure or lattice parameters as a function of temperature. As discussed by Carretta et al.,[111] the change in lattice parameters as a function of temperature from 293 K to 520 K can account for less than 1% change in $^{63}\nu_Q$, while the experimental change is about 15% (figure 6-19). Similarly, we found that the change of lattice parameters would indicate a change of any component of $^{17}\nu_Q$ of 1.5% or less, while the experimentally observed change is as much as 20%. Clearly, the change in lattice parameters cannot account for the change in quadrupole interaction. Another option is that there is a local distortion in the crystal structure. Using point charge calculations, we attempted to reproduce the experimentally observed changes in $^{63,17}\nu_Q$ by shifting the ionic positions in the lattice. We did not find any local lattice distortions that could produce the experimentally measured sign of the temperature dependence for both the copper and two oxygen sites. Qualitatively, the increase in the quadrupole interaction for copper requires that the Cu-O bond length increase with temperature, while the increase in the quadrupole interaction for the oxygen sites requires a decrease in the Cu-O bond length. This contradiction indicates that lattice changes are not responsible for the large change in electric field gradient.

A second possible source for a change in electric field gradient is a change in the Sternheimer antishielding factor, γ . For CuO_2 planes in high T_c superconductors, the value of γ is estimated as $^{63}\gamma \approx -20$ and $^{17}\gamma \approx -9$ for ^{63}Cu and ^{17}O , respectively.[38, 41] Shimizu[38] showed that $^{63}\gamma = -20$ for copper does not vary significantly between copper oxide materials with doping and temperature. Lattice point charge calculations of the electric field gradient for $\text{La}_6\text{Ca}_8\text{Cu}_{24}\text{O}_{41}$ were done with ionic charges of +2.429 for the (La,Ca) site (the average of La 3+ and Ca 2+), +2 for Cu, and -2 for O. Oxygen results for $\gamma = -8$ are in units of kHz (-193, +564, -371) for the O(1) ladder site and (-713, +331, +381) for the O(2) rung site, in reasonable agreement with the experimental values (± 60 , ± 516 , $\mp 540 \pm 40$) and (∓ 690 , ± 170 , $\pm 540 \pm 40$) at 291 K. For the copper ladder site, using $\gamma = -20$ and an axial electric field gradient from the hole of 77 MHz, point charge calculations give (+1.1, +16.9, -17.9) MHz in rough agreement with (∓ 3.3 , ± 16.8 , ∓ 13.5) MHz from measurements at room temperature. This implies that $^{63,17}\gamma$ are not significantly different from other high T_c materials. To reproduce the experimental temperature dependence of $^{17}\nu_Q$ of as much as 20% would require an equal change (20%) of γ . Since γ is a property of the structure of the electron orbitals of the ion and therefore, of electron-volt energy scale, we do not expect significant temperature dependence. Therefore, we conclude that temperature dependent $^{63,17}\gamma$ in hole-doped ladders is very unlikely.

The third and only remaining possibility is that a change in the hole concentration in the ladder Cu_2O_3 layer changes eq_{hole} of the doped samples. In the following, we will estimate the change in local hole concentration in the Cu_2O_3 ladder required to account for the changes in the electric field gradient.

Additional holes affect the electric field gradient in two ways. First, a hole produces an electric field gradient at the nuclear site of its own atom through eq_{hole} of eq.(2). Second, a hole changes the charge of the ion, altering the charge environment of neighboring atoms. This changes the lattice electric field gradient, $eq_{lattice}$, for neighboring atoms. We calculate the effect of the holes on the neighboring atoms by point charge lattice summations using the values of γ estimated for $\text{La}_6\text{Ca}_8\text{Cu}_{24}\text{O}_{41}$. For our calculations, we consider the possibility of holes in the oxygen 2p orbitals of

Table 6.1: Magnitude of quadrupole interaction [kHz] measured at room temperature

$\text{La}_6\text{Ca}_8\text{Cu}_{24}\text{O}_{41}$	a	b	c
O(1) ladder	60	516	550 ± 40
O(2) rung	690	170	550 ± 40
Cu	3,300	16,800	13,500

$\text{Sr}_{14}\text{Cu}_{24}\text{O}_{41}$	a	b	c
O(1) ladder	60	560	605
O(2) rung	770	170	630
Cu (350 K)		14,900	

both oxygen sites and in the copper $3d_{a^2-c^2}$ or $3d_{3b^2-r^2}$ orbitals. The subscripts, a, b, and c, refer to the crystal axes where b is perpendicular to the ladder layer, a is along the rungs of the ladder, and c is along the ladder direction. We determined the amount of doped holes in each oxygen and copper orbital from $^{63}\nu_Q$ and the tensor components of $^{17}\nu_Q(1, 2)$ considering consistently both the direct effect of a hole on its own nucleus and the indirect effect of a hole on nearby atoms. The nuclear quadrupole interactions are given in table 6.1 for $\text{La}_6\text{Ca}_8\text{Cu}_{24}\text{O}_{41}$ and $\text{Sr}_{14}\text{Cu}_{24}\text{O}_{41}$. For the other uniaxially aligned powder samples, we have only measured b axis quadrupole frequency and we assumed that the distribution of holes between the oxygen and copper orbitals was the same as in $\text{Sr}_{14}\text{Cu}_{24}\text{O}_{41}$.

We summarize the total number of additional holes required in the ladder Cu_2O_3 layer to produce the experimentally observed changes of $^{17,63}\nu_Q$ in Figure 6-12(c), and the distribution of the holes between the oxygen 2p orbitals and Cu 3d orbitals in table 6.2 for $\text{Sr}_{14}\text{Cu}_{24}\text{O}_{41}$ at 500 K. Primarily, the holes go into the oxygen 2p σ orbitals, the O(1) leg site 2p $_a(1)$ and 2p $_c(1)$ and the O(2) rung site 2p $_a(2)$. There is possibly also some hole transfer to the ladder copper site, but there is much larger uncertainty in the calculation of the holes on the copper site. The larger uncertainty for the copper site arises from the wider copper linewidths and larger Sternheimer anti-shielding factor, γ ($^{63}\gamma \approx -20$, $^{17}\gamma \approx -8$). Also, we cannot estimate the absolute number of holes in the ladder Cu_2O_3 layer because of the uncertainty in the nearly temperature independent contribution of $eq_{lattice}$ to the electric field gradient.

Table 6.2: Additional holes in ladder layer orbitals of $\text{Sr}_{14}\text{Cu}_{24}\text{O}_{41}$ at 500 K deduced from temperature dependence of ν_Q

O $2p_a(1)$	O $2p_c(1)$	O $2p_a(2)$	O $2p_c(2)$	Cu $3d_{a^2-c^2}$
1.3 ± 0.3 %	1.3 ± 0.3 %	1.0 ± 0.3 %	0.3 ± 0.3 %	0.9 ± 0.6 %

We emphasize that figure 6-12(c) just shows the additional holes necessary to account for the temperature dependence of the electric field gradient. The low temperature region of ν_Q for $\text{Sr}_{14}\text{Cu}_{24}\text{O}_{41}$ was taken as a starting point from which the additional holes necessary to account for the temperature dependence of $^{17,63}\nu_Q$ are calculated. This is done to avoid uncertainties in the lattice contribution to the electric field gradient. Lattice point charge calculations are clearly a simplified approximation which prevents an absolute determination of the hole concentration in the ladder Cu_2O_3 layer. We emphasize however that the physical picture given by this analysis, that holes are transferred into the ladder layer as temperature increases above T^* , primarily into the ladder oxygen $2p\sigma$ orbitals, is independent of the lattice point charge calculation and the value of γ . That the holes reside in oxygen $2p\sigma$ orbitals is consistent with other copper oxide materials, such as $\text{YBa}_2\text{Cu}_3\text{O}_7$ and $(\text{La,Sr})_2\text{CuO}_4$. [124, 41] The symmetry of the electric field gradient changes, as shown by η for $\text{Sr}_{14}\text{Cu}_{24}\text{O}_{41}$ in figure 6-18, supports the idea that holes are responsible for the ν_Q changes.

Other measurements of these $\text{A}_{14}\text{Cu}_{24}\text{O}_{41}$ materials also point towards changes in hole concentration at T^* . Optical conductivity measurements [114] of the Drude peak at low frequency are attributed to carriers in the ladder layer. The temperature dependence of the integral of that peak, which represents N/m^* (carrier number over effective mass), is similar to that of the electric field gradient. Charge transport [119, 125] shows a peak in the effective activation energy (inset to figure 6-20). The temperature of this charge anomaly is very close to the temperature T^* for the onset of the change of the quadrupole interaction. The charge anomaly is noted as T_{tran} for several doping levels as summarized in figure 6-23. In addition, magnetic susceptibility [119, 125] indicates that the ladder layer contributes to the susceptibility

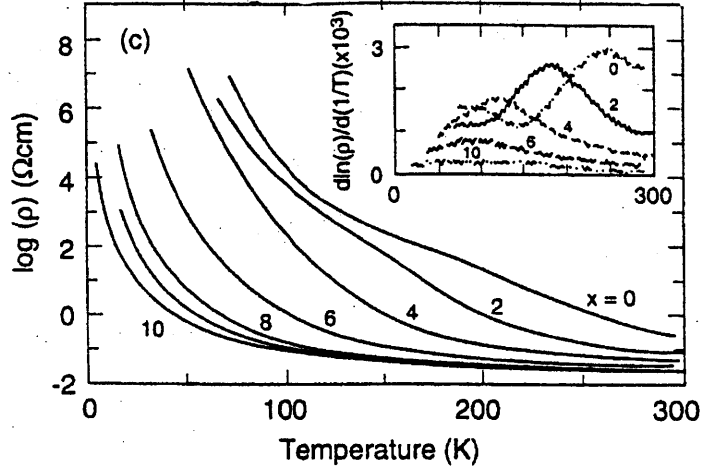


Figure 6-20: Resistivity, ρ , data for $\text{Sr}_{14-x}\text{Ca}_x\text{Cu}_{24}\text{O}_{41}$ from Carter, *et al.* [119] The resistivity decreases with Ca doping. A peak in the effective activation energy of the resistivity is seen in the inset and the temperature of the peak (which we will call T_{tran}) decreases with Ca doping.

only above T^* .

These changes in the electric field gradient are correlated with the magnetic changes seen in the nuclear spin lattice relaxation rate, $1/T_1$, for ^{63}Cu . [107] The onset of the change in the electric field gradient, T^* , is at the beginning of the crossover from the low temperature gapped regime to the paramagnetic regime. In addition, for $\text{Sr}_{14}\text{Cu}_{24}\text{O}_{41}$, Takigawa *et al.* [112] and Carretta *et al.* [111] noted that for $T \leq 225$ K, the fit of the nuclear magnetization decay to the standard solution of the rate equations becomes poor, and the ratio $(^{65}1/T_1) / (^{63}1/T_1)$ decreases from $(^{65}\gamma/^{63}\gamma)^2 = 1.15$ indicating that charge fluctuations are contributing to the relaxation. The quadrupolar relaxation is maximum at about 100 K for $\text{Sr}_{14}\text{Cu}_{24}\text{O}_{41}$ indicating that charge fluctuations have slowed down to the NMR frequency. [112, 111] As shown in Figure 6-21, we found that quadrupolar relaxation is significant below $T \approx \Delta_{T1}$ for all hole doped samples. Most likely, these charge fluctuations are associated with hole motion in the ladder plane.

The most likely source of additional holes doped into the Cu_2O_3 ladder above T^* is holes transferred from the CuO_2 chain layer. This scenario is quite plausible, in view of the fact that ^{63}Cu nuclear spin lattice relaxation rate, $^{63}1/T_1$, at the chain site

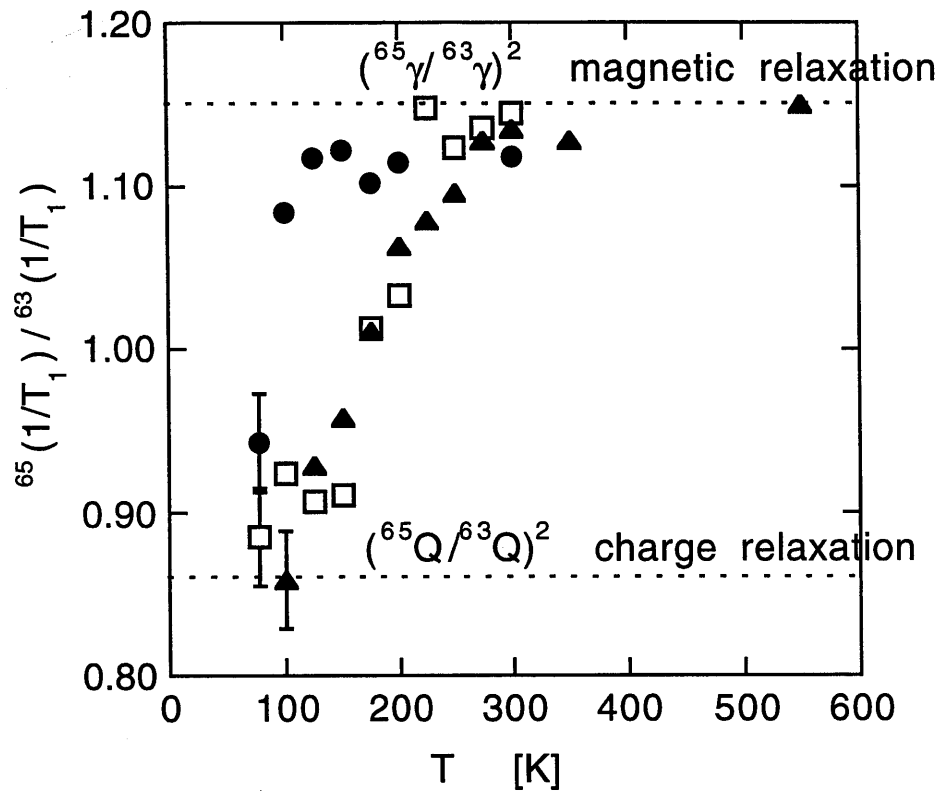


Figure 6-21: Ratio of $1/T_1$ for the two Cu isotopes, 65 and 63: $(^{65}1/T_1)/(^{63}1/T_1)$ for $\text{Sr}_{14}\text{Cu}_{24}\text{O}_{41}$ (\blacktriangle , $P_L \sim 0.06$), $\text{Sr}_{11}\text{Ca}_3\text{Cu}_{24}\text{O}_{41}$ (\square , $P_L \sim 0.12$), $\text{Sr}_6\text{Ca}_8\text{Cu}_{24}\text{O}_{41}$ (\bullet , $P_L \sim 0.17$). Dotted lines show theoretical expectations for magnetic and charge relaxation.

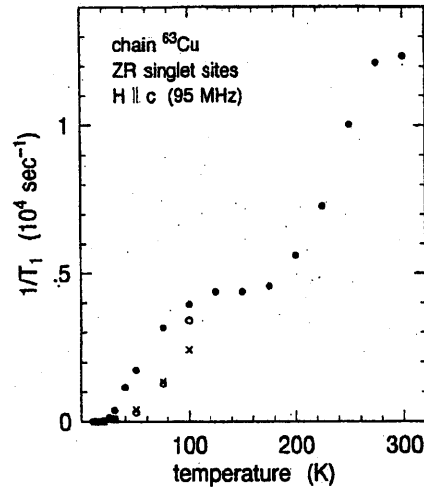


Figure 6-22: Temperature dependence of chain ^{63}Cu $1/T_1$ from Takigawa, *et al.* [112].

dramatically increases above T^* (figure 6-22) and the holes in the chain delocalize at around T^* for $\text{Sr}_{14}\text{Cu}_{24}\text{O}_{41}$. [112] Alternatively, the hole concentration in the Cu_2O_3 ladder below T^* can be smaller for the majority of the Cu and O(1,2) sites, if holes are localized within the NMR time scale ($\sim \mu\text{sec}$) below T^* . The anomalies in charge transport and magnetic susceptibility measurements have been interpreted as charge localization at T^* , [125] but this does not seem to account for the NMR results. This scenario requires NMR line broadening or splitting around T^* due to the localization of holes, but we did not observe any significant broadening of the NMR lineshape around T^* . Some NMR quadrupole satellite lines are slightly split, but the size of the splitting is temperature independent (shown by η in figure 6-18) for the entire temperature range with no apparent change around T^* . Additionally, the peak in quadrupole relaxation for $\text{Sr}_{14}\text{Cu}_{24}\text{O}_{41}$ implies that the hole motion slows down to the NMR frequency only at around 100 K, so the charge dynamics at higher temperatures such as $T^*=210$ K should be faster than the NMR time scale, not slower. Therefore, this “self-doping” scenario does not seem consistent, but we cannot completely exclude it.

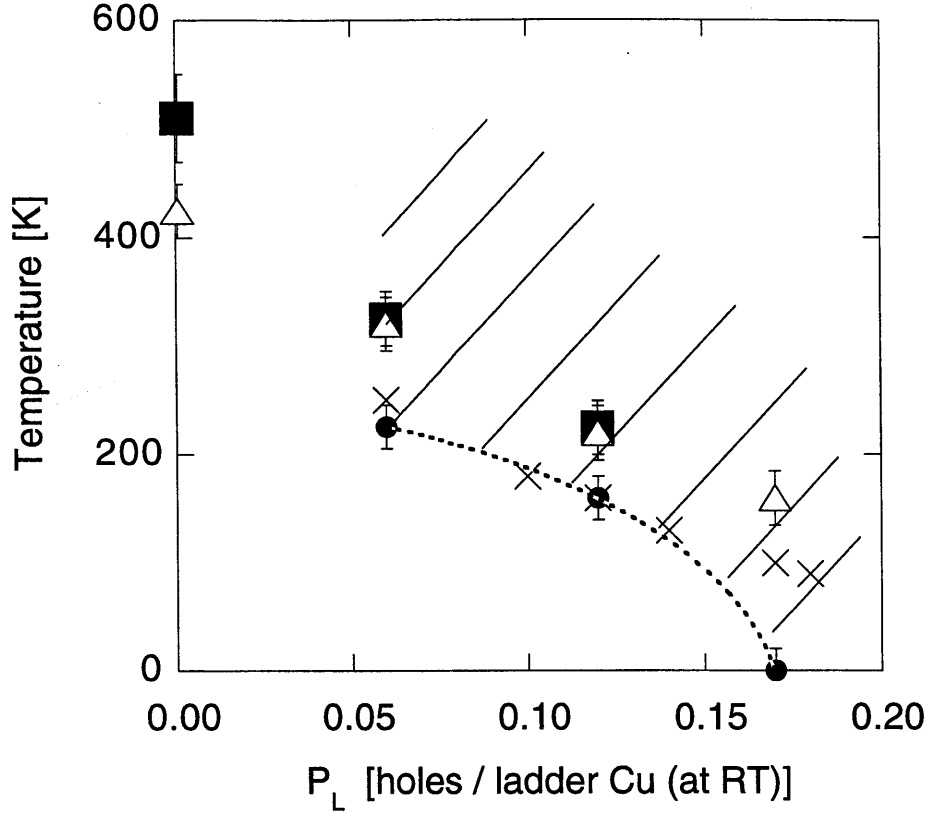


Figure 6-23: T^* (\bullet), T_{tran} (\times , after Ref. [119]), Δ_{T_1} (Δ), and Δ_χ (\blacksquare , from Ref. [125]) for various room temperature hole-doping levels P_L [Ref. [114]], $\text{La}_6\text{Ca}_8\text{Cu}_{24}\text{O}_{41}$ ($P_L = 0$), $\text{Sr}_{14}\text{Cu}_{24}\text{O}_{41}$ ($P_L \sim 0.06$), $\text{Sr}_{11}\text{Ca}_3\text{Cu}_{24}\text{O}_{41}$ ($P_L \sim 0.12$), and $\text{Sr}_6\text{Ca}_8\text{Cu}_{24}\text{O}_{41}$ ($P_L \sim 0.17$). Crosshatched region indicates where hole transfer occurs.

6.5 Summary

Figure 6-23 gives a summary of the magnetic and charge results for the two-leg ladder materials. The prototypical undoped 2-leg ladder, SrCu_2O_3 , and the undoped $\text{La}_6\text{Ca}_8\text{Cu}_{24}\text{O}_{41}$, show nearly identical results for $^{63}\text{Cu}/T_1$. The results for Knight shift, $1/T_1$, and $1/T_{2G}$ exhibit the crossover from the low temperature gapped regime to the high temperature paramagnetic regime. This provides concrete estimates of the spin gap, Δ . The changes in ^{17}O quadrupole interaction clearly show that in the doped two-leg ladder material, $\text{A}_{14}\text{Cu}_{24}\text{O}_{41}$, the doped holes are mobile above a temperature scale, T^* , which is correlated with the spin gap energy scale. The effective doping of the measured oxygen sites increases with increasing temperature.

Chapter 7

Three-leg ladder, $\text{Sr}_2\text{Cu}_3\text{O}_5$

In this chapter, NQR and NMR experiments on the three-leg $S=1/2$ spin ladder material, $\text{Sr}_2\text{Cu}_3\text{O}_5$, are described. The behavior of $S=1/2$ spin ladders depends strongly on the number of chains coupled together. As discussed in the previous chapter, for a two-leg spin ladder, a large spin excitation gap exists. However, for the three-leg ladder, the excitation spectrum is expected to be gapless. Unlike the two-leg ladder, the three spin $1/2$ of the rung cannot form a singlet ground state.

Another important reason to study the undoped three-leg spin ladder is because of its possible direct importance to high T_c superconductivity. Under-doped high T_c superconductors show a stripe structure [8, 126](figure 7-1) which has been proposed as undoped three-leg spin ladders coupled across rivers of doped holes. Studying the magnetic behavior of three-leg ladders may help understand this stripe phase and high T_c superconductivity. Concentrated theoretical effort is underway to reproduce the stripe phase based on the anisotropic non-linear sigma model [127]. This extends the fundamental importance of spin ladders beyond the field of magnetism to the mechanism of high T_c superconductivity.

For $\text{Sr}_2\text{Cu}_3\text{O}_5$, spin susceptibility by Azuma, *et al.* [29] and pioneering high field ^{63}Cu NMR between 100 K and 300 K by Ishida, *et al.* [108] revealed the qualitative difference of magnetic properties between two- and three-leg ladders in the low temperature limit. However, the nature of spin correlations at finite temperatures remains largely untested, despite recent theoretical developments [128, 30, 129, 36, 122].

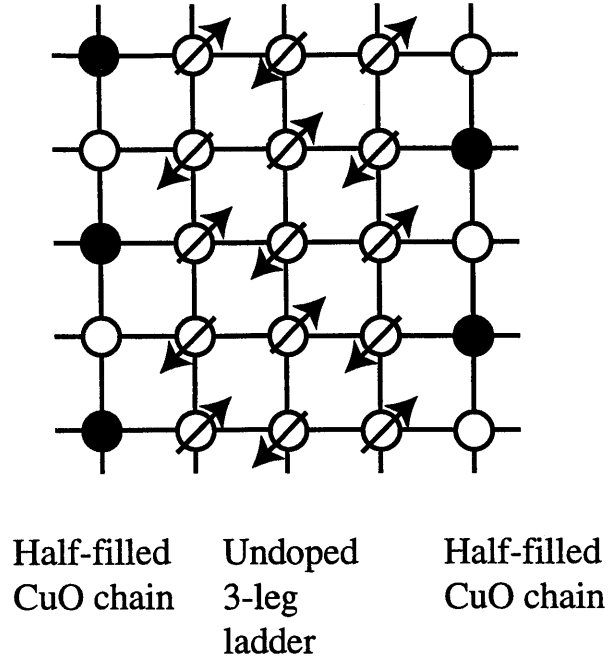


Figure 7-1: Proposed stripe order of charge and spin in high T_c superconductors at 1/8 doping [8]. Undoped three-leg spin ladders are separated by rivers of doped holes.

The large exchange interaction $J = 1300\sim 1600$ K in copper-oxide ladders [29, 130, 107, 116] makes measurements of spin-correlations at elevated temperatures essential to understanding the statistical properties at finite temperatures.

We report the first ^{63}Cu NQR measurements of the ^{63}Cu nuclear spin-lattice relaxation rate $1/T_1$ and the Gaussian component of spin-spin relaxation rate $1/T_{2G}$ for the three-leg ladder $\text{Sr}_2\text{Cu}_3\text{O}_5$ from 83 K up to 725 K. The Gaussian component of the ^{63}Cu nuclear spin-spin relaxation rate, $1/T_{2G}$, probes the spin-spin correlation length, ξ , as demonstrated earlier for the 2d square-lattice[27, 26] and the 1d spin-chain[48]. We present evidence that the spin-spin correlation length ξ in the three-leg ladder follows the 1d form $\xi \sim \frac{1}{T}$ above 300 K. To our surprise, however, we found that weak inter-ladder coupling along the c axis results in dimensional crossover to a quasi-2d regime below 300 K, where ξ diverges exponentially, $\xi \sim \exp \frac{2\pi\rho_s}{T}$ ($2\pi\rho_s=290\pm 30$ K is the effective spin stiffness). The anisotropic non-linear sigma model [127] successfully describes the static and dynamic NQR/NMR properties in the quasi-2d regime. To the best of our knowledge, this is the first experimental demonstration of the validity

of the anisotropic non-linear sigma model in a quantum Heisenberg antiferromagnet.

7.1 Structure & Experimental Details

The polycrystalline sample of the three-leg ladder, $\text{Sr}_2\text{Cu}_3\text{O}_5$, was grown at Kyoto under high pressure [29]. Technically, the present NQR approach used for $\text{Sr}_2\text{Cu}_3\text{O}_5$ is much harder than the high field NMR method, because the low resonance frequency of NQR (11.32 MHz at 300 K for the edge chain in $\text{Sr}_2\text{Cu}_3\text{O}_5$) makes the signal intensity two orders of magnitude weaker. However, NQR allows us to conduct measurements at elevated temperatures limited only by sample decomposition. For our NMR experiments, the powder sample is uniaxially aligned along the c axis in epoxy. The epoxy will decompose at elevated temperatures, limiting the NMR measurements to below 500 K. In addition, the three-leg ladder structure shown in figure 7-2 has two different copper sites, the atoms in the central chain and those in the two edge chains. Unlike earlier NMR measurements by Ishida, *et al.*[108], our NQR and NMR experiments measure the relaxation times for the two sites separately without line superposition. The Cu NQR and NMR lineshapes with the resonance lines from the two different sites labeled are shown in figures 7-3 and 7-5. The quadrupole interactions for ^{63}Cu are ($\nu_{a,b}=\pm 2.845, \pm 4.045, \nu_c=\mp 6.89$) MHz for the central chain site and ($\nu_{a,b}=\pm 1.89, \pm 8.69, \nu_c=\mp 10.58$) MHz for the edge chain site at 300 K. The two Cu NMR lines can be assigned to the specific sites by comparing the intensity (2:1 for edge chain:central chain) (see figure 7-6). Also, the quadrupole interactions are very close to those for similar sites in other materials: the edge chain site is similar to the site in the two-leg ladder SrCu_2O_3 ($\pm 1.65, \pm 8.75, \mp 10.40$) MHz, and the central chain site is similar to the infinite layer compound $(\text{Ca,Sr})\text{CuO}_2$ $\nu_Q \approx 6.7$ MHz [131].

Separation of the two signals is essential because the two copper sites do not necessarily have the same values of $1/T_1$ and $1/T_{2G}$. In fact, the magnitude of $1/T_{1c}$ is very different for the two sites, $(1/T_{1c})_{\text{central chain}} / (1/T_{1c})_{\text{edge chain}} = 2.3$ and $(1/T_{2G})_{\text{central chain}} / (1/T_{2G})_{\text{edge chain}} \approx 1.03$. Even though the magnitude of $1/T_1$ is very different, the temperature dependence of $1/T_1$ and $1/T_{2G}$ at the two sites

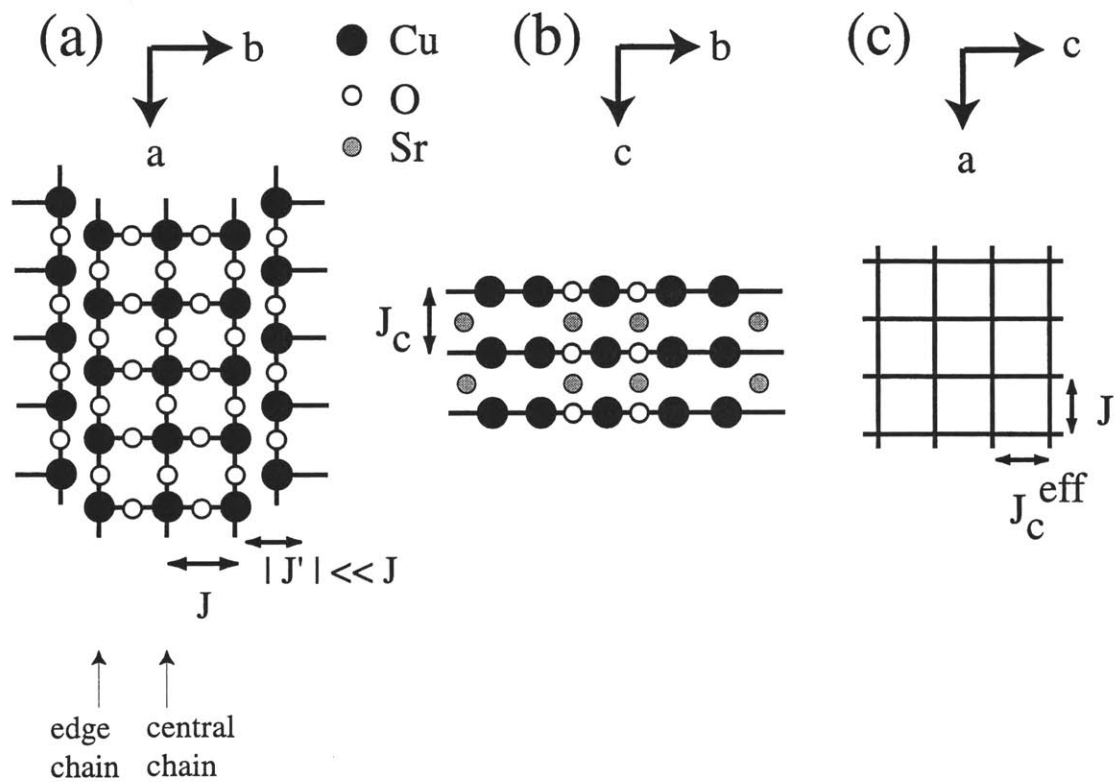


Figure 7-2: Structure of three leg ladder material, $\text{Sr}_2\text{Cu}_3\text{O}_5$, (a) top view, (b) side view, and (c) effective structure in anisotropic 2d regime below 300 K.

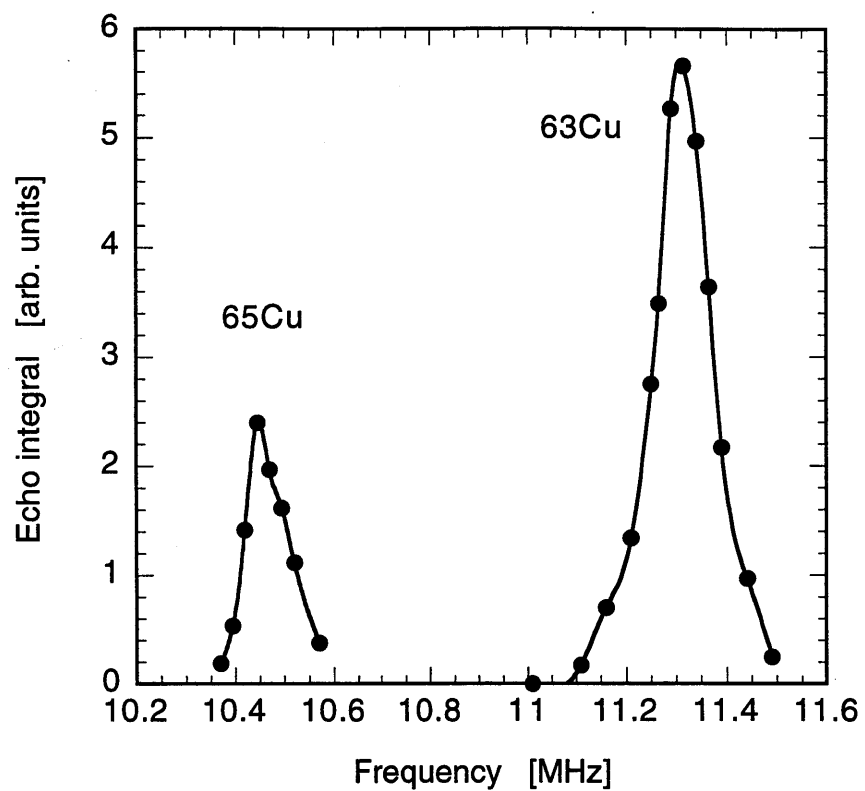


Figure 7-3: $^{63,65}\text{Cu}$ NQR lineshape for the edge chain copper site of $\text{Sr}_2\text{Cu}_3\text{O}_5$ at 293 K.

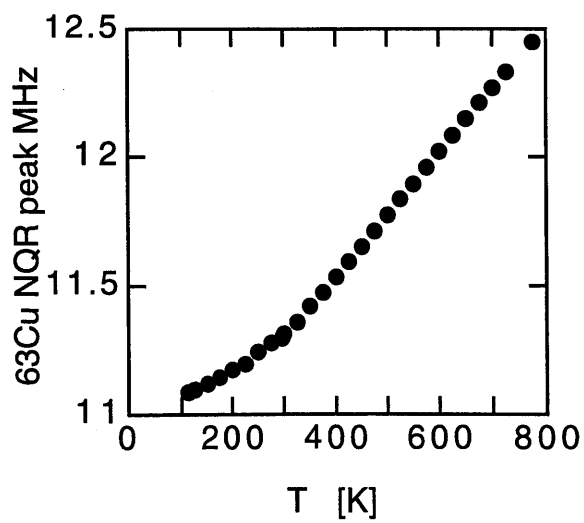


Figure 7-4: Temperature dependence of the ^{63}Cu edge chain NQR resonance.

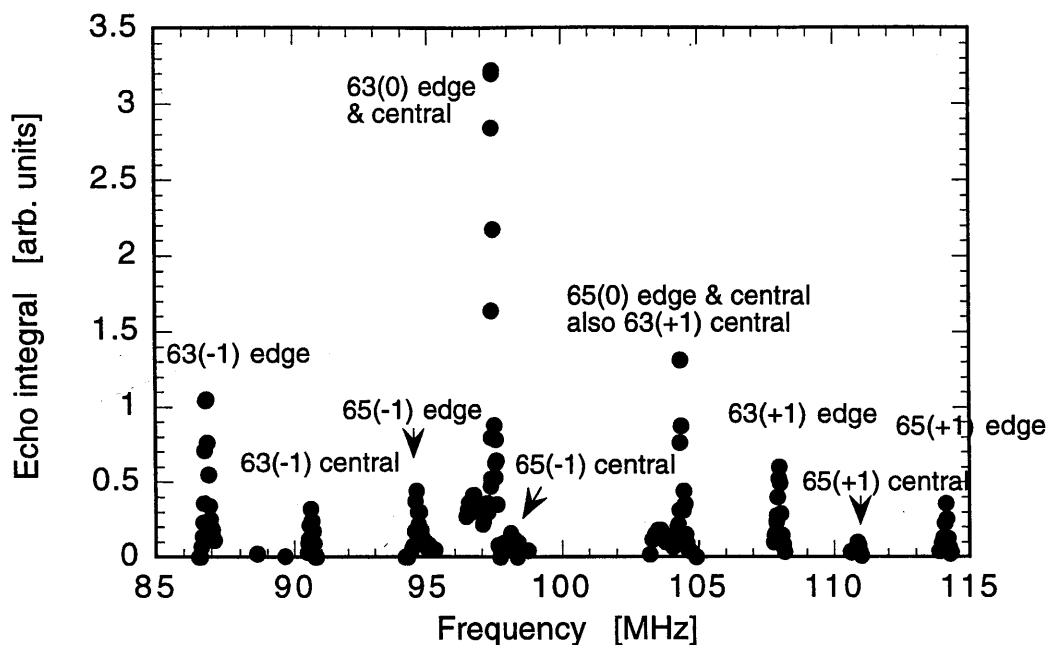


Figure 7-5: $^{63,65}\text{Cu}$ NMR lineshape for $\text{Sr}_2\text{Cu}_3\text{O}_5$ at 300 K, ($H = 8.53 \text{ T} \parallel c$).

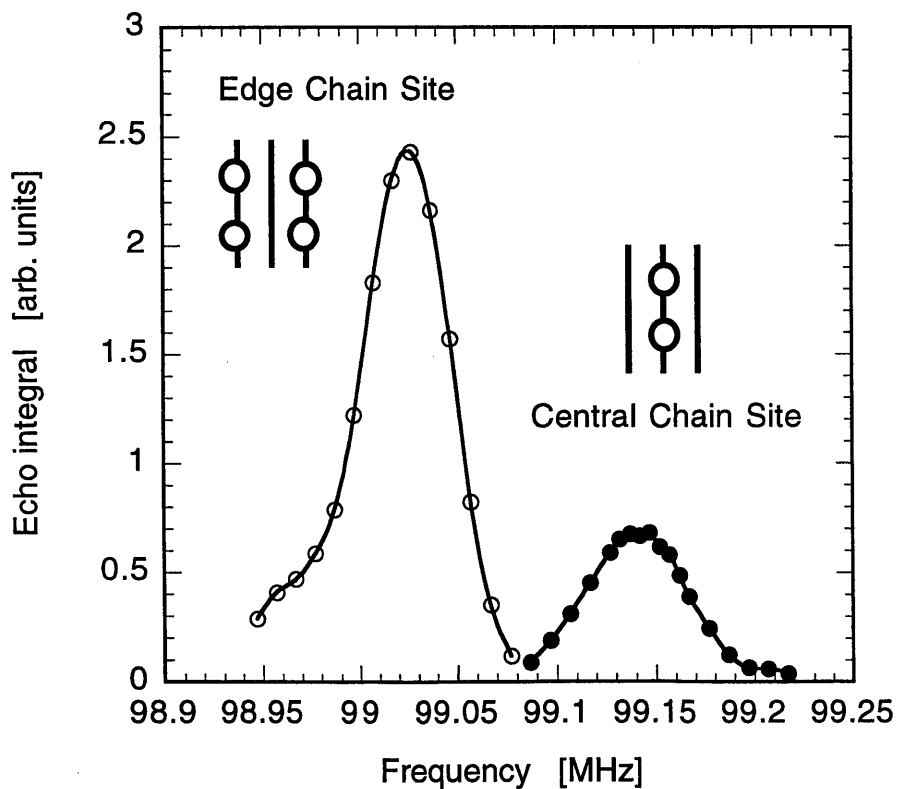


Figure 7-6: ^{63}Cu NMR central transition showing edge chain [o] and central chain [•] sites at 375 K, ($H = 8.67 \text{ T} \parallel c$).

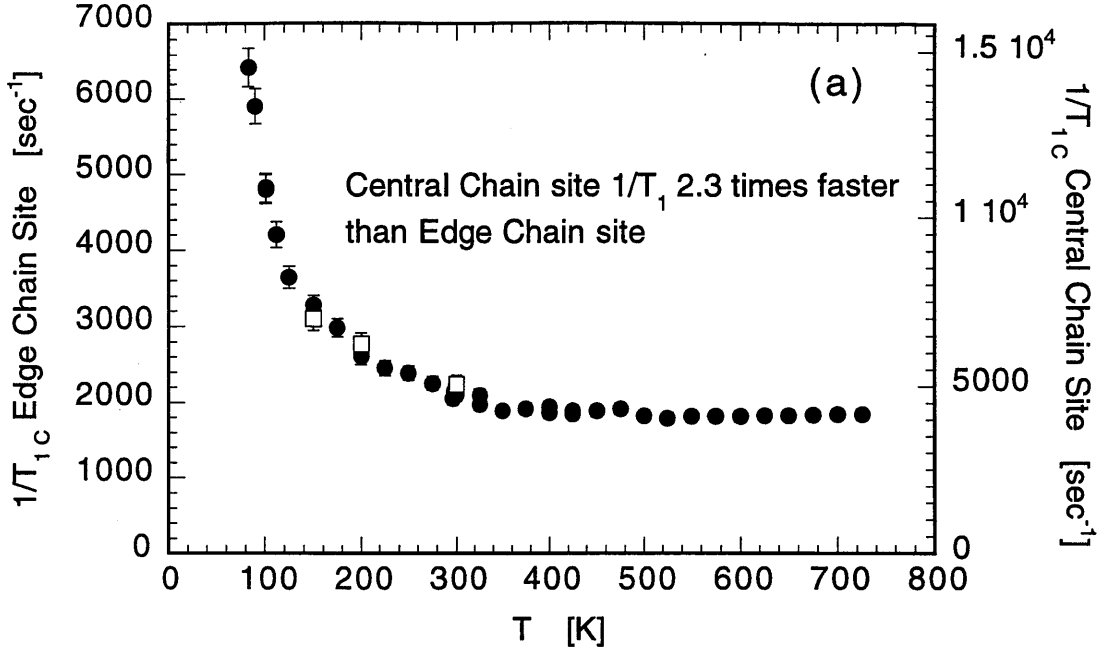


Figure 7-7: ^{63}Cu $1/T_{1c}$ for the edge chain site [●, left axis] and central chain site [□, right axis] of $\text{Sr}_2\text{Cu}_3\text{O}_5$.

is similar, as shown in figures 7-7 and 7-8. The simplest explanation for the similar temperature dependence, but different magnitude is that the hyperfine coupling is smaller for the edge chain Cu site, but that the magnetic susceptibility is the same at the two sites. Different hyperfine couplings for the two Cu sites is logical because the two sites have different local environments. Most notably, the edge chain site has only 3 Cu nearest neighbors, while the central chain site has 4 neighbors. The experimental fact that the two Cu sites have similar temperature dependence of the susceptibility is in contrast to a theoretical hint [132] that the central chain might even have a gapped form of the electron susceptibility.

We can confirm that the hyperfine couplings are different at wavevector $q = 0$ by comparing the Knight shift for the two sites. The Knight shift for the c axis at room temperature is 1.13% for the edge chain site and 1.30% for the central chain site. Knight shift for the a and b axes is $\approx 0.26\%$ for the edge chain site. Line superposition prevents any better measurement of the Knight shift along a and b. The $q = 0$ c axis hyperfine couplings (temperature dependence of Knight shift) are $-90 \pm 20 \text{ KOe}/\mu_B$ for the edge chain site and $-35 \pm 25 \text{ KOe}/\mu_B$ for the central chain

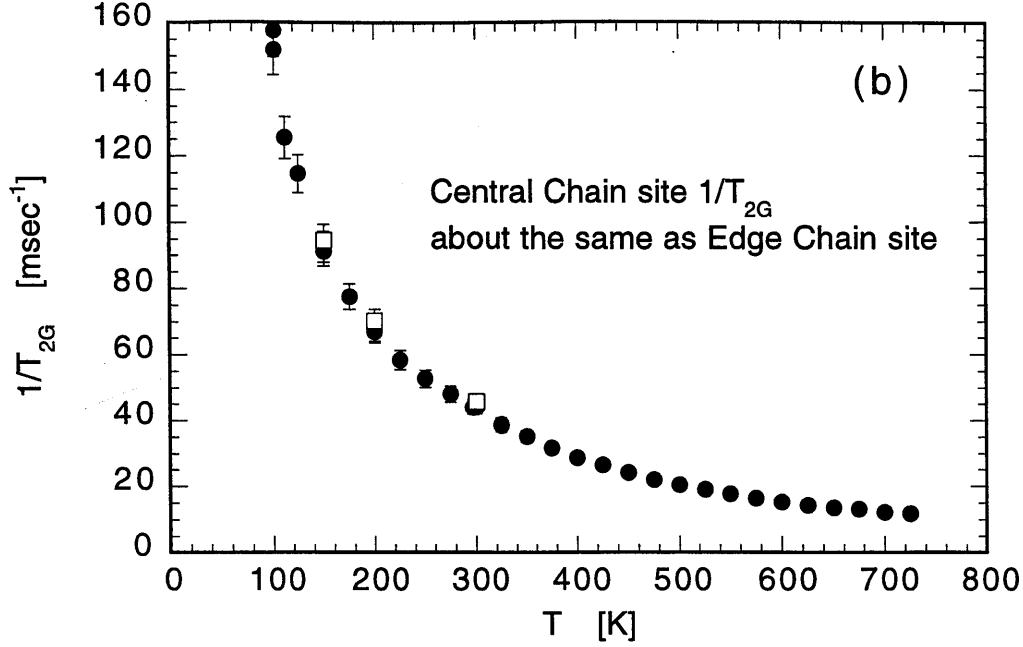


Figure 7-8: ^{63}Cu $1/T_{2G}$ for the edge chain site [●] and central chain site [□] of $\text{Sr}_2\text{Cu}_3\text{O}_5$.

site.

7.2 $1/T_1$ and $1/T_{2G}$

For this sample, $\text{Sr}_2\text{Cu}_3\text{O}_5$, $1/T_1$ and $1/T_{2G}$ have been measured below room temperature with both NQR and NMR. In addition to probing at different frequencies (NQR ~ 11 MHz and NMR ~ 100 MHz), NQR and NMR have slight differences in what is measured by $1/T_1$ and $1/T_{2G}$. For $1/T_1$, there are two major differences. First, the form of the exponential relaxation curve will be different. Second, for NMR the quantization axis of the spin is chosen by the applied magnetic field. However, for NQR the quantization axis is determined by the electric field gradient. As discussed in appendix A, if the electric field gradient is not symmetric about a crystal axis ($\eta \neq 0$), then $(1/T_1)_{NQR}$ is a combination of $(1/T_1)_{NMR}$ for different axes.

$$\left(\frac{1}{T_1}\right)_{NQR} = \left(\frac{1}{9 + 3\eta^2}\right) \left[4\eta^2 \frac{1}{T_{1ab}} + (9 - \eta^2) \frac{1}{T_{1c}}\right] \quad (7.1)$$

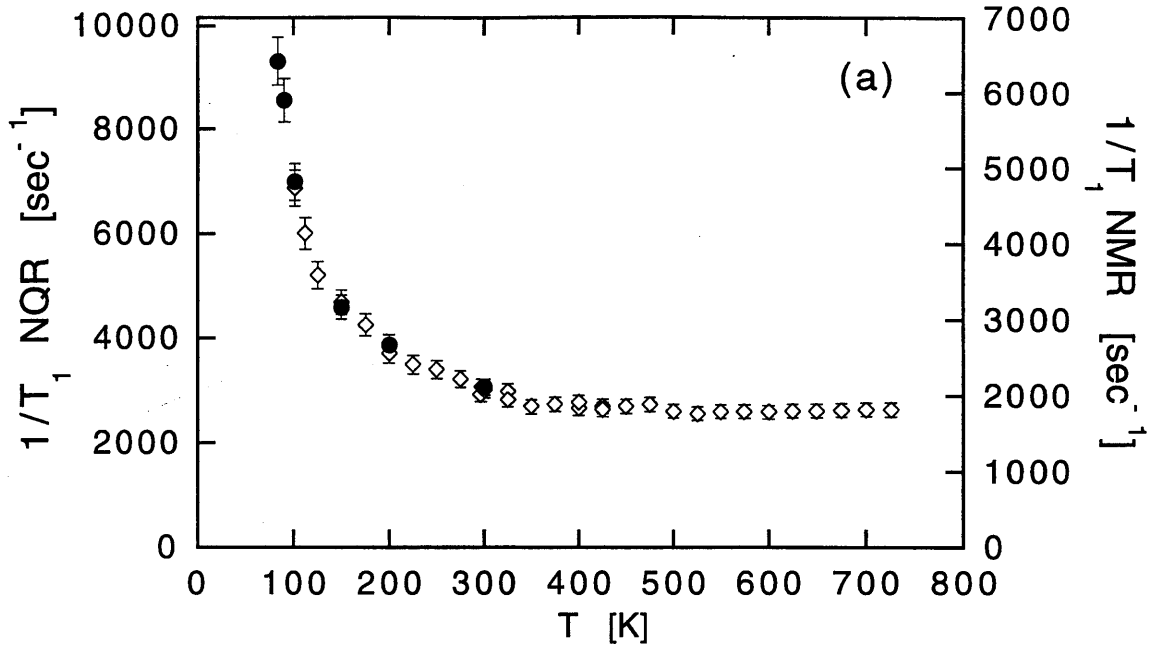


Figure 7-9: ^{63}Cu $1/T_1$ from NQR [◇, left axis] and ^{63}Cu $1/T_{1c}$ from NMR [●, right axis] for the edge chain site of $\text{Sr}_2\text{Cu}_3\text{O}_5$.

where subscript ab and c denote the direction of magnetic field.

The nuclear quadrupole interaction tensor $\nu_{Q\alpha}$ at the copper sites in ladders is not axially symmetric with respect to the c axis, $\eta = (\nu_{Qa} - \nu_{Qb})/\nu_{Qc} = 0.64$ and 0.17 for the edge and central chain of ladders, respectively [108]. For the edge chain site, we measured $1/T_1$ with both NQR and high field NMR as shown in figure 7-9, and confirmed the consistency of the experimental ratios, $T_{1c}/T_{1ab} = 3.4 \pm 0.2$ and $T_{1c}/T_{1,NQR} = 0.70 \pm 0.03$ with the theoretical expression, $T_{1c}/T_{1,NQR} = 0.72 \pm 0.02$. This implies that there is no significant frequency dependence in $1/T_1$ between 11 and 100 MHz. For the purpose of systematic comparison with other materials, we multiplied a factor 0.70 to the NQR results to deduce $\frac{1}{T_{1c}}$.

The theoretical comparison of $1/T_{2G}$ for NMR and NQR is discussed in appendix B and the experimental comparison for $\text{Sr}_2\text{Cu}_3\text{O}_5$ is shown in figure 7-10. Theoretically, $(1/T_{2G} \text{ NQR}) = \sqrt{2}\sqrt{6/7} (1/T_{2G} \text{ NMR}) = 1.31 (1/T_{2G} \text{ NMR})$ [26]. The factor of $\sqrt{2}$ arises from the fact that for nuclear spin $3/2$, there are twice as many same spin neighbors for NQR than for NMR. The small correction of $\sqrt{6/7}$ is from the measurement in a unaligned powder sample as compared to measurement in a crystal

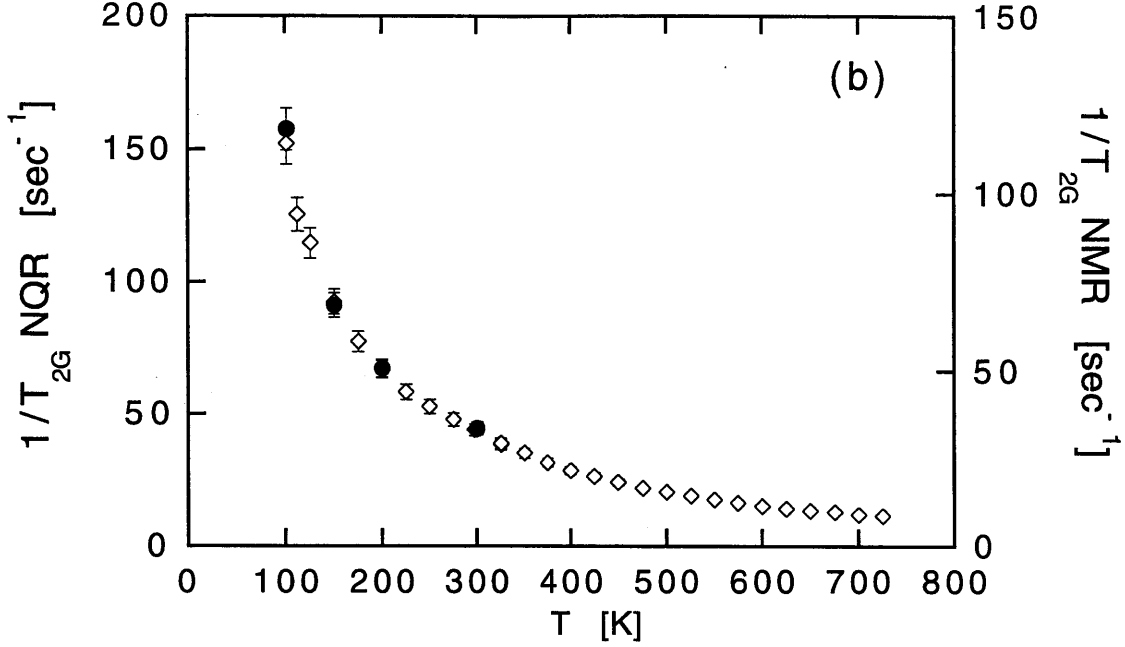


Figure 7-10: ^{63}Cu $1/T_{2G}$ from NQR [◇, left axis] and from NMR [●, right axis] for the edge chain site of $\text{Sr}_2\text{Cu}_3\text{O}_5$.

or aligned powder. Experimentally, $(1/T_{2G} \text{ NQR}) = 1.33 \pm 0.03 (1/T_{2G} \text{ NMR})$, in good agreement with the theoretical expectation.

The $1/T_1$ and $1/T_{2G}$ results for the three-leg ladder, $\text{Sr}_2\text{Cu}_3\text{O}_5$, both show diverging behavior with decreasing temperature. Qualitatively, this shows that the spin correlation length, ξ , is increasing strongly as the temperature decreases. This is as expected, in strong contrast to the 2-leg ladder, SrCu_2O_3 , which has a large spin gap and constant ξ at low temperatures.

For a more quantitative understanding, we can compare the results with recent theoretical results. According to recent weak coupling continuum theory by Buragohain and Sachdev[128], which is applicable $25 \text{ K} \ll T \lesssim 500 \text{ K}$ for $J = 1500 \text{ K}$, the spin structure factor is given as

$$\chi(q) = \frac{S(q)}{k_B T} \propto \left(\frac{1}{k_B T}\right) \left(\ln\left(\frac{T}{\Lambda_{MS}}\right)\right)^2 \frac{\xi}{(1 + (q - \pi)^2 \xi^2)} \quad (7.2)$$

with the cutoff, Λ_{MS} , roughly predicted as 25 K . $\Lambda_{MS} \sim J \exp(-2\pi/g)$ with the

coupling constant, g , given by [128]

$$g \approx \frac{2}{Sp} \left[1 + \left(1 - \frac{1}{p} \right) \frac{J_{\perp}}{J} \right]^{1/2} \quad (7.3)$$

where p is the number of legs of the ladder. Inserting this expression into eq. 2.33, the leading order temperature dependence of $1/T_{2G}$ is given as $1/T_{2G} \propto \sqrt{\xi}/T$, with logarithmic corrections that become significant at low temperatures. Since the spin-spin correlation length in a three-leg ladder is given as $\xi \sim \frac{1}{T}$ [128, 30], we expect $1/T_{2G} \sim T^{-3/2}$. Indeed, as shown in figure 7-11, we found power law behavior with exponent $-\frac{3}{2}$ above 300 K. We should note that this theory by Buragohain and Sachdev should also apply to the two-leg ladder at temperatures above the spin gap, $\Delta \approx 425$ K for SrCu_2O_3 . Indeed, $1/T_{2G}$ for the two-leg ladder at high temperatures is very similar to $1/T_{2G}$ for the three-leg ladder and does approach a $T^{-3/2}$ temperature dependence. Comparison of $1/T_1$ with the analytic theory is more difficult because we cannot estimate the large diffusive (i.e. $q = 0$) contributions in the quasi-1d regime. As in 2d copper-oxides, $1/T_1$ is constant at high temperatures ($T \sim \frac{J}{2}$).

In contrast with the mild temperature dependence at elevated temperatures, the divergence below 300 K is quite surprising. As shown in figure 7-12, the temperature dependence is exponential, similar to the case of the 2d square-lattice. The linearity in the semi-logarithmic plot extends for an order of magnitude. Within the framework of an isolated three-leg ladder, we expect that at $T \ll J$ the exchange interaction along a rung strongly couples the three $S = \frac{1}{2}$ spins into an effective $S_{eff} = \frac{1}{2}$, forming a $S_{eff} = \frac{1}{2}$ chain. Therefore, an isolated three-leg ladder would exhibit $1/T_{2G} \propto 1/\sqrt{T}$ and $1/T_1 \sim \text{constant}$ at low temperatures [45] as observed for 1d spin-chain Sr_2CuO_3 [48]. This clearly contradicts with the exponential divergence we find. Three-dimensional spin freezing observed at $T_{SF} = 52$ K [133] is unlikely to be the origin of the observed divergence, either, because the onset of the exponential divergence (~ 300 K) is nearly a factor of 6 higher than $T_{SF} = 52$ K. Furthermore, the temperature dependence is exponential rather than the ordinary power law divergence of $1/T_1$ and $1/T_{2G}$ expected near 3d orderings. The lack of 3d character is consistent

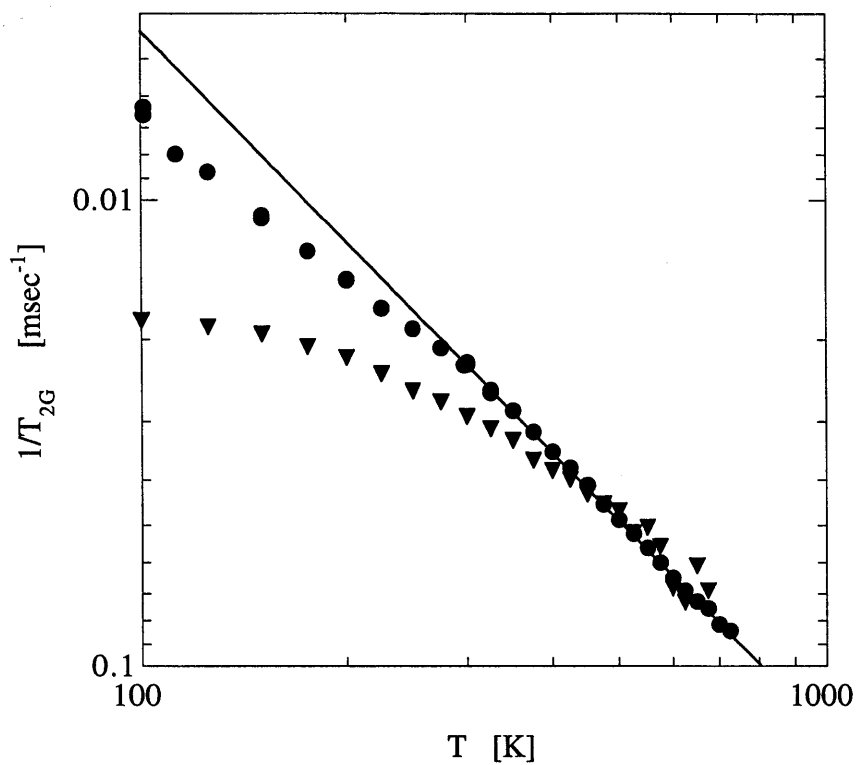


Figure 7-11: Temperature dependence of $^{63}\text{Ni}/T_{2G}$ plotted on a log-log scale for 3-leg ladder $\text{Sr}_2\text{Cu}_3\text{O}_5$ [•] and 2-leg ladder SrCu_2O_3 [▼]. Solid line shows fit to $1/T_{2G} \propto T^{-3/2}$ for $\text{Sr}_2\text{Cu}_3\text{O}_5$ above 300 K.

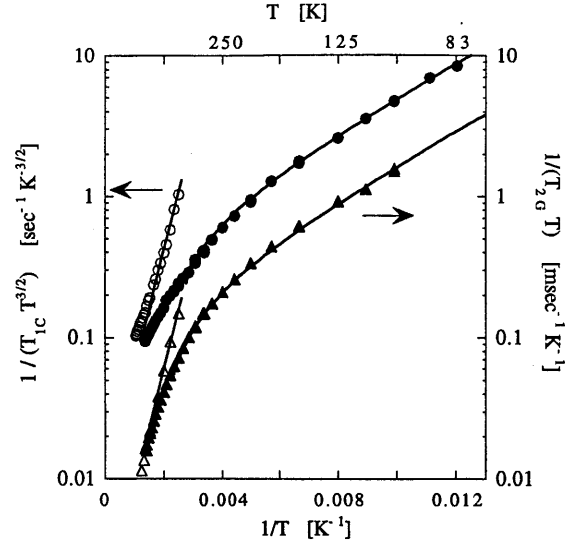


Figure 7-12: $1/(T_{1c}T^{3/2})$ (circles) and $1/(T_{2G}T)$ (triangles) versus $1/T$ for three-leg $\text{Sr}_2\text{Cu}_3\text{O}_5$ (solid symbols) and 2-d $\text{Sr}_2\text{CuO}_2\text{Cl}_2$ (open symbols). The fit to renormalized classical (exponential) behavior for $\text{Sr}_2\text{Cu}_3\text{O}_5$ $T < 225$ K gives $2\pi\rho_S^{eff} = 290 \pm 30$ K, implying anisotropy $\alpha = 0.16 \pm 0.02$ for $J = 1500$ K.

with the fact that the exchange coupling along the b axis is frustrated due to opposing pairs of 90° Cu-O-Cu bonds, which suppresses 3d correlations [36]. In a recent inelastic neutron scattering measurement for SrCuO_2 [53], which contains the same frustrated local structure, the spin correlation length along the direction equivalent to the b-axis in the present case (figure 7-2) is only 2.2 lattice spacings even at $T=0.35$ K. The frustrated interactions seem to prevent long range ordering in the direction of the frustrated interactions.

The key point to note is that, along the c axis, the three-leg ladders are stacked directly on top of one another as shown in figure 7-2(b). We recall that the so-called infinite layer compound $\text{Ca}_{0.85}\text{Sr}_{0.15}\text{CuO}_2$ has 2d square-lattice layers with a similar c-axis stacking, and has an equivalent structure to $\text{Sr}_2\text{Cu}_3\text{O}_5$ except for the line defect between adjacent three-leg ladders. In $\text{Ca}_{0.85}\text{Sr}_{0.15}\text{CuO}_2$, Néel ordering driven by the large c axis coupling, J_c , occurs at extremely high temperature, 539 K, and the dimensional crossover from isolated 2d square-lattice behavior to 3d behavior occurs as high as 600 K [131]. This was demonstrated by R. Pozzi, *et al.* (figure 7-13)

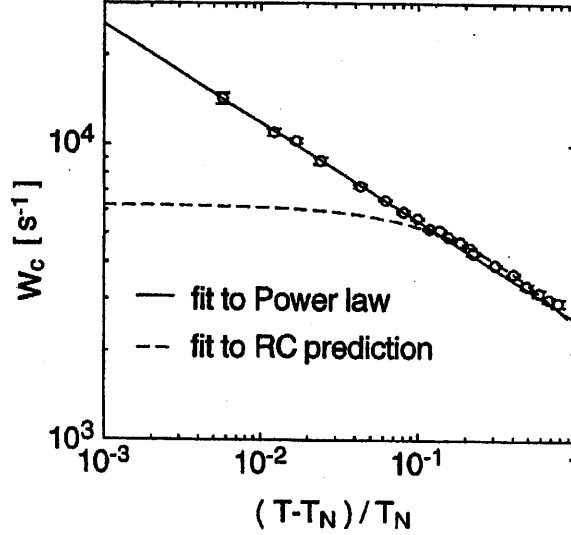


Figure 7-13: ^{63}Cu $1/T_1 = 2W_c$ for infinite layer compound, $\text{Ca}_{0.85}\text{Sr}_{0.15}\text{CuO}_2$ showing 3 dimensional critical behavior below 600 K (power law with the critical exponent $1/T_1 \propto [(T - T_N)/T_N]^w$, $w = -0.33$). (Néel temperature, $T_N = 540$ K.) From R. Pozzi, *et al.*[131]

showing that ^{63}Cu $1/T_1$ deviates from the exponential divergence expected of isolated 2d layers at ≈ 600 K and instead follows a 3d power law divergence. This evidence for strong c-axis coupling between the Cu-O layers in $\text{Ca}_{0.85}\text{Sr}_{0.15}\text{CuO}_2$ suggests that the three-leg ladders in $\text{Sr}_2\text{Cu}_3\text{O}_5$ will also couple strongly along the c-axis.

The existence of strong c-axis coupling in $\text{Sr}_2\text{Cu}_3\text{O}_5$ is supported by two sets of recent Monte Carlo simulations. First, Greven and Birgeneau showed that inter-layer coupling J_c along c-axis was essential to understand the 3d long-range order of Zn-doped two-leg ladder SrCu_2O_3 [134, 135]. Second, more recent Monte-Carlo simulations by Y.J. Kim *et al.* showed that inter-ladder coupling two-orders of magnitude smaller than J is sufficient to induce dimensional crossover from quasi-1d behavior of an isolated three-leg ladder to anisotropic 2d behavior of coupled three-leg ladders [129]. In the present case, the inter-ladder coupling along c-axis is large, $J_c^{\text{eff}}/J \cong (0.15 - 0.22)$ using estimates $J_c \sim 75 - 110$ K [136, 134], and $J = 1500$ K.

Coupled along the c-axis, the stacked three-leg ladders form a tri-layered 2d system with anisotropic exchange interactions, J along the ladders (a axis) and J_c (c axis). Since we do not have any theoretical treatment of such a complicated system, we

approximate the tri-layered system as a single layer system. This should be a good approximation for low temperatures where the spin correlation length ξ along the legs of the ladders is greater than the width of the ladders ($\xi > 3$). Both the 1-d ladder theory by Buragohain and Sachdev and our following anisotropic 2-d analysis show that we expect $\xi \approx 4$ to 5 at 250 K, where the crossover occurs. Below this temperature, the stacked three-leg ladders form an effective 2d plane of $S_{eff} = \frac{1}{2}$ with anisotropic exchange interactions, J along the a axis and the effective c axis coupling for the 2d model, $J_c^{eff} \approx 3J_c$, as shown in figure 7-2(c).

7.3 Anisotropic 2d model

This anisotropic 2 dimensional Heisenberg antiferromagnet has been studied theoretically with the anisotropic non-linear σ model [127, 129]. The anisotropic non-linear σ model is the same non-linear σ model discussed in chapter 5 [65], but with different exchange interactions for the two directions in the 2d plane. The non-linear σ model is a continuum field theory which should have the same long wavelength, low energy behavior as the Heisenberg antiferromagnet [65]. The anisotropic non-linear σ model has been discussed in recent papers [127] as a possible model for the magnetism of the stripe structure in doped high T_c superconductors. As shown in figure 7-1, the proposed stripe structure has undoped three-leg ladders separated by lines of doped holes. It has been suggested that the stripe structure would be well described by an anisotropic 2d model because the exchange interaction between the ladders is weakened by the line of doped holes compared to the exchange interaction along the ladders. However, we are not aware of any previous experimental evidence in an actual material that provides clear support for the relevance of the anisotropic non-linear σ model. In the following, we show that $1/T_1$ and $1/T_{2G}$ of the three-leg ladder material, $Sr_2Cu_3O_5$, are completely consistent with the anisotropic non-linear sigma model at low temperatures.

Theoretically, the anisotropy $\alpha = J_c^{eff}/J$ of the exchange interaction introduces anisotropy in the spin wave velocity c_0 and spin-spin correlation length ξ for the two

orthogonal directions, and reduces the isotropic spin stiffness $2\pi\rho_s$ to an effective $2\pi\rho_s^{eff}$ [127].

$$c_{\parallel}(\alpha) = \sqrt{(1+\alpha)/2} \cdot c_0 \quad (7.4)$$

$$c_{\perp}(\alpha) = \sqrt{\alpha}c_{\parallel}(\alpha) \quad (7.5)$$

$$2\pi\rho_s^{eff} = (1 - g_0(1)/g_c(\alpha)) \sqrt{\alpha}2\pi\rho_s \quad (7.6)$$

where $g_c(\alpha)$ is the critical coupling constant, and $g_0(1)$ is the bare coupling constant for $\alpha = 1$ [127]. The dependence of $g_c(\alpha)$ on α is given by [127]

$$g_c(\alpha) = \frac{4\pi\sqrt{2}}{\sqrt{1+\alpha} \left[1 + \left(\frac{2}{\pi}\right) \left\{ \sinh^{-1}(\sqrt{\alpha})/\sqrt{\alpha} + \ln(1 + \sqrt{1+\alpha}) - \ln(\sqrt{\alpha}[1 + \sqrt{2}]^2) \right\} \right]} \quad (7.7)$$

The critical coupling constant, $g_c(\alpha)$, determines the boundary between the renormalized classical and quantum disordered phases of the non-linear sigma model (see figure 5-1). Otherwise the theoretical framework of the renormalized classical regime in isotropic 2d square lattice [84, 26], which was successfully employed to analyze ^{63}Cu NQR/NMR relaxation rates in 2d square-lattice La_2CuO_4 [7, 26] and $\text{Sr}_2\text{CuO}_2\text{Cl}_2$ [63], is applicable to the anisotropic case. The renormalized classical regime will be valid for low temperatures, about $T < 2\pi\rho_s^{eff}$. For this renormalized classical regime of the non-linear sigma model, we have [127, 84, 26]

$$\frac{1}{T_1 T^{3/2}} \propto \left(\frac{1}{2\pi\rho_s^{eff}} \right)^{5/2} \exp\left(\frac{2\pi\rho_s^{eff}}{T} \right) \quad (7.8)$$

$$\frac{1}{T_{2G} T} \propto \frac{\hbar\sqrt{c_{\parallel}c_{\perp}}}{(2\pi\rho_s^{eff})^3} \exp\left(\frac{2\pi\rho_s^{eff}}{T} \right) \quad (7.9)$$

One important idea to note from these two equations is that the temperature dependencies of $1/T_1 T^{3/2}$ and $1/T_{2G} T$ are both exponential in $2\pi\rho_s^{eff}$. By fitting $1/T_1 T^{3/2}$ and $1/T_{2G} T$ in figure 7-12 to exponential form, we obtain the same slope for both, $2\pi\rho_s^{eff} = 290 \pm 30$ K. This implies an anisotropy, $\alpha = 0.16(0.17) \pm 0.02$ for $J = 1500(1300)\text{K}$, hence $J_c^{eff} = 230 \pm 30$ K. The obtained value of $\alpha = J_c^{eff}/J =$

0.16 ± 0.02 is consistent with the estimate of 0.15 - 0.22 in the previous section.

Another idea to note from equations 7.8 and 7.9 is that $1/(T_1 T^{3/2})$ and $1/(T_{2G} T)$ have prefactors to the exponential that depend differently on $c_{\parallel,\perp}$ and ρ_s^{eff} , and thus depend differently on α . We can use this to test the consistency of the preceding renormalized classical analysis by estimating α based on a different method that does not require knowing J . We will compare the prefactors to the exponential by taking the ratio, R , of $1/(T_1 T^{3/2})$ and $1/(T_{2G} T)$, which will cancel out the exponential term.

$$\begin{aligned}
R(\alpha, 2\pi\rho_s^{eff}) &= (T_1 T^{3/2})/(T_{2G} T) \cdot (F_{ab}(\pi)/F_c(\pi))^2 & (7.10) \\
&\propto \sqrt{(\hbar^2 c_{\parallel}(\alpha) c_{\perp}(\alpha)/2\pi\rho_s^{eff})} \cdot (F_{ab}(\pi)/F_c(\pi))^2 \\
&= f(\alpha) \sqrt{2\pi\rho_s^{eff}} \cdot (F_{ab}(\pi)/F_c(\pi))^2
\end{aligned}$$

where the function of α , $f(\alpha)$, is

$$f(\alpha) = \frac{1.48\sqrt{(1+\alpha)/2}}{\alpha^{1/4}(1-g_0(1)/g_c(\alpha))} \quad (7.11)$$

In the low-temperature renormalized classical limit, we expect the ratio, R , to be independent of temperature. The ratio of hyperfine form factors, $F_{ab}(\pi)/F_c(\pi)$, can be determined experimentally as 0.42 ± 0.02 from $T_{1c}/T_{1ab} = 3.4 \pm 0.2$. This results from the fact that $1/T_1$ from NMR measures the hyperfine form factors for the two axes perpendicular to the applied field, for example $1/T_{1c} \propto F_a(\pi)^2 + F_b(\pi)^2$. The hyperfine form factors for the a and b axes are the same within the experimental error. For $2\pi\rho_s^{eff}$, we take $2\pi\rho_s^{eff} = 290 \pm 30$ K from the fit in figure 7-12. In addition, we use the expression for c_0 in terms of $2\pi\rho_s^0$, $c_0 = \sqrt{2}Z_c J a/\hbar$ where $Z_c = 1.18$ [68] and $2\pi\rho_s^0 = 1.13J$. As a result, $\hbar c_0/a = 1.482\pi\rho_s^0$. $2\pi\rho_s^0$ can be expressed in terms of $2\pi\rho_s^{eff}$ and α (eq. 7.6). This leaves α as the only unknown parameter in $R(\alpha, 2\pi\rho_s^{eff})$. Shown in figure 7-14, the ratio $R(\alpha, 2\pi\rho_s^{eff})$ indeed approaches a constant 61 ± 5 at low temperatures, which implies $\alpha = 0.15 \pm 0.03$, in agreement with our earlier estimate, 0.16 ± 0.02 .

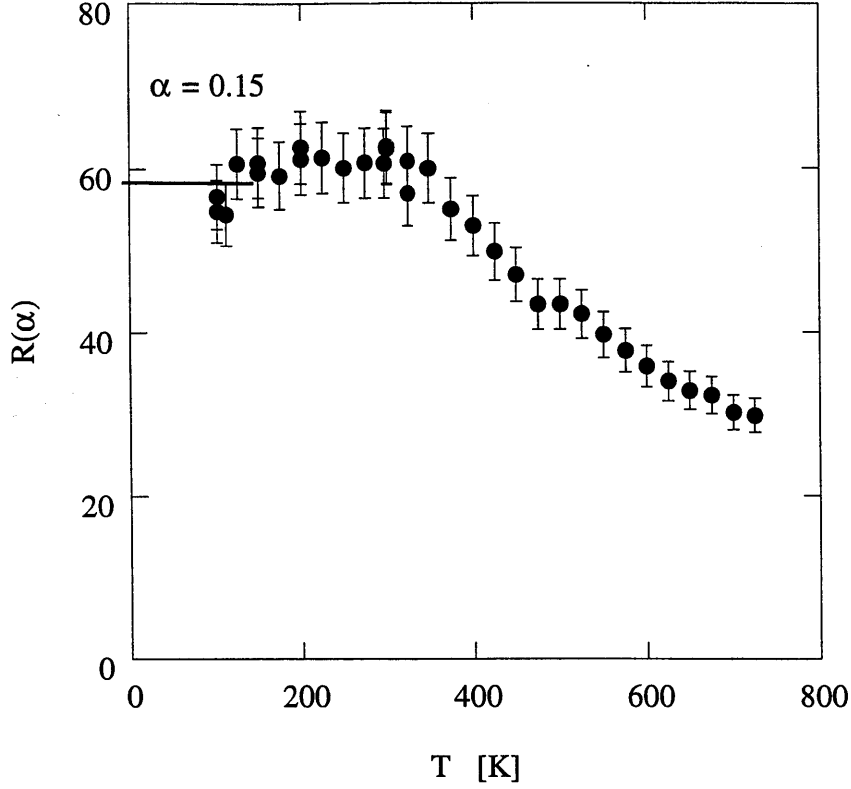


Figure 7-14: Ratio $R(\alpha, 2\pi\rho_s^{eff}) = (T_{1c}T^{3/2}/T_{2GT}) \cdot (F_{ab}^2/F_c^2)$ for three-leg $\text{Sr}_2\text{Cu}_3\text{O}_5$. The ratio should be constant in the low temperature limit deep inside the renormalized classical regime. The solid line shows the value of $R(\alpha, 2\pi\rho_s^{eff})$ calculated for $\text{Sr}_2\text{Cu}_3\text{O}_5$ ($\alpha = 0.15$, $2\pi\rho_s^{eff} = 290$ K).

From the fit of $1/(T_1T^{3/2})$ and $1/(T_{2GT})$ to the renormalized classical form, we obtain $|F_{a,b}(\pi)| = |A_{a,b} - 3B| \approx 65 \text{ KOe}/\mu_B$ and $|F_c(\pi)| = |A_c - 3B| \approx 160 \text{ KOe}/\mu_B$ for the edge chain copper site. Together with the values for the $q = 0$ hyperfine coupling, $F_{a,b}(0) = A_{a,b} + 3B \approx +60 \text{ KOe}/\mu_B$ [108] and $F_c(0) = A_c + 3B \approx -90 \text{ KOe}/\mu_B$, these values are consistent with a small transferred hyperfine coupling, $B \sim 10 - 20 \text{ KOe}/\mu_B$, as suggested by Ishida, *et al.* [108] and onsite hyperfine couplings, $A_{ab} \approx 0$ and $A_c \approx -125 \text{ KOe}/\mu_B$. These can be compared to results for 2d materials, such as $\text{Sr}_2\text{CuO}_2\text{Cl}_2$ discussed earlier in this thesis, [80, 7], $A_c \approx -90$ to $-170 \text{ kOe}/\mu_B$, $A_{ab} \approx 38 \text{ kOe}/\mu_B$, and $B \approx 40$. Most notably, the transferred hyperfine coupling is much smaller in the three-leg ladder, $\text{Sr}_2\text{Cu}_3\text{O}_5$, than in the 2d materials.

To conclude, we demonstrated that the temperature dependence of the spin-spin

correlation length ξ in $\text{Sr}_2\text{Cu}_3\text{O}_5$ is consistent with the isolated three-leg ladder behavior $\xi \sim \frac{1}{T}$ from 300 K to 725 K ($\sim J/2$). Below 300 K, we discovered dimensional crossover to anisotropic 2d regime, where spin correlations diverge exponentially. Our result is the first experimental demonstration of the validity of the anisotropic non-linear sigma model, which was recently proposed for the stripe phase of high T_c cuprates, in a $S = \frac{1}{2}$ quantum Heisenberg antiferromagnet. This should encourage further theoretical analysis of the stripe physics of high T_c cuprates based on the anisotropic non-linear sigma model.

Chapter 8

Conclusions

In this chapter, we summarize the conclusions from the NMR/NQR measurements on the copper-oxide materials. All of the copper oxide materials show symmetry of the quadrupole interaction and Knight shift that supports the accepted picture for the crystal chemistry of these materials. This picture is that there is one hole in the Cu $3d_{x^2-y^2}$ orbital, which is strongly hybridized with the neighboring oxygen $2p\sigma$ orbitals. In general, we use the comparison of ^{17}O and ^{63}Cu $1/T_1$ to reveal the wave-vector, q , dependence of the low energy electron spin excitations.

For the 1 dimensional compounds, Sr_2CuO_3 and SrCuO_2 , we can separate the $q = 0$ and $q = \pi$ contributions to $1/T_1$ using ^{17}O NMR. We find that in Sr_2CuO_3 the chain oxygen $1/T_1(q = 0) \propto aT + bT^2$ over the whole temperature range 10 to 700 K. The low temperature limit of these experimental results is in reasonable agreement with the low T scaling theory of Sachdev,[44] $1/T_1(q = 0) = aT$ where $a = F_{\perp}^2(q = 0) \frac{1}{\pi^3 J^2}$, but even at the lowest temperatures measured $T = 10\text{K}$ ($T/J \approx 0.005$), $1/T_1$ does not show the expected linear temperature dependence. Frequency dependence measurements show that diffusive contributions dominate $T_1(q \approx 0)$ for SrCuO_2 . The spin diffusion constant is estimated to be roughly two orders of magnitude larger at room temperature ($T/J \approx 0.13J$) than the high temperature value for the classical 1d spin chain. High temperature (up to 800 K) ^{63}Cu $1/T_1$ measurements in Sr_2CuO_3 and SrCuO_2 also show the increase in contributions to $1/T_1$ from $q = 0$ at high temperatures. However, the increase in $1/T_1$ at high temperatures is only seen for

the magnetic field applied in the plane of the Cu-O square for both materials. $1/T_1$ for the magnetic field perpendicular to the Cu-O plane seems to follow the expectations of the theory for $q = \pi$ by Starykh, *et al.*[45]. We do not understand why this is the opposite of what one would expect theoretically based on the relative sizes of the hyperfine interactions at $q = \pi$ and $q = 0$. The Knight shift of Sr_2CuO_3 for the oxygen chain site shows a sharp decrease at low temperatures ($T < 25$ K). This provides solid confirmation of the bulk susceptibility measurement [51] which also shows a sharp decrease, partly obscured by the impurity Curie susceptibility. Such a sharp decrease in the spin susceptibility is predicted theoretically for the spin $1/2$ 1d Heisenberg chain. However, the decrease does not agree quantitatively between experiment and theory, with the experimental decrease of the spin susceptibility being larger and beginning at higher temperatures. The double chain compound, SrCuO_2 , shows 1-d behavior analogous to that of Sr_2CuO_3 in the NMR measurements above 10 K, implying that the frustrated interactions between the pairs of chains do not affect the spin dynamics above 10 K.

For the 2d material, $\text{Sr}_2\text{CuO}_2\text{Cl}_2$, we demonstrated that ^{63}Cu $1/T_1$ and $1/T_{2G}$ have the exponential temperature dependence expected for the renormalized classical regime of the quantum non-linear sigma model [65]. This was previously shown for La_2CuO_4 [7, 26]. We also show that ^{17}O NMR measures the spin wave damping, Γ , in the undoped antiferromagnet for short wavelengths [63]. We deduced the effective damping Γ of the short wavelength magnons of the $S = 1/2$ 2d Heisenberg antiferromagnet in a broad range of temperature ($0.2 \leq T/J \leq 0.5$), contrary to the prevailing perception in the community that Γ was not measurable with current technology [3]. The spin wave damping is small even at temperatures as high as $T = 0.4J$, well above T_N . This clarifies one of the unique properties of these 2d copper-oxide antiferromagnetic materials: there is a wide temperature range where short range spin excitations exist with long lifetimes, without long range 3-dimensional order. The low energy, short wavelength excitations in the hole-doped, weakly-metallic CuO_2 planes show a similar temperature dependence to the undoped sample, but with a weakly temperature dependent increase from the addition of electron-hole pair excitations. We

suggest that the spin waves may interact strongly with electron-hole pair excitations.

For the two-leg ladder, we have NMR/NQR experiments on both undoped, SrCu_2O_3 and $\text{La}_6\text{Ca}_8\text{Cu}_{24}\text{O}_{41}$, and doped materials, $\text{A}_{14}\text{Cu}_{24}\text{O}_{41}$ ($\text{A} = \text{La}, \text{Sr}, \text{Ca}$). By measuring ^{63}Cu $1/T_1$ and $1/T_{2G}$ to temperatures well above the spin gap, $\Delta \leq 425$ K, we demonstrate the crossover in spin dynamics from the gapped low temperature regime ($1/T_1 \sim \exp(-\Delta/k_B T)$) to the high temperature paramagnetic regime. This allows the spin gap, Δ , to be well-determined as well as exploring the temperature dependence in the paramagnetic regime. Curiously, we found that the temperature dependence of $1/T_1$ in the paramagnetic regime differs for the undoped and doped 2-leg ladder samples. At temperatures above the spin gap, for the undoped samples, $1/T_1 \propto T$, while the doped samples show constant $1/T_1$. This new finding has not been understood theoretically [123, 122]. Also reported are the first ^{17}O NMR results in these materials. Comparison of Cu and O NMR results provides wave vector dependent information about spin excitations. Oxygen NMR can also allow us to estimate the exchange couplings for the ladder, J_\perp/J_\parallel .

In the doped two-leg ladder materials, $\text{A}_{14}\text{Cu}_{24}\text{O}_{41}$, the crossover of the spin excitations from the spin gapped regime to the paramagnetic regime is accompanied by changes in the charge properties. The changes in ^{17}O quadrupole interaction clearly show that in the doped two-leg ladder material, $\text{A}_{14}\text{Cu}_{24}\text{O}_{41}$, the doped holes are mobile above a temperature scale, T^* , which is correlated with the spin gap energy scale. The effective doping of the measured oxygen sites increases with increasing temperature.

For the three-leg ladder $\text{Sr}_2\text{Cu}_3\text{O}_5$, we report the first ^{63}Cu NQR measurements of the ^{63}Cu nuclear spin-lattice relaxation rate $1/T_1$ and the Gaussian component of spin-spin relaxation rate $1/T_{2G}$ from 83 K up to 725 K. From the Gaussian component of the ^{63}Cu nuclear spin-spin relaxation rate, $1/T_{2G}$, we present evidence that the spin-spin correlation length ξ in the three-leg ladder follows the 1d form $\xi \sim \frac{1}{T}$ above 300 K. To our surprise, however, we found that weak inter-ladder coupling along the c axis results in dimensional crossover to a quasi-2d regime below 300 K, where ξ diverges exponentially, $\xi \sim \exp\left(\frac{2\pi\rho_s}{T}\right)$ ($2\pi\rho_s = 290 \pm 30$ K is the effective spin

stiffness). The anisotropic non-linear sigma model [127] successfully describes the static and dynamic NQR/NMR properties in the quasi-2d regime. To the best of our knowledge, our result is the first experimental demonstration of the validity of the anisotropic non-linear sigma model, which was recently proposed for the stripe phase of high T_c cuprates, in a $S = \frac{1}{2}$ quantum Heisenberg antiferromagnet. This should encourage further theoretical analysis of the stripe physics of high T_c cuprates based on the anisotropic non-linear sigma model.

Appendix A

$1/T_1$ and $1/T_{2L}$ for NQR, $\eta \neq 0$, $I=3/2$

In this appendix, I will discuss how $1/T_1$ and $1/T_{2L}$ differs when measured by NMR versus NQR. The difference arises from the difference in the axis for the interaction of the nuclear spin. For NMR, the applied magnetic field determines the axis for the nuclear spin interactions. For NQR, the electric field gradient tensor of the crystal defines the geometry of the quadrupole interactions. In general, $1/T_1$ as measured by NMR and NQR are sensitive to magnetic fluctuations in different directions. If there is anisotropy in the magnetic fluctuations that cause the relaxation of the nuclear spin, there can be a difference in the measured $1/T_1$ values. First, we will derive the expectation for $1/T_1$ measured by NQR and we relate that to $1/T_1$ from NMR measured along the crystal axes. Second, we will use the result for $1/T_1$ to also provide the contribution to $1/T_2$ from these T_1 processes, $1/T_{2L}$. All of the following results are specific for $I=3/2$ and relaxation via fluctuation of magnetic fields.

For $\eta \neq 0$, the spin eigenvectors for NQR are not along any of the crystal axes. As a reference, these calculations were done for $\eta = 1$ in Pennington's thesis [14]. For NQR, we have the hamiltonian [13],

$$\mathcal{H} = \frac{e^2qQ}{4I(2I-1)} \left\{ 3I_Z^2 - I(I+1) + \frac{1}{2}\eta(I_+^2 + I_-^2) \right\} \quad (\text{A.1})$$

The X, Y, and Z axes are the principle axes of the electric field gradient tensor defined so that the components of the electric field gradient,

$$|V_{ZZ}| \geq |V_{YY}| \geq |V_{XX}|, eq = V_{ZZ} \quad (\text{A.2})$$

$$\eta = \frac{V_{XX} - V_{YY}}{V_{ZZ}} \quad (\text{A.3})$$

By choosing the basis of spin states as $[-+3/2i, -+1/2i, -1/2i, -3/2i]$ for I_Z , the hamiltonian in matrix form for the spin quantization axis along Z is

$$\mathcal{H} = \frac{e^2qQ}{4I(2I-1)} \begin{pmatrix} 3 & 0 & \sqrt{3}\eta & 0 \\ 0 & -3 & 0 & \sqrt{3}\eta \\ \sqrt{3}\eta & 0 & -3 & 0 \\ 0 & \sqrt{3}\eta & 0 & 3 \end{pmatrix} \quad (\text{A.4})$$

Since this is only a 4x4 matrix, finding the eigenvalues and eigenvectors is not too difficult. The eigenvalues are

$$\pm \frac{e^2qQ}{4I(2I-1)} \left(3\sqrt{1 + \frac{\eta^2}{3}} \right) \quad (\text{A.5})$$

with eigenvectors a, b, c, d

$$\begin{aligned} a &: \frac{1}{N_1} (0, -\sqrt{3} - \sqrt{3 + \eta^2}, 0, \eta) \\ b &: \frac{1}{N_2} (0, -\sqrt{3} + \sqrt{3 + \eta^2}, 0, \eta) \\ c &: \frac{1}{N_2} (\sqrt{3} - \sqrt{3 + \eta^2}, 0, \eta, 0) \\ d &: \frac{1}{N_1} (\sqrt{3} + \sqrt{3 + \eta^2}, 0, \eta, 0) \end{aligned} \quad (\text{A.6})$$

where the normalization constants, $N_{1,2}$ are

$$N_1 = \sqrt{6 + 2\eta^2 + 2\sqrt{3}\sqrt{3 + \eta^2}} \quad (\text{A.7})$$

$$N_2 = \sqrt{6 + 2\eta^2 - 2\sqrt{3}\sqrt{3 + \eta^2}} \quad (\text{A.8})$$

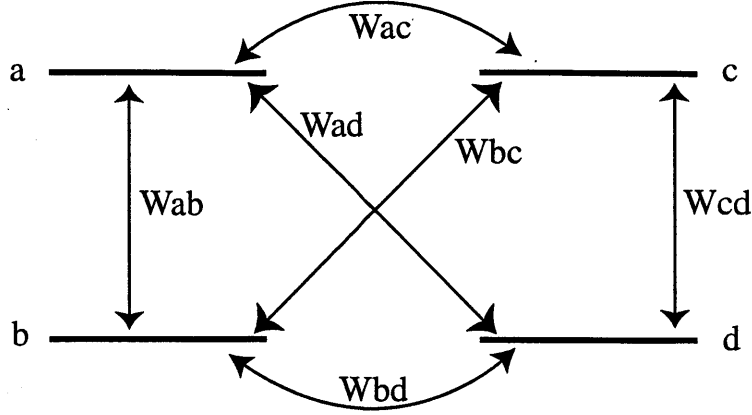


Figure A-1: NQR energy level diagram for the $I=3/2$ eigenstates with transition rates, W_{km} shown.

When $\eta = 0$, (d) is $-+3/2i$, (a) is $-+1/2i$, (c) is $--1/2i$, (b) is $--3/2i$.

The energy level diagram with the possible transitions between the levels is shown in figure A-1. For the rest of these calculations, we will be following the procedure of Slichter, p. 190-198 [15] and Pennington's thesis p. 119 [14].

We need to calculate the transition probabilities, W_{km} , between the energy levels, k , m . For correlation time, τ_0 , of the magnetic fluctuations much shorter than the NQR or NMR time scale $1/\omega_n$, [15]

$$W_{km} = \sum_q \gamma_n^2 h_q^2 | \langle m | I_q | k \rangle |^2 2\tau_0 \quad (\text{A.9})$$

where h_q is the magnetic field of the fluctuation and the sum is over the crystal axes (q). With this definition,

$$\left(\frac{1}{T_1} \right)_{NMR} = 2W_{1/2, -1/2} \quad (\text{A.10})$$

Applying this formalism, for NMR with the magnetic field applied along the z axis,

$$\left(\frac{1}{T_{1,z}} \right)_{NMR} = \gamma_n^2 \tau_0 (h_x^2 + h_y^2) \quad (\text{A.11})$$

We will use this result (and the symmetric results for the other axes) for comparison with the derivation for NQR $1/T_1$.

Now we need to know the transition probabilities shown in figure A-1. Actually,

we do not need to know all of them, just the ones which transition between the different energy levels. Using eq.A.9 and the eigenvectors,

$$W_{ab} = 2\gamma_n^2\tau_0 \left(\frac{\eta^2}{3 + \eta^2} \right) h_z^2 \quad (\text{A.12})$$

$$W_{ad} = \frac{1}{2}\gamma_n^2\tau_0 \left(\frac{1}{3 + \eta^2} \right) [(3 + \eta)^2 h_x^2 + (3 - \eta)^2 h_y^2] \quad (\text{A.13})$$

Also, $W_{cd} = W_{ab}$ and $W_{bc} = W_{ad}$ as might be expected by symmetry. As we expect $W_{ab} \rightarrow 0$ as $\eta \rightarrow 0$, because this transition is not allowed for $\eta = 0$.

The differential equation for these energy levels is [14],

$$\frac{d}{dt} \begin{pmatrix} a \\ b \\ c \\ d \end{pmatrix} = \begin{pmatrix} -(1+2+3) & 1 & 2 & 3 \\ 1 & -(1+3+4) & 3 & 4 \\ 2 & 3 & -(1+2+3) & 1 \\ 3 & 4 & 1 & -(1+3+4) \end{pmatrix} \begin{pmatrix} a \\ b \\ c \\ d \end{pmatrix} \quad (\text{A.14})$$

where $1 \equiv W_{ab}$, $2 \equiv W_{ac}$, $3 \equiv W_{ad}$, $4 \equiv W_{bd}$.

In an NQR T_1 experiment, we reverse the populations of the higher and lower energy states, so the initial condition (the difference between the excited state and thermal equilibrium) is

$$(1, -1, 1, -1) \quad (\text{A.15})$$

This is an eigenvector of the transition matrix with eigenvalue $-2(W_{ab} + W_{ad})$. This means that the NQR relaxation is a single exponential with spin-lattice relaxation rate,

$$\left(\frac{1}{T_1} \right)_{NQR} = 2(W_{ab} + W_{ad}) \quad (\text{A.16})$$

$$\left(\frac{1}{T_1} \right)_{NQR} = \gamma_n^2\tau_0 \left\{ \left(\frac{1}{3 + \eta^2} \right) [(3 + \eta)^2 h_x^2 + (3 - \eta)^2 h_y^2] + \left(\frac{4\eta^2}{3 + \eta^2} \right) h_z^2 \right\} \quad (\text{A.17})$$

Using eq. A.11, we can write $1/T_{1,NQR}$ in terms of the values that would be obtained

for $1/T_1$ by NMR with the magnetic field applied along each of the crystal axes.

$$\left(\frac{1}{T_1}\right)_{NQR} = \left(\frac{1}{3 + \eta^2}\right) \left[2\eta(\eta - 3)\frac{1}{T_{1,x}} + 2\eta(\eta + 3)\frac{1}{T_{1,y}} + (9 - \eta^2)\frac{1}{T_{1,z}} \right] \quad (\text{A.18})$$

where $1/T_{1,\alpha}$ refers to the value for NMR with the magnetic field applied along the axis α .

We remind the reader that this applies *only* to $I=3/2$ and magnetic relaxation. This formula has the correct limiting behavior as $\eta = 0$,

$$\left(\frac{1}{T_1}\right)_{NQR,(\eta=0)} = 3\frac{1}{T_{1,z}} \quad (\text{A.19})$$

A.1 $1/T_{2L}$ for $\eta \neq 0$

The same processes that cause spin-lattice relaxation, $1/T_1$ also cause transverse relaxation, $1/T_2$. These processes will cause Lorentzian (exponential) relaxation, $1/T_{2L}$. In fact, for magnetic relaxation, we can calculate the expected value of the exponential component of T_2 , T_{2L} , from T_1 using Redfield theory ([15] section 5.4-5.11). We can use the above results for $1/T_1$ to also calculate the contribution to $1/T_2$ from these T_1 processes, $1/T_{2L}$.

To calculate for NQR when $\eta \neq 0$, we follow the density matrix calculations strategy laid out in Slichter chapter 5 [15].

$$\frac{1}{T_{2L}} = \sum_{\alpha, \alpha', \beta, \beta'} R_{\alpha\alpha'\beta\beta'} \rho_{\beta\beta'} \langle \alpha' | I_x | \alpha \rangle \quad (\text{A.20})$$

where $\alpha, \alpha', \beta, \beta'$ refer to the quantum states and $\rho_{\beta\beta'}$ is the density matrix.

$$R_{\alpha\alpha'\beta\beta'} = \frac{1}{2\hbar^2} \left[J_{\alpha\beta\alpha'\beta'}(\alpha' - \beta') + J_{\alpha\beta\alpha'\beta'}(\alpha - \beta) - \delta_{\alpha'\beta'} \sum_{\gamma} J_{\gamma\beta\gamma\alpha}(\gamma - \beta) - \delta_{\alpha\beta} \sum_{\gamma} J_{\gamma\alpha'\gamma\beta'}(\gamma - \beta') \right] \quad (\text{A.21})$$

$$J_{\alpha\alpha'\beta\beta'}(\omega) = \int_{-\infty}^{\infty} \langle \alpha | H_f(t) | \alpha' \rangle \langle \beta' | H_f(t + \tau) | \beta \rangle \exp(-i\omega\tau) d\tau \quad (\text{A.22})$$

where H_f is the fluctuating magnetic field causing the relaxation.

We should note that it is also possible to calculate $1/T_1$ this way, but this would be the hard way.

$$\frac{1}{T_1} = \sum_{\alpha, \alpha', \beta, \beta'} R_{\alpha\alpha'\beta\beta'} \rho_{\beta\beta'} \langle \alpha' | I_z | \alpha \rangle \quad (\text{A.23})$$

For example, for NMR these expressions simplify quite a bit.

$$\frac{1}{T_{2L}} = R_{\alpha, \alpha-1, \alpha, \alpha-1} \quad (\text{A.24})$$

$1/T_{2L}$ has been previously calculated for $I = 3/2$ for NMR, and for NQR when $\eta = 0$ [14].

$$\left(\frac{1}{T_{2L,z}} \right)_{1/2 \leftrightarrow -1/2} = \frac{1}{2} \left(\frac{1}{T_{1,x}} + \frac{1}{T_{1,y}} \right) + 3 \left(\frac{1}{T_{1,z}} \right) \quad (\text{A.25})$$

$$\left(\frac{1}{T_{2L,z}} \right)_{\pm 3/2 \leftrightarrow \pm 1/2} = \frac{1}{2} \left(\frac{1}{T_{1,x}} + \frac{1}{T_{1,y}} \right) + 2 \left(\frac{1}{T_{1,z}} \right) \quad (\text{A.26})$$

where $1/T_{1,\alpha}$ refers to the value of $1/T_1$ for NMR when the magnetic field is applied along the direction α .

When $\eta \neq 0$, unfortunately many terms that were previously zero are no longer obviously zero, so the calculation involves many $J_{\alpha\alpha'\beta\beta'}(\omega)$ terms. For example,

$$J_{b,a,b,a} = \frac{\eta^2}{(3 + \eta^2)} \hbar^2 k_{zz}(\omega_n) \quad (\text{A.27})$$

$$J_{d,b,a,c} = \frac{\eta(\eta - 3)}{(3 + \eta^2)} \hbar^2 k_{xx}(0) + \frac{-\eta(\eta + 3)}{(3 + \eta^2)} \hbar^2 k_{yy}(0) \quad (\text{A.28})$$

where the states a,b,c,d were defined at the beginning of this appendix. These terms are obviously zero when $\eta = 0$.

Summing up all the relevant $R_{\alpha\alpha'\beta\beta'}$ terms, we derive results for $1/T_{2L}$. Using the formalism of Slichter [15],

$$\left(\frac{1}{T_{2L}} \right)_{NQR} = \left(\frac{1}{3 + \eta^2} \right) \left[\frac{(15 + 3\eta^2)}{2} (\hbar_x^2 + \hbar_y^2) \tau_0 + (3 + 3\eta^2) \hbar_z^2 \tau_0 \right] \quad (\text{A.29})$$

Using eq. A.11,

$$\left(\frac{1}{T_{2L}}\right)_{NQR} = \left(\frac{1}{3 + \eta^2}\right) \left[(3 + 3\eta^2) \frac{1}{T_{1,xy}} + 6 \frac{1}{T_{1,z}} \right] \quad (\text{A.30})$$

We remind the reader that $1/T_{1,\alpha}$ refers to the *NMR* results for the field along the axis α . This means that NQR $1/T_1$ alone is not enough to specify $1/T_{2L}$. The anisotropy for $1/T_1$ by NMR along the different axes needs to be known or estimated. We should note that the change in $1/T_{2L}$ as a function of η is not that strong because all three crystal axes are included in the original expression. In contrast, the difference between $1/T_1$ measured by NMR and NQR can be considerable. This happens because non-zero η adds an h_z component to NQR $1/T_1$. In these copper-oxides, there is a large anisotropy in the magnetic field fluctuations at the copper nucleus with $h_z > h_x \approx h_y$. As an example, we take the edge chain copper site of $\text{Sr}_2\text{Cu}_3\text{O}_5$, which has a large $\eta = 0.64$ and an anisotropy of $1/T_1$, $(1/T_{1,xy}/1/T_{1,z}) = 3.6$. $1/T_{2L}$ differs from the $\eta = 0$ value by only 15%, while $1/T_1$ from NQR is 43% larger than $1/T_{1,z}$ from NMR. As a final note, then, it is crucial to remember that the $1/T_1$ values on the right hand side of equation A.30 are the NMR values. Also, it is interesting to note that this result for $1/T_{2L}$ can be more easily derived from the result that we obtained above for $1/T_1$.

Appendix B

$1/T_{2G}$ NQR for unaligned samples

In a two spin system, the Gaussian nuclear spin-spin relaxation rate, $1/T_{2G}$, measures the coupling, a , between nuclear spins.

$$\left(\frac{1}{T_{2G}}\right)^2 = \frac{a_{zz}^2}{4} \quad (\text{B.1})$$

$$\mathcal{H} = a_{zz}I_z(1)I_z(2) \quad (\text{B.2})$$

This nuclear spin-spin relaxation occurs even with a spin echo pulse sequence. This happens because both nuclei that are interacting are flipped by the π pulse, so the spin dephasing is not canceled by the spin echo pulse sequence. If the second nuclei spin, $I_z(2)$, is “different” from the first, in the sense that the second spin is not flipped by the π pulse that flips the first spin, the spin dephasing caused by the spin-spin interaction will cancel out. Deriving the coupling constant between the nuclei spins from the experimental value of $1/T_{2G}$ relies on accurate knowledge of how many of the coupled nuclei can be considered as “like” nuclei. “Like” nuclei are defined by the fact that their spins are flipped by the applied π pulse.

Our goal in this calculation is to calculate what the measured value of $1/T_{2G}$ is for NQR when the sample is unaligned, so the crystal axes are random with respect to H_1 , the rf magnetic field applied for the spin flip pulses. The overall plan is to calculate the measured $1/T_{2G}$ for an arbitrary angle, θ , between the principle axis of the quadrupole interaction and H_1 . Then, at the end, we will average over θ to

account for the random distribution of angles. We shall assume that $\eta = 0$, so the spin eigenvectors for NQR are quantized along the principle axis of the quadrupole interaction. As an added bonus, along the way we shall determine the relative NQR intensity for an unaligned sample versus an aligned sample with H_1 perpendicular to the principle axis of the quadrupole interaction.

For this calculation, I will use a spin 1/2 model. This is appropriate because here we are dealing with NQR which is effectively a two state system, $\pm 1/2$ and $\pm 3/2$. Of course, using a two state system simplifies the calculation immensely. The quantum state of any two state system, like spin 1/2, can be represented as a unit vector in three-dimensional space. The transformations that we apply can be represented by rotations in three-dimensional space (for reference see Slichter, back cover [15]).

The pulse sequence used to measure $1/T_{2G}$ is $\pi/2$ pulse- τ - π pulse- τ -echo where the delay time τ is varied to measure the τ dependence of the echo integral, $M(2\tau)$.

$$M(2\tau) = M(0) \exp\left(\frac{-2\tau}{T_{2L}}\right) \exp\left(\frac{-(2\tau)^2}{2T_{2G}^2}\right) \quad (\text{B.3})$$

The length of the two pulses are designed to “rotate” the spin through an angle of $\pi/2$ and π . Experimentally, the pulse lengths are chosen to maximize the echo integral. In an unaligned sample, it is not clear a priori that this criteria corresponds to the same pulse lengths as would be used in an aligned sample. In the end, we shall find that the peak of intensity in an unaligned sample corresponds to the same ($\pi/2$ - π) pulse lengths as used in an aligned sample, but for the calculations we shall use arbitrary angles h and $2h$ for the rotation angles of the first and second pulses respectively.

To demonstrate the method of calculation, I will first show the calculation of the intensity for the unaligned sample relative to an aligned sample without any spin-spin coupling. Once the nuclear spin-spin coupling is added, the calculation follows the same format, only the complexity increases.

The calculation essentially follows the pulse sequence. We start with the initial conditions with a net spin aligned with the quadrupole axis. Then, we apply the appropriate transformations in sequence. The transformation that we need is for

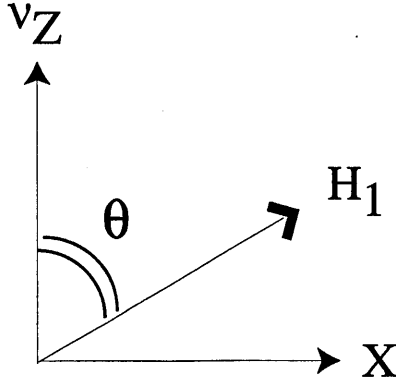


Figure B-1: Geometry of H_1 and the quadrupole interaction for this calculation. The axes X, Y, Z , are defined by the quadrupole interaction with Z being the principle axis. H_1 lies in the Z - X plane at an angle θ with the Z (quadrupole) axis.

rotation around the z axis by an angle x ,

$$R_z[x] = \begin{pmatrix} \cos(x) & -\sin(x) & 0 \\ \sin(x) & \cos(x) & 0 \\ 0 & 0 & 1 \end{pmatrix} \quad (\text{B.4})$$

The other tool that we need is the change of coordinates transformation between the quadrupole axes and the axis of H_1 . Since we have assumed that $\eta = 0$, we are free to choose H_1 as being in the z - x plane and having an angle θ with the principle quadrupole axis (figure B-1).

$$R_{toH1} = \begin{pmatrix} \cos(\theta) & 0 & \sin(\theta) \\ 0 & 1 & 0 \\ -\sin(\theta) & 0 & \cos(\theta) \end{pmatrix} \quad (\text{B.5})$$

Note that there is a fundamental difference between these two different transformations. The R_z matrix represents the actual rotation around the z axis of the nuclear spin with an applied magnetic field along the z axis. The R_{toH1} matrix just represents a coordinate transformation. For this pseudo-spin 1/2 system, however, we do not need to distinguish between the two different types of transformations. So, we

take the initial condition of spin along the quadrupole z axis,

$$I_{initial} = (0, 0, 1) \quad (\text{B.6})$$

and apply the appropriate transformations,

$$I_{final} = \text{Rz}[\Omega\tau] \cdot \text{RtoH1}^{-1} \cdot \text{Rz}[2h] \cdot \text{RtoH1} \cdot \text{Rz}[\Omega\tau] \cdot \text{RtoH1}^{-1} \cdot \text{Rz}[h] \cdot \text{RtoH1} \cdot I_{initial} \quad (\text{B.7})$$

This implements the pulse sequence: $\pi/2$ pulse - rotation angle h , dephasing angle $\Omega\tau$, π pulse - rotation angle $2h$, and another dephasing angle $\Omega\tau$. Note that the combination of transformations, $\text{RtoH1}^{-1} \cdot \text{Rz}[h] \cdot \text{RtoH1}$, rotates the spin around H_1 by an angle h . At the end, the spin is in the coordinate system of the quadrupole interaction.

We integrate the final spin over the dephasing angle $\Omega\tau$. We assume that this dephasing magnetic field is uniformly distributed over the entire range from $\Omega\tau = -\pi$ to π .

$$I_{av} = \int_{-\pi}^{\pi} I_{final} d\Omega\tau \quad (\text{B.8})$$

The results for I_{av} are

$$I_{x,av} = -8 \cos(\theta) \sin^3(\theta) \cos^2(h/2) \sin^4(h/2) \quad (\text{B.9})$$

$$I_{y,av} = -\sin^3(\theta) \sin^3(h) \quad (\text{B.10})$$

The z component, I_z , is not important since it will be static and will not contribute to the intensity.

Now, we want to derive the intensity. For an aligned experiment, where $\theta = \pi/2$ and $h = \pi/2$, the intensity is maximized and equals $I_y = -1$. The negative sign just arises from our choice of phase for the pulses which puts the nuclear magnetization pointing along the negative y -axis. For the unaligned experiment, we need to average over θ . The spin will precess around the axis of the quadrupole interaction (in the x - y plane), but the intensity is measured with an inductive coil with the axis in the

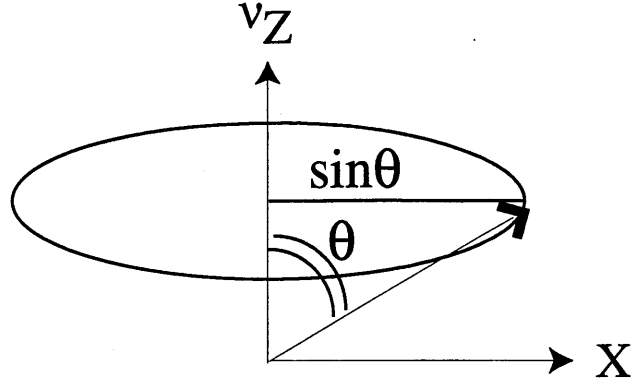


Figure B-2: Probability for the angle θ between H_1 and the crystal Z axis. The relative probability for any angle θ is the circumference of the circle shown, $2\pi \sin \theta$.

direction of H_1 . The component of the precessing magnetic field along the inductive coil will be $\propto \sin \theta$. Also, the distribution of the angle θ for the crystallites in the powder will be (figure B-2)

$$\frac{2\pi \sin \theta d\theta}{\int d\theta} = \frac{1}{2} \sin \theta \quad (\text{B.11})$$

So, to derive the overall intensity, we integrate over the possible angles, θ , between the crystallites Z axis and H_1 .

$$\text{Intensity} = \int_0^\pi \frac{1}{2} I_{av} \sin^2(\theta) d\theta \quad (\text{B.12})$$

The result is

$$\text{Intensity}_x = 0 \quad (\text{B.13})$$

$$\text{Intensity}_y = \frac{-16 \sin^3(h)}{30} \quad (\text{B.14})$$

The spin along the x direction cancels out, but the y direction gives us a maximum intensity of $16/30$ for $h = \pi/2$. So, NQR in unaligned powder will use the same pulse length as in a sample with $H_1 \perp Z$, but the intensity will be roughly half ($16/30$).

Now, a similar procedure of calculation is used for the change in $1/T_{2G}$ in unaligned powder. The nuclear spin-spin interaction is added during the times τ . The nuclear spin interaction is

$$\mathcal{H} = a_{zz} I_z S_z \quad (\text{B.15})$$

where I have called the two nuclear spins, I and S , just for bookkeeping purposes. The spin-spin interaction transformation on spin I is [15]

$$S-S = \begin{pmatrix} \cos(a\tau/2) & -2S_z \sin(a\tau/2) & 0 \\ 2S_z \sin(a\tau/2) & \cos(a\tau/2) & 0 \\ 0 & 0 & 1 \end{pmatrix} \quad (\text{B.16})$$

The complicated part arises from the fact that the components of the nuclear spin, S , also transform in the same way that the components of the spin, I , do when rf pulses are applied. We make the approximation that only the z-component (along the quadrupole axis) of the spin-spin interaction is important. This is a reasonable approximation in the copper-oxide materials because the hyperfine coupling to the electron spin is 2-3 times stronger along the z axis, so $a_{zz} \gg a_{xx}, a_{yy}$ [27]. This helps simplify the calculations because then this spin-spin interaction commutes with the dephasing interaction. We can ignore the fact that both of these interactions occur simultaneously, and apply them in whatever order we wish.

In order to make things look a little simpler, we define the interaction, $\text{Rpulse}[h] = \text{RtoH1}^{-1} \cdot \text{Rz}[h] \cdot \text{RtoH1}$. This interaction then implements the entire pulse of length h , including the coordinate transformations to and from the H_1 coordinates. So the interactions we apply are

$$I_{\text{before } \pi \text{ pulse}} = S-S_I \cdot \text{Rz}_I[\Omega_I \tau] \cdot \text{Rpulse}_I[h] \cdot I_{\text{initial}} \quad (\text{B.17})$$

$$I_{\text{final}} = \text{Rz}_S[\Omega_S \tau] \cdot \text{Rz}_I[\Omega_I \tau] \cdot S-S_S \cdot S-S_I \cdot \text{Rpulse}_S[2h] \cdot \text{Rpulse}_I[2h] \cdot I_{\text{before } \pi \text{ pulse}} \quad (\text{B.18})$$

where the subscript I or S denotes which nuclear spin the interaction is applied to. Also, the random dephasing interaction will in general be different for the two spins, so the rotation angle is $\Omega_I \tau$ for spin I and $\Omega_S \tau$ for spin S . As before, we integrate over the random dephasing interactions, $\Omega_I \tau$ and $\Omega_S \tau$. In addition, we take the trace over the spin S . This is done because the spin S has nearly equal probability to be in any particular direction before the pulse sequence begins. The polarization of the

nuclear spins is very tiny at our experimental temperatures, $\sim 10^{-4}$ at 5 K. We also use our result from the previous part of this calculation that the intensity is maximum for $h = \pi/2$. The result is

$$I_{av} = Tr_S \int_0^\pi d\Omega_I \tau \int_0^\pi d\Omega_S \tau I_{final}(h = \pi/2) \quad (\text{B.19})$$

$$I_{y,av} = -\sin^3 \theta [(1 - \cos^2 \theta) \cos(a\tau) + (\cos \theta - \cos^3 \theta) \sin(a\tau) + \cos^2 \theta] \quad (\text{B.20})$$

We can see here that for $\theta = \pi/2$, the interaction dependence is $\cos(a\tau)$ as we expect and the intensity is unity (-1). Now, we integrate this expression over the random distribution of the crystal axes as before,

$$\text{Spin-spin intensity} = \int_0^\pi \frac{1}{2} I_{y,av} \sin^2(\theta) d\theta = -\frac{16}{30} \frac{1}{7} (1 + 6 \cos(a\tau)) \quad (\text{B.21})$$

In the Gaussian approximation for T_{2G} , we match the second moments.

$$\exp\left(\frac{-(2\tau)^2}{2T_{2G}^2}\right) \approx 1 - \frac{(2\tau)^2}{2T_{2G}^2} \quad (\text{B.22})$$

$$\cos(a\tau) \approx 1 - \frac{(a\tau)^2}{2} \quad (\text{B.23})$$

$$\left(\frac{1}{T_{2G}}\right)^2 = \frac{a^2}{4} \quad (\text{B.24})$$

In this case, we have

$$\frac{1}{7} (1 + 6 \cos(a\tau)) \approx 1 - \frac{6}{7} \frac{(a\tau)^2}{2} \quad (\text{B.25})$$

$$\left(\frac{1}{T_{2G}}\right)_{\text{powder}}^2 = \frac{6}{7} \left(\frac{1}{T_{2G}}\right)_{z \text{ axis}}^2 \quad (\text{B.26})$$

In order to compare between $1/T_{2G}$ for NQR and NMR, we need to also include the factor of $\sqrt{2}$ which arises from the fact that for NQR there are twice as many ‘‘like’’ spins [27, 26]. For NQR, both the $+3/2 \leftrightarrow +1/2$ and the $-3/2 \leftrightarrow -1/2$ transitions have the same frequency, so the nuclei are flipped for all values of I_z . For NMR with a quadrupole interaction, the transitions all have different frequencies. So, if $1/T_{2G}$ is measured using the $+1/2 \leftrightarrow -1/2$ transition, the spins with $I = +3/2$ or $-3/2$ are not

flipped. Therefore, for NMR, equation B.1 requires another factor of 1/2 on the right hand side.

$$\left(\frac{1}{T_{2G}}\right)_{NMR, I=3/2}^2 = \frac{a_{zz}^2}{8} \quad (\text{B.27})$$

$$\left(\frac{1}{T_{2G}}\right)_{NQR, powder} = \sqrt{2}\sqrt{\frac{6}{7}} \left(\frac{1}{T_{2G}}\right)_{NMR, z \text{ axis}} = 1.31 \left(\frac{1}{T_{2G}}\right)_{NMR, z \text{ axis}} \quad (\text{B.28})$$

where the Z axis is defined both as the principle axis of the quadrupole interaction with $\eta = 0$ and the important spin component of the nuclear spin-spin interaction. Of course, this calculation only applies to spin $I=3/2$. This result is in good agreement with recent experiments, such as the experiments on the three-leg ladder, $\text{Sr}_2\text{Cu}_3\text{O}_5$, described in this thesis where the ratio of $1/T_{2G}$ from NQR versus NMR is 1.33 ± 0.03 . However, the results for the two-leg ladder, SrCu_2O_3 , are not in such good agreement with the ratio being 1.5 ± 0.1 . Also, these materials have $\eta \neq 0$, but the effect of this on the measured NQR $1/T_{2G}$ should be small since it is a slight alteration in the 7% effect of the calculation described in this appendix.

We should note that the $\approx 7\%$ effect ($\sqrt{6/7}$) calculated here is different from previous calculations done several years ago which arrived at a 3% effect [26]. The difference is that the previous calculations only considered the effect of the component of H_1 perpendicular to the Z axis. This approximation is perfectly valid as long as the nuclear spin is close to the Z axis (which would correspond to very short pulses). However, for the π pulses that we are considering, there is a significant difference in the resulting nuclear spin direction. To be specific, for example, if H_1 makes an angle of 45 degrees with the z axis, then a π pulse leaves the nuclear spin only 90 degrees away from the z axis. Approximating H_1 by its perpendicular component would give the result, $180 \sin(45)$ in degrees, or 127 degrees.

Of course, we should emphasize the limitations of this calculation also. This calculation applies only to $I=3/2$ and $\eta = 0$. In addition, it assumes that the Z axis is both the principle axis of the quadrupole interaction and the only important direction for the nuclear spin-spin indirect coupling. However, these assumptions seem well fulfilled for ^{63}Cu in high T_c copper-oxides.

Appendix C

NMR/NQR units notes

For conversion of hyperfine interactions from kOe/μ_B to energy units,

$$\text{hyperfine in eV} = \left(\frac{\gamma_e \hbar}{\mu_B} \right) (\gamma_n \hbar) (\text{hyperfine in kOe}/\mu_B) \quad (\text{C.1})$$

For a specific conversion [137],

$$\text{hyperfine in eV} = (2) (\gamma_n \hbar \text{ in J/gauss}) (6.24 \times 10^{21}) (\text{hyperfine in kOe}/\mu_B) \quad (\text{C.2})$$

For ^{63}Cu ,

$$\text{hyperfine in eV} = (9.3610^{-9}) (\text{hyperfine in kOe}/\mu_B) \quad (\text{C.3})$$

For ^{17}O ,

$$\text{hyperfine in eV} = (4.7410^{-9}) (\text{hyperfine in kOe}/\mu_B) \quad (\text{C.4})$$

This is really a conversion between two different quantities. The hyperfine given in kOe/μ_B is the magnetic field created at the nucleus per Bohr magneton of electron spin. The advantage of this formulation is that it is independent of the nucleus involved. To convert this into an energy requires the interaction energy of the nucleus with this magnetic field. The energy units provides the energy of interaction of the electron spin-nuclear spin system, A .

$$\mathcal{H}_{e-n} = AI \cdot S \quad (\text{C.5})$$

For conversion of susceptibility to Knight shift [79],

$$Kn_{spin} = \frac{A}{N_A \mu_B} \chi_{spin} \quad (C.6)$$

where A is the hyperfine coupling and N_A is Avogadro's number.

$$A \text{ in kOe}/\mu_B = 5.580 \frac{Kn_{spin}}{(\chi_{spin} \text{ in cm}^3/\text{mole})} \quad (C.7)$$

For calculations involving $1/T_1$, it is easiest to use the hyperfine interaction in units of electron volts. However, the equation given in chapter 2 is written for kOe/μ_B since that is conventional in NMR. Converting the earlier equations (eq. 2.13) shown here,

$$\left(\frac{1}{T_1}\right) = \frac{\gamma_n^2 \hbar}{2\mu_B^2} \sum_{\mathbf{q}} (F_{\perp,1}(\mathbf{q})^2 + F_{\perp,2}(\mathbf{q})^2) S(\mathbf{q}, \omega_n) \quad (C.8)$$

$$S(\mathbf{q}, \omega) = \chi''(\mathbf{q}, \omega) / (1 - \exp(-\hbar\omega/k_B T)) \quad (C.9)$$

The result for the equation of $1/T_1$ for the hyperfine in terms of electron volts and using the imaginary electron susceptibility, χ'' , instead of the spin structure factor, S .

$$\frac{1}{T_1} = \frac{kT}{2(\gamma_e \hbar)^2 \hbar^2 \omega_n} \sum_{\mathbf{q}} (F_{\perp,1}(\mathbf{q})^2 + F_{\perp,2}(\mathbf{q})^2) \chi''(\mathbf{q}, \omega_n) \quad (C.10)$$

For this equation, the units used are electron volts for kT , ω_n , and hyperfine coupling F . The units for \hbar are eV-sec and for $\chi''(\mathbf{q}, \omega_n)$ is the full susceptibility with the factor $(g\mu_B)^2$. To simplify calculation with the susceptibility, often the susceptibility has the factor $(g\mu_B)^2$ which cancels the factor of $(\gamma_e \hbar)^2$ in the denominator of the expression for $1/T_1$. With this simplification,

$$\frac{1}{T_1} = \frac{kT}{2\hbar^2 \omega_n} \sum_{\mathbf{q}} (F_{\perp,1}(\mathbf{q})^2 + F_{\perp,2}(\mathbf{q})^2) \chi''(\mathbf{q}, \omega_n) \quad (C.11)$$

and the imaginary susceptibility is in units of states/(eV spin).

The susceptibility in terms of states/(eV spin) can easily be converted to conven-

tional experimental units, cm^3/mole .

$$\chi \text{ (in cm}^3/\text{mole)} = (g\mu_B)^2 N_A \chi \text{ (in states/(eV spin))} \quad (\text{C.12})$$

Often, theoretical results for the susceptibility are given without any units specified. The energy scale in the susceptibility is set by the problem (in this case the exchange coupling J), so the units are states/(J spin) [66].

Bibliography

- [1] J.G. Bednorz and K.A. Müller, *Z. Phys. B* **64**, 189 (1986).
- [2] J. Bardeen, L.N. Cooper, and J.R. Schrieffer, *Phys. Rev.* **108**, 1175 (1957).
- [3] E. Manousakis, *Rev. Mod. Phys.* **63**, 1 (1991).
- [4] Y.J. Uemura *et al.*, *Phys. Rev. Lett.* **59**, 1045 (1987).
- [5] M. Greven *et al.*, *Z. fur Physik* **96**, 465 (1995).
- [6] R.J. Birgeneau, *et al.*, *Phys. Rev. B* **59**, 13788 (1999).
- [7] T. Imai *et al.*, *Phys. Rev. Lett.* **70**, 1002 (1993).
- [8] J. M. Tranquada *et al.*, *Nature (London)* **375**, 561 (1995).
- [9] P. Lee, MIT physics colloquium.
- [10] Neil W. Ashcroft and N. David Mermin, *Solid State Physics*, (Harcourt Brace, Fort Worth, 1976).
- [11] V. Jaccarino, *Proc. of Int. School of Physics, Enrico Fermi*, Academic Press, New York, 1967.
- [12] C. Kittel, *Introduction to Solid State Physics, 6th ed.*, (John Wiley and Sons, New York, 1986).
- [13] A. Abragam, *Principles of Nuclear Magnetism* (Oxford University Press, Oxford, 1961).

- [14] C.H. Pennington, PhD thesis (1989) University of Illinois.
- [15] C.P. Slichter, *Principles of Magnetic Resonance*, (Springer-Verlag, New York, 1990).
- [16] T. Moriya, J. Phys. Soc. Jpn. **18**, 516 (1963).
- [17] B. Shastry, Phys. Rev. Lett. **63**, 1288 (1989).
- [18] A. Narath, Phys. Rev. **162**, 320 (1967).
- [19] T. Imai *et al.*, J. Phys. Soc. Jpn. **57**, 1771 (1988); T. Imai *et al.*, J. Phys. Soc. Jpn. **57**, 2280 (1988).
- [20] S. M. Hayden *et al.*, Phys. Rev. Lett. **67**, 3622 (1991); *ibid*, **76**, 1344 (1996).
- [21] A. W. Sandvik, Phys. Rev. B **52**, R9831 (1995) and unpublished work by F. Naef and A. W. Sandvik.
- [22] F. Mila and T.M. Rice, Physica C **157**, 561 (1989).
- [23] B. Bleaney, K.D. Bowers, and M.H.L. Pryce, Proc. Royal Soc. London, A **228**, 166 (1955); A. Abragam and B. Bleaney, *Electron Paramagnetic Resonance of Transition Ions* (Oxford Univ. Press, New York, 1980).
- [24] T. Nakamura, Prog. Theor. Phys. **20**, 542 (1958).
- [25] M.A. Ruderman and C. Kittel, Phys. Rev. **96**, 99 (1954).
- [26] T. Imai *et al.*, Phys. Rev. Lett. **71**, 1254 (1993).
- [27] C. H. Pennington and C. P. Slichter, Phys. Rev. Lett. **66**, 381 (1991).
- [28] D. Thelen and D. Pines, Phys. Rev. B **49**, 3528 (1994).
- [29] M. Azuma *et al.*, Phys. Rev. Lett. **73**, 3463 (1994).
- [30] M. Greven, R. J. Birgeneau, and U.-J. Wiese, Phys. Rev. Lett. **77**, 1865 (1996).

- [31] A.K. McMahan, R.M. Martin, and S. Satpathy, Phys. Rev. B **38**, 6650 (1988).
- [32] P. Anderson, Phys. Rev. **79**, 950 (1950).
- [33] A. Abragam and Pryce, Proc. Roy. Soc. A **205**, 135 (1951).
- [34] A. Okazaki, K. C. Turberfield, and R. W. H. Stevenson, Phys. Lett. **8**, 9 (1964).
- [35] J.S. Smart, *Magnetism*, Vol. III (Academic Press, New York, 1963).
- [36] S. Gopalan, T. M. Rice, and M. Sigrist, Phys. Rev. B **49**, 8901 (1994).
- [37] M. H. Cohen and F. Reif, Solid State Phys. **5**, 321 (1957).
- [38] T. Shimizu, J. Phys. Soc. Japan **62**, 772 (1993).
- [39] C. H. Pennington *et al.*, Phys. Rev. B **39**, 2902 (1989).
- [40] J. Owen and J.H.M. Thornley, Rep. Prog. Phys. **29**, 675 (1966).
- [41] M. Takigawa *et al.*, Phys. Rev. Lett. **63**, 1865 (1989).
- [42] H. A. Bethe, Z. Phys. **71**, 205 (1931).
- [43] R. R. P. Singh, M. E. Fisher, and R. Shankar, Phys. Rev. B **39**, 2562 (1989).
- [44] S. Sachdev, Phys. Rev. B **50**, 13006 (1994).
- [45] O. A. Starykh, A. W. Sandvik, and R. R. P. Singh, Phys. Rev. B **55**, 14953 (1997).
- [46] S. Eggert, I. Affleck, and Minoru Takahashi, Phys. Rev. Lett. **73**, 332 (1994).
- [47] M. Takahashi and T. Sakai, Haldane Magnets and Related 1D Magnets: Properties in Magnetic Field in *Computational Physics as a New Frontier in Condensed Matter Research*, edited by H. Takayama, *et al.*, Phys. Soc. of Japan (1995).
- [48] M. Takigawa, *et al.*, Phys. Rev. B **56**, 13681 (1997); M. Takigawa, *et al.*, Phys. Rev. Lett. **76**, 4612 (1996).

- [49] M. Tanaka, M. Hasegawa, and H. Takei, *Physica C* **261**, 309 (1996).
- [50] T. M. Rice, S. Gopalan, and M. Sigrist, *Europhys. Lett.* **23**, 445 (1993).
- [51] N. Motoyama, H. Eisaki, and S. Uchida, *Phys. Rev. Lett.* **76**, 3212 (1996).
- [52] A. Keren *et al.*, *Phys. Rev. B* **48**, 12926 (1993); K. M. Kojima *et al.*, *Phys. Rev. Lett.* **78**, 1787 (1997).
- [53] I.A. Zaliznyak, *et al.*, cond-mat/9812440, Los Alamos e-print archives.
- [54] M. Matsuda *et al.*, *Phys. Rev. B* **55**, R11953 (1997).
- [55] O. A. Starykh, R. R. P. Singh, and A. W. Sandvik, *Phys. Rev. Lett.* **78**, 539 (1997).
- [56] M. Takigawa *et al.*, *Phys. Rev. B* **55**, 14129 (1997).
- [57] K. Fabricius and B. McCoy, *Phys. Rev. B* **57**, 8340 (1998).
- [58] P.G. deGennes, in *Magnetism*, edited by G. Rado and H. Suhl (Academic, New York, 1963), Vol. 3, p. 115.
- [59] F. Borsa and M. Mali, *Phys. Rev. B* **9**, 2215 (1974); D. Hone, C. Scherer, and F. Borsa, *Phys. Rev. B* **9**, 965 (1974).
- [60] B. N. Narozhny *et al.*, *Phys. Rev. B* **58**, R2921 (1998); B. N. Narozhny, *Phys. Rev. B* **54**, 3311 (1996).
- [61] M. Takigawa, *et al.*, *Phys. Rev. Lett.* **76**, 2173 (1996).
- [62] M. A. Kastner *et al.*, *Rev. Mod. Phys.* **70**, 897 (1998).
- [63] K. R. Thurber *et al.*, *Phys. Rev. Lett.* **79**, 171 (1997).
- [64] P.C. Hohenberg, *Phys. Rev.* **158**, 383 (1967); N.D. Mermin and H. Wagner, *Phys. Rev. Lett.* **17**, 1133 (1966).
- [65] S. Chakravarty, B. I. Halperin, and D. R. Nelson, *Phys. Rev. B* **39**, 2344 (1989).

- [66] M. Takahashi, Phys. Rev. B **40**, 2494 (1989).
- [67] A. W. Sandvik and D. J. Scalapino, Phys. Rev. B **51**, 9403 (1995) and unpublished.
- [68] R. R. P. Singh and M. Gelfand, Phys. Rev. B **42**, 996 (1990).
- [69] S. Tyc, B. I. Halperin, and S. Chakravarty, Phys. Rev. Lett. **62**, 835 (1989); S. Tyc and B. I. Halperin, Phys. Rev. B **42**, 2096 (1990).
- [70] P. Hasenfratz and F. Niedermayer, Phys. Lett. B **268**, 231 (1991).
- [71] A.V. Chubukov, S. Sachdev, and J. Ye, Phys. Rev. B **49**, 11919 (1994).
- [72] D. Vaknin, *et al.*, Phys. Rev. B **41**, 1926 (1990).
- [73] A. Cuccoli, V. Tognetti, R. Vaia, and P. Verrucchi, Phys. Rev. B **56**, 14456 (1997).
- [74] B. J. Suh *et al.*, Phys. Rev. Lett. **75**, 2212 (1995).
- [75] Y. Tokura *et al.*, Phys. Rev. B **41**, 11657 (1990).
- [76] Z. Hiroi, N. Kobayashi, and M. Takano, Physica C **266**, 191 (1996).
- [77] L.L. Miller, *et al.*, Phys. Rev. B **41**, 1921 (1990).
- [78] M. Takigawa *et al.*, Phys. Rev. B **43**, 247 (1991).
- [79] Y. Yoshinari, *et al.*, J. Phys. Soc. Japan **59**, 3698 (1990).
- [80] H. Monien, D. Pines, and M. Takigawa, Phys. Rev. B **43**, 258 (1991).
- [81] M. Makivic and H-Q. Ding, Phys. Rev. B **43**, 3562 (1991).
- [82] J. S. M. Harvey, Proc. Royal Soc. London A **285**, 581 (1965).
- [83] Lema, *et al.*, cond-mat 9705316, Los Alamos archive (1997).
- [84] S. Chakravarty and R. Orbach, Phys. Rev. Lett. **64**, 224 (1990).

- [85] A. Sokol, R. R. P. Singh, and N. Elstner, *Phys. Rev. Lett.* **76**, 4416 (1996).
- [86] A. Sokol, E. Gagliano, and S. Bacci, *Phys. Rev. B* **47**, R14646 (1993).
- [87] P. Kopietz, *Phys. Rev. B* **41**, 9228 (1990); P. Kopietz and S. Chakravarty, *Phys. Rev. B* **56**, 3338 (1997).
- [88] A. M. Tsvelik, *Quantum Field Theory in Condensed Matter Physics* (Cambridge University Press, 1995).
- [89] S. Chakravarty *et al.*, *Phys. Rev. B* **43**, 2796 (1991).
- [90] M. Makivic and M. Jarrell, *Phys. Rev. Lett.* **68**, 1770 (1992).
- [91] D. R. Grempel, *Phys. Rev. Lett.* **61**, 1041 (1988); T. Becher and G. Reiter, *Phys. Rev. Lett.* **64**, 109 (1990); G. M. Wysin and A. R. Bishop, *Phys. Rev. B* **42**, 810 (1990); Y. A. Kosevich and A. Chubukov, *JETP* **64**, 654 (1987).
- [92] B. Keimer *et al.*, *Phys. Rev. B* **46**, 14034 (1992). Also see H. Casalta, H. Alloul, and J.-F. Marucco, *Physica C* **204**, 331 (1993).
- [93] R. J. Gooding *et al.*, *Phys. Rev. B*, **55**, 6360 (1997).
- [94] H. Takagi *et al.* *Phys. Rev. Lett.* **69**, 2975 (1992).
- [95] F. C. Chou *et al.*, *Phys. Rev. Lett.* **75**, 2204 (1995).
- [96] S. Wakimoto *et al.*, *Phys. Rev. B* **60**, R769 (1999).
- [97] L. Reven *et al.*, *Phys. Rev. B* **43**, 10466 (1991).
- [98] B. O. Wells *et al.*, *Phys. Rev. Lett.* **74**, 964 (1995).
- [99] R. M. White, *Quantum Theory of Magnetism* (Springer-Verlag, New York, 1983), p. 209.
- [100] F.D.M. Haldane, *Phys. Lett.* **93A**, 464 (1983); *Phys. Rev. Lett.* **50**, 1153 (1983); *J. Appl. Phys.* **57**, 3359 (1985); I. Affleck, *Nucl. Phys.* **B257**, 397 (1985).

- [101] M. Troyer, H. Tsunetsugu, and T.M. Rice, Phys. Rev. B **50**, 13515 (1994).
- [102] E. Dagotto and T. M. Rice, Science **271**, 618 (1996).
- [103] P.W. Anderson, Science **235**, 1196 (1987).
- [104] X.-G. Wen and P.A. Lee, Phys. Rev. Lett. **76**, 503 (1996).
- [105] M. Troyer, H. Tsunetsugu, and D. Wurtz, Phys. Rev. B **50** 13515 (1994).
- [106] M. Uehara *et al.*, J. Phys. Soc. Jpn. **65**, 2764 (1996).
- [107] T. Imai *et al.*, Phys. Rev. Lett. **81**, 220 (1998).
- [108] K. Ishida *et al.*, Phys. Rev. B **53**, 2827 (1996).
- [109] K. Kumagai *et al.*, Phys. Rev. Lett. **78**, 1992 (1997).
- [110] H. Mayaffre *et al.*, Science **279**, 345 (1998).
- [111] P. Carretta, P. Ghigna, and A. Lascialfari, Phys. Rev. B **57**, 11545 (1998); P. Carretta *et al.*, Phys. Rev. B **56**, 14587 (1997).
- [112] M. Takigawa, N. Motoyama, H. Eisaki, and S. Uchida, Phys. Rev. B **57**, 1124 (1998).
- [113] K. Magishi *et al.*, Physica (Amsterdam) **282C-287C**, 1115 (1997)
- [114] T. Osafune, N. Motoyama, H. Eisaki, and S. Uchida, Phys. Rev. Lett. **78**, 1980 (1997); and unpublished.
- [115] M. Kato, K. Shiota, and Y. Koike, Physica C **258**, 284 (1996).
- [116] R. S. Eccleston *et al.*, Phys. Rev. Lett. **81**, 1702 (1998).
- [117] M. Matsuda, unpublished.
- [118] M. Arai and H. Tsunetsugu, Phys. Rev. B **56**, R4305 (1997); Y. Mizuno, T. Tohyama, and S. Maekawa, Phys. Rev. B **58**, R14713 (1998).

- [119] S. A. Carter *et al.*, Phys. Rev. Lett. **77**, 1378 (1996).
- [120] M. Azuma *et al.*, J. Phys. Soc. Japan **67**, 740 (1998).
- [121] S. Katano *et al.*, Phys. Rev. Lett. **82**, 636 (1999).
- [122] A. W. Sandvik *et al.*, Phys. Rev. B **53**, R2934 (1996).
- [123] D. Ivanov and P. Lee, cond-mat 9807187.
- [124] N. Nücker *et al.*, Phys. Rev. B **37**, 5158 (1988); A. Fujimori, E. Takayama-Muromachi, Y. Uchida, and B. Okai, Phys. Rev. B **35**, 8814 (1987).
- [125] T. Adachi *et al.*, Solid State Comm. **105**, 639 (1998).
- [126] A. W. Hunt *et al.*, Phys. Rev. Lett. **82**, 4300 (1999).
- [127] A. H. Castro Neto and Daniel Hone, Phys. Rev. Lett. **76**, 2165 (1996); C. N. A. van Duin and J. Zaanen, Phys. Rev. Lett. **80**, 1513 (1998); Z. Wang, Phys. Rev. Lett. **78**, 126 (1997).
- [128] C. Buragohain and S. Sachdev, Phys. Rev. B **59**, 9285 (1999).
- [129] Y. J. Kim *et al.*, cond-mat/9902248.
- [130] D. C. Johnston, Phys. Rev. B **54**, 13009 (1996).
- [131] R. Pozzi *et al.*, Phys. Rev. B **56**, 759 (1997).
- [132] I. Ichinose and Y. Kayama, Nuclear Physics B **522**, 569 (1998).
- [133] K. Kojima *et al.*, Phys. Rev. Lett. **74**, 2812 (1995).
- [134] M. Greven and R. J. Birgeneau, Phys. Rev. Lett. **81**, 1945 (1998).
- [135] M. Azuma *et al.*, Phys. Rev. B **55**, R8658 (1997).
- [136] D. Reznik *et al.*, Phys. Rev. B **53**, R14741 (1996).
- [137] A.J. Millis, H. Monien, and D. Pines, Phys. Rev. B **42**, 167 (1990).